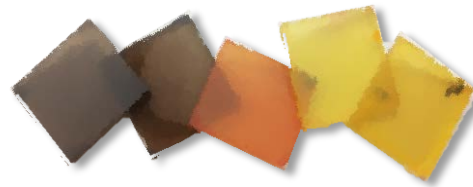




Prifysgol Abertawe
Swansea University

Coleg Peirianeg
College of Engineering

IMPROVING THE AESTHETICS AND PERFORMANCE OF PEROVSKITE MATERIALS FOR PHOTOVOLTAICS



Tamara D. McFarlane

Submitted to Swansea University in fulfilment
of the requirements for the degree of
Doctor of Philosophy

Swansea University
Department of Materials Engineering
2021

DECLARATION

This work has not previously been accepted in substance for any degree and is not being concurrently submitted in candidature for any degree.

Signed 

Date...28th April 2021

STATEMENT 1

This thesis is the result of my own investigations, except where otherwise stated. Other sources are acknowledged by footnotes giving explicit references. A bibliography is appended.

Signed... 

Date...28th April 2021

STATEMENT 2

I hereby give consent for my thesis, if accepted, to be available for photocopying and for inter-library loan, and for the title and summary to be made available to outside organisations.

Signed... 

Date...28th April 2021

Summary

Within the last decade, lead halide perovskite solar cells have rapidly evolved to the cusp of commercialisation. Current record device efficiencies have surpassed 25% however; a principal limitation of these materials is their instability on exposure to ambient conditions. Methylammonium lead tri-bromide (MAPbBr₃) perovskite has shown superior stability over other lead halide perovskite materials, yet the efficiencies of MAPbBr₃ devices are significantly lower with a record efficiency of 10.4%.

This research investigates the treatment of MAPbBr₃ perovskite solar cells with organic dyes of complementary absorbance in a bid to maximise the light harvesting, increase the photocurrent and improve the device efficiency.

Initial investigations focused on developing an optimised build method capable of manufacturing MAPbBr₃ devices which consistently achieve above 1% efficiency. The optical characterisation of six organic dyes revealed a red indoline dye, D205 and a blue squaraine, SQ2 (which both absorb strongly between 300-700 nm) would offer the best complementary absorbance to MAPbBr₃ perovskite. On adding the dyes, the perovskite layer underwent an evident colour change highlighting the potential for coloured perovskite cells which could be beneficial for building-integrated applications. MAPbBr₃ cells co-sensitised using a novel method (which sensitises the film after perovskite crystallisation) show improved efficiency (2.6% SQ2, 3.1% D205) over perovskite-only devices (2%) with a 10% photocurrent contribution from the dye. Whilst increases in the photocurrent are observed with co-sensitisation, increased device efficiencies are mainly derived from improvements in the fill factor. We also see lower series resistance and increased photoluminescence lifetime with co-sensitisation where control and co-sensitised MAPbBr₃ thin-films produce average lifetimes of 0.44 ns and 0.80 ns, respectively.

Further investigation has revealed the dye solvent, toluene, and the dye both help to improve device performance acting as both a treatment and a second sensitiser in the device by passivating defects and lowering recombination losses whilst providing additional photocurrent through increased absorbance. As a result, co-sensitised devices show slower recombination kinetics resulting in increased open-circuit voltage under lower light levels. These effects have proven beneficial for thicker co-sensitised devices (>0.7 μm) where they have often translated into large increases in device efficiency. In future, this may be beneficial for indoor or lower light level PV systems including within the rapidly expanding internet of things market.

Acknowledgements

I would firstly like to express my gratitude to the EPSRC, Innovate UK and the European Regional Development Fund (administered through the Welsh Government) for the generous financial support to the Sêr Solar program and the SPECIFIC Innovation and Knowledge Centre. I am also grateful to Swansea University and the College of Engineering for their support over the course of this research program.

Thank you to my supervisors Dr. Matthew Davies and Dr. Cecile Charbonneau for entrusting me with this project and for welcoming me into the Applied Photochemistry Group at Swansea University. I am extremely grateful to Matthew in particular, whose continued guidance, patience and understanding throughout was instrumental in getting me to the finish line. I would also like to thank to Dr. Peter Douglas for kindly lending me several books which have helped with the write-up of this work.

I wish to thank the members and staff of both the Applied Photochemistry Group and the SPECIFIC PV team for their support, help and input over the last 4 years. In particular, my fellow postgraduate students and friends: Dr. Ben Smith, Dave Richards and Amirah Way who's offer of coffee and the opportunity to procrastinate was always warmly welcomed. Thanks also to, Dr. Adam Pockett and Dr. Catherine De Castro for kindly carrying out the impedance spectroscopy and TCSPC measurements included in this work. Lastly I'd like to thank my friends and family. Writing a thesis during a global pandemic has been quite the challenge but it was made considerably easier due to several people who I can't thank enough for their continued support and encouragement.

Here's to my best butties, Carys and Nia for their invaluable friendship and who, as successful female engineers, continue to motivate and inspire me as I move forward in my career. To two of my oldest friends Lauren and Emily, whose solid support and friendship for the last 19 years has been irreplaceable, thank you both for the walks and the laughs!

Finally, to my parents, who have kept me going through thick and thin with their words of wisdom and ample gin supply. Thank you to my dad, Allan, who has fixed my car and helped get me to the lab more times in the last 4 years than I'm able to remember.

And to my mum, Anita - without your supporting hugs, pep-talks and head-clearing dog walks this wouldn't have been possible, this one's for you.

Contents

Abbreviations.....	1
1 Introduction	4
1.1 Preface	5
1.2 The absorption of sunlight.....	7
1.3 A history of solar cells.....	11
1.3.1 First generation.....	11
1.3.2 Second generation	12
1.3.3 Third generation	13
1.3.3.1 Dye-sensitised solar cells	13
1.3.3.2 Solid state dye-sensitised solar cells	18
1.4 Perovskite solar cells	19
1.4.1 Lead halide perovskites.....	19
1.4.2 Early development of perovskite solar cells	22
1.4.3 General lead halide perovskite device architectures	26
1.4.4 Device operating principle	28
1.4.5 Recombination losses.....	31
1.4.6 Hysteresis	36
1.5 References	39
2 Experimental methods	53
2.1 Manufacture of perovskite solar cells.....	53
2.1.1 Preparation of perovskite thin-films.....	53
2.1.2 Preparation of the perovskite layer.....	55
2.1.3 Full device manufacture	56
2.2 Co-sensitisation of perovskite solar cells	59
2.2.1 Preparation of dye solutions.....	59
2.2.2 Solid state dyed thin-film preparation.....	59
2.2.3 Co-sensitisation methods	59

2.2.3.1	'Dye before' (DB) method	59
2.2.3.2	'Dye after' (DA) method.....	59
2.3	Characterisation of perovskite thin-films	60
2.3.1	UV-Visible-near Infrared (UV-Vis-NIR) spectroscopy.....	60
2.3.2	Fluorescence spectroscopy.....	61
2.3.2.1	Steady-state	62
2.3.2.2	Time-correlated single photon counting (TCSPC).....	63
2.3.3	X-ray diffraction (XRD).....	66
2.3.4	Optical microscopy	68
2.3.5	Profilometry measurements.....	68
2.4	Characterisation of perovskite solar cells.....	69
2.4.1	Current-voltage measurements (J-V)	69
2.4.2	Incident photon-to-current efficiency (IPCE)	74
2.4.3	Light box stability storage.....	76
2.4.4	Impedance spectroscopy (IS)	77
2.5	Data processing.....	82
2.5.1	Statistical analysis	82
2.6	References	83
3	Optimisation and characterisation of MAPbBr₃ perovskite solar cells	86
3.1	Introduction	86
3.2	Experimental methods	89
3.2.1	Anti-solvent drip	90
3.2.2	PTAA hole transport layer	90
3.3	Results and discussion	91
3.3.1	Characterisation of MAPbBr ₃ perovskite.....	91
3.3.2	Method optimisation	93
3.3.2.1	Perovskite annealing temperature	95
3.3.2.2	Solvent system	99
3.3.2.3	Blocking layer deposition.....	104

3.3.2.4	Anti-solvent drip	105
3.3.2.5	Hole transport layer	108
3.3.2.6	Final build results	109
3.4	Conclusions	112
3.5	References	113
4	Photochemical characterisation of organic dyes for co-sensitisation	118
4.1	Introduction	118
4.2	Experimental methods	120
4.2.1	Co-sensitising dyes.....	120
4.2.2	UV-Visible-near Infrared (UV-Vis-NIR) spectroscopy of organic dyes	121
4.2.3	Steady-state fluorescence of organic dyes	121
4.2.4	Determination of dye molar extinction coefficients.....	121
4.2.5	Preparation of dye solutions and solid state thin-films	125
4.3	Results and discussion	126
4.3.1	Indoline dyes – D149, D205 and D131	126
4.3.2	Squaraine dye - SQ2.....	129
4.3.3	Diketopyrrolopyrrole dye - Dyenamo blue	131
4.3.4	Triphenylamine dye - LEG4	133
4.3.5	Comparison of dyes for co-sensitisation	135
4.3.6	Solid state DSSC performance	137
4.4	Conclusions	142
4.5	References	143
5	Co-sensitisation of perovskite solar cells with organic dyes	147
5.1	Introduction	147
5.2	Experimental methods	151
5.2.1	Mesoporous titania preparation for varied thickness	151
5.2.2	Determination of molar extinction coefficient of D205 in DMSO	151
5.2.3	Desorption of D205 from co-sensitised thin-films.....	152
5.3	Results and discussion	153

5.3.1	Proof of principle	153
5.3.2	Methods of co-sensitisation.....	155
5.3.3	Dye loading	161
5.3.3.1	Dye concentration	161
5.3.3.2	Mesoporous layer thickness	165
5.3.3.3	Quantitation of dye loading.....	180
5.3.4	Co-sensitisation of MAPbI ₃ perovskite.....	185
5.4	Conclusions	191
5.5	References	193
6	The interaction between perovskite and dye	197
6.1	Introduction	197
6.2	Experimental methods	200
6.2.1	Planar cells	200
6.2.2	Mesoporous titania preparation for varied thickness	200
6.2.3	Toluene soak	200
6.2.4	Approximate series resistance.....	200
6.3	Results and discussion.....	202
6.3.1	Effect of toluene on active layer	206
6.3.2	Photoluminescence.....	209
6.3.3	Series resistance	214
6.3.4	Impedance spectroscopy	220
6.3.5	Stability	226
6.4	Conclusions	233
6.5	References	235
7	Conclusions and further work	240

Abbreviations

ACN	Acetonitrile
AM	Air mass
ADC	Analogue-to-digital converter
CO ₂	Carbon dioxide
CdTe	Cadmium telluride
CDCA	Chenodeoxycholic acid
CB	Chlorobenzene
CFD	Constant fraction discriminator
CIGS	Copper indium gallium (di)selenide
Cds	Copper sulphide
C _B	Conduction band
c-Si	Crystalline silicon
c-TiO ₂	Compact titania
DFT	Density functional theory
DEE	Diethyl ether
DLSR	Digital single-lens reflex camera
DPP	Diketopyrrolopyrrole
DMF	Dimethylformamide
DMSO	Dimethyl sulfoxide
D-A-D	Donor-acceptor-donor
D- π -A	Donor- π -acceptor
DA	Dye after method
DB	Dye before method
DSSC	Dye-sensitised solar cell
ESM	Earth system models
EM	Electromagnetic radiation
ETL	Electron transport layer
EA	Ethyl acetate
ETOH	Ethanol

EJ	Exajoule
EQE	External quantum efficiency
FF	Fill factor
FTO	Fluorine doped tin oxide
FRET	Förster resonance energy transfer
FWHM	Full width at half-maximum
Hex	Hexane
HOMO	Highest occupied molecular orbital
HTL	Hole transport layer
IS	Impedance spectroscopy
IPCE	Incident photon to current efficiency
IR	Infrared
IRF	Instrument response function
IoT	Internet of things
ICT	Intramolecular charge transfer
J_{sc}	Short-circuit current density
KRICT	Korea research institute of chemical technology
LHE	Light harvesting efficiency
LUMO	Lowest unoccupied molecular orbital
MABr	Methylammonium bromide
MAI	Methylammonium iodide
MAPbBr ₃	CH ₃ NH ₃ PbBr ₃
MAPbI ₃	CH ₃ NH ₃ PbI ₃
MIT	Massachusetts institute of technology
mp-TiO ₂	Mesoporous titania
MSSC	Meso-superstructured solar cell
NIR	Near infrared
NREL	National renewable energy laboratory
PTAA	Polytriarylamine
PCE	Power conversion efficiency
PMT	Photomultiplier tube

PL	Photoluminescence
PSC	Perovskite solar cell
PV	Photovoltaic
SA	Solvent annealing
SRH	Shockley-read hall
SS-DSSC	Solid state dye-sensitised solar cell
ss-PL	Steady-state photoluminescence
TBA	Tert-butanol
Tol	Toluene
TCSPC	Time-correlated single photon counting
TRPL	Time-resolved photoluminescence
TAC	Time-to-analogue converter
TiO ₂	Titania/titanium dioxide
TCO	Transparent conductive oxide
V _B	Valence band
Vis	Visible
V _{oc}	Open-circuit voltage
UNFCCC	United nations framework convention on climate change
U.S. EIA	United States energy information administration
UV	Ultraviolet
XRD	X-ray diffraction

1 Introduction

The introductory Chapter below provides a basic overview of photovoltaics and a background to perovskite solar cells including their development and operating principle. This is followed by an experimental Chapter which explains the various methods and techniques used to manufacture and characterise the perovskite thin-films and devices used in this work. The subsequent Chapters then illustrate and discuss the research included in this thesis, which overall aims to improve the aesthetics and performance of lead halide perovskite solar cells through co-sensitisation with organic dyes of complementary absorbance. This is in a bid to extend the light harvesting range and therefore, the cell efficiency. Initial investigations aim to characterise MAPbBr₃ perovskite and develop an optimised build method capable of manufacturing MAPbBr₃ devices which consistently achieve over 1% efficiency. The second research Chapter then aims to optically characterise several organic dyes to identify which can offer the best complementary absorbance to MAPbBr₃ perovskite. Chapter 5 explores the co-sensitisation of MAPbBr₃ perovskite solar cells and aims to develop an optimised co-sensitisation method capable of achieving higher device efficiencies. The final research Chapter then focusses on investigating the effects of co-sensitisation on the perovskite and aims to clarify and discuss the relationship between the two sensitisers.

1.1 Preface

A solar or photovoltaic (PV) cell is an electrical device capable of harnessing the sun's light for the generation of clean and renewable energy. The sun provides an infinite and high-energy resource which supplies the Earth's surface with an estimated 3,400,000 EJ of solar energy per annum, where an exajoule (EJ) is equivalent to one quintillion (10^{18}) joules. To put this into perspective, this figure is 7 to 8 thousand times the annual primary energy consumption for the entire globe.¹

In 2019, the U.S. Energy Information Administration (EIA) predicted that the global annual primary energy consumption will grow by nearly 50% from 2018 to 2050.² Despite significant advances in solar cell technology over the last 60 years, fossil fuels such as coal, natural gas and oil are still used as a major resource to meet global energy demands and currently supply over 84% of the world's energy.³

Fossil fuels are widely recognised as the main cause of global warming primarily due to the high levels of carbon dioxide (CO_2) released on combustion. Within the energy sector, the largest share of greenhouse gas emissions come from transportation (28%), electricity generation (27%) and industry (22%).⁴

Since the beginning of the industrial revolution in the 18th century, atmospheric CO_2 concentrations have risen from 280 ppm (pre-industrial levels) to 415 ppm, present day.^{5,6} As a result, the average global surface temperature increased by 0.99 °C between the years 1880 and 2019.⁷ Should the current rate of CO_2 and greenhouse gas emission be allowed to continue, Earth System Models (ESMs) have predicted this temperature to rise between 1.0 and 3.7 °C during the 21st century alone.⁸ This is anticipated to have devastating effects worldwide including: extreme weather changes, rising sea levels, human health risks and damage to wildlife and ecosystems amongst a range of other issues.⁹ In 2016, at the United Nations Framework Convention on Climate Change (UNFCCC), 196 countries signed The Paris Agreement which pledges to improve or introduce measures aimed at keeping the increase in global average temperature to well below 2 °C above pre-industrial levels.¹⁰ This will require replacing fossil fuel energy sources with sources of clean and renewable energy, such as solar. As a nation committed to The Paris Agreement, the UK is currently increasing the amount of solar technology deployed year on year. As of July 2020, the Department for

Business, Energy & Industrial Strategy, reported the overall UK solar PV capacity as 13,447 MW across 1,041,745 installations, an increase of 18 % compared to 4 years ago (11,429 MW, July 2016).¹¹ The vast majority of solar installations in the UK are manufactured using crystalline silicon. But despite dominating the commercial PV market, silicon solar cell manufacture is an uneconomical, high energy process in which 100,000 tons of silicon is lost as waste per year during the cropping and sawing of high purity silicon ingots.¹²⁻¹⁴

Perovskite solar cells (PSC's) present the potential for a cost effective, solution-processed, low-embodied energy solar technology. Their high absorbance in the visible enables their use as flexible lightweight thin-films compatible with roll-to roll printing allowing for low-cost, large scale manufacture under high throughput.¹⁵⁻¹⁹ As a result, PSC's can be manufactured for 1/20th of the cost of current silicon based technologies.²⁰ PSC's also maintain high performance under diffuse radiation and low light conditions making them potential candidates for indoor applications especially within the rapidly expanding Internet of Things (IoT) market.²¹⁻²³ Due to a culmination of these commercially attractive properties, lead halide perovskites have now become one of, if not the fastest growing and most widely researched solar technologies in the world.

1.2 The absorption of sunlight

Sunlight is comprised of electromagnetic (EM) waves where each EM wave is transmitted as a ‘packet or bundle’ of energy referred to as a photon.²⁴ As energy carrying waves, each photon has a specific wavelength (λ) and frequency (ν) which are inversely related:

$$\lambda = c/\nu \quad (1)$$

where c is the speed of light (3.0×10^{10} cm s⁻¹ in a vacuum).

The wavelength and frequency dictate the photon energy (E), where the energy (in Joules) is directly proportional to the frequency:

$$E = h\nu \quad (2)$$

and inversely proportional to the wavelength:

$$E = \frac{h \cdot c}{\lambda}$$

Where h is Planck’s constant ($6.62607004 \times 10^{-34}$ m² kg/s).

The sunlight which arrives at the Earth’s surface is comprised of ultraviolet, visible and infrared wavelengths which collectively provide a high-energy resource supplying approximately 0.9 to 3.2 electronvolts per photon or 87 to 308 kilojoules per mole.²⁵ On absorbing this energy, a molecule can undergo electronic transitions which involve the movement of electrons.

For organic molecules, the ability to absorb ultraviolet or visible light is facilitated by chromophoric functional groups comprised of unsaturated π -bonds which are capable of absorbing light >200 nm. These functional groups contain discrete energy levels also called molecular orbitals which are separated into π and π^* (bonding and anti-bonding) orbitals by an energy gap. A photon with energy equal to or in excess of the energy gap can be absorbed by the chromophore causing the excitation of an electron from the highest occupied molecular orbital (HOMO) i.e. the highest energy orbital which contains electrons

to the lowest unoccupied molecular orbital (LUMO) i.e. the lowest energy orbital which doesn't contain electrons. Electronic transition between the HOMO and LUMO level represents the lowest energy transition possible and results in the conversion of the molecule from the ground state to the excited state. This process is referred to as 'excitation'.

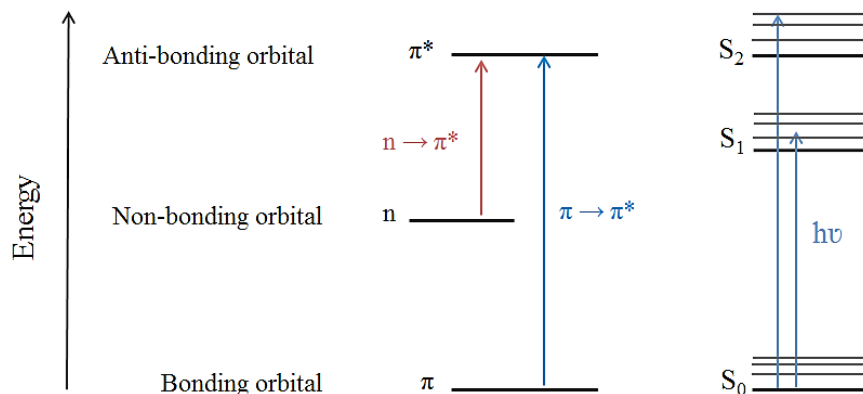


Figure 1.0: (Left) Basic schematic showing the electronic transition of π -electrons (contained within π -bonds) to the excited state i.e. the anti-bonding, π^* orbital and the electronic transition of lone electrons (non-bonding electrons, n) to the anti-bonding, π^* orbital. (Right) Excitation of an electron from the HOMO level (ground state, S_0) to the LUMO level (excited state, S_1) following the absorption of a photon, $h\nu$.

For organic molecules, the most common and important transitions involve those pictured in Figure 1.0, i.e. $n \rightarrow \pi^*$ and $\pi \rightarrow \pi^*$ as these transitions both occur in the visible range (200-800 nm). Therefore, they can be measured using UV/Vis spectroscopy, a technique which is explained further in Section 2.3.1.

In large molecular systems such as inorganic semiconductors, the overlap and mixing of many molecular orbitals causes the energy levels to adopt a band-like structure, where quantised energy levels are no longer distinguishable. This band-like structure is comprised of a lower energy valence band (V_B) and a higher energy conduction band (C_B) separated by a band-gap. These two bands are analogous to the HOMO and LUMO levels of organic molecules as described above. On illumination, photons are absorbed within the semiconductor causing the excitation of an electron from the valence band into the conduction band. This concomitantly creates a vacancy within the valence band ((referred to as a hole (h^+)) and an electron-hole pair is formed. The electron and hole (charge carriers)

rapidly relax (thermalise) to the lowest energy configuration, i.e. the bottom (minimum) of the conduction band and top (maximum) of the valence band, respectively (Figure 1.1).²⁶

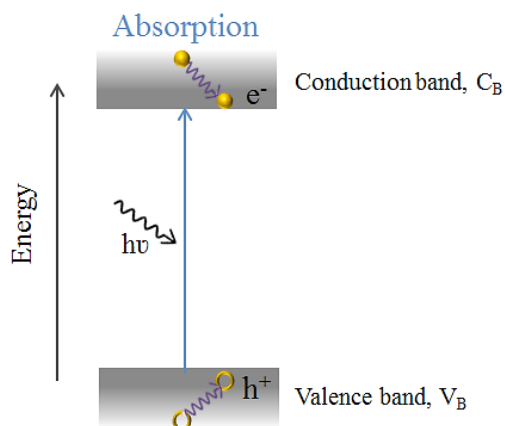


Figure 1.1: Schematic showing the basic photo-excitation of an inorganic semiconductor and the generation of an electron (e^-) hole (h^+) pair. Each charge carrier relaxes to the band edge by losing excess energy in the form of heat (thermalisation). Upward electronic transitions involve the excitation of electrons to higher energy levels generating an electronically excited molecule.

The bandgap (E_g) describes the minimum amount of energy required to generate an electron-hole pair and can be described as direct or in-direct based on the crystal momentum (a vector related to the movement of electrons in a crystal lattice) of the two bands.²⁷ For semiconductors with a direct bandgap, the valence and conduction bands share the same crystal momentum i.e. the valence band maximum and conduction band minimum occur at the same momentum therefore, the absorbed energy has to only equal the bandgap energy of the semiconductor to create an electron-hole pair.

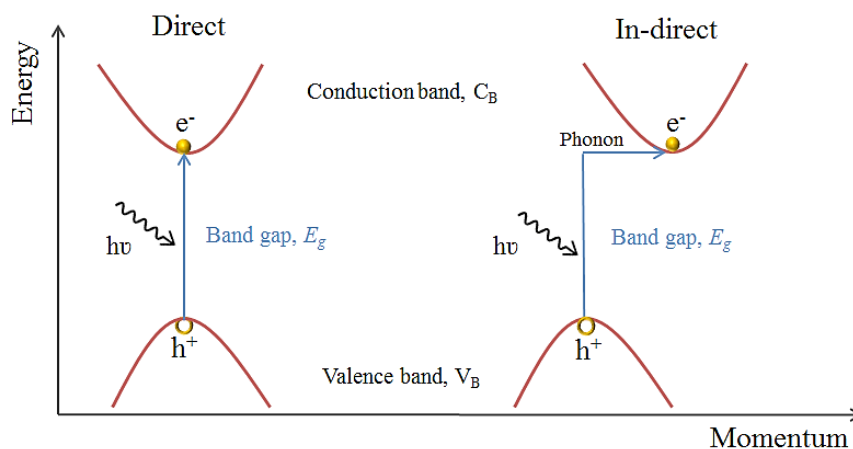


Figure 1.2: Schematic demonstrating photo-excitation in a direct and in-direct bandgap semiconductor.

For semiconductors with an in-direct bandgap, the valence and conduction bands have different crystal momentums and a photon of bandgap energy does not have sufficient momentum to generate an electron-hole pair. Therefore, a phonon (a lattice vibration) is required to supply the additional momentum required for excitation. As a result, in-direct bandgap materials can suffer from poor optical absorption requiring thicker layers to match the absorption of direct band gap materials.

In addition to the generation of charge carriers, upon illumination, semiconductors also generate excitons which are electron-hole pairs bound *via* Coulombic interaction. Excitons are formed through the absorption of sub-bandgap energies but must dissociate in order to generate free charge carriers.²⁷ For both electron-hole pairs and excitons alike, the generation of electrical power is only achievable if the electrons are extracted before recombining with the hole. This is achievable using an electrical or chemical potential and can allow the utilisation of the absorbed energy in alternative forms to heat.²⁵

1.3 A history of solar cells

In the presence of an electric field, the electrons generated from the separation of the electron-hole pair produce a current which can be used in an external circuit.²⁸ This principle, referred to as the photovoltaic effect, describes the generation of power by a material through light absorption and was first recognised by Edmond Becquerel in 1839. At the young age of 19, Becquerel observed the generation of electric current upon exposing copper and silver halide electrodes (immersed in electrolyte) to solar light.²⁹ This discovery ultimately laid the foundations upon which years of PV development have been built and essentially, helped researchers to understand and develop novel materials and architectures with the aim of achieving high performing systems which could be reproducibly manufactured at low cost. Today, the development of solar cells is generally categorised into three definitive generations.

1.3.1 First generation

First generation solar cells are manufactured from crystalline silicon (c-Si) and were initially developed in 1954 by Chapin, Fuller and Pearson who reported a ‘silicon p-n junction photocell’ capable of 6% efficiency.³⁰ Silicon has since become the most extensively studied semiconductor for photovoltaics and today, the record silicon cell efficiency currently stands at 27.6%.^{31,32}

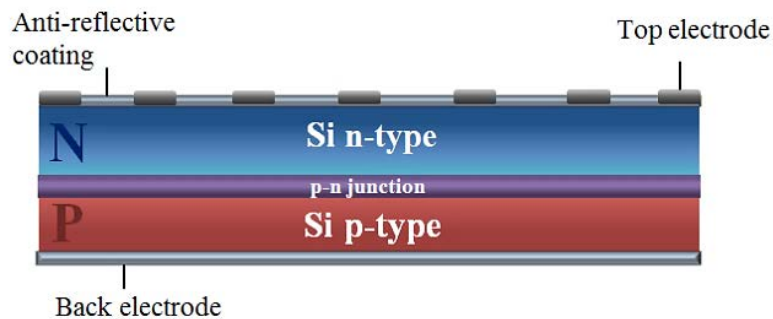


Figure 1.3: Schematic of a basic silicon solar cell comprised of a p-n junction which forms at the interface between a n-type semiconductor (high electron density) and a p-type semiconductor (high hole density). Upon illumination, photon absorption at the p-n junction generates electron hole pairs which are subsequently separated by the electric field within the p-n junction.

Crystalline silicon is typically favoured for its high abundance and non-toxicity however, silicon is an in-direct bandgap semiconductor and therefore, for this type of cell, more material is required to attain the same level of absorbance as thin-film semiconductors. As a result, the manufacture of such cells can prove expensive and often require extensive processing which can be accompanied by high material wastage.¹²

1.3.2 Second generation

Second generation solar cells were developed to be more cost-effective and primarily incorporate alternative semiconductors such as: cadmium telluride (CdTe) and copper indium gallium (di)selenide (CIGS). Whereas first generation cells were traditionally manufactured as thick modules (~200 μm), second generation cells introduced thin-film technology (<10 μm) and facilitated the manufacture of low-cost lightweight cells.³³ Introduced in the mid 1950's, CdTe cells are comprised of an n-type cadmium sulphide (CdS) layer and a p-type CdTe layer which collectively form a heterojunction 4-6 μm in thickness.³⁴ CIGS cells later emerged in the 1980's and contain an n-type CdS layer paired with a p-type CIGS layer (forming a heterojunction of 3-4 microns).^{34,35} In the last decade, CIGS cells have been successfully manufactured on metal foil and plastic which has created a new branch of thinner more flexible solar cells.^{36,37}

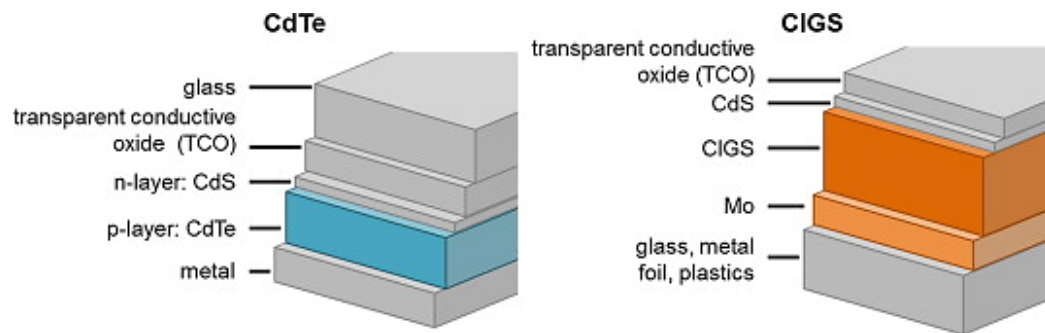


Figure 1.4: Schematic representation showing the architecture of both cadmium telluride (CdTe, left) and copper indium gallium (di)selenide (CIGS, right).³³

Current record efficiencies for both CdTe and CIGS cells have surpassed 22% however, the rare metals (indium, gallium and tellurium) used in their manufacture have limited availability which will eventually affect mass scale production.³² The abundance of

tellurium is particularly questionable with a decline predicted following 2020 thereby limiting the sustainability of the cells.^{38,39}

1.3.3 Third generation

Third generation photovoltaics built upon the thin-film technologies of second generation cells but were developed using wide band-gap semiconductors and typically include the metal oxides of titanium, zinc and tin. Dye-sensitised solar cells (DSSC's) and perovskite solar cells represent two examples of low-cost photovoltaic materials which fall under the third generation category.

1.3.3.1 Dye-sensitised solar cells

As wide band gap semiconductors, metal oxides generally absorb light in the UV region therefore, sensitisation through the adsorption of a dye monolayer to the surface increases its spectral bandwidth to the visible. Research into the sensitisation of wide band gap semiconductors was first published in 1969 by Gerischer and Tributsch, who reported photocurrent generation on placing photosensitised single crystal ZnO electrodes in electrolyte.⁴⁰ A year later, in a follow up publication, Gerischer and Tributsch attributed this effect to electron injection between the excited dye molecules and the conduction band of the semiconductor.^{41,42}

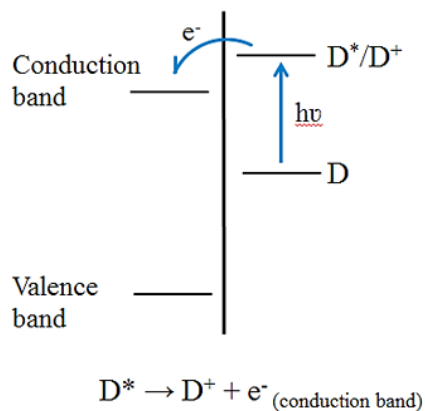


Figure 1.5: Basic schematic showing electron (e^-) injection from an excited state donor into the conduction band of a semiconductor. The sensitised metal oxide semiconductor provides the electronic energy levels required to accept an electron through injection. Where D^* represents the electronically excited donor and D^+ represents the oxidised donor.

This work was furthered by Memming and Hauffe *et al.* who studied electron injection into single crystals of ZnO when sensitised with organic dyes.^{43,44} By the mid 1970's, other researchers had begun to investigate alternative sensitisers and semiconductors including Gleria *et al.* and Clark *et al.* who evaluated the electron injection of polypyridine ruthenium sensitisers with SnO₂ and TiO₂ electrodes, respectively.^{45,46} Although fundamental from a theory perspective, the initial research described above used single crystal semiconductors which proved problematic due to limited surface area/dye uptake and low light harvesting efficiencies as a result of limited optical path length.⁴⁷ The development of the dye-sensitised solar cell (DSSC) by O'Regan and Grätzel in 1991 overcame this problem through the incorporation of a 10 µm mesoporous titania electrode which increased the surface area for sensitisation ca. 1000 fold.⁴⁸ This allowed the absorption of >99% of the photons transmitted though the cell windows in the ca. 450–550 nm wavelength range (after correcting for scatter) and ultimately higher efficiencies (7.1-7.9%) were achieved.⁴⁸ The general architecture of a DSSC (Figure 1.6) consists of a semiconducting metal oxide layer (typically mesoporous titania) sintered onto a conductive glass electrode. A monolayer of sensitising dye is adsorbed to the semiconductor surface. A redox electrolyte reduces the dye molecule (after photo-excitation) to its original state and also acts as a transport medium allowing the free movement of ions. The circuit is then completed using an electro-catalysed (typically platinum) conductive glass counter electrode.

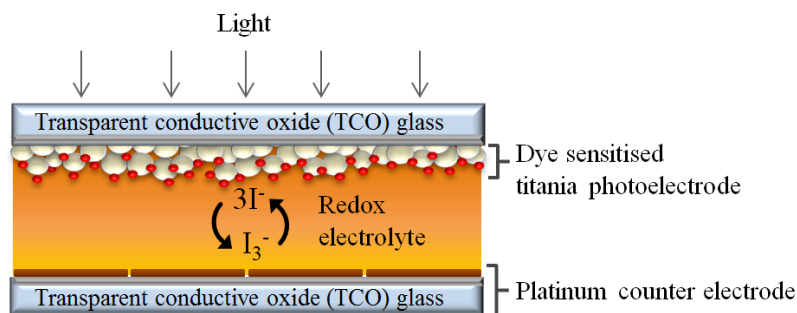


Figure 1.6: A schematic representation of a typical dye-sensitized solar cell which includes: a transparent conductive oxide support, a metal oxide semiconductor layer (usually titania), the sensitiser adsorbed to the semiconductor surface, the redox electrolyte and a counter electrode typically coated with a platinum catalyst.

Upon photo-excitation, the incident light is absorbed by the sensitising dye causing the promotion of an electron from the HOMO level (S_0) to the LUMO level (S_1) (Fig 1.7 (1)).

The influence of a small positive voltage causes the formation of an electrochemical gradient at the titania photo-electrode surface. This encourages electron injection from the LUMO level of the photo-excited dye into the conduction band of the semiconductor (Fig 1.7 (2)) leaving the dye in an oxidised state. Following injection, the electrons transverse the titania layer and are collected by the transparent conductive oxide (TCO) glass (Fig 1.7 (3)). They are then carried to the external circuit and passed through a load (generating electrical power) before being collected at the counter electrode. The oxidised dye molecule is reduced by a redox couple (typically iodide/triiodide, I^-/I_3^-) present within the electrolyte which reverts the dye molecule to its original state (Fig 1.7 (5)). The electrolyte redox couple is then reduced by the platinum counter electrode (Fig 1.7 (4)) which renews the process and generates a continuous electron flow from cathode to anode.

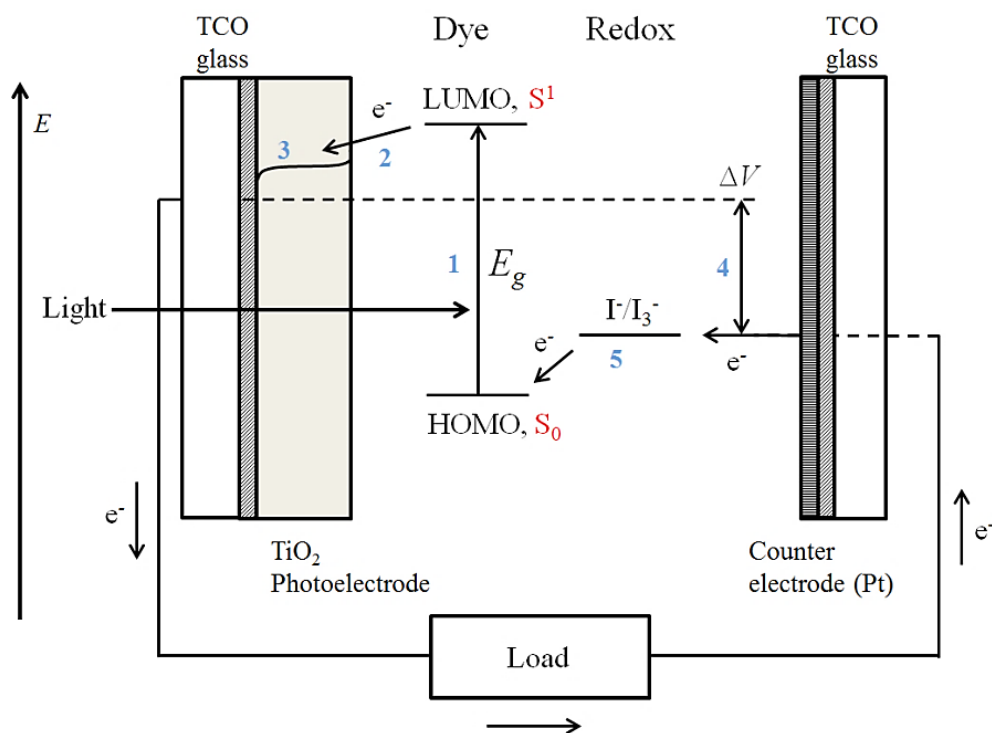


Figure 1.7: A schematic representation of the operating principle of a dye-sensitised solar cell. The photo-voltage, ΔV generated by the cell corresponds to the difference between the semiconductor Fermi level under illumination and the electrochemical potential of the redox couple / electrolyte.

The incident photon to current efficiency (IPCE) or quantum efficiency (QE) of a DSSC describes the conversion efficiency of incident light energy into electrochemical energy and is governed by three parameters: the light harvesting efficiency (φ_{LH}), the charge injection efficiency (φ_{inj}) and the efficiency of electron collection at the electrodes (φ_{COLL}):

$$IPCE = \varphi_{LH} \times \varphi_{inj} \times \varphi_{COLL} \quad (3)$$

The light harvesting efficiency represents the fraction of incident photons absorbed by the dye and depends on the level of dye loading and the spectral response of the sensitiser.⁴⁸ To ensure a high level of light harvesting, the sensitiser should have a high molar extinction coefficient in the visible to NIR region and remain stable in the presence of the electrolyte.⁴⁹ The efficiency of charge collection describes the ratio of charges transported through the semiconductor to the charges that recombine and as such, depends on the electron transport to the photo-sensitised anode and the level of recombination.⁵⁰

The electron injection efficiency is governed by several factors which include: the energetics and electronic coupling of the sensitising dye and titania, the nature of the titania surface and the surrounding electrolyte and the type of sensitiser and the binding group.^{51,52} Electron injection is largely dependent on the energy band positioning of the semiconductor and the dye and therefore, the redox potentials of these are pivotal to the efficient operation of the DSSC.⁵³ Excited dye molecules may fail to inject an electron into the semiconductor conduction band if the conduction band potential is close to or above the oxidation potential of the excited dye.⁵⁴ The electron injection and recombination rate also depend on the strength of electronic coupling between the sensitiser and the semiconductor. A stronger electronic coupling between the excited state of the adsorbed dye and the TiO₂ conduction band facilitates faster electron injection and prevents non-radiative recombination processes, which are discussed further in Section 1.4.5.⁵⁵ Ideally, the sensitising dye should strongly bind to the semiconductor surface with the ability to inject electrons into the semiconductor conduction band with a high quantum yield.

The separation of charge generation, carried out by the sensitizer, and charge transport, carried out by the semiconductor, affords flexibility of optimising these processes

individually through tailoring material design and selection. In particular, this has led to a plethora of sensitizers capable of injecting electrons into titania with a high quantum yield, often approaching unity. Much of the early work surrounding dye development focused on metal complex sensitizers such as ruthenium (II) polypyridyl complexes which were particularly popular as they provided the necessary redox, spectroscopic and excited-state properties required for titania based DSSCs.⁵⁶ In 1993, Gratzel *et al.* investigated the use of various mononuclear Ru complexes and found the thiocyanate derivative cis-[Ru(dcbH₂)₂(SCN)₂] achieved high device efficiencies and strong adsorption to the semiconductor surface. Today, this sensitizer is more commonly known as N3.⁵⁷ Further dye development gave rise to N749 or the ‘black dye’ which exhibits extended spectral response into the NIR region.⁵⁸ Structurally N749 incorporates three thiocyanate ligands and a terpyridine ligand which reduce the HOMO-LUMO energy gap resulting in higher absorption in the NIR region.^{49,59}

The proton content of a sensitizer can also affect the redox potentials of the dye.⁵⁹ Protons present on the anchoring group partially transfer to the titania surface during binding which alters the net surface charge thereby causing a downward shift of the titania Fermi level. The resultant effect reduces the energy gap between the quasi-fermi level of the TiO₂ and redox electrolyte leading to a higher electron injection driving force and increased short circuit current.⁴⁹ This effect is exemplified by the N719 dye (a doubly protonated form of N3) which in 1999, was demonstrated by Nazeeruddin *et al.* to achieve a higher efficiency.⁶⁰

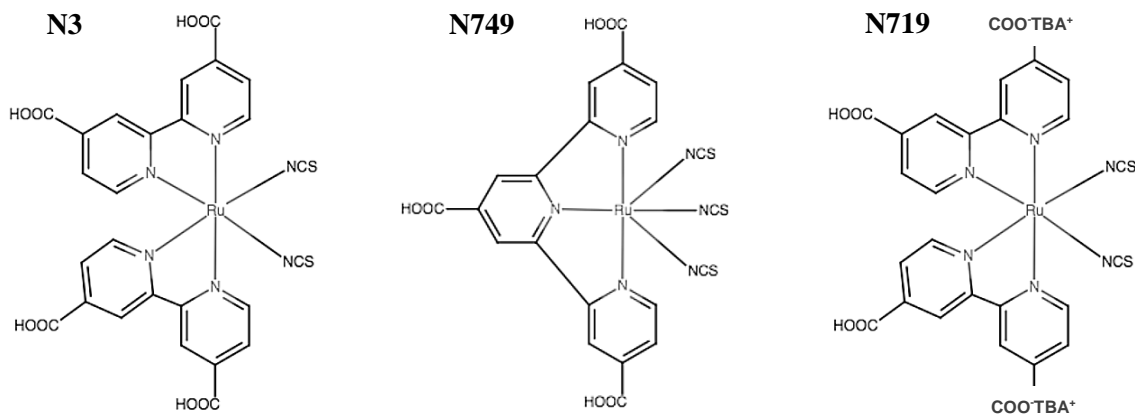


Figure 1.8: Molecular structure of three ruthenium dyes, N3, N749 and N719. Each dye is comprised of a central ruthenium ion surrounded by ancillary and anchoring ligands. The central metal ion generally dictates the overall properties of the sensitizer, however the ancillary ligands which are usually bi- or terpyridines can be modified to alter the photo-physical properties.

The use of alternative electrolytes namely, cobalt bi-pyridine redox complexes has also led to efficiency increases (over 13%) compared to the standard iodine/triiodide electrolyte.⁶¹ Alternative metal oxides investigated have included zinc, tin and niobium however, titania remains the most commonly used.^{59,62,63} This includes its use in the current record efficiency architecture which reached 14% when using an alkoxysilyl-anchor dye and a carboxy-anchor organic dye and a cobalt(III/II)tris(1,10-phenanthroline) complex electrolyte.⁶⁴

1.3.3.2 Solid state dye-sensitised solar cells

It is without question that the discovery and development of alternative materials for DSSCs has led to increased performance. Further advances in DSSC design however, have included the development of cells which incorporate solid state hole conductors in place of the liquid electrolyte. These cells termed solid-state DSSCs (ss-DSSCs) employ a hole conducting/transport layer (HTL) which is typically a wide band-gap small molecule material such as 2,20,7,70-tetrakis-(N,N-di-p-methoxyphenylamine)-9,90-spirobifluorene (spiro-OMeTAD) or semiconducting polymers such as poly(3,4-ethylenedioxythiophene) (PEDOT) or poly(3-hexylthiophene) (P3HT).⁶⁵⁻⁶⁷ Currently, the highest performing ss-DSSC was reported by Cao *et al.* who achieved an efficiency of 11% when using an amorphous copper blend Cu(II/I) HTL alongside a Y123 sensitizer and electrodeposited PEDOT as a counter electrode.⁶⁶ Although ss-DSSCs are yet to match the leading efficiencies of standard DSSCs, they omit the need for liquid electrolyte which can often leak out of the device due to its corrosive and volatile nature.⁶⁸

1.4 Perovskite solar cells

The development and success of the DSSC later lead to the birth of the perovskite solar cell. The perovskite mineral was first discovered in 1839 by Gustav Rose and was subsequently named after fellow mineralogist, Lev Perovski. The term perovskite, collectively describes a large family of crystal structures which resemble, or are related to the crystalline structure of the calcium titanate mineral (CaTiO_3).⁶⁹ The chemical formula, ABX_3 gives rise to the eminent crystalline structure which is commonly described as ‘corner-sharing’ due to eight three-dimensional octahedra each of the formula BX_6 sharing an X (corner) atom (Figure 1.9). The cation (A) resides within the cubo-octahedral cavity created at the centre of the octahedral formation.⁷⁰

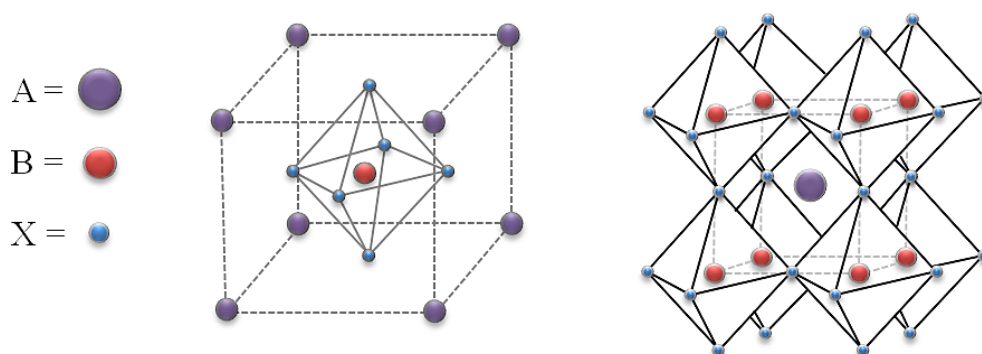


Figure 1.9: Ball and stick schematics showing the structural features of perovskite materials, left: the unit cell of a typical cubic perovskite, right: octahedral co-ordination around the central cation.

Perovskites can undergo phase transitioning during processing due to stimuli such as: temperature, pressure and magnetic or electric fields. This can produce a variety of structural polymorphs which include: cubic, tetragonal, orthorhombic, trigonal and monoclinic forms.⁷¹ Each form is typically dictated by rotation and tilting of the BX_3 polyhedra within the perovskite structure i.e. the octahedral positioning.⁶⁹

1.4.1 Lead halide perovskites

Metal halide perovskites were first reported by Weber in the late 1970's. Weber's work closely studied the ABX_3 structure and described how A^+ can be either methylammonium ($\text{CH}_3\text{NH}_3^+ / \text{MA}^+$) or formamidinium ($\text{NH}_2\text{CHNH}_2^+ / \text{FA}^+$), B^{2+} can be lead (Pb^{2+}) or tin

(Sn^{2+}) and X^- represents the halides I^- , Br^- or Cl^- .^{72,73} In the mid 1990's, Mitzi *et al.* reported the semiconducting capabilities of metal halide perovskites and since then, lead halide perovskites in particular, have become some of the most widely studied photovoltaic materials due to their attractive optoelectronic properties and ease of manufacture.^{74,75} Methylammonium lead triiodide ($\text{MAPbI}_3/\text{CH}_3\text{NH}_3\text{PbI}_3$) is a highly popular variant which offers long charge diffusion lengths of 0.1-1 μm ^{76,77} and a charge mobility of 8 $\text{cm}^2 \text{V}^{-1} \text{s}^{-1}$, which is considered remarkably high for a solution-processed material.⁷⁸ However, one major disadvantage of MAPbI_3 , is its instability to moisture which results from the hygroscopic methylammonium cation (CH_3NH_3^+).⁷⁹

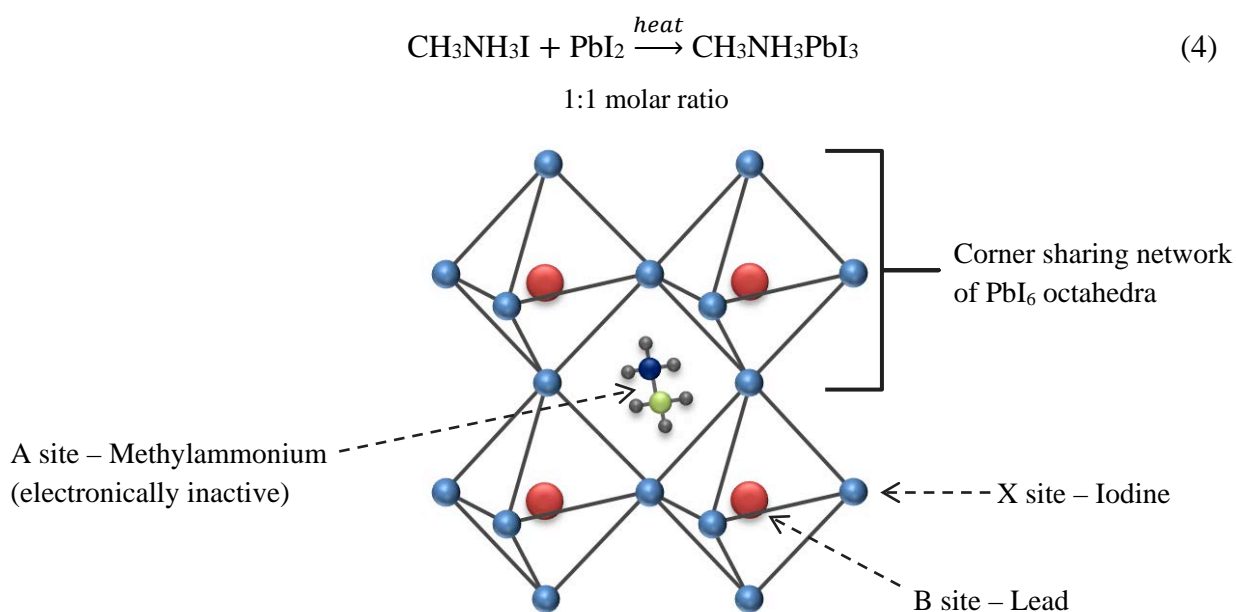


Figure 1.10: Schematic showing the perovskite crystal structure of methylammonium lead triiodide (MAPbI_3) perovskite and the chemistries which comprise the A, B and X lattice sites.

Figure 1.10 shows the perovskite crystal structure of MAPbI_3 with respect to the A, B and X lattice sites. The metal halide (BX_3^- anionic) framework is held together by heteropolar bonding (mixed ionic/covalent interactions). The A site cation, CH_3NH_3^+ is held within the negatively charged metal halide framework by a strong electrostatic potential.⁸⁰ However, in the presence of moisture, CH_3NH_3^+ forms weak hydrogen bonds with water molecules causing decomposition of the crystal lattice into its constituent molecules i.e. lead iodide and methylammonium iodide.⁸¹

Methods developed to counteract this issue have included elemental substitution in which the A site organic-inorganic cation is replaced with cesium^{82,83} (CsPbI₃) or rubidium ions (RbPbI₃).⁸⁴⁻⁸⁶ Substitution of the X site halide anion can also contribute to improved stability and was first shown in 2013 by Noh *et al.* who introduced bromide ions into the MAPbI₃ perovskite lattice.⁸⁷ Noh monitored the efficiencies of un-encapsulated MAPbI₃ PSC's prepared with increasing levels of bromide ((MAPb(I_{1-x}Br_x))₃ (where $x = 0, 0.06, 0.20$ and 0.29)) under controlled humidity for a period of 20 days.⁸⁷ The MAPbI₃ cells with the lowest bromide content ($x = 0$ and 0.06) showed high degradation and a large reduction in efficiency ($\sim 4.5\%$) after 1 days exposure to a relatively high humidity ($\geq 55\%$). Contrastingly, the cells with higher Br content, $x = 0.20$ and 0.29 remained stable and showed consistent efficiencies over the 20 days of device monitoring.⁸⁷

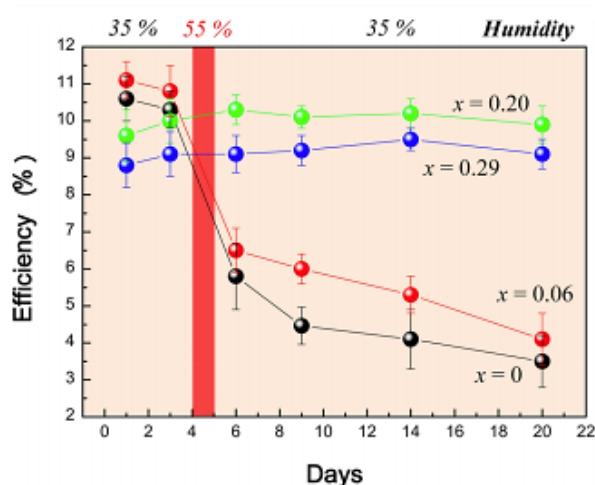
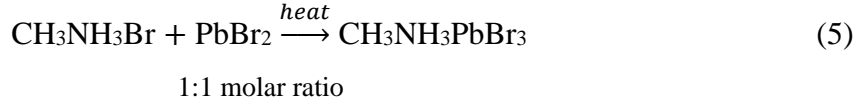


Figure 1.11: Variation in the efficiencies of un-encapsulated MAPbI₃ perovskite devices with increasing bromide content ((CH₃NH₃Pb(I_{1-x}Br_x))₃ ($x = 0, 0.06, 0.20$ and 0.29)) when measured under controlled humidity and time. Image reproduced from ref ⁸⁷.

The enhanced stability of the MAPbI₃ devices with higher bromide content (MAPb(I_{1-x}Br_x))₃ ($x \geq 2$) is believed to result from differences in the: perovskite structure, bond strength and exciton parameters which vary when substituting the halides.⁸⁸ Bromide and iodide ions have different ionic radii (1.96 and 2.2 Å, respectively) which causes differences in the perovskite crystal structure.⁸⁸ Therefore, due to its smaller ionic radius, bromide only perovskite i.e. methylammonium lead bromide (MAPbBr₃/CH₃NH₃PbBr₃) adopts a compact cubic structure at room temperature, whereas MAPbI₃ is tetragonal.⁸⁹



Additionally, the Pb-Br bonds, which comprise the metal halide framework of MAPbBr₃, are shorter and stronger than the corresponding Pb-I bonds of MAPbI₃.⁹⁰ MAPbBr₃ also has a smaller exciton Bohr radius (i.e. the distance between the electron and hole) compared to MAPbI₃ which causes a higher exciton binding energy and a lower dielectric constant meaning the electron in the former is less easily displaced (Table 1).^{91–93}

Table 1: Determined exciton parameters of the three-dimensional crystals of MAPbBr₃ and MAPbI₃ as reported in ref⁹².

	MAPbBr ₃	MAPbI ₃
Exciton Bohr radius a_B (Å)	20	22
Exciton binding energy E_b (meV)	76	50
Dielectric constant	4.8	6.5 ⁹⁴

Collectively, these factors mean the cubic structure of MAPbBr₃ perovskite is denser and more stable compared to the tetragonal structure of MAPbI₃ and therefore, less susceptible to attack from external species such as water.⁸⁸ However, although beneficial from a stability perspective, the increased binding energy of MAPbBr₃ limits its obtainable photocurrent and results in lower cell efficiencies which is discussed further in Chapter 3.

1.4.2 Early development of perovskite solar cells

The first photovoltaic application of lead halide perovskites was published in 2009 by Kojima *et al.* who replaced the dye sensitiser in a DSSC with MAPbBr₃ and MAPbI₃ perovskite. Initially, this substitution produced a relatively low efficiency cell (3.8%) which also proved to be unstable due to the electrolyte dissolving the perovskite.⁹⁵ In 2011, Park *et al.* furthered Kojima’s work using MAPbI₃ quantum dots on a nano-crystalline titania surface and achieved an increased efficiency of 6.5%.⁹⁶ The following year, a pivotal publication by Snaith’s research group opened up the design field for perovskite

photovoltaics through four significant developments: the removal of the sensitising dye, the successful use of a HTL, the use of a mixed halide perovskite ($\text{CH}_3\text{NH}_3\text{PbI}_{3-x}\text{Cl}_x$) layer as opposed to quantum dots and the replacement of the mesoporous titania layer with a non-conducting alumina (Al_2O_3) layer.⁹⁷ Snaith's team produced what was then, a high efficiency (10.9%) solid state perovskite cell termed a 'meso-superstructured solar cell' (MSSC) which incorporated an Al_2O_3 scaffold layer and a spiro-MeOTAD (2,2', 7,7'-tetrakis(N,N-di-p-methoxyphenamine)-9,9'-spirobiflourene) HTL in place of the electrolyte.⁹⁸ Charge injection from the perovskite into Al_2O_3 is not energetically possible and therefore, this work showed the ability of perovskite to not only act as a sensitiser, but also behave as an effective charge transport material.⁹⁸

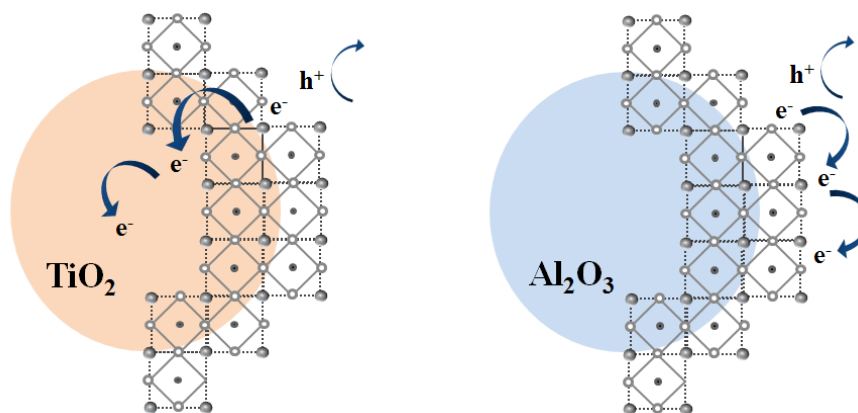


Figure 1.12: Schematic highlighting the difference in charge transport pathways when using a titania and alumina mesoporous layer in perovskite solar cells.

Following this publication, investigation into solid-state device architectures ensued with Kim *et al.* of Park's group reporting an efficiency of 9.7% for a solid-state perovskite cell with a reduced mesoporous titania layer thickness of $0.6 \mu\text{m}$.⁹⁹ The investigation of alternate HTLs soon followed and was published by Heo *et al.* in 2013 who studied poly-3-hexylthiophene (P3HT), poly-[2,1,3-benzothiadiazole-4,7-diyl][4,4-bis(2-ethylhexyl)-4H-cyclopenta[2,1-b:3,4-b']dithiophene-2,6 diyl] (PCPDTBT), (poly-[[9-(1-octylnonyl)-9H-carbazole-2,7-diyl]-2,5-thiophenediyl-2,1,3-benzothiadiazole-4,7-diyl-2,5-thiophenediyl]) (PCDTBT) and poly-triarylamine (PTAA) with lead iodide perovskite. Using PTAA, Heo demonstrated an improved open-circuit voltage (0.997 V), fill factor (0.727) and short-

circuit current density (16.5 mA/cm^2) which ultimately yielded a power conversion efficiency of 12.0% under standard AM 1.5 conditions.¹⁰⁰ Published the same year, by Seok's research group based at the Korea Research Institute of Chemical Technology (KRICT), was a 12.3% efficiency device which used a mixed-halide perovskite with a PTAA HTL. The perovskite formula incorporated bromide at varying percentages $\text{CH}_3\text{NH}_3\text{Pb}(\text{I}_{1-x}\text{Br}_x)_3$ which was found to permit 'chemical tuning' of the bandgap over the entire visible spectrum – an attractive feature for a light harvesting layer.⁸⁷

In 2013, Snaith's group developed a 'planar' architecture using a mesoporous Al_2O_3 scaffold capped with $\text{CH}_3\text{NH}_3\text{PbI}_{3-x}\text{Cl}_x$ perovskite achieving a 12.3% efficiency.¹⁰¹ Efficiencies exceeding 15% were then achieved through depositing the perovskite layer using a sequential two-step deposition method as opposed to the traditional single step method.¹⁰² In 2014, Jeon *et al.* developed and introduced the anti-solvent method and reported an efficiency of 16.2% when drop casting toluene onto a $\text{MAPb}(\text{I}_{1-x}\text{Br}_x)_3$ precursor during spin coating.¹⁰³ In the same year, an efficiency of 19.3% was achieved by Zhou *et al.* by manufacturing PSC's in controlled humidity conditions and doping the titania with Yttrium which enhanced carrier concentration and reduced recombination.¹⁰⁴ By the end of 2015, PSC efficiencies were surpassing 21.0% through the use alternative perovskite blends which included both formamidinium and methylammonium monovalent cations $[(\text{FAI})_{0.81}(\text{PbI}_2)_{0.85}(\text{MAPbBr}_3)_{0.15}]$ and an acrylic (poly(methyl methacrylate)) template as a means to control nucleation.¹⁰⁵ Today, the certified record efficiency of a PSC has reached 25.2% achieved by researchers at KRICT and the Massachusetts Institute of Technology (MIT).³² As evidenced in the text, over the last twenty years PSC's have rapidly evolved to become a worthy competitor in the field of photovoltaics. This is shown more clearly overleaf in the National Renewable Energy Laboratory (NREL), best cell efficiency chart which depicts the increase in perovskite solar cell efficiencies vs other established PV technologies between the years 1976 and 2020 (Figure 1.13).

Best Research-Cell Efficiencies

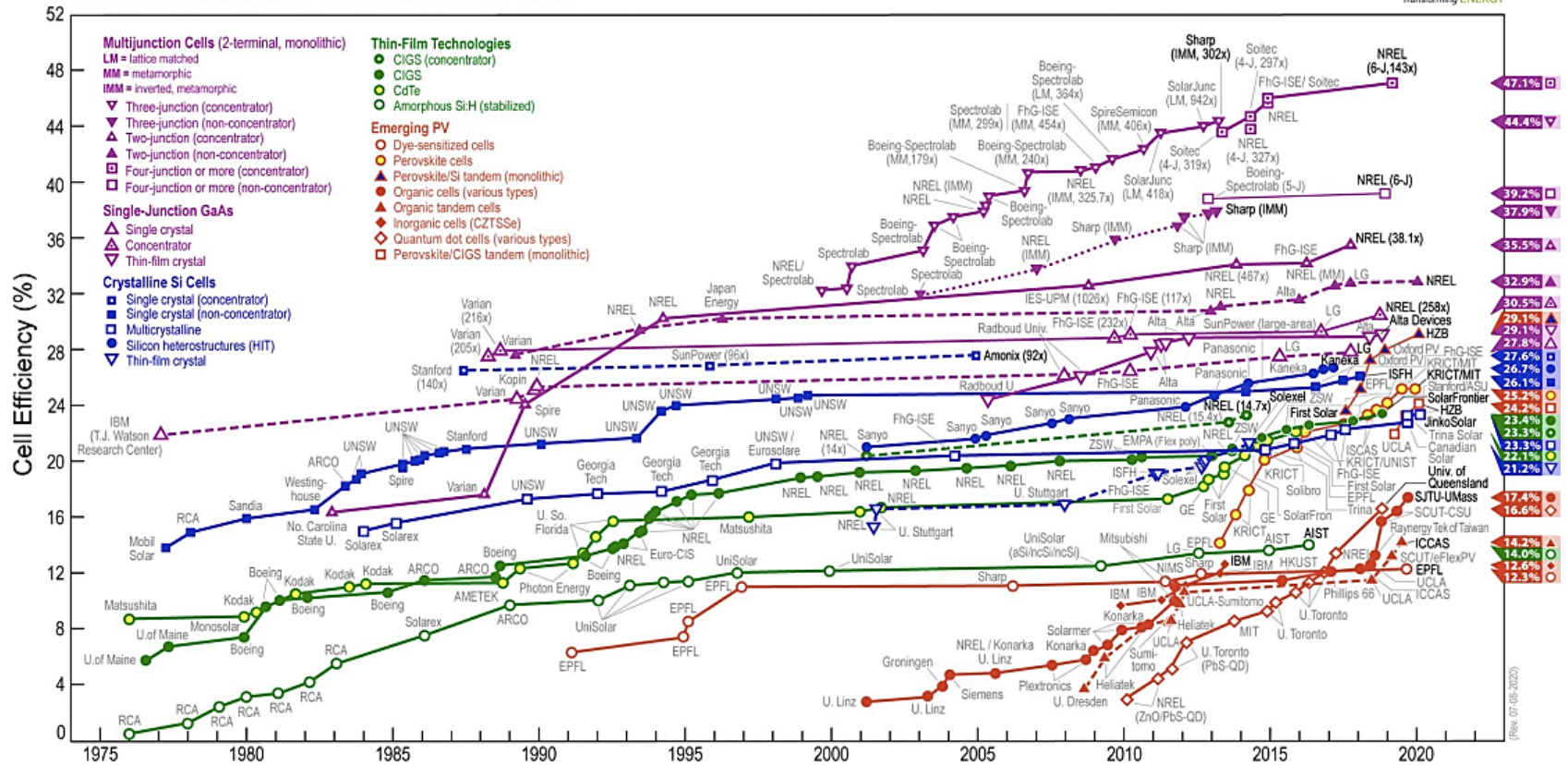


Figure 1.13: National Renewable Energy Laboratory (NREL), best cell efficiency chart of the highest confirmed conversion efficiencies for research cells for a range of photovoltaic technologies, plotted from 1976 to the present.³²

1.4.3 General lead halide perovskite device architectures

The basic format of a perovskite thin-film solar cell involves sandwiching the perovskite between two charge selective layers namely, an electron transport layer (ETL) and a hole transport layer (HTL). During manufacture, the n-type ETL is deposited first followed by the perovskite (intrinsic) and the p-type HTL. Cells prepared in this format are commonly referred to as n-i-p. Two conventional n-i-p architectures commonly used for lead halide perovskite photovoltaics include the mesoporous and planar cell design.

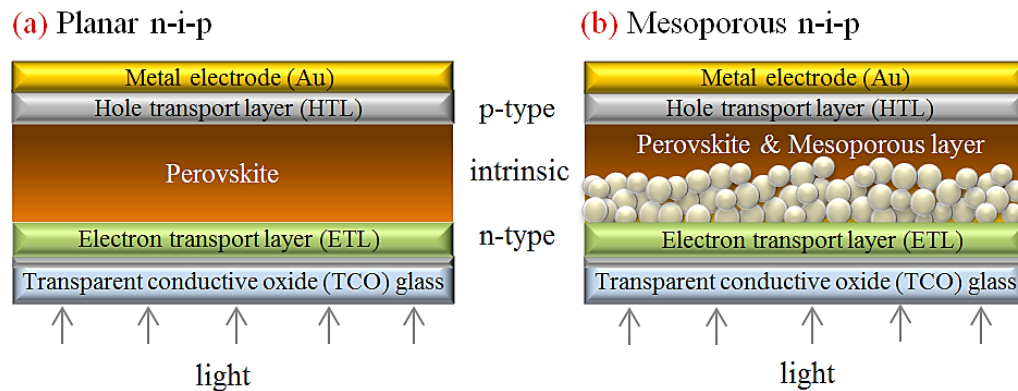


Figure 1.14: Schematic of the two n-i-p cell architectures where (a) and (b) demonstrate the standard layers present in a planar and mesoporous perovskite cell, respectively. When measuring performance, each architecture is illuminated through the glass electrode.

Both architectures are typically manufactured on TCO glass which acts as the top electrode and provides a support on which the rest of the thin-film is constructed. Fluorine doped tin oxide (FTO) is a metal oxide commonly used as a conductive coating on the glass electrode in photovoltaic cells.¹⁰⁶ Due to its wide band-gap (3.7 eV), tin oxide (SnO_2) offers high transmittance in the visible but is also an insulator and therefore (in order to become conductive) its resistivity is reduced *via* doping with fluorine.¹⁰⁷

The ETL accepts photo-generated electrons from the perovskite and transfers them to the FTO electrode. Therefore, in order to achieve high device efficiencies, an ETL should have good optical transmittance, favourable energetic alignment (with the perovskite) and high electron mobility for efficient charge extraction.¹⁰⁸ In a 'planar' cell architecture, the ETL is comprised solely of a compact metal oxide layer which, in addition to transporting

electrons, also prevents direct contact between the HTL and FTO which would otherwise cause severe recombination.¹⁰⁹ Titania is currently the most widely used compact layer (c-TiO₂) in perovskite solar cells primarily due to its excellent photoelectric properties, good photo-stability and corrosion-resistant nature.^{110,111} However, other metal oxides such as those of zinc (ZnO), tin (SnO) and nickel (NiO) have also been successfully used for this purpose.^{112–114} Lead halide perovskites can successfully operate in a planar format due to their ambi-polar semiconducting nature, meaning they are able to separate and transport both holes and electrons over relatively long distances without a mesoporous layer.¹⁰¹

Mesoporous cell architectures also contain a compact metal oxide layer here, however, as the name suggests, a mesoporous layer (typically titania) is also included. This layer provides a large surface area scaffold for perovskite crystallisation and also accepts photo-generated electrons from the perovskite. Therefore, for this device architecture, electron transport can proceed through the mesoporous layer and/or the bulk of the perovskite itself.¹¹⁵

The differences between the two types of ETL largely affect the separation, transport and recombination of the photo-induced charges within a device. This in turn affects the overall cell performance and causes differences in efficiency where mesoporous devices generally come out on top. The current record efficiencies for planar and mesoporous perovskite devices have reached 23.7%¹¹⁶ and 25.2%³², respectively where the increased efficiencies of the latter are typically attributed to reduced levels of hysteresis and improved charge extraction efficiency.¹¹⁷ In 2018, Liu *et al.* studied the charge injection and interfacial recombination rates of both planar and mesoporous MAPbI₃ devices using transient emission and absorption spectroscopy.¹¹⁸ Liu found that electron injection from the perovskite to the c-TiO₂ was extremely slow (injection time constant, 160 ns) and occurred on a much slower time when compared to the PL lifetime of the perovskite (34 ns). Conversely, electron injection from the perovskite into the mesoporous TiO₂ occurred on a much faster timescale (1.2 ns) resulting in reduced interfacial charge recombination and improved charge extraction. Liu concluded that a mesoporous TiO₂ layer is essential to maximize charge extraction in MAPbI₃ devices as it provides a larger contact area for rapid electron injection.¹¹⁸

The fast electron extraction properties described for mesoporous titania are particularly desirable to minimise electron accumulation at the perovskite/titania interface. Charge accumulation is often listed as one of the main reasons for the high levels of hysteresis observed in planar MAPbI₃ devices.^{108,119} This results from the electron mobility of compact titania (ca. 10^{-4} cm² V⁻¹ s⁻¹) which is lower than the hole mobility of many of the commonly used hole transport layers (ca. 10^{-3} cm² V⁻¹ s⁻¹).^{108,120} Overall, planar PSC's offer a simpler cell architecture requiring less production and material, but can also suffer from increased hysteresis and poorer charge extraction due to limited contact between the perovskite and titania.^{109,121} Conversely, mesoporous cells require a higher degree of processing including high temperature sintering which limits their use in both tandem and flexible cell architectures, but can offer improved charge extraction and higher device efficiencies.^{122,123}

The aforementioned p-type hole transport layer mediates the collection and transport of holes from the perovskite to the electrode but also acts as an electron blocking layer. As a photoactive material, perovskite is relatively conductive and is therefore susceptible to short-circuit if it comes into contact with the conductive electrode. A p-type HTL 'capping' layer can rectify this but the materials used for such application are typically less conductive meaning thicker layers can cause increased series resistance and reduced charged transport.¹²⁴ Standard HTL's include wide band-gap small molecule materials such as 2,20,7,70-tetrakis-(N,N-di-p-methoxyphenylamine)-9,90-spirobifluorene (spiro-OMeTAD) or semiconducting polymers such as poly-triarylamine (PTAA) or poly(3-hexylthiophene) (P3HT).^{100,125}

The cell is then complete by the addition of a thin metal counter electrode where precious metals such as gold or silver are commonly used due to their high conductivity.¹²⁶

1.4.4 Device operating principle

Following light absorption, electron-hole pairs and excitons are generated within the perovskite layer. Lead halide perovskites produce Mott-Wannier excitons in which the electron and hole share coulombic interaction over a distance which is typically larger than the lattice spacing (~ 100 Å).¹²⁷ These excitons have a low binding energy (due to the large

dielectric constant) and are believed to contribute to the long diffusion lengths of lead halide perovskites (0.1-1 μm).^{76-78,128} Ponseca *et al.* previously studied the generation of charge carriers in lead halide perovskites and reported the almost instant generation of electron-hole pairs after photoexcitation. These then dissociate within a 2 picosecond timeframe to produce highly mobile charges.¹²⁹

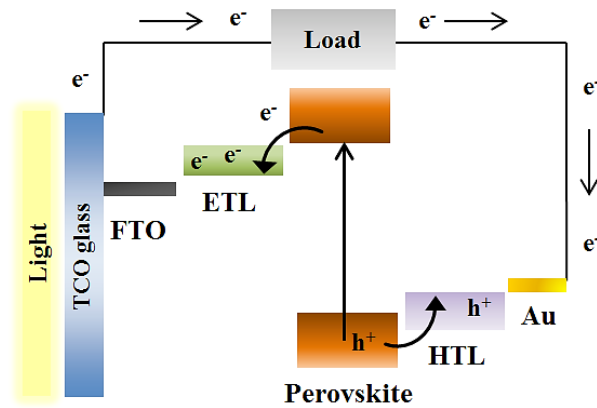


Figure 1.15: Schematic showing the basic operating principle of a perovskite solar cell under illumination.

Charge separation is driven by a potential difference formed between the charge selective layers. As mentioned in the previous Section, perovskite solar cells adopt a p-i-n junction format whereby the intrinsic (i) or un-doped perovskite layer is sandwiched between a p-type layer (p) and an n-type layer (n). In isolation, each of these materials has an independent Fermi level (i.e. the electrochemical potential of the electrons). When brought together as in a p-i-n junction, the Fermi levels must align which causes a gradient between the vacuum level/work function of the materials (Figure 1.16).²⁷ The work function of the p-type gold anode (ϕ_p) is larger than that of the n-type FTO cathode (ϕ_n) which causes a built-in potential, V_{bi} between the two contacts. This voltage generates an intrinsic electric field which, in addition to an external bias voltage, drives the electrons and holes generated in the intrinsic perovskite layer toward their respective electrodes.¹³⁰ This encourages charge separation which can then occur *via* two mechanisms: injection of the photo-generated electrons into the conduction band of titania and/or injection of the holes into the HTL.¹³¹ Charge separation has previously been shown to occur simultaneously at both the HTL and

ETL junctions with ultrafast electron and hole injection from the perovskite occurring within similar timeframes (femto to picoseconds).^{131,132} Following charge separation the free electrons are then transferred through the ETL and collected at the FTO cathode whereas the free holes are concomitantly transported through the HTL to the gold anode. The electrons are then carried to an external circuit and passed through a load before collection at the metal counter electrode.

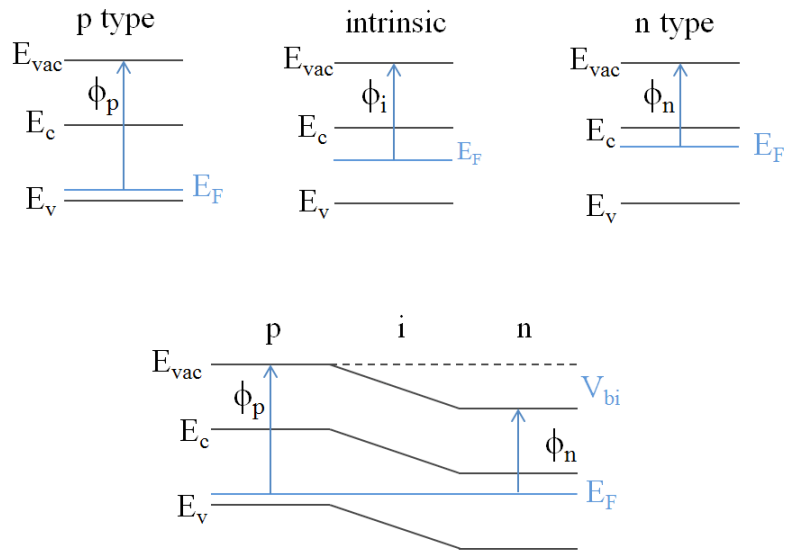


Figure 1.16: Schematic showing the energy band profiles of a p-type, intrinsic and n-type semiconductor in isolation (top) and the energy band profile of a p-i-n junction in equilibrium. E_{vac} , E_c , E_v and E_F represent the vacuum, the conduction band, the valence band and the Fermi equilibrium. V_{bi} is the built-in potential and ϕ_p , and ϕ_n represent the work function of the holes and electrons, respectively. Adapted from ref ²⁷.

Figure 1.16 shows the Fermi level position of the intrinsic perovskite layer at equilibrium i.e. in the absence of light at absolute zero. Here, the valence band is full and the conduction band is empty meaning the Fermi level lies somewhat central within the bandgap.²⁷ Under illumination however, the semiconductor is disturbed from equilibrium, which increases the density of electrons and holes above their equilibrium values.²⁷ The electron and hole populations in the conduction and valence bands, respectively re-distribute themselves as if they were at equilibrium with their own Fermi levels (Figure 1.17). The new Fermi levels for the electrons and holes are called the electron and hole quasi Fermi

levels, E_{Fn} and E_{Fp} , respectively.²⁷ It is the splitting of and difference between these levels that generates the photo-voltage (V_{oc}) of the device.

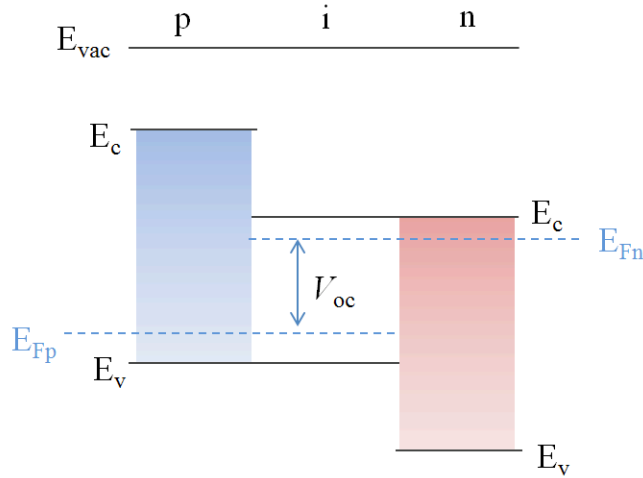


Figure 1.17: Schematic showing the energy band profile of a p-i-n junction at open-circuit under illumination. E_{vac} , E_c , E_v and E_{Fn} and E_{Fp} represent the vacuum, the conduction band, the valence band and the quasi Fermi levels of electrons and holes, respectively. V_{oc} is open-circuit voltage. Adapted from ref¹³³.

1.4.5 Recombination losses

The photocurrent generated by a PSC can be limited by a series of radiative and non-radiative recombination processes where the electron and hole recombine prior to extraction. Each process constitutes a loss mechanism which competes with charge transfer to limit the performance of PSC's.

Radiative recombination, also referred to as band to band recombination, is simply the opposite process of absorption where the electron in the conduction band (C_B) loses its excitation energy to directly recombine with the hole in the valence band (V_B). This process results in the emission (of a photon of lower energy than was initially absorbed) and is referred to as fluorescence (Figure 1.18).

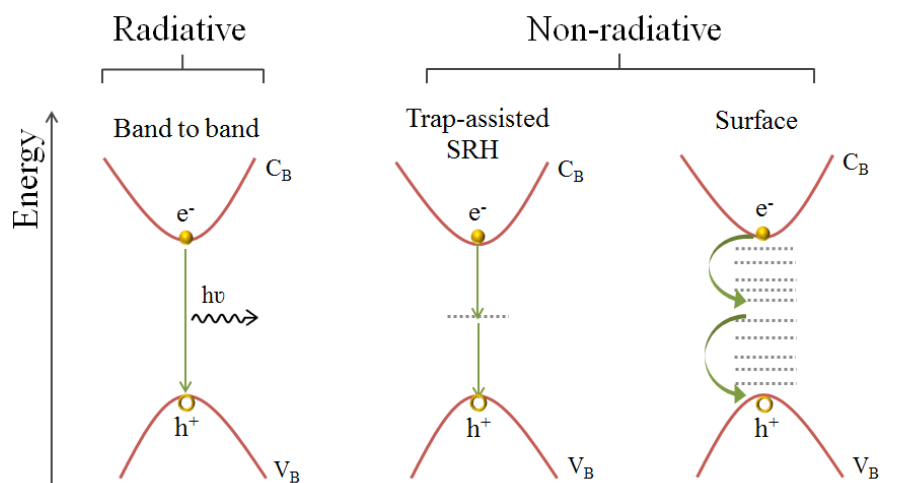


Figure 1.18: Schematic showing both radiative and non-radiative recombination processes in lead halide perovskites. Non-radiative processes arise due to defects within the perovskite layer.

Non-radiative recombination also involves the recombination of the excited electron and hole; here however, the electron energy is released as a lattice vibration i.e. a phonon. This type of recombination generally results from defects within the bulk of the crystal lattice or at surfaces such as grain boundaries and interfaces and, as a result, is largely related to the processing conditions of the perovskite.^{134–136} Figure 1.19 shows example point defects common to the crystalline structure of lead halide perovskites which can give rise to trap states and contribute to non-radiative recombination.^{137–140}

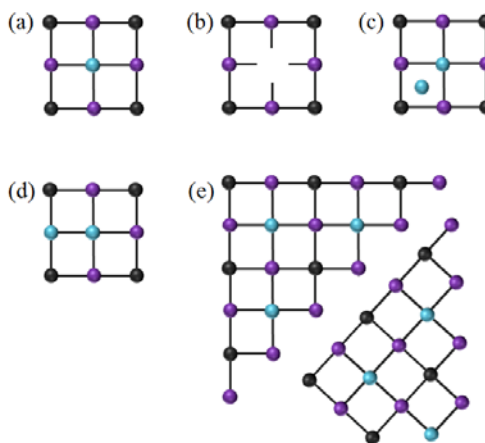


Figure 1.19: Schematic showing examples of point defects commonly encountered in lead halide perovskites (a) perfect lattice; (b) vacancy; (c) interstitial; (d) anti-site and (e) grain boundaries.¹³⁹

Two prevalent forms of non-radiative recombination, experienced by PSC's are shown in Figure 1.18. Trap-assisted or Shockley-Read Hall (SRH) recombination, results from intermediate energy states ('traps') located within the bandgap which arise due to defects in the bulk of the perovskite crystal lattice. Excited state electrons and holes can become caught in these trap states which can then act as recombination centers.¹⁴¹

Surface recombination is an interfacial non-radiative process which occurs due to surface defects across the interfaces within the cell i.e. between the perovskite and charge transport layers.^{142,143} Surface atoms have a different bonding environment to those in the bulk and therefore, due to a lack of neighbouring atoms they have vacancies which occupy the bandgap as 'dangling' bonds. These 'dangling' bonds then act as trap states as shown in Figure 1.18.¹⁴⁴

In comparison to radiative, non-radiative recombination is recognised as the dominant process in PSC's and can be highly detrimental to the overall performance. Solution-based perovskite films are more susceptible to trap state formation due to fast crystal growth during processing which can encourage both surface and grain boundary defects.^{145,146} The trap states present within these defects reduce the lifetimes of charge carriers which subsequently suppresses the open-circuit voltage and fill factor and damages the cell efficiency.¹⁴⁷⁻¹⁵⁰ As a result, researchers have fervently tried to develop methods which limit or passivate trap states within the perovskite layer.^{136,149,151} This has included extensive investigation into morphology/compositional engineering which is aimed at optimising the crystallisation process of the perovskite in a bid to limit defects and produce thin-films of large grain size and high crystallinity.¹⁵² This can include methods such as precursor/solvent engineering,^{103,153} thermal engineering,^{101,154} anti-solvent drip engineering^{135,136} and surface engineering using self-assembled monolayers (SAMS).¹⁵⁷

SAMS are organic molecules which can be adsorbed to the metal oxide ETL to form an organised monolayer, 1-3 nm in thickness. Each molecule is comprised of an anchoring group (e.g. silane, phosphonate, carboxylate) a linker (typically an alkane chain) and a terminal functional group.¹⁵⁷

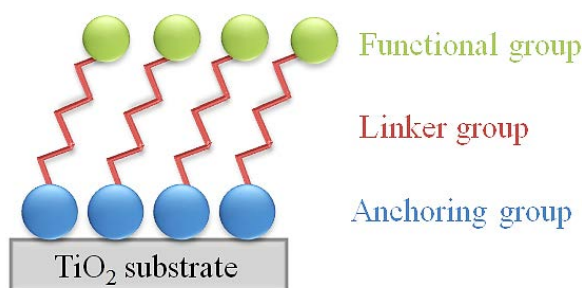


Figure 1.20: Basic schematic of a self-assembled monolayer. The anchoring group has a high affinity for the surface and binds the molecule to the metal oxide whereas the functional group alters the surface properties of the ETL and interacts with the perovskite.¹⁵⁸

SAMs are typically deposited through vapour deposition, by immersing the substrate in a SAMS solution or *via* spin coating and can be used to improve the surface properties of the ETL prior to perovskite deposition.¹⁵⁹ The surface of metal oxides are rich in hydrogen or hydroxyl ‘dangling’ bonds which can introduce deep trap states at the perovskite-metal oxide interface. The organic molecules which comprise a SAM can alter or saturate these bonds and passivate the deep trap states thereby improving the charge extraction efficiency and fill factor of a device.^{159,160}

The concept of SAMs was first applied to DSSC’s in 2012, where a phosphonate dipole monolayer, formed on the mesoporous titania surface, reduced recombination in the metal oxide through trap state passivation.¹⁶¹ In 2014, Henry Snaith and co-workers then applied a fullerene (C₆₀) SAM to a planar PSC reporting efficiency increases (from 11.5% to 15.7%) due to trap passivation and reduced non-radiative recombination at the titania-perovskite interface.¹⁶²

Since then, SAMS such as: 4-aminobenzoic acid (Figure 1.21),¹⁶³ 4-pyridinecarboxylic acid,¹⁶⁴ 3-aminopropyltriethoxysilane,¹⁶⁵ terephthalic acid¹⁶⁶ and ethylphosphonic acid¹⁶⁷ have also been applied to mesoporous architectures having increased the overall cell performance through: improved energy band alignment,¹⁶⁸ strengthened electronic coupling between the ETL and perovskite¹⁶⁴ and generally through improved charge carrier dynamics i.e. transport, injection and recombination.¹⁶⁰

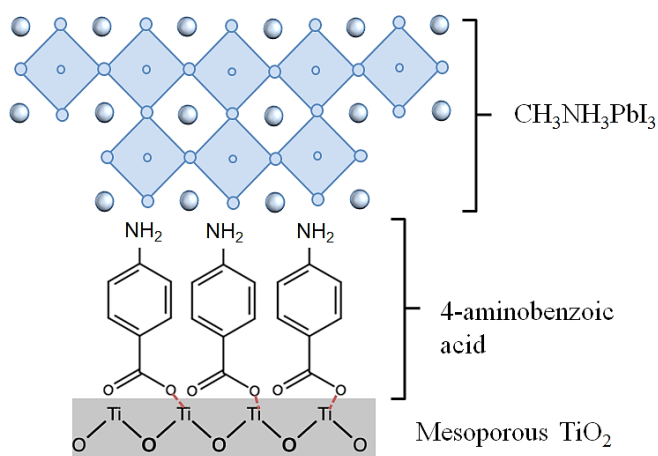


Figure 1.21: Schematic showing the application of a 4-aminobenzoic acid SAM in a mesoporous $\text{CH}_3\text{NH}_3\text{PbI}_3$ (MAPbI₃) PSC.¹⁶³

SAMs can also be directly deposited on and used to modify the perovskite surface which can readily interact with various functional groups due to its ionic nature and Pb^{2+} ions.¹⁵⁹ This has led to improvements in both performance and stability as evidenced by Zhang *et al.* who increased the hydrophobicity of MAPbI₃ perovskite using a dodecyltrimethoxysilane (C12-silane) SAM, where the long alkyl chains impeded charge recombination and increased the moisture resistance of the perovskite layer.¹⁶⁹ Increased moisture resistance was also demonstrated by Wang *et al.* through the use of a fluorinated silane SAM [Trichloro(3,3,3-trifluoropropyl)silane] which formed a hydrophobic crosslinking layer a top the MAPbI₃ perovskite. Remarkably, these devices were shown to work under water and achieved high efficiencies of 18.9%.¹⁷⁰

Similar to SAMS and another avenue of morphology engineering involves the use of additive treatments which can be added to the precursor solution or used to treat the perovskite layer after deposition. This method involves treating/doping the perovskite with chemistries capable of passivating trap states within the active layer therefore, leading to reduced non-radiative recombination and increased performance.^{171–173} Both morphology and additive engineering form an integral part of this thesis and therefore, literature and developments surrounding these two methods have been discussed further to coincide with the research conducted in Chapters 3 and 6.

1.4.6 Hysteresis

The efficiencies of PSC's are calculated from a current-voltage (J-V) curve where under illumination, an applied bias (of a set voltage range) is swept across the terminals of the cell whilst measuring the current flow in the external circuit.¹⁷⁴ The cell is measured or 'scanned' in two directions: the reverse scan, where the voltage is swept from open-circuit (V_{oc}) to short-circuit (J_{sc}) and the forward scan, where the voltage is swept from J_{sc} to V_{oc} . The term hysteresis describes a disparity or lag between the input and output of a system on changing direction. Therefore, here, the hysteresis represents the difference between the J-V curves generated for the forward and reverse scans. The degree of hysteresis can vary depending on the scan rate,¹²⁰ range¹⁷⁵ and direction.¹⁷⁶ It is typically found that higher efficiencies are generated for the reverse scan as forward scans tend to show lower V_{oc} and fill factor values.¹⁷⁷

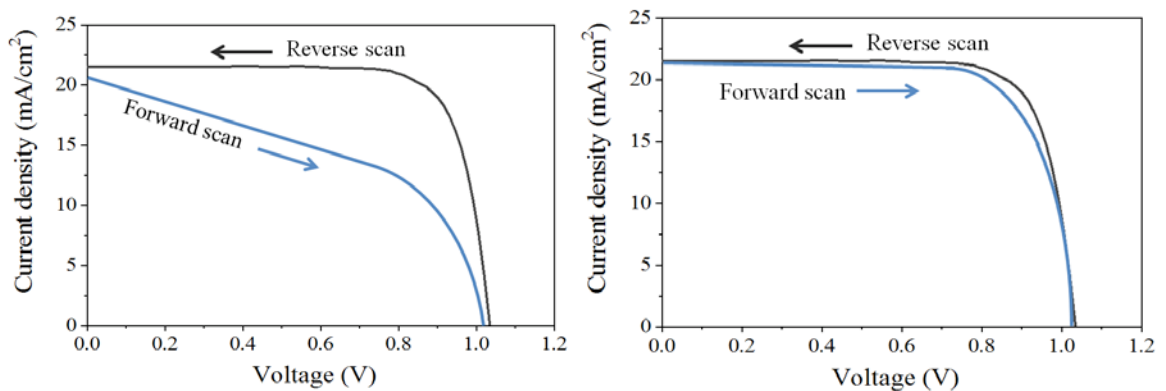


Figure 1.22: Example current-voltage (J-V) curves for perovskite solar cells showing: a high level of hysteresis (left) and a low level of hysteresis (right).

Early research into the hysteresis of PSC's was first conducted by Snaith *et al.* in 2014.¹⁷⁴ Snaith's research not only demonstrated the variability of hysteresis with scan direction and rate, but also highlighted the importance of overcoming this issue for the future development of perovskite PV.¹⁷⁴ This is due to the fact that hysteresis can have a significant impact on both the efficiency and stability of perovskite devices.¹⁷⁸ As a result, in the years that followed Snaith's paper, researchers have fervently focused on elucidating and understanding the causes of hysteresis, which have commonly been listed as:

- i. Ferroelectric polarization - due to the high dielectric constant and cubic-tetragonal phase transition of MAPbI_3 .^{179,180}
- ii. Charge trapping at the perovskite interface(s) - due to bulk and surface defects.¹⁸¹
- iii. Ionic displacement or migration.^{120,182}
- iv. Capacitive effects.^{183,184}

In the last few years however, a lot of the research in this field has mainly focused on the links between hysteresis, ion migration and charge trapping.^{83,120,182,185} Both ion migration and charge trapping can cause an accumulation of electrons and holes at the perovskite interface(s). This subsequently increases recombination which lowers the photocurrent and reduces the device efficiency.¹⁸²

Mobile ions have been shown to have a screening effect on the built-in electric field which alters the transport properties of the photo-generated charge carriers with time thereby leading to hysteresis.^{180,186,187} This arises namely due to the covalent-ionic bonding of the crystal structure, the perovskite lattice is more susceptible to ionic defects such as ion vacancies and interstitials (discussed further in Section 1.4.5).¹⁸⁸ Such defects can lead to mobile ionic species (such as iodide vacancies) which migrate under the in-built electric field from the defect location toward the electrode of opposite polarity. However, these ions are not extracted and accumulate at the perovskite/charge transport layer interface.¹⁸⁹ This in turn generates a space charge which counteracts and decreases the intrinsic electric field thereby impeding the ability of charges to diffuse to either electrode resulting in a lower driving force for charge extraction.¹²⁰ This ultimately decreases the quasi Fermi level splitting and subsequently the V_{oc} which impacts the overall device efficiency.¹²⁰ Therefore, in order to reduce hysteresis in PSC's, it is essential to reduce the number of mobile ionic species and/or the number of defects in the perovskite which cause charge trapping. A reduction of the former has previously been achieved *via* halide substitution. Zhang *et al.* reported reduced hysteresis for MAPbI_3 devices on introducing bromide ions into the perovskite precursor solution. This created a hybrid halide perovskite $\text{MAPbBr}_x\text{I}_{3-x}$ ($x \sim 0-0.6$) which demonstrated reduced hysteresis and increased device efficiencies. Br substitution was found to increase the activation energy of iodide migration from ~ 0.34 eV

in MAPbI₃ to ~0.46 eV in MAPbBr_xI_{3-x} resulting in a more stable perovskite structure. This ultimately reduced and/or stabilised the mobile ionic species arising from defects within the perovskite layer which in turn reduced the hysteresis.¹⁹⁰ Hysteresis can also be reduced through the use of additives which passivate defects within the bulk of the perovskite layer. One example includes the use of the organic cross linker 2,2'-(ethylenedioxy)bis(ethylammonium iodide) (EDAI). When introduced into the perovskite precursor solution, EDAI was shown to passivate defect states in the bulk of the perovskite as well as those present at the grain boundaries and film surface. Devices without EDAI had a larger hysteresis index (i.e. the magnitude of the J-V hysteresis) (~0.08) compared to devices with EDAI (~0.00–0.02). The negligible hysteresis of the passivated devices subsequently led to increased device efficiencies and improved stability.¹⁹¹

1.5 References

1. Breeze, P. Chapter 13 - Solar Power. in *Power Generation Technologies*, (Third ed.) pp. 293–321. Newnes, Oxford, UK (2019). doi:<https://doi.org/10.1016/C2017-0-03267-6>.
2. U.S. Energy Information Administration. International Energy Outlook 2019. *U.S. Energy Information Administration Website* (2019). Available at: <https://www.eia.gov/outlooks/ieo/>. [accessed: 29th August 2020].
3. BP. Statistical Review of World Energy, 2020 | 69th Edition. *bp Website* **69**, pp. 1–68 (2020). Available at: <https://www.bp.com/en/global/corporate/energy-economics/statistical-review-of-world-energy.html>. [accessed: 29th October 2020].
4. United States Environmental Protection Agency. Sources of Greenhouse Gas Emissions. *United States Environmental Protection Agency Website* (2018). Available at: <https://www.epa.gov/ghgemissions/sources-greenhouse-gas-emissions>. [Accessed: 27th October 2020].
5. National Oceanic and Atmospheric Administration (NOAA). Carbon Dioxide. *NASA Website* (2020). Available at: <https://climate.nasa.gov/vital-signs/carbon-dioxide/>. [accessed: 29th August 2020].
6. Stavins, R. N. The problem of the commons: Still unsettled after 100 years. *Am. Econ. Rev.* **101**, pp. 81–108 (2011).
7. NASA’s Goddard Institute for Space (GISS). Global Temperature. *NASA Website* (2020). Available at: <https://climate.nasa.gov/vital-signs/global-temperature/>. [accessed: 30th August 2020].
8. Anderson, T. R., Hawkins, E. & Jones, P. D. CO₂, the greenhouse effect and global warming: from the pioneering work of Arrhenius and Callendar to today’s Earth System Models. *Endeavour* **40**, pp. 178–187 (2016).
9. Henderson, R., Reinert, S. A., Dekhtyar, P. & Migdal, A. Climate Change in 2018: Implications for Business. *Harvard Bus. Publ.* pp. 15-25 (2018).
10. United Nations Framework Convention on Climate Change. The Paris Agreement. *United Nations Climate Change Website* (2020). Available at: <https://cop23.unfccc.int/process-and-meetings/the-paris-agreement/the-paris-agreement>. [accessed: 03rd Septemeber 2020].
11. Lucking, B. Solar photovoltaics deployment. National Statistics (2020). Available at: <https://www.gov.uk/government/statistics/solar-photovoltaics-deployment> [accessed: 03rd September 2020].
12. Beier, M. *et al.* Silicon waste from the photovoltaic industry – A material source for the next generation battery technology? *Mater. Sci. Forum* **959**, pp. 107–112 (2019).

13. Moen, M., Halvorsen, T., Mørk, K. & Velken, S. Recycling of silicon metal powder from industrial powder waste streams. *Met. Powder Rep.* **15**, pp. 62–65 (2017).
14. Sergiienko, S. A., Pogorelov, B. V. & Daniliuk, V. B. Silicon and silicon carbide powders recycling technology from wire-saw cutting waste in slicing process of silicon ingots. *Sep. Purif. Technol.* **133**, pp. 16–21 (2014).
15. Dou, B. *et al.* Roll-to-Roll Printing of Perovskite Solar Cells. *ACS Energy Lett.* **3**, pp. 2558–2565 (2018).
16. Hwang, K. *et al.* Toward large scale roll-to-roll production of fully printed perovskite solar cells. *Adv. Mater.* **27**, pp. 1241–1247 (2015).
17. Li, H. *et al.* Recent progress towards roll-to-roll manufacturing of perovskite solar cells using slot-die processing. *Flex. Print. Electron.* **5**, pp. 1–40 (2020).
18. Burkitt, D. *et al.* Roll-to-roll slot-die coated P-I-N perovskite solar cells using acetonitrile based single step perovskite solvent system. *Sustain. Energy Fuels* **4**, pp. 3340–3351 (2020).
19. Galagan, Y. *et al.* Roll-to-Roll Slot Die Coated Perovskite for Efficient Flexible Solar Cells. *Adv. Energy Mater.* **8**, pp. 180–193 (2018).
20. Couderc, E. Perovskite photovoltaics: Manufacturing costs. *Nat. Energy* **2**, 17080 (2017).
21. Juang, S. S. Y. *et al.* Energy harvesting under dim-light condition with dye-sensitized and perovskite solar cells. *Front. Chem.* **7**, pp. 1–9 (2019).
22. Reb, L. K. *et al.* Perovskite and Organic Solar Cells on a Rocket Flight. *Joule* **4**, pp. 1880–1892 (2020).
23. Mathews, I., Kantareddy, S. N., Buonassisi, T. & Peters, I. M. Technology and Market Perspective for Indoor Photovoltaic Cells. *Joule* **3**, pp. 1415–1426 (2019).
24. Lewis, G. N. The Conservation of Photons. *Nature* **118**, pp. 874–875 (1926).
25. Bard, A. J. Photoelectrochemistry. *Science (80-.)*. **207**, pp. 139–144 (1980).
26. Nayak, P. K., Garcia-Belmonte, G., Kahn, A., Bisquert, J. & Cahen, D. Photovoltaic efficiency limits and material disorder. *Energy Environ. Sci.* **5**, pp. 6022–6039 (2012).
27. Nelson, J. Properties of Semiconductor Materials, in *The Physics of Solar Cells*. Imperial College Press, London, UK. (2003). Available from: doi:10.1142/9781848161269_0001.
28. Mills, A. & Le Hunte, S. An overview of semiconductor photocatalysis. *J. Photochem. Photobiol. A Chem.* **108**, pp. 1–35 (1997).

29. Becquerel, E. On Electrode Effect under the Influence of Solar Radiation. *C.R. Acad. Sci.* **9**, 561 (1839).
30. Chapin, D. M., Fuller, C. S. & Pearson, G. L. A new silicon p-n junction photocell for converting solar radiation into electrical power. *J. Appl. Phys.* **25**, pp. 676 (1954).
31. Yoshikawa, K. *et al.* Silicon heterojunction solar cell with interdigitated back contacts for a photoconversion efficiency over 26%. *Nat. Energy* **2**, pp. 282–294 (2017).
32. National Renewable Energy Laboratory, Best Research-Cell Efficiencies. *NREL Website* (2020). Available at: <<https://www.nrel.gov/pv/cell-efficiency.html>>. [accessed: 03 September 2020].
33. Helbig, C., Bradshaw, A. M., Kolotzek, C., Thorenz, A. & Tuma, A. Supply risks associated with CdTe and CIGS thin-film photovoltaics. *Appl. Energy* **178**, pp. 422–433 (2016).
34. Acevedo-Luna, A., Bernal-Correa, R., Montes-Monsalve, J. & Morales-Acevedo, A. Design of thin film solar cells based on a unified simple analytical model. *J. Appl. Res. Technol.* **15**, pp. 599–608 (2017).
35. Lincot, D. The new paradigm of photovoltaics: From powering satellites to powering humanity. *Comptes Rendus Phys.* **18**, pp. 381–390 (2017).
36. Liu, W. S., Hu, H. C., Pu, N. W. & Liang, S. C. Developing flexible CIGS solar cells on stainless steel substrates by using Ti/TiN composite structures as the diffusion barrier layer. *J. Alloys Compd.* **631**, pp. 146–152 (2015).
37. Chirilă, A. *et al.* Highly efficient Cu(In,Ga)Se₂ solar cells grown on flexible polymer films. *Nat. Mater.* **10**, pp. 857–861 (2011).
38. Marwede, M. & Reller, A. Future recycling flows of tellurium from cadmium telluride photovoltaic waste. *Resour. Conserv. Recycl.* **69**, pp. 35–49 (2012).
39. Fthenakis, V. Sustainability of photovoltaics: The case for thin-film solar cells. *Renewable and Sustainable Energy Reviews* **13**, pp. 2746–2750 (2009).
40. Gerischer, H. Tributsch, H. Elektrochemische Untersuchung der spektralen Sensibilisierung von ZnO-Einkristallen. *Ber. Bunsenges. Phys. Chem.* **72**, pp. 437–445 (1968).
41. Gerischer H. and Tributsch H. Elektrochemische Untersuchung über den Mechanismus der Sensibilisierung und Übersensibilisierung an ZnO-Einkristallen. *Ber. Bunsenges. Phys. Chem.* **73**, pp. 251–260 (1969).
42. Tributsch, H. & Calvin, M. Electrochemistry of Excited Molecules: Photo-electrochemical Reactions of Chlorophylls *. *Photochem. Photobiol.* **14**, pp. 95–112 (1971).

43. Memming, R. Photochemical and Electrochemical Processes of Excited Dyes at Semiconductor and Metal Electrodes. *Photochem. Photobiol.* **16**, pp. 325–333 (1972).
44. Hauffe, K., Danzmann, H. J., Pusch, H., Range, J. & Volz, H. New Experiments on the Sensitization of Zinc Oxide by Means of the Electrochemical Cell Technique. *J. Electrochem. Soc.* **117**, pp. 993 (1970).
45. Gleria, M & Memming, R. Charge transfer processes at large band gap semiconductor electrodes: reactions at SiC-electrodes. *J. Electroanal. Chem.* **65**, pp. 163–175 (1975).
46. Clark, W. D. K. & Sutin, N. Spectral Sensitization of n-Type TiO₂ Electrodes by Polypyridineruthenium(II) Complexes. *J. Am. Chem. Soc.* **99**, pp. 4676–4682 (1977).
47. Nozik, A. J. Photoelectrochemistry: Applications of solar energy conversion. *J. Chem. Inf. Model.* **29**, pp. 189–222 (1978).
48. O'Regan, B. & Grätzel, M. A low-cost, high-efficiency solar cell based on dye-sensitized colloidal TiO₂ films. *Nature* **353**, pp. 737–740 (1991).
49. Gao, P., Gratzel, M. & Nazeeruddin, M. D. K. CHAPTER 6 Chemistry of Sensitizers for Dye-sensitized Solar Cells, in *Advanced Concepts in Photovoltaics*. Energy and Environment Series. Royal Society of Chemistry, London, UK (2014). Available from: doi:10.1039/9781849739955-00186
50. Barnes, P. R. F., Anderson, A. Y., Koops, S. E., Durrant, J. R. & O'Regan, B. C. Electron injection efficiency and diffusion length in dye-sensitized solar cells derived from incident photon conversion efficiency measurements. *J. Phys. Chem. C* **113**, pp. 1126–1136 (2009).
51. Listorti, A., O'Regan, B. & Durrant, J. R. Electron transfer dynamics in dye-sensitized solar cells. *Chemistry of Materials* **23**, pp. 3381–3399 (2011).
52. van Grondelle, R., Dekker, J. P., Gillbro, T. & Sundstrom, V. Energy transfer and trapping in photosynthesis. *Biochim. Biophys. Acta - Bioenerg.* **1187**, pp. 1–65 (1994).
53. Brennan, T. P. *et al.* TiO₂ conduction band modulation with In₂O₃ recombination barrier layers in solid-state dye-sensitized solar cells. *J. Phys. Chem. C* **117**, pp. 24138–24149 (2013).
54. Sommeling, P. M. *et al.* Influence of a TiCl₄ post-treatment on nanocrystalline TiO₂ films in dye-sensitized solar cells. *J. Phys. Chem. B* **110**, pp. 19191–19197 (2006).
55. Geiger, T. *et al.* Molecular design of unsymmetrical squaraine dyes for high efficiency conversion of low energy photons into electrons using TiO₂ nanocrystalline films. *Adv. Funct. Mater.* **19**, pp. 2720–2727 (2009).

56. Polo, A. S., Itokazu, M. K. & Murakami Iha, N. Y. Metal complex sensitizers in dye-sensitized solar cells. *Coordination Chemistry Reviews* **248**, pp. 1343–1361 (2004).
57. Nazeeruddin, M. K. *et al.* Conversion of light to electricity by cis-X₂bis(2,2'-bipyridyl-4,4'-dicarboxylate)ruthenium(II) charge-transfer sensitizers (X = Cl-, Br-, I-, CN-, and SCN-) on nanocrystalline titanium dioxide electrodes. *J. Am. Chem. Soc.* **115**, pp. 6382–6390 (1993).
58. Zakeeruddin, S. M. *et al.* Molecular Engineering of Photosensitizers for Nanocrystalline Solar Cells: Synthesis and Characterization of Ru Dyes Based on Phosphonated Terpyridines. *Inorg. Chem.* **36**, pp. 5937–5946 (1997).
59. Hagfeldt, A., Boschloo, G., Sun, L., Kloo, L. & Pettersson, H. Dye-sensitized solar cells. *Chem. Rev.* **110**, pp. 6595–6663 (2010).
60. Nazeeruddin, M. K. *et al.* Acid–Base Equilibria of (2,2'-Bipyridyl-4,4'-dicarboxylic acid)ruthenium(II) Complexes and the Effect of Protonation on Charge-Transfer Sensitization of Nanocrystalline Titania. *Inorg. Chem.* **38**, pp. 6298–6305 (1999).
61. Mathew, S. *et al.* Dye-sensitized solar cells with 13% efficiency achieved through the molecular engineering of porphyrin sensitizers. *Nat. Chem.* **6**, pp. 242–247 (2014).
62. Tennakone, K., Kumara, G. R. R. a., Kottegoda, I. R. M. & Perera, V. P. S. An efficient dye-sensitized photoelectrochemical solar cell made from oxides of tin and zinc. *Chem. Commun.* **1**, pp. 15–16 (1999).
63. Jose, R., Thavasi, V. & Ramakrishna, S. Metal oxides for dye-sensitized solar cells. *J. Am. Ceram. Soc.* **92**, pp. 289–301 (2009).
64. Kakiage, K. *et al.* Highly-efficient dye-sensitized solar cells with collaborative sensitization by silyl-anchor and carboxy-anchor dyes. *Chem. Commun.* **51**, pp. 15894–15897 (2015).
65. Shen, Z. *et al.* High performance solid-state dye-sensitized solar cells based on organic blue-colored dyes. *J. Mater. Chem. A* **5**, pp. 1242–1247 (2017).
66. Cao, Y. *et al.* 11% efficiency solid-state dye-sensitized solar cells with copper(II/I) hole transport materials. *Nat. Commun.* **8**, pp. 15390 (2017).
67. Liu, Q., Li, C., Jiang, K., Song, Y. & Pei, J. A high-efficiency solid-state dye-sensitized solar cell with P3HT polymer as a hole conductor and an assistant sensitizer. *Particuology* **15**, pp. 71–76 (2014).
68. El Chaar, L., lamont, L. A. & El Zein, N. Review of photovoltaic technologies. *Renew. Sustain. Energy Rev.* **15**, pp. 2165–2175 (2011).
69. Glazer, A. M. The classification of tilted octahedra in perovskites. *Acta Crystallogr. Sect. B Struct. Crystallogr. Cryst. Chem.* **28**, pp. 3384–3392 (1972).

70. J Johansson, M. & Lemmens, P. Crystallography and Chemistry of Perovskites. in *Handbook of Magnetism and Advanced Magnetic Materials*. John Wiley and Sons, Ltd. New Jersey, USA. (2007). Available from: doi:10.1002/9780470022184.hmm411
71. Frost, J. M. & Walsh, A. Molecular motion and dynamic crystal structures of hybrid halide perovskites. in *Organic-Inorganic Halide Perovskite Photovoltaics: From Fundamentals to Device Architectures* pp. 1–17 (2016). doi:10.1007/978-3-319-35114-8_1
72. Weber, D. CH₃NH₃PbX₃, a Pb(II)-System with Cubic Perovskite Structure. *Zeitschrift für Naturforsch. B* **33b**, pp. 1443–1445 (1978).
73. Weber, D. CH₃NH₃SnBr_xI_{3-x} (x = 0–3), a Sn(II)-System with the Cubic Perovskite Structure.e. *Zeitschrift für Naturforsch* **33b**, pp. 862–865 (1978).
74. Mitzi, D. B., Feild, C. A., Harrison, W. T. A. & Guloy, A. M. Conducting tin halides with a layered organic-based perovskite structure. *Nature* **369**, pp. 467–469 (1994).
75. Mitzi, D. B., Wang, S., Feild, C. A., Chess, C. A. & Guloy, A. M. Conducting layered organic-inorganic halides containing <110> -oriented perovskite sheets. *Science (80-.)*. **267**, pp. 1473–1476 (1995).
76. Xing, G. *et al.* Long-range balanced electron-and hole-transport lengths in organic-inorganic CH₃NH₃PbI₃. *Science (80-.)*. **342**, pp. 344–347 (2013).
77. Stranks, S. D. *et al.* Electron-hole diffusion lengths exceeding 1 micrometer in an organometal trihalide perovskite absorber. *Science (80-.)*. **342**, pp. 341–344 (2013).
78. Wehrenfennig, C., Eperon, G. E., Johnston, M. B., Snaith, H. J. & Herz, L. M. High charge carrier mobilities and lifetimes in organolead trihalide perovskites. *Adv. Mater.* **26**, pp. 1584–1589 (2014).
79. Yang, J., Siempelkamp, B. D., Liu, D. & Kelly, T. L. An Investigation of CH₃NH₃PbI₃ Degradation Rates and Mechanisms in Controlled Humidity Environments Using in situ Techniques. *ACS Nano* **9**, pp. 1955–1963 (2015).
80. Walsh, A. Principles of chemical bonding and band gap engineering in hybrid organic-inorganic halide perovskites. *J. Phys. Chem. C* **119**, pp. 5755–5760 (2015).
81. Habisreutinger, S. N. *et al.* Carbon nanotube/polymer composites as a highly stable hole collection layer in perovskite solar cells. *Nano Lett.* **14**, pp. 5561–5568 (2014).
82. Zhang, Y.-Y. *et al.* Intrinsic Instability of the Hybrid Halide Perovskite Semiconductor CH₃NH₃PbI₃. *Nat. Commun.* **35**, 036104 (2015).
83. Saliba, M. *et al.* Cesium-containing triple cation perovskite solar cells: improved stability, reproducibility and high efficiency. *Energy Environ. Sci.* **9**, pp. 1989–1997 (2016).

84. Saliba, M. *et al.* Incorporation of rubidium cations into perovskite solar cells improves photovoltaic performance. *Science* (80-.). **354**, pp. 206–209 (2016).
85. Duong, T. *et al.* Structural engineering using rubidium iodide as a dopant under excess lead iodide conditions for high efficiency and stable perovskites. *Nano Energy* **30**, pp. 330–340 (2016).
86. Zhang, M. *et al.* High-Efficiency Rubidium-Incorporated Perovskite Solar Cells by Gas Quenching. *ACS Energy Letters* **2**, pp. 438–444 (2017).
87. Noh, J. H., Im, S. H., Heo, J. H., Mandal, T. N. & Seok, S. Il. Ch1. Noh, J. H., Im, S. H., Heo, J. H., Mandal, T. N. & Seok, S. Il. Chemical management for colorful, efficient, and stable inorganic-organic hybrid nanostructured solar cells. *Nano Lett.* **13**, pp. 1764–1769 (2013).
88. Misra, R. K. *et al.* Temperature- and component-dependent degradation of perovskite photovoltaic materials under concentrated sunlight. *J. Phys. Chem. Lett.* **6**, pp. 326–330 (2015).
89. Baikie, T. *et al.* Synthesis and crystal chemistry of the hybrid perovskite (CH₃NH₃)PbI₃ for solid-state sensitised solar cell applications. *J. Mater. Chem. A* **1**, pp. 5628–5641 (2013).
90. Benavides-Garcia, M. & Balasubramanian, K. Bond energies, ionization potentials, and the singlet-triplet energy separations of SnCl₂, SnBr₂, SnI₂, PbCl₂, PbBr₂, PbI₂, and their positive ions. *J. Chem. Phys.* **100**, pp. 2821–2830 (1994).
91. Tanaka, K. & Kondo, T. Bandgap and exciton binding energies in lead-iodide-based natural quantum-well crystals. *Sci. Technol. Adv. Mater.* **4**, pp. 599–604 (2003).
92. Tanaka, K. *et al.* Comparative study on the excitons in lead-halide-based perovskite-type crystals CH₃NH₃PbBr₃ CH₃NH₃PbI₃. *Solid State Commun.* **127**, pp. 619–623 (2003).
93. Knoester, J. & Agranovich, V. M. Chapter 1 Frenkel and charge-transfer excitons in organic solids. *Thin Film. Nanostructures* **31**, pp. 1–96 (2003).
94. Hirasawa, M., Ishihara, T., Goto, T., Uchida, K. & Miura, N. Magnetoabsorption of the lowest exciton in perovskite-type compound (CH₃NH₃)PbI₃. *Phys. B Phys. Condens. Matter* **201**, pp. 427–430 (1994).
95. Kojima, A., Teshima, K., Shirai, Y. & Miyasaka, T. Organometal Halide Perovskites as Visible-Light Sensitizers for Photovoltaic Cells. *J. Am. Chem. Soc.* **131**, pp. 6050–6051 (2009).
96. Im, J.-H., Lee, C.-R., Lee, J.-W., Park, S.-W. & Park, N.-G. 6.5% efficient perovskite quantum-dot-sensitized solar cell. *Nanoscale* **3**, 4088 (2011).

97. Green, M. A. & Ho-Baillie, A. Perovskite Solar Cells: The Birth of a New Era in Photovoltaics. *ACS Energy Lett.* **2**, pp. 822–830 (2017).
98. Lee, M. M., Teuscher, J., Miyasaka, T., Murakami, T. N. & Snaith, H. J. Efficient Hybrid Solar Cells Based on Meso-Superstructured Organometal Halide Perovskites. *Science (80-.)*. **338**, pp. 643–647 (2012).
99. Kim, H.-S. *et al.* Lead Iodide Perovskite Sensitized All-Solid-State Submicron Thin Film Mesoscopic Solar Cell with Efficiency Exceeding 9%. *Sci. Rep.* **2**, 591 (2012).
100. Heo, J. H. *et al.* Efficient inorganic–organic hybrid heterojunction solar cells containing perovskite compound and polymeric hole conductors. *Nat. Photonics* **7**, pp. 486–491 (2013).
101. Ball, J. M. *et al.* Low-temperature processed meso-superstructured to thin-film perovskite solar cells. *Energy Environ. Sci.* **6**, 1739 (2013).
102. Burschka, J. *et al.* Sequential deposition as a route to high-performance perovskite-sensitized solar cells. *Nature* **499**, pp. 316–319 (2013).
103. Jeon, N. J. *et al.* Solvent engineering for high-performance inorganic–organic hybrid perovskite solar cells. *Nat. Mater.* *2014* **139** **13**, pp. 897–903 (2014).
104. Zhou, H. *et al.* Interface engineering of highly efficient perovskite solar cells. *Science (80-.)*. **345**, pp. 542–546 (2014).
105. Bi, D. *et al.* Polymer-templated nucleation and crystal growth of perovskite films for solar cells with efficiency greater than 21%. *Nat. Energy* **1**, 16142 (2016).
106. Kim, C. Y. & Riu, D. H. Texture control of fluorine-doped tin oxide thin film. *Thin Solid Films* **519**, pp. 3081–3085 (2011).
107. Banyamin, Z., Kelly, P., West, G. & Boardman, J. Electrical and Optical Properties of Fluorine Doped Tin Oxide Thin Films Prepared by Magnetron Sputtering. *Coatings* **4**, pp. 732–746 (2014).
108. Yang, D. *et al.* High efficiency planar-type perovskite solar cells with negligible hysteresis using EDTA-complexed SnO₂. *Nat. Commun.* **9**, 3239 (2018).
109. Kim, H., Lim, K. G. & Lee, T. W. Planar heterojunction organometal halide perovskite solar cells: Roles of interfacial layers. *Energy Environ. Sci.* **9**, pp. 12–30 (2016).
110. Mills, A., Davies, R. H. & Worsley, D. Water purification by semiconductor photocatalysis. *Chem. Soc. Rev.* **22**, pp. 417–425 (1993).
111. Singh, T. & Miyasaka, T. Stabilizing the Efficiency Beyond 20% with a Mixed Cation Perovskite Solar Cell Fabricated in Ambient Air under Controlled Humidity. *Adv. Energy Mater.* **25**, 1700677 (2018).

112. An, Q. *et al.* High performance planar perovskite solar cells by ZnO electron transport layer engineering. *Nano Energy* **39**, pp. 400–408 (2017).
113. Hu, L. *et al.* Sequential Deposition of CH₃NH₃PbI₃ on Planar NiO Film for Efficient Planar Perovskite Solar Cells. *ACS Photonics* **1**, pp. 547–553 (2014).
114. Ke, W. *et al.* Lower temperature solution-processed tin oxide as an alternative electron transporting layer for efficient perovskite solar cells. *J. Am. Chem. Soc.* **137**, pp. 6730–6733 (2015).
115. Guillén, E., Ramos, F. J., Anta, J. A. & Ahmad, S. Elucidating transport-recombination mechanisms in perovskite solar cells by small-perturbation techniques. *J. Phys. Chem. C.* **40**, pp. 22913–22922 (2014).
116. Jiang, Q. *et al.* Surface passivation of perovskite film for efficient solar cells. *Nat. Photonics* **13**, pp. 460–466 (2019).
117. Chen, W. *et al.* A comparative study of planar and mesoporous perovskite solar cells with printable carbon electrodes. *J. Power Sources*, **412**, pp. 118–124 (2019).
118. Liu, M., Endo, M., Shimazaki, A., Wakamiya, A. & Tachibana, Y. Identifying an Optimum Perovskite Solar Cell Structure by Kinetic Analysis: Planar, Mesoporous Based, or Extremely Thin Absorber Structure. *ACS Appl. Energy Mater.* **8**, pp. 3722–3732 (2018).
119. Xing, G. *et al.* Interfacial Electron Transfer Barrier at Compact TiO₂/CH₃NH₃PbI₃ Heterojunction. *Small* **11**, pp. 3606–3613 (2015).
120. Tress, W. *et al.* Understanding the rate-dependent J-V hysteresis, slow time component, and aging in CH₃NH₃PbI₃ perovskite solar cells: The role of a compensated electric field. *Energy Environ. Sci.* **8**, pp. 995–1004 (2015).
121. Pascoe, A. R. *et al.* Planar versus mesoscopic perovskite microstructures: The influence of CH₃NH₃PbI₃ morphology on charge transport and recombination dynamics. *Nano Energy* **22**, pp. 439–452 (2016).
122. Ouedraogo, N. A. N. *et al.* Stability of all-inorganic perovskite solar cells. *Nano Energy* **67**, 104249 (2020).
123. Singh, R., Sandhu, S. & Lee, J. J. Elucidating the effect of shunt losses on the performance of mesoporous perovskite solar cells. *Sol. Energy* **193**, pp. 956–961 (2019).
124. Lee, S., Park, T., Lee, J. & Pang, Y. Ultrafast Electron Injection from the S₂ State of Carotenoids into TiO₂ Nanoparticles. *J. Nanosci. Nanotechnol.* **17** (4), pp. 2685–2689 (2017).

125. Lee, M. M., Teuscher, J., Miyasaka, T., Murakami, T. N. & Snaith, H. J. Efficient Hybrid Solar Cells Based on Meso-Superstructured Organometal Halide Perovskites. *Science* (80-.). **338**, pp. 643–647 (2012).
126. Kato, Y. *et al.* Silver Iodide Formation in Methyl Ammonium Lead Iodide Perovskite Solar Cells with Silver Top Electrodes. *Adv. Mater. Interfaces* **2**, 1500195 (2015).
127. La Rocca, G. Wannier–Mott Excitons in Semiconductors. in *Thin Films and Nanostructures*, **18**, pp. 97–128 (2003).
128. Kedem, N. *et al.* Light-Induced Increase of Electron Diffusion Length in a p-n Junction Type CH₃NH₃PbBr₃ Perovskite Solar Cell. *J. Phys. Chem. Lett.* **6**, pp. 2469–2476 (2015).
129. Ponseca, C. S. *et al.* Organometal Halide Perovskite Solar Cell Materials Rationalized: Ultrafast Charge Generation, High and Microsecond-Long Balanced Mobilities, and Slow Recombination. *J. Am. Chem. Soc.* **136**, pp. 5189–5192 (2014).
130. Sandberg, O. J. *et al.* On the Question of the Need for a Built-In Potential in Perovskite Solar Cells. *Adv. Mater. Interfaces* **7**, 2000041 (2020).
131. Marchioro, A. *et al.* Unravelling the mechanism of photoinduced charge transfer processes in lead iodide perovskite solar cells. *Nat. Photonics* **8**, pp. 250–255 (2014).
132. Wang, L., McCleese, C., Kovalsky, A., Zhao, Y. & Burda, C. Femtosecond Time-Resolved Transient Absorption Spectroscopy of CH₃NH₃PbI₃ Perovskite Films: Evidence for Passivation Effect of PbI₂. *J. Am. Chem. Soc.* **110**, 14082 (2014).
133. Mora-Seró, I. How Do Perovskite Solar Cells Work? *Joule* **2**, pp. 583–593 (2018).
134. Sherkar, T. S. *et al.* Recombination in Perovskite Solar Cells: Significance of Grain Boundaries, Interface Traps, and Defect Ions. *ACS Energy Lett.* **2**, pp. 1214–1222 (2017).
135. Yang, Y. *et al.* Top and bottom surfaces limit carrier lifetime in lead iodide perovskite films. *Nat. Energy* **2**, 16207 (2017).
136. Tress, W. *et al.* Interpretation and evolution of open-circuit voltage, recombination, ideality factor and subgap defect states during reversible light-soaking and irreversible degradation of perovskite solar cells. *Energy Environ. Sci.* **11**, pp. 151–165 (2018).
137. Droseros, N., Tsokkou, D. & Banerji, N. Photophysics of Methylammonium Lead Tribromide Perovskite: Free Carriers, Excitons, and Sub-Bandgap States. *Adv. Energy Mater.* **10**, 1903258 (2020).
138. Wang, J., Zhang, A., Yan, J., Li, D. & Chen, Y. Revealing the properties of defects formed by CH₃NH₂ molecules in organic-inorganic hybrid perovskite MAPbBr₃. *Appl. Phys. Lett.* **110**, 123903 (2017).

139. Ball, J. M. & Petrozza, A. Defects in perovskite-halides and their effects in solar cells. *Nat. Energy* **1**, 16149 (2016).
140. Zhou, Y., Hu, X., Xie, D. & Tian, Y. Mechanisms of Oxygen Passivation on Surface Defects in MAPbI₃ Revealed by First-Principles Study. *J. Phys. Chem. C* **124**, pp. 3731–3737 (2020).
141. Hoffmann, M. R., Martin, S. T., Choi, W. & Bahnemann, D. W. Environmental Applications of Semiconductor Photocatalysis. *Chem. Rev.* **95**, pp. 69–96 (1995).
142. Baloch, A. A. B., Hossain, M. I., Tabet, N. & Alharbi, F. H. Practical Efficiency Limit of Methylammonium Lead Iodide Perovskite (CH₃NH₃PbI₃) Solar Cells. *J. Phys. Chem. Lett.* **9**, pp. 426–434 (2018).
143. Agarwal, S. *et al.* On the uniqueness of ideality factor and voltage exponent of perovskite-based solar cells. *J. Phys. Chem. Lett.* **5**, pp. 4115–4121 (2014).
144. Viswanath, A. K. Chapter 3 - Surface and Interfacial Recombination in Semiconductors. *in Handbook of Surfaces and Interfaces of Materials*. pp. 218–221. Academic Press, London, UK. (2001). Available from: 10.1016/B978-012513910-6/50010-4.
145. Wetzelaer, G. J. A. H. *et al.* Trap-Assisted Non-Radiative Recombination in Organic-Inorganic Perovskite Solar Cells. *Adv. Mater.* **27**, pp. 1837–1841 (2015).
146. Buin, A. *et al.* Materials processing routes to trap-free halide perovskites. *Nano Lett.* **14**, pp. 6281–6286 (2014).
147. Stranks, S. D. *et al.* Recombination Kinetics in Organic-Inorganic Perovskites: Excitons, Free Charge, and Subgap States. *Phys. Rev. Appl.* **2**, 034007 (2014).
148. Wehrenfennig, C., Liu, M., Snaith, H. J., Johnston, M. B. & Herz, L. M. Charge carrier recombination channels in the low-temperature phase of organic-inorganic lead halide perovskite thin films. *APL Mater.* **2**, 081513 (2014).
149. Wolff, C. M., Caprioglio, P., Stolterfoht, M. & Neher, D. Nonradiative Recombination in Perovskite Solar Cells: The Role of Interfaces. *Adv. Mater.* **31**, 1902762 (2019).
150. Yang, Y. *et al.* Low surface recombination velocity in solution-grown CH₃NH₃PbBr₃ perovskite single crystal. *Nat. Commun.* **6**, 7961 (2015).
151. Yang, W. S. *et al.* Iodide management in formamidinium-lead-halide-based perovskite layers for efficient solar cells. *Science (80-.)*. **356**, pp. 1376–1379 (2017).
152. Jeon, N. J. *et al.* Compositional engineering of perovskite materials for high-performance solar cells. *Nature* **517**, pp. 476–480 (2015).

153. Li, W., Fan, J., Li, J., Mai, Y. & Wang, L. Controllable grain morphology of perovskite absorber film by molecular self-assembly toward efficient solar cell exceeding 17%. *J. Am. Chem. Soc.* **137**, pp. 10399–10405 (2015).
154. Dualeh, A. *et al.* Effect of annealing temperature on film morphology of organic-inorganic hybrid perovskite solid-state solar cells. *Adv. Funct. Mater.* **24**, pp. 3250–3258 (2014).
155. Gedamu, D. *et al.* Solvent-Antisolvent Ambient Processed Large Grain Size Perovskite Thin Films for High-Performance Solar Cells. *Sci. Rep.* **8**, 12885 (2018).
156. Li, Y., Wang, J., Yuan, Y., Dong, X. & Wang, P. Anti-solvent dependent device performance in CH₃NH₃PbI₃ solar cells: the role of intermediate phase content in the as-prepared thin films. *Sustain. Energy Fuels* **1**, pp. 1041–1048 (2017).
157. Love, J. C., Estroff, L. A., Kriebel, J. K., Nuzzo, R. G. & Whitesides, G. M. Self-assembled monolayers of thiolates on metals as a form of nanotechnology. *Chem. Rev.* **105**, pp. 1103–1170 (2005).
158. Choi, K. *et al.* A Short Review on Interface Engineering of Perovskite Solar Cells: A Self-Assembled Monolayer and Its Roles. *Sol. RRL* **35**, 1900251 (2020).
159. Qiao, R. & Zuo, L. Self-assembly monolayers boosting organic-inorganic halide perovskite solar cell performance. *J. Mater. Res.* **33**, pp. 387–400 (2018).
160. Zuo, L. *et al.* Enhanced photovoltaic performance of CH₃NH₃PbI₃ perovskite solar cells through interfacial engineering using self-assembling monolayer. *J. Am. Chem. Soc.* **137**, 15540 (2015).
161. Cho, C. P., Chu, C. C., Chen, W. T., Huang, T. C. & Tao, Y. T. Molecular modification on dye-sensitized solar cells by phosphonate self-assembled monolayers. *J. Mater. Chem.* **22**, pp. 2915–2921 (2012).
162. Wojciechowski, K. *et al.* Heterojunction modification for highly efficient organic-inorganic perovskite solar cells. *ACS Nano* **8**, pp. 12701–12709 (2014).
163. Li, B., Chen, Y., Liang, Z., Gao, D. & Huang, W. Interfacial engineering by using self-assembled monolayer in mesoporous perovskite solar cell. *RSC Adv.* **5**, 94290–94295 (2015).
164. Zuo, L. *et al.* Tailoring the interfacial chemical interaction for high-efficiency perovskite solar cells. *Nano Lett.* **17**, pp. 269–275 (2017).
165. Yang, G. *et al.* Interface engineering in planar perovskite solar cells: Energy level alignment, perovskite morphology control and high performance achievement. *J. Mater. Chem. A* **5**, pp. 1658–1666 (2017).

166. Hou, X. *et al.* Constructing Efficient and Stable Perovskite Solar Cells via Interconnecting Perovskite Grains. *ACS Appl. Mater. Interfaces* **9**, pp. 35200–35208 (2017).
167. Anizelli, H., David, T. W., Tyagi, P., Laureto, E. & Kettle, J. Enhancing the stability of perovskite solar cells through functionalisation of metal oxide transport layers with self-assembled monolayers. *Sol. Energy* **203**, pp. 157–163 (2020).
168. Wang, Q. *et al.* Effects of Self-Assembled Monolayer Modification of Nickel Oxide Nanoparticles Layer on the Performance and Application of Inverted Perovskite Solar Cells. *ChemSusChem* **10**, pp. 3794–3803 (2017).
169. Zhang, J. *et al.* Bifunctional alkyl chain barriers for efficient perovskite solar cells. *Chem. Commun.* **51**, pp. 7047–7050 (2015).
170. Wang, Q., Dong, Q., Li, T., Gruverman, A. & Huang, J. Thin Insulating Tunneling Contacts for Efficient and Water-Resistant Perovskite Solar Cells. *Adv. Mater.* **28**, pp. 6734–6739 (2016).
171. Liang, P. W. *et al.* Additive enhanced crystallization of solution-processed perovskite for highly efficient planar-heterojunction solar cells. *Adv. Mater.* **26**, pp. 3748–3754 (2014).
172. Chueh, C.-C. *et al.* The roles of alkyl halide additives in enhancing perovskite solar cell performance. *J. Mater. Chem. A* **3**, pp. 9058–9062 (2015).
173. Mabrouk, S. *et al.* Higher efficiency perovskite solar cells using additives of LiI, LiTFSI and BMImI in the PbI₂ precursor. *Sustain. Energy Fuels* **1**, pp. 2162–2171 (2017).
174. Snaith, H. J. *et al.* Anomalous Hysteresis in Perovskite Solar Cells. *J. Phys. Chem. Lett.* **5**, pp. 1511–1515 (2014).
175. Nemnes, G. A. *et al.* How measurement protocols influence the dynamic J-V characteristics of perovskite solar cells: theory and experiment. *Sol. Energy* **173**, pp. 976–987 (2018).
176. Wu, F. *et al.* Bias-Dependent Normal and Inverted J- V Hysteresis in Perovskite Solar Cells. *ACS Appl. Mater. Interfaces* **10**, pp. 25604–25613 (2018).
177. Kang, D.-H. & Park, N.-G. On the Current–Voltage Hysteresis in Perovskite Solar Cells: Dependence on Perovskite Composition and Methods to Remove Hysteresis. *Adv. Mater.* **31**, 1805214 (2019).
178. Park, N.-G., Gratzel, M., Miyasaka, T., Zhu, K. & Emery, K. Towards stable and commercially available perovskite solar cells. *Nat. Energy* **16152**, pp. 124–128 (2016).

179. Wei, J. Z. *et al.* Hysteresis Analysis Based on the Ferroelectric Effect in Hybrid Perovskite Solar Cells. *J. Phys. Chem. Lett.* **5**, pp. 3937–3945 (2014).
180. Elumalai, N. K. & Uddin, A. Hysteresis in organic-inorganic hybrid perovskite solar cells. *Sol. Energy Mater. Sol. Cells* **157**, pp. 476–509 (2016).
181. Shao, Y., Xiao, Z., Bi, C., Yuan, Y. & Huang, J. Origin and elimination of photocurrent hysteresis by fullerene passivation in CH₃NH₃PbI₃ planar heterojunction solar cells. *Nat. Commun.* **5**, 5784 (2014).
182. Van Reenen, S., Kemerink, M. & Snaith, H. J. Modeling Anomalous Hysteresis in Perovskite Solar Cells. *J. Phys. Chem. Lett.* **6**, pp. 3808–3814 (2015).
183. Almora, O., Aranda, C., Zarazua, I., Guerrero, A. & Garcia-Belmonte, G. Noncapacitive Hysteresis in Perovskite Solar Cells at Room Temperature. *ACS Energy Lett.* **1**, pp. 209–215 (2016).
184. Ebadi, F., Taghavinia, N., Mohammadpour, R., Hagfeldt, A. & Tress, W. Origin of apparent light-enhanced and negative capacitance in perovskite solar cells. *Nat. Commun.* **10**, 1574 (2019).
185. Correa-Baena, J.-P. *et al.* Unbroken Perovskite: Interplay of Morphology, Electro-optical Properties, and Ionic Movement. *Adv. Mater.* **28**, pp. 5031–5037 (2016).
186. Van Reenen, S., Kemerink, M. & Snaith, H. J. Modeling Anomalous Hysteresis in Perovskite Solar Cells. *J. Phys. Chem. Lett.* **6**, pp. 3808–3814 (2015).
187. Belisle, R. A. *et al.* Interpretation of inverted photocurrent transients in organic lead halide perovskite solar cells: proof of the field screening by mobile ions and determination of the space charge layer widths[†]. *Energy Environ. Sci.* **10**, pp. 192–204 (2017).
188. Eames, C. *et al.* Ionic transport in hybrid lead iodide perovskite solar cells. *Nat. Commun.* **6**, pp. 1–8 (2015).
189. Weber, S. A. L. *et al.* How the formation of interfacial charge causes hysteresis in perovskite solar cells. *Energy Environ. Sci.* **11**, pp. 2404–2413 (2018).
190. Zhang, T. *et al.* Understanding the relationship between ion migration and theanomalous hysteresis in high-efficiency perovskite solar cells: A freshperspective from halide substitution. *Nano Energy* **26**, pp. 620–630 (2016).
191. Aidarkanov, D. *et al.* Passivation engineering for hysteresis-free mixed perovskite solar cells. *Sol. Energy Mater. Sol. Cells* **215**, 110648 (2020).

2 Experimental methods

This Chapter lists and describes the general experimental and characterisation techniques used within this thesis. Where applicable, the experimental methods used for a specific application are given in the experimental section of the relevant Chapter along with the respective sample preparation methods.

2.1 Manufacture of perovskite solar cells

All chemicals were acquired from Sigma-Aldrich and used as supplied unless otherwise stated. All thin-films and full devices were fabricated in an ambient environment.

2.1.1 Preparation of perovskite thin-films

The device working electrode was prepared on 2 mm thick fluorine-doped tin oxide (FTO) glass ($7 \Omega \text{ sq}^{-1}$, NSG Pilkington). A 28 mm wide section of FTO glass was masked using 3M Scotch Tape (19 mm width) by positioning the tape centrally along the glass leaving a 4.5 mm unmasked region at either edge. The unmasked regions were then chemically etched using Zn powder and 2M HCl. This process prevents device shunting by removing FTO from the regions which would be in contact with the counter-electrode pins during device measurement (Figure 2.0).

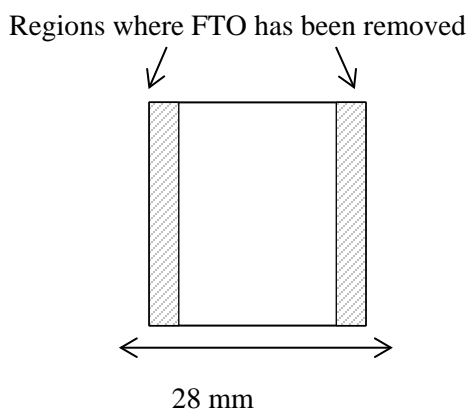


Figure 2.0: Schematic of an FTO glass thin-film showing areas of FTO removal through chemical etching.

Following removal of the Scotch Tape, oil-based contaminants were removed from the glass through cleaning with a soft bristle toothbrush and a 2% by volume solution of Hellmanex III (Sigma-Aldrich) in deionised water. The glass was then cut into 28 x 28 mm thin-films, added to a beaker of deionised water and sonicated under heat to 80 °C in an ultrasonic water bath. The films were then rinsed in deionised water, acetone, ethanol and isopropanol before drying under compressed nitrogen. The films were transferred to an oxygen plasma cleaner (Diener Electronic) for 10 minutes to provide further cleaning and ensure activation of the FTO glass surface.

A thin (~50 nm) compact titania (c-TiO₂) layer was deposited onto each film using spray pyrolysis. A titania precursor solution (0.2 M titanium diisopropoxide bis(acetylacetonate) in isopropanol) was prepared and loaded into an airbrush gun coupled with an air compressor. The films were arranged on a hot plate and subsequently heated to 300 °C. With the airbrush gun positioned 30 cm above the film surface, the c-TiO₂ layer was then deposited over 25 horizontal spray passes.

A mesoporous titania (mp-TiO₂) solution was prepared by diluting titania paste (30-NRD, Dyesol) in isopropanol (2:7 by weight). The solution was sonicated for 30 minutes and filtered prior to use through a 1.0 µm filter (Minisart, Sartorius). The mp-TiO₂ layer was then deposited by spin coating (Laurell Technologies) 150 µL of the aforementioned solution onto the c-TiO₂ layer of each film at 6000 rpm/2000 rpms⁻¹ for 30 seconds.



Figure 2.1: Photographs showing the inside of the spin-coater used for thin-film deposition (left) and a MAPbBr₃ thin-film positioned in the spin-coater prior to deposition of the hole transport layer (right).

Residual isopropanol was removed from the films by drying for 10 minutes on a pre-heated hotplate (110 °C) followed by annealing at 550 °C for 30 minutes (Figure 2.2). Following annealing, the films were cooled to room temperature before removal from the hot plate.



Figure 2.2: Photograph showing the drying of several mesoporous thin-films on a pre-heated (110 °C) hotplate to encourage the removal residual isopropanol.

2.1.2 Preparation of the perovskite layer

To synthesis a 1 mL solution of $\text{CH}_3\text{NH}_3\text{PbBr}_3$, 140 mg of methyl ammonium bromide powder (MABr, GreatCell Solar) was combined with 459 mg of lead (II) bromide powder (99.9%, Sigma-Aldrich).

To synthesis a 1 mL solution of $\text{CH}_3\text{NH}_3\text{PbI}_3$, 199 mg of methyl ammonium iodide powder (MAI, GreatCell Solar) was combined with 576 mg of lead iodide powder (99.9%, Sigma-Aldrich).

A 1 mL 4:1 volume solution of N, N-dimethylformamide (DMF) and dimethyl sulfoxide (DMSO) was prepared by adding 0.8 mL of DMF to 0.2 mL of DMSO. The combined powders were then dissolved in the DMF: DMSO solution through stirring and heating at 60 °C on a pre-heated hot plate. Once fully dissolved, the perovskite precursor solution was removed from the hot plate and filtered through a 0.2 μm PTFE syringe filter (Minisart, Sartorius).



Figure 2.3: Photographs showing a colourless MAPbBr₃ perovskite precursor solution (left) and a yellow MAPbI₃ perovskite precursor solution (right).

The perovskite layer was deposited onto the titania coated glass by spin coating 100 μ L of perovskite precursor solution at two spin speeds. Initially, the solution was spun at 1000 rpm/2000 rpm^{-1} for 10 seconds followed by an increased speed of 4000 rpm/2000 rpm^{-1} for 20 seconds. For MAPbI₃ films, an anti-solvent drip was used which involved depositing 200 μ L of ethyl acetate in the center of the film within the last 10 seconds of spin coating. The perovskite layer was then annealed on a pre-heated hot plate for 10 minutes, the temperature of which was dependent up on the perovskite precursor solution used. An annealing temperature of 60 $^{\circ}$ C and 100 $^{\circ}$ C were used for MAPbBr₃ and MAPbI₃, respectively. During annealing, a visible and characteristic colour change was indicative of successful perovskite formation. For MAPbI₃ films this involved a colour transition from pale yellow to dark brown whereas MAPbBr₃ films transitioned from colourless to orange.



Figure 2.4: Photographs showing perovskite thin-films of: MAPbI₃ (left) and MAPbBr₃ (right) following annealing.

2.1.3 Full device manufacture

Thin-films were made into full devices through the deposition of a hole transport layer (HTL) and the addition of gold contacts. The HTL solution was prepared in a nitrogen-filled glovebox (<0.5 ppm H₂O, <0.5 ppm O₂, MBraun) and involved the dissolution of 90 mg of

2, 20, 7, 70-tetrakis-(N, N-di-p-methoxyphenylamine)-9, 90-spirobifluorene (spiro-OMeTAD) in 1 mL of chlorobenzene. 34 μL of 4-tert-butylpyridine (4-TBP) and 19 μL of lithium bis(trifluoromethanesulfonyl)- imide (LiTFSI) in acetonitrile (520 mg/mL) was then added to this solution. The spiro-OMeTAD HTL solution was then filtered (0.2 μm , Minisart, Sartorius) and deposited onto each thin-film *via* spin coating 70 μL of solution at 4000 rpm/2000 rpm⁻¹ for 20 seconds. The films were stored overnight in a dark and dry atmosphere to encourage oxidation of the spiro-OMeTAD layer. To complete as full devices, 80 nm gold contacts were deposited on each film by thermally evaporating gold wire (Kurt. J. Lesker) through a shadow mask at 10⁻⁴ torr (Edwards 306 bell-jar evaporator).

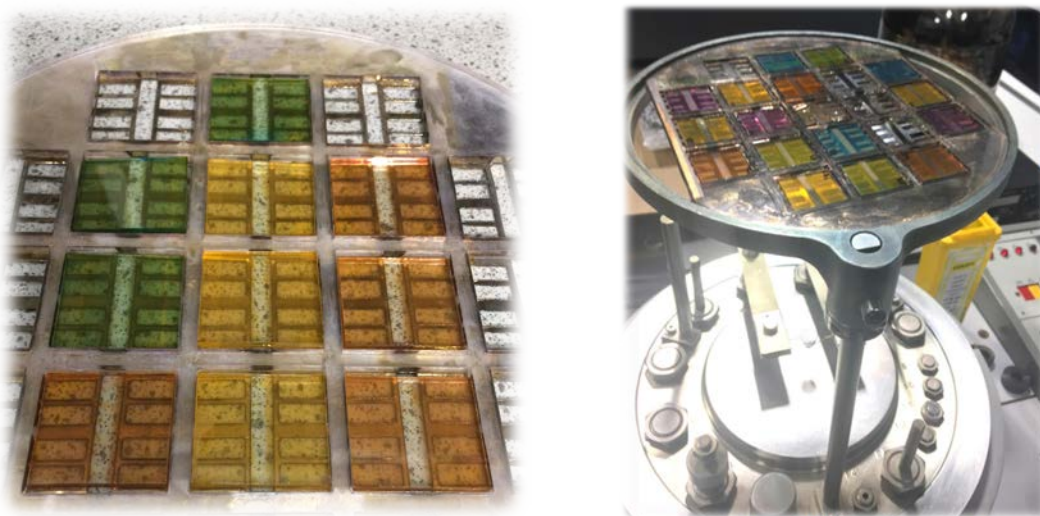


Figure 2.5: Photographs showing control and co-sensitised MAPbBr₃ thin-films: loaded into the shadow mask (left) and subsequently prior to evaporation of the gold contacts using the bell-jar evaporator (right).

The shadow mask generated 8 counter-electrodes or ‘pixels’ per device, each pixel had an area of 0.1 cm². Figures 2.6 and 2.7 overleaf show the full device stack architecture and complete MAPbI₃ and MAPbBr₃ perovskite devices including the 8 gold pixels.

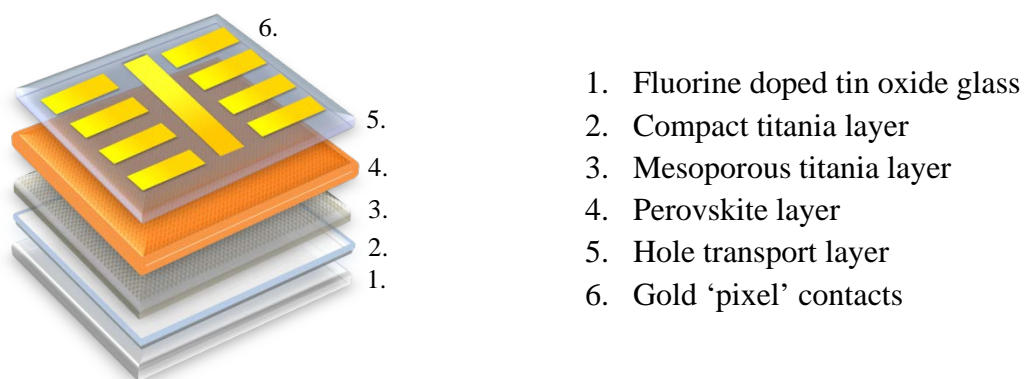


Figure 2.6: Schematic of a complete / full perovskite device highlighting the arrangement of the 8 pixels with a central common working electrode.

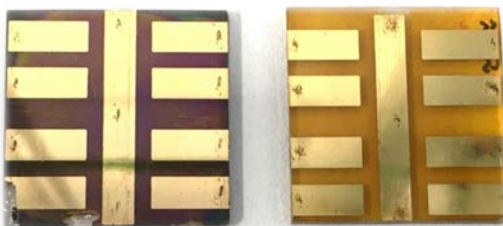


Figure 2.7: Photographs of MAPbI_3 and MAPbBr_3 devices complete with gold pixels, left and right, respectively.

2.2 Co-sensitisation of perovskite solar cells

2.2.1 Preparation of dye solutions

All dye solutions were prepared as 1 mM stock solutions in anhydrous toluene unless otherwise stated. Each stock solution was used to prepare solutions of a lower concentration (where required) by dilution in anhydrous toluene.

2.2.2 Solid state dyed thin-film preparation

Solid state dyed thin-films were prepared by submerging mp-TiO₂ coated thin-films (preparation described in Section 2.1.1) in a dye solution for 10 minutes followed by drying with an air gun. The dyed thin-films were then completed as full devices through the deposition of a spiro-OMeTAD HTL and the addition of gold contacts as described in Section 2.1.3.

2.2.3 Co-sensitisation methods

The perovskite thin-films were co-sensitised using one of two methods:

2.2.3.1 ‘Dye before’ (DB) method

The mesoporous titania layer was dyed prior to deposition of the perovskite layer by submerging the titania coated thin-film in the appropriate dye solution for 10 minutes. The thin-films were then removed from the dye solution and dried *via* air gun. Once dry, 100 µL of perovskite precursor solution was deposited onto the mesoporous titania layer *via* spin coating using the method described in Section 2.1.2. After spin coating, the co-sensitised perovskite thin-films were annealed on a pre-heated hot plate at the required temperature for 10 minutes.

2.2.3.2 ‘Dye after’ (DA) method

Co-sensitisation of perovskite thin-films was carried out following the deposition and annealing of the perovskite. Once cooled to room temperature, the perovskite thin-films were submerged in the appropriate dye solution for 10 minutes and subsequently dried with an air gun.

2.3 Characterisation of perovskite thin-films

The following sections detail and expand on the characterisation techniques, instruments and parameters used for the characterisation of perovskite thin-films. All characterisation measurements were made prior to deposition of the hole transport layer and performed in an ambient environment.

2.3.1 UV-Visible-near Infrared (UV-Vis-NIR) spectroscopy

UV-Vis-NIR spectroscopy measures the absorption of a sample in the UV-Vis-NIR regions of the EM spectrum. A spectrophotometer directs a beam of monochromatic incident light through the sample which can be absorbed, scattered or reflected. The wavelengths of light which cause electronic excitation are absorbed and any remaining unabsorbed wavelengths are transmitted to the detector. This produces an absorption spectrum which shows the wavelengths at which a chromophore absorbs light within the UV-Vis-NIR range.

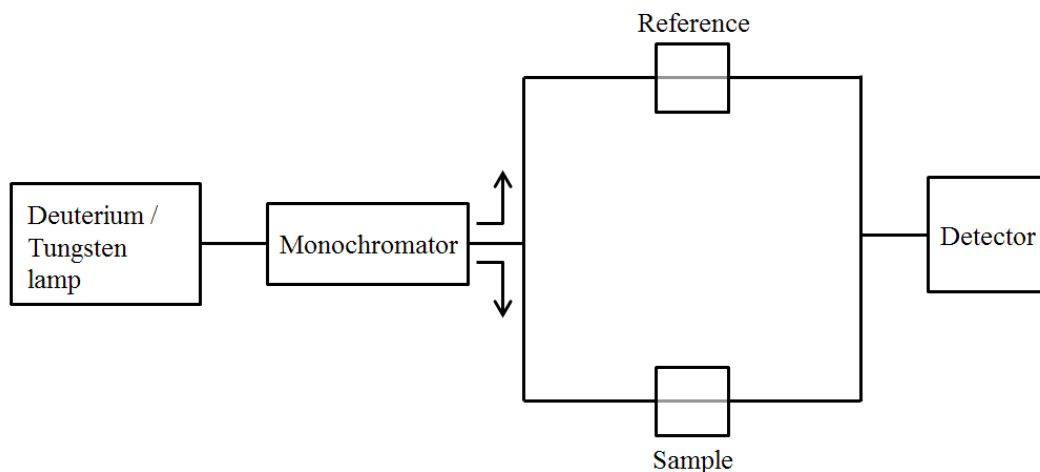


Figure 2.8: Schematic showing the basic components of a double beam spectrophotometer. Deuterium and tungsten lamps are generally used as the ultraviolet and visible light sources, respectively. The monochromator selectively controls the wavelengths of the incident beam, which is subsequently divided into two fractions by a beam splitter. One of the beams is directed towards a reference and the other toward the sample; the two beams pass through each material and subsequently recombine before reaching the detector. The data output includes an absorption spectrum where the spectral response of the reference can then be compared or extracted from the spectral response of the sample.

The absorbance, Abs, of a sample at a particular wavelength, λ can be quantified by comparing the intensities of the reference light beam (initial light intensity) to the sample light beam (final light intensity):

$$Abs = \log \frac{I_t}{I_0} \quad (6)$$

Where:

I_0 = initial light intensity

I_t = final light intensity

The absorbance is affected by the concentration (c) and molar extinction coefficient (ϵ) of the absorbing medium and the absorption path length (l). These factors are related by the Beer-Lambert law which states there is a linear relationship between the concentration and absorbance:

$$Abs = \log_{10} \frac{I_t}{I_0} = \epsilon cl \quad (7)$$

In this work, UV-Vis-NIR spectroscopy of perovskite thin-films was performed using a Perkin Elmer Lambda 9 UV-Visible-NIR spectrophotometer. The absorbance was measured over a wavelength range of 350-800 nm at a scan speed of 240 nm/s and a step rate of 1 nm.

2.3.2 Fluorescence spectroscopy

Measuring the steady-state and time-resolved photoluminescence (PL) of lead halide perovskites can provide valuable insight into the optoelectronic properties of the material including defects and trap states present within the perovskite layer. The PL of the perovskite thin-films could not be measured at voltage due to measurement of the perovskite layer in the absence of the HTL and contacts. Therefore, as no load was connected, the PL should be maximised and any quenching would be indicative of non-radiative recombination.^{1,2}

2.3.2.1 Steady-state

Steady-state fluorescence spectroscopy measures the PL emission of a sample following irradiation with UV, Visible or near-Infrared light. A fluorescence spectrophotometer directs light of a fixed ‘excitation’ wavelength at a sample, which subsequently absorbs the light and re-emits (steady-state decay) it at a longer wavelength. The emitted light is then detected over a set wavelength range. This produces an emission spectrum (Figure 2.10) which shows the fluorescence intensity as a function of the wavelength.

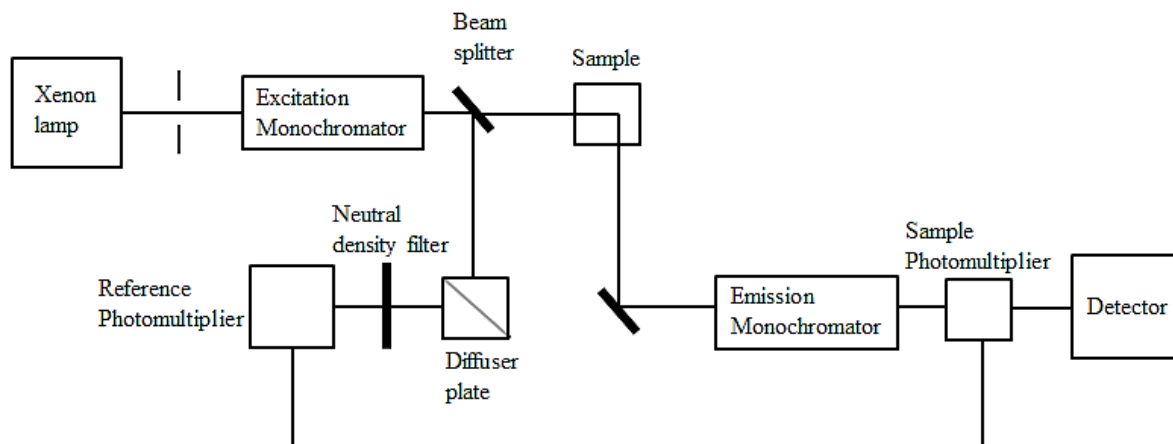


Figure 2.9: General schematic of a fluorescence spectrophotometer. A high pressure xenon arc lamp is used as the excitation source. The excitation and emission monochromators selectively control the excitation wavelength and the emission wavelength range, where the excitation wavelength is generally fixed. Each monochromator contains entry and exit slits, the widths of which can be altered to control the resolution. The beam splitter directs the excitation light through both the sample and a reference. The neutral density filter attenuates the intensity of the reference beam. The photomultipliers form part of the detector system and amplify the emission signal.

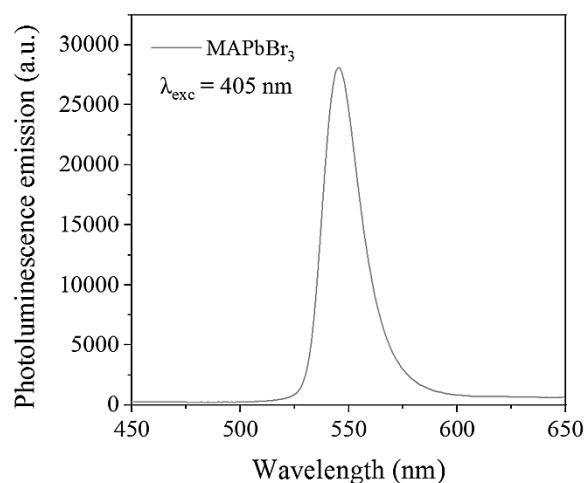


Figure 2.10: Example steady state photoluminescence spectral response of a MAPbBr₃ perovskite thin-film using an excitation wavelength (λ_{exc}) of 405 nm.

In this work, steady state PL emission spectra of perovskite thin-films were recorded using a Horiba FluoroMax 4 spectrophotometer. Control, co-sensitised and toluene soaked MAPbBr₃ thin-films were measured using an excitation wavelength of 405 nm with PL emission detected over a wavelength range of 430-680 nm. Control, co-sensitised and toluene soaked MAPbI₃ films were measured using an excitation wavelength of 635 nm with PL emission detected over a wavelength range of 720-850 nm. All thin-films were measured using slit widths of 7.0 mm and 1.0 mm for the excitation and emission monochromators, respectively. All measurements were made using an increment of 1.0 nm and an integration time of 0.1 s.

2.3.2.2 Time-correlated single photon counting (TCSPC)

Time-correlated single photon counting (TCSPC) is a technique used to measure the fluorescence decay of a sample by counting photons which are time-correlated in relation to an excitation pulse.⁴ The fluorescence lifetime(s), which can then be calculated, describes the length of time a molecule remains excited prior to emitting a photon and returning to the ground state. The excitation source generally consists of a pulsed laser with a high repetition rate (e.g. a Ti:Sapphire laser) which continuously excites the sample encouraging repetitive fluorescence.

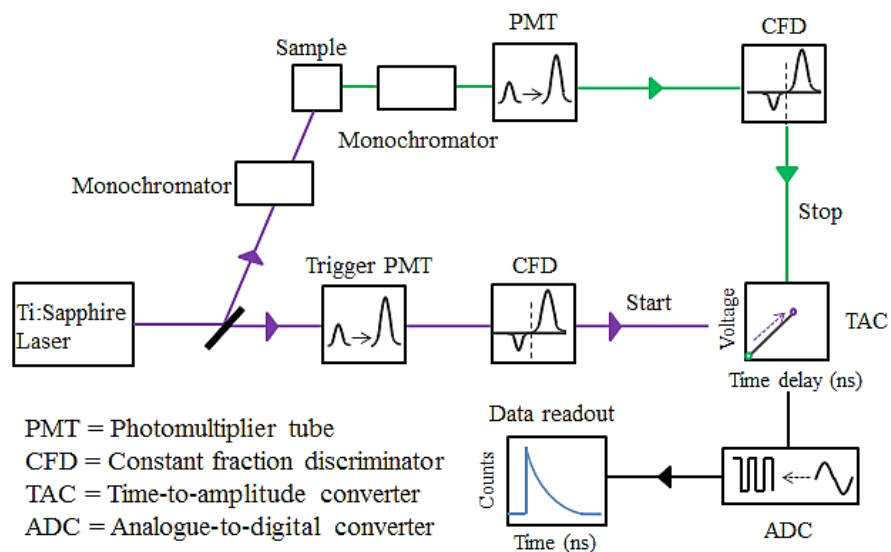


Figure 2.11: General schematic of a time-correlated single photon counting (TCSPC) instrument.

A measurement begins by exciting the sample with an excitation pulse, which starts the time measurement. At the same time, a trigger/electrical pulse is received by a photomultiplier tube (PMT) and transferred to a constant fraction discriminator (CFD) which outputs the start signal. This subsequently initiates a voltage ramp within the time-to-amplitude converter (TAC).⁴ On detection of the first photon (from the sample), the photomultiplier sends a signal to the second CFD which then outputs a stop signal which halts the charging ramp in the TAC. The TAC then generates a pulse, the voltage of which is equivalent to time difference between the start and stop signals.⁵ This voltage is then fed into the analogue-to-digital converter (ADC) which gives the TAC output a numerical value. A 'count' is stored in a data storage device at a location corresponding to the numerical value / arrival time. Excitation and storage are repeated until a histogram is built of counts vs number (or time), which represents the decay curve of the sample.^{5,6} An example decay curve is shown in Figure 2.12.

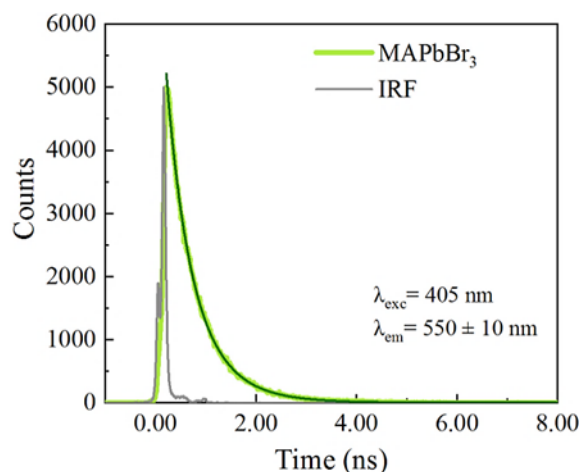


Figure 2.12: Example time resolved photoluminescence spectral response of a MAPbBr₃ perovskite thin-film using an excitation and emission wavelength of 405 and 550 nm, respectively. The instrument response function (IRF) relates to the timing precision of the instrument i.e. the accuracy of the electronics and detectors. Ideally the IRF should be narrow as a broader response can indicate errors within the system.

For perovskites, following excitation due to light absorption, the trap states located deep within the bandgap (which contribute to non-radiative recombination) are filled first, followed by the shallower traps located at the band edge. When all the traps are filled, a longer PL lifetime/decay is observed which can provide valuable insight into the trap density within the perovskite layer.³

In this work, time-resolved PL measurements were performed using a time-correlated single photon counting (TCSPC) fluorescence lifetime spectrometer (LifeSpec II, Edinburgh Instruments). Control and co-sensitised MAPbBr₃ films and solid state dyed thin-films were measured using an excitation wavelength (λ_{exc}) of 405 nm (EPL405) and monitored at emission wavelengths of 550 nm and 700 nm, respectively. Control and co-sensitised MAPbI₃ films were measured using an λ_{exc} of 635 nm (EPL635) and the emission was monitored at 780 nm.

The PL decays and the instrumental response functions (IRF) were measured using 1024 channels with time ranges of 5, 50 and 100 ns/channels used for solid state dyed thin-films, MAPbBr₃ and MAPbI₃, respectively. Each was measured until 5×10^3 counts were reached and the time was stopped after 30 minutes. Each IRF was determined by measuring a film at the aforementioned excitation wavelengths. The IRF values were then convoluted with the

necessary theoretical function for decay analysis. The full width at half-maximum (FWHM) of the IRFs were approximately 0.15, 0.17 and 0.05 ns for MAPbI₃, MAPbBr₃ and the solid state dyed thin-films, respectively. Each appeared highly reproducible with identical system parameters.

The PL lifetimes were estimated by fitting the decays with a bi-exponential function:

$$f(t) = A_1 \exp(-t/\tau_1) + A_2 \exp(-t/\tau_2) \quad (8)$$

Where:

$f(t)$ = Fluorescence intensity at time, t

A_1 = Relative amplitude of τ_1

A_2 = Relative amplitude of τ_2

τ_1 = Fast decay component

τ_2 = Slow decay component

2.3.3 X-ray diffraction (XRD)

X-ray diffraction is a powerful analytical technique which can provide valuable information about the atomic structure of a crystalline material. This technique is particularly useful for lead halide perovskites as it can be used to study and provide insight into the lattice structure which largely determines the photovoltaic performance of the material.

A diffractometer directs a beam of X-rays at the sample at a given incidence angle, the incident beam is subsequently scattered or diffracted into several directions by the atoms present with the lattice planes of the crystal. If the lattice planes are symmetrically spaced (with separation, d) then the scattered X-rays constructively interfere in directions where the path length difference ($2d\sin\theta$) equals an integer multiple of the wavelength, this is given by Braggs Law:

$$n\lambda = 2d \sin \theta \quad (9)$$

Where:

λ = X-Ray wavelength

d = Spacing of the crystal planes

θ = X-ray angle of incidence

n = Integer

Therefore, the measurement of these waves generates a diffraction pattern which provides information about the fundamental properties of the crystal including the unit cell and its symmetry.^{18,19}

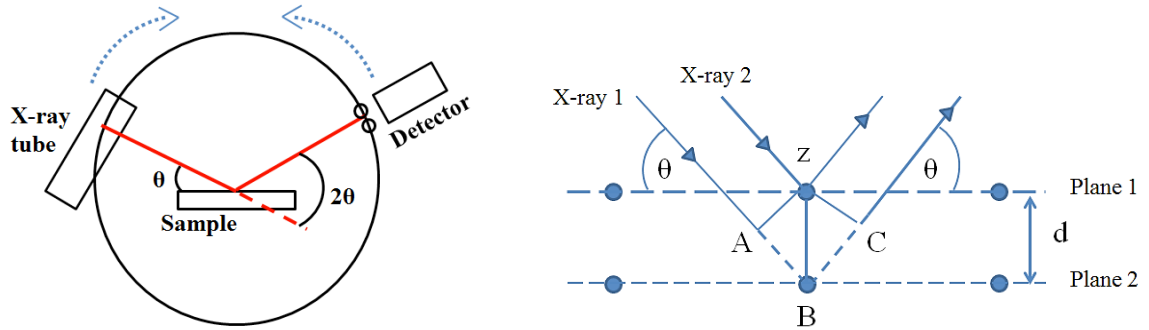


Figure 2.13: Left, schematic of a basic diffractometer set-up. Most diffractometers operate using Bragg-Brentano geometry where the X-ray tube and detector move in an arc around the sample. The detector then records the X-rays observed at each angle (2θ). Right, schematic showing constructive interference which only occurs if the lattice planes are symmetrically spaced and $n\lambda = AB+BC$.

Each peak of a diffraction pattern represents the X-ray-diffraction from a different lattice plane in the crystal. Each lattice plane is represented by a series of integers called the Miller indices: h , k and l which are based on the Cartesian co-ordinate system of the vectors (axis) x , y and z . The x , y and z axis directions are denoted as $[100]$, $[010]$ and $[001]$, respectively. The crystal planes are perpendicular to the corresponding axis and are labelled using parentheses e.g. the (100) plane is perpendicular to the x -axis $[100]$.

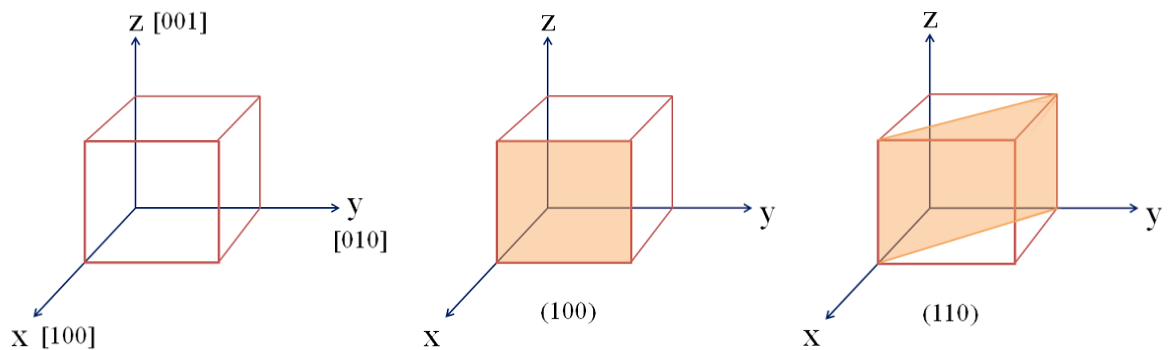


Figure 2.14: Left, the Cartesian co-ordinate system of the vectors (axis) x , y and z . Center and right, the (100) and (110) crystal planes, respectively.

Figure 2.15 shows an example XRD pattern for MAPbBr₃ perovskite which shows peaks at 15° and 21° which correspond to the (100) and (110) crystal planes, respectively.^{20–22}

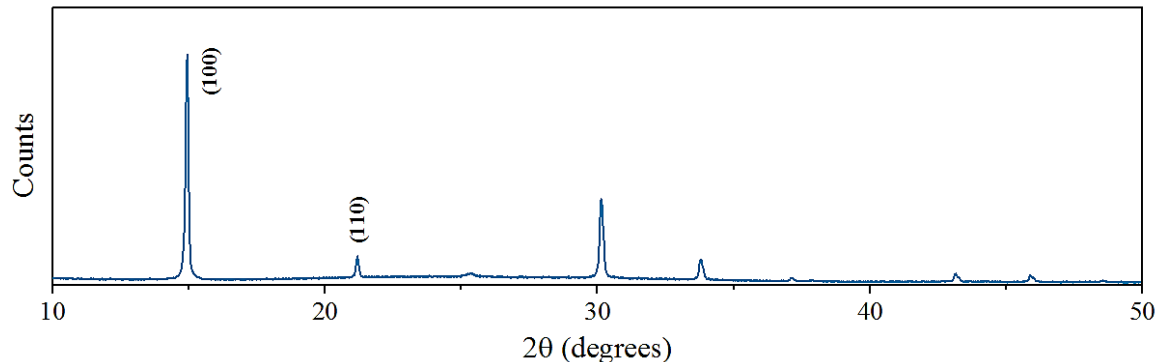


Figure 2.15: Example XRD pattern for a MAPbBr₃ thin-film where the X-ray intensity (counts) is plotted as a function of the detector angle, 2θ .

In this work, XRD measurements of perovskite thin-films were made using a D8 Discover X-ray diffractometer (Bruker, Germany) using a Cu K-alpha beam at 40 kV and 40 mA. Each measurement was made using a 0.5 s/step at 0.02° 2θ step size over a 2θ range of 10–60°. All XRD spectra were processed using the Bruker DIFFRAC.EVA programme.

2.3.4 Optical microscopy

Optical microscopy of thin-films was carried out using the x20 and x40 objectives of an Olympus BH-2 microscope with a 100 W halogen lamp. Images were captured from directly above the sample using a computer controlled integrated camera (Canon, EOS 6D DSLR).

2.3.5 Profilometry measurements

Mesoporous titania layer thickness measurements were performed using a Dektak D150 profilometer with a 25 μm diameter stylus. A razor blade was used to remove a section of the layer thereby creating a 'step'. Measurements were made 10 mm across the step over a period of 26 seconds. All measurements were made using a stylus force of 6 mg.

2.4 Characterisation of perovskite solar cells

The following sections detail and expand on the characterisation techniques, instruments and parameters used for the characterisation of perovskite solar cells. All characterisation measurements were performed in an ambient environment.

2.4.1 Current-voltage measurements (J-V)

For solar energy conversion the solar light arriving at the Earth's surface differs from the extra-terrestrial light due to absorption and scattering by the Earth's atmosphere. The spectrum of light received by the Earth's surface is therefore altered in shape. The term 'air mass (AM)' is used to describe the optical path length of solar light through the atmosphere and helps characterise the terrestrial solar spectrum. For solar cell characterisation, the standard spectral conditions (which conform to ASTM G173-03) are an air mass of 1.5 otherwise known as AirMass 1.5 Global (AM1.5G).

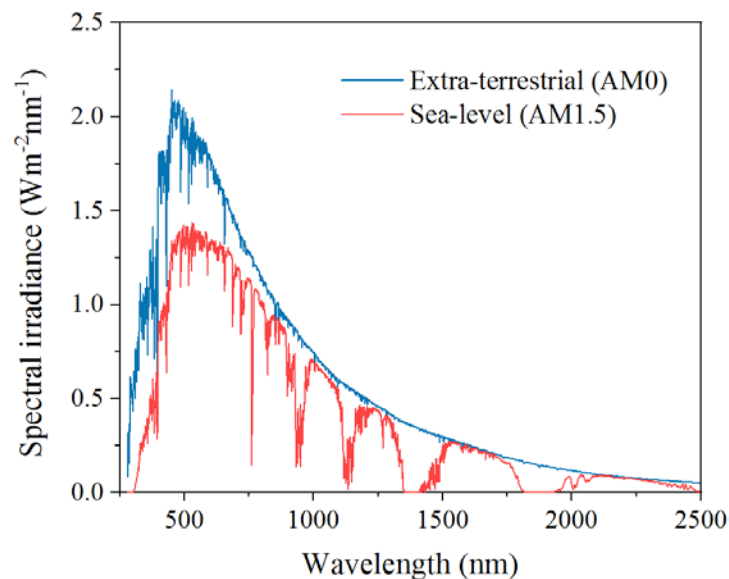


Figure 2.16: Spectral irradiance of extra-terrestrial radiation (AM0) and terrestrial radiation (AM1.5).

The AM1.5G spectrum has an integrated power of 1000 W m^{-2} also referred to as 1 sun.⁷ Therefore, as a global standard, when measuring solar cells, the irradiance is set to equal 1000 W m^{-2} at AM1.5G standard illumination. This essentially means that the cell is exposed to the same number of photons as it would be under standard AM1.5 sunlight.⁸

Solar cells are illuminated using a solar simulator light source which closely mimics the terrestrial solar spectrum by using a xenon lamp and optical filters.⁸ A calibrated reference diode (of known spectral response) is typically used to ensure the light source is set to an irradiance of 1 sun.⁸ Illumination of the photoactive layer causes the movement of electrons and holes between the two electrodes which in-turn causes a current density flow, I and a subsequent photo-voltage, V .⁹ These two values give rise to the electrical power output, P from the cell:

$$P = V \cdot I \quad (10)$$

The current is measured as a function of voltage under illumination which generates a current-voltage or I-V curve. The current density is found by normalising the area under illumination which gives the J-V characteristic.

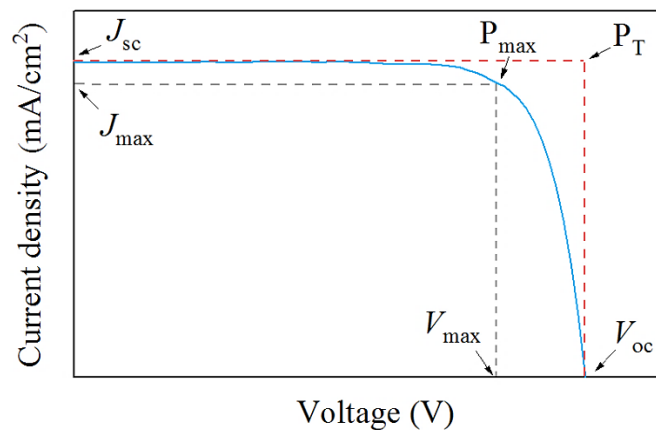


Figure 2.17: Example current–voltage (J-V) curve (blue) for a solar cell including parameters J_{\max} and V_{\max} which represent the current and voltage at the actual maximum power point, P_{\max} , respectively and P_T which represents the theoretical maximum power point.

Figure 2.17 includes two of the key photovoltaic parameters derived from the J-V curve which are often included when reporting the performance of solar cells. The short-circuit current, J_{sc} also referred to as the photocurrent, is defined as the current measured when the cell voltage is zero. This value is generally governed by the light harvesting efficiency (LHE) and the efficiency of charge extraction and collection.⁷ Therefore, increases in the J_{sc} of a cell can be indicative of improved charge separation/collection and reduced

recombination possibly through improved perovskite morphology – i.e. lower defect/traps states.¹⁰

The open-circuit voltage, V_{oc} also referred to as the photo-voltage, is defined as the voltage measured when the cell current is zero. This value represents the difference between the electrochemical potentials (quasi-Fermi levels) of the contacts. The V_{oc} is largely affected by recombination processes at open-circuit and therefore, will be lower than the bandgap value when measured at 1 sun.⁷

In addition to the J_{sc} and V_{oc} , the fill factor (FF) is another important photovoltaic parameter commonly reported when characterising solar cells. This value represents the maximum power available from a cell and is the fraction of the actual maximum power point (P_{max}) and the theoretical maximum power point (P_T):

$$FF = \frac{P_{max}}{J_{sc} \cdot V_{oc}} \quad (11)$$

Where P_{max} is derived from the photo-current and photo-voltage when the power output from the cell is at maximum, $J_{max} \cdot V_{max}$. For perovskite solar cells, the FF is largely governed by the internal series resistance but is also affected by non-radiative recombination.^{11,12}

An effective solar cell should ideally have a high J_{sc} , V_{oc} and FF as these three photovoltaic parameters are then collectively used to calculate the percentage solar to electrical energy conversion efficiency, η :

$$\% \eta = \left(\frac{J_{sc} \cdot V_{oc} \cdot FF}{P_{in}} \right) \times 100 \quad (12)$$

Where P_{in} is the intensity of the incident light.

The J-V characteristics of a solar cell can be represented by an equivalent circuit model which consists of a current source (J_L) in parallel with a single diode and resistors both in series (series resistance) and in parallel (shunt resistance).

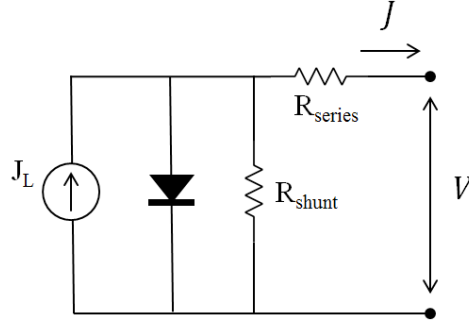


Figure 2.18: Equivalent circuit model for a solar cell where: J_L is the photo generated current, R_{shunt} is the shunt resistance and R_{series} is the series resistance.

In the absence of light, the cell behaves like a diode. A voltage develops between the cell terminals which generates a current in the opposite direction to the photocurrent. This current, referred to as the dark saturation current, J_0 acts to reduce the net current from the J_{sc} value.¹³ The current through the diode can be expressed as a function of voltage using the diode equation:

$$J = J_L - J_0 \left(\exp \frac{qV}{nkT} - 1 \right) \quad (13)$$

Where: J is the net current through the diode, J_L is the photo generated current J_0 is the dark saturation current, q is the elementary charge, V is the voltage across the terminals, n is the diode ideality factor, T is the absolute temperature and k is the Boltzmann constant.

On including the series (R_{series}) and shunt (R_{shunt}) resistors (as shown in Figure 2.18) the diode equation now becomes:

$$J = J_L - J_0 \left[\exp \frac{q(V + JR_{series})}{nkT} - 1 \right] - \frac{V + JR_{series}}{R_{shunt}} \quad (14)$$

Both resistances are parasitic and can lead to reduced performance in solar cells. Ideally, the shunt resistance should be high and series should be low however, when this deviates, the shape of the J-V curve is characteristically altered by each resistance (Figure 2.19).

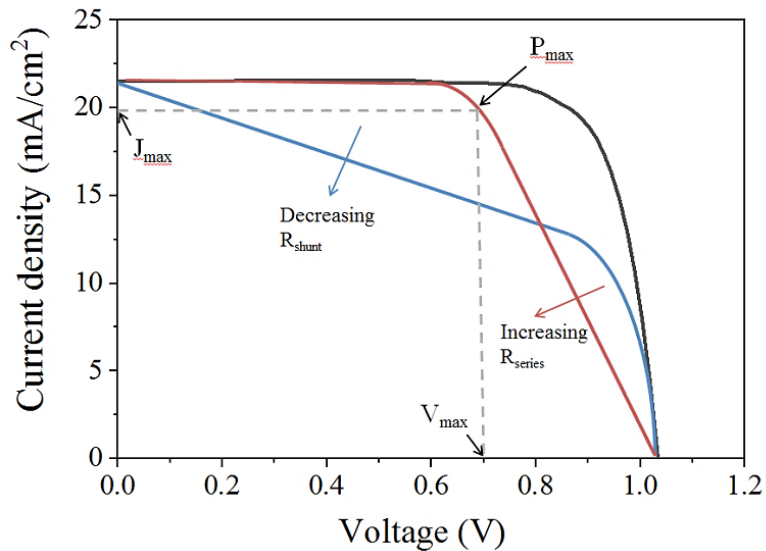


Figure 2.19: Example current–voltage (J-V) curve for a solar cell highlighting the effect of decreasing shunt (blue) and increasing series (red) resistance on the curve shape.

For PSC's, mesoporous architectures are susceptible to resistive losses through low shunt resistance which stems from current leakage and recombination due to pin-holes and trap states at the perovskite-titania interface, respectively.¹⁴ This negatively impacts the photocurrent leading to a reduced J_{sc} value. Series resistance is generally governed by current movement through the cell and is affected by internal resistances e.g. between active layer interfaces, charge collection layers and between the metal contacts. Figure 2.19 shows how a high series resistance reduces the maximum power point (P_{max}) and therefore the FF of the cell.¹⁵

In this work, current-voltage (J-V) measurements were performed on full devices where each pixel was measured individually generating 8 measurements per device. Prior to testing, the device active area was masked using a sheet of black-painted steel which provided an active area aperture of 0.1 cm². The current–voltage (JV) curves of the masked devices were measured using a class AAA solar simulator (Newport Oriel Sol3A) which was calibrated against a KG5-filtered silicon reference cell (Newport Oriel 91150-KG5) to

provide an irradiance of 1 sun (AM 1.5 and 100 mW cm⁻²). Voltage sweeps across the device were applied using a Keithley Instruments 2400 source meter from 1.2 V to -0.1 V at 0.015 Vs⁻¹ with a 100 ms dwell time between points. A 3 mA current limit was also used.

2.4.2 Incident photon-to-current efficiency (IPCE)

The quantum efficiency of a solar cell represents the ratio of the number of charges extracted to the number of incident photons of a given energy. The incident photon-to-current efficiency (IPCE) also referred to as the external quantum efficiency (EQE) is a useful technique which measures the short-circuit current density produced under monochromatic light as a function of wavelength.¹⁶ Therefore, measurement of the EQE provides information about the monochromatic quantum efficiencies of a PV device and is calculable as follows:

$$EQE[\%] = \frac{1240 \cdot J_{sc}}{\lambda \cdot \phi} \times 100 \quad (15)$$

Where:

J_{sc} = Short-circuit current density

λ = Given wavelength

ϕ = Intensity of the monochromatic light (μWcm^{-2})

EQE measurements can be used to corroborate the J_{sc} value obtained from a J-V curve by integrating the EQE spectra (Figure 2.20) over the AM1.5G solar spectrum.¹⁶ In theory, these values should be equivalent however; deviations can occur due to IPCE measurements being conducted with a monochromatic light of lower intensity than 1 sun irradiation. This can occasionally be mitigated by introducing a white bias light.¹⁶ Reasonable correlation is generally assumed when the J_{sc} value extracted from the J-V curve lies within 20% of the IPCE generated value.¹⁷

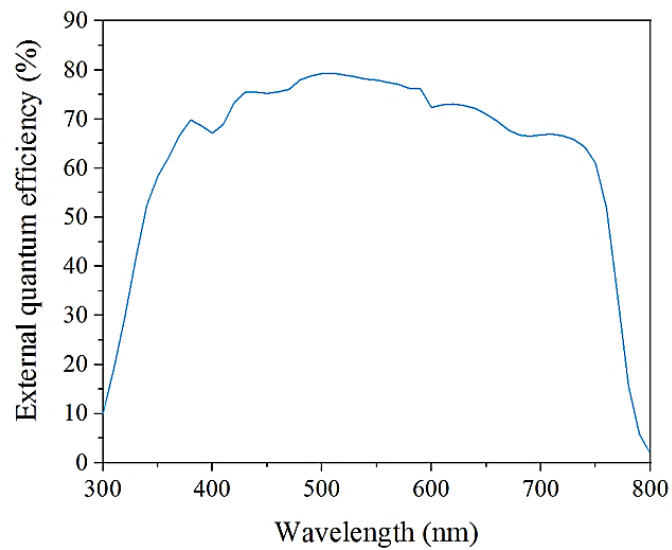


Figure 2.20: Example external quantum efficiency spectral response for a MAPbI₃ perovskite solar cell. EQE measurements can be used to study the absorbance and charge collection properties of a solar cell.

In this work, EQE measurements were made using a PV Measurements QEX10. Each spectral response was measured in DC mode between 300-800 nm with a step size of 10 nm. A white light bias was not used. EQE measurements were made for the highest performing 'hero' pixel per variable measured.

2.4.3 Light box stability storage

Un-encapsulated control and co-sensitised (using 1.0 mM D205) devices were stored at room temperature (relative humidity ~50%) for 56 days in a photo light box (Ortery, Photosimile 200).



Figure 2.21: Photographs of the outside and inside of the Ortery Photosimile 200 lightbox, left and right, respectively.

Uniform light exposure was provided by an integrated 6500K daylight lighting system comprised of 12 fluorescent tube-bulbs, additional reflection and scattering was facilitated by the white interior of the light box.

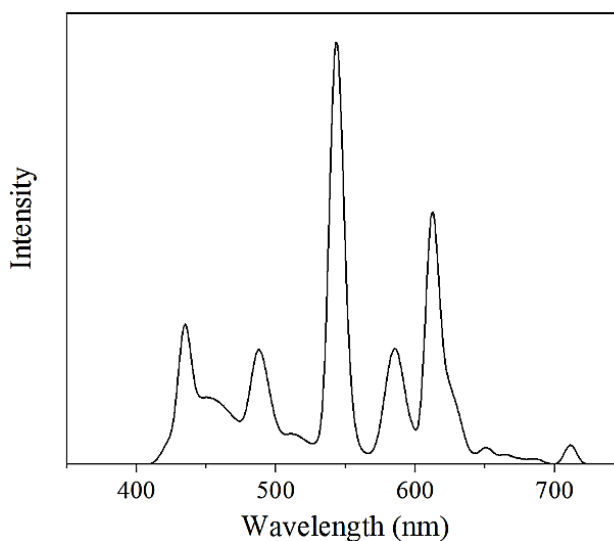


Figure 2.22: Measured spectra for the Ortery, Photosimile 200 lightbox.

The average cell performance and EQE response was measured intermittently during the 56 days of storage. Average performance parameters were calculated from the 8 pixels of a single cell. Performance measurements were suspended once the average efficiency of the cell had dropped below 0.1%.

2.4.4 Impedance spectroscopy (IS)

Impedance spectroscopy (IS) can be used to calculate the impedance of an electrical system by measuring the opposition to AC current flow when applying an AC voltage.²³ The response of the cell as a function of the AC frequency can supply information about the cells internal dynamics including the bulk and surface properties.²⁴

Samples are perturbed using a small amplitude AC voltage signal (V_{AC}) superimposed on a DC level (V_{DC}). The voltage input is given by:

$$V = V_{AC} + V_{DC} \cos(\omega t) = V_0 e^{j\omega t} \quad (16)$$

Where:

V_0 = Magnitude of the voltage

ω = Angular frequency

t = Time

The measured AC current response (I_{AC}) is of the form:

$$I = I_{AC} + I_{DC} \cos(\omega t - \phi) = I_0 e^{j\omega t} e^{-j\phi} \quad (17)$$

Where:

ϕ = Phase shift compared to the input signal

The impedance is therefore given as:

$$Z = \frac{V}{I} = \frac{V_0}{I_0} e^{j\phi} = |Z| e^{j\phi} \quad (18)$$

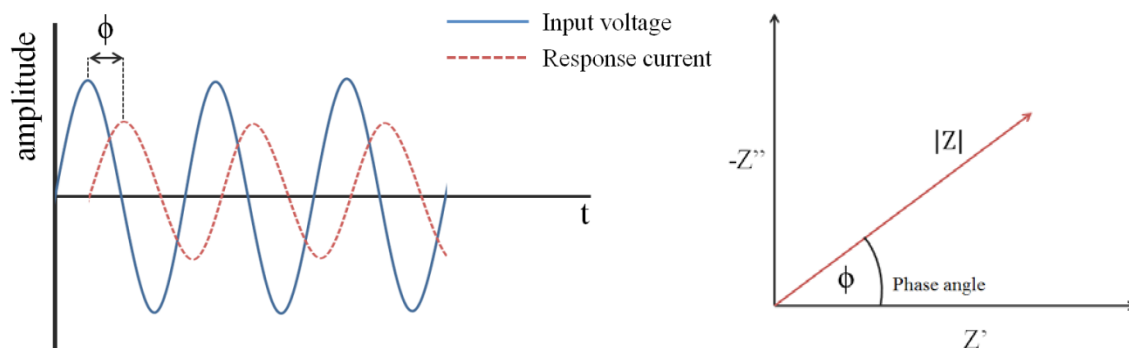


Figure 2.23: Schematic showing the phase shift between the input AC voltage and response AC current (left). Basic Nyquist plot where the phase angle represents the phase difference between the input AC voltage and response AC current (right).

The AC current response is measured over a frequency range (typically 1 Hz to 1 MHz) where the frequency is swept from low to high. Different components (resistive, capacitive or inductive) within the sample respond on different time scales to each frequency. This allows the user to separate the components and determine their respective contributions to the overall impedance of the cell. The data generated from IS is often represented as a Nyquist or Bode plot (Figure 2.24). The impedance value, $|Z|$ is a complex number and therefore has real and imaginary units. A Nyquist plot shows the negative imaginary unit, $-Z''$ vs the real impedance unit, Z' . Here, the data is depicted as a series of semi-circles where each arc represents a different component that can be translated into an equivalent circuit model. The Randles cell (Figure 2.24, inset) is the simplest electrochemical circuit model used for impedance data and contains components of: series resistance (R_s) calculated from the high frequency x-axis intercept, low-frequency limit resistance (R_s+R_{ct}) and the capacitance which is found from the characteristic frequency which occurs at the highest complex impedance value, $\omega = 1/(R_{ct}C_{dl})$.²⁴

A Bode plot shows the impedance as a function of the frequency (Hz) or phase shift. The maximum point of the semi-circle in the Nyquist plot represents the highest point of the frequency peak in the Bode plot.

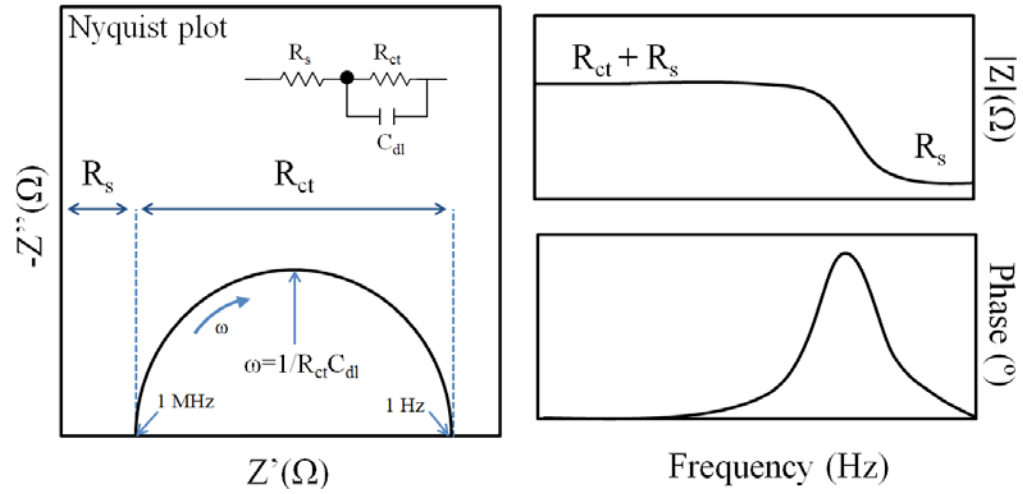


Figure 2.24: Representation of impedance spectra of the standard Randles cell (inset, left) using a Nyquist plot (left) and Bode plots (right). Where R_s is series resistance, R_{ct} is polarization or charge transfer resistance (equal to the semi-circle diameter) and C_{dl} is a double layer capacitor.

Equivalent circuit models can be used to describe the behavior of systems such as semiconductors and solar cells. For perovskites, IS has been used to provide information about charge transport and transfer resistance, capacitive behavior, series resistance and recombination resistance within the perovskite layer.²⁵⁻²⁷

The recombination resistance, R_{rec} represents the radiative and non-radiative processes present within a cell and is given by:

$$R_{rec} = \left(\frac{\partial V}{\partial j_{rec}} \right) \quad (19)$$

Where:

j_{rec} = Recombination current density

V = Voltage

For perovskite solar cells, high values of R_{rec} are desirable in order to maximise charge extraction and larger R_{rec} values often signify reduced non-radiative recombination processes.²⁸

The capacitive behaviour of a cell relates to the accumulation of charge in the conduction band.²⁹ For dye-sensitised solar cells this is referred to as chemical capacitance, C_{μ}

and corresponds to charge accumulation in the mesoporous titania layer. The chemical capacitance has an exponential dependence on the voltage and is given by:^{30,31}

$$C_{\mu} = \frac{q^2}{k_B T} n \quad (20)$$

Where:

n = Electron density in the conduction band

k_B = Boltzmann constant

T = Temperature

q = Electric charge

In contrast, the capacitance of perovskite solar cells is related to the dielectric properties of the perovskite layer and is described as geometric. The geometric capacitance, C_g is bias independent and varies with active layer area and thickness.³⁰

Therefore, the capacitance of PSC's do not show an exponential increase with voltage and typically show a constant capacitance which is given by:³⁰

$$C_g = \left(\frac{\epsilon_0 \epsilon_r A}{d} \right) \quad (21)$$

Where:

ϵ_0 = Vacuum permittivity

ϵ_r = Relative dielectric constant of the perovskite

A = Active area

d = Layer thickness

In this work, impedance spectroscopy (IS) measurements were performed on unmasked devices using a Zahner CIMPS-X photoelectrochemical workstation. Each device was scanned using a frequency range of 10 MHz to 1 Hz at the open-circuit voltage under red LED illumination (630 nm) at intensities from 1 sun to 0.01 sun (equivalent intensities were determined by matching the J_{sc} to the value obtained under AM1.5 illumination). The incident intensity of the LED was controlled *via* a series of neutral density filters. The open-circuit voltage of each cell was monitored until it reached a steady-state, the impedance

measurement was then started. Experimental data fitting was completed using Z-View software (Scribner Associates). The data obtained was plotted as Nyquist plots and fitted using an equivalent circuit model consisting of a series of resistors and constant phase elements. The series resistance, R_s values presented in Chapter 6, Section 6.3.3 were extracted from the semi-circular response of the respective Nyquist plots where R_s is equivalent to the high frequency x-axis intercept of the semi-circle (Figure 2.24). The recombination resistance in solar cells is equivalent to the charge transfer or polarisation resistance, R_{ct} and was therefore calculated from the diameter of each semi-circle. Capacitance values were calculated by dividing the charge transfer resistance, R_{ct} by the time constant relating to $R_{ct}C_{dl}$.

2.5 Data processing

The raw data files generated for each technique were processed using OriginPro 2018 and Microsoft Excel unless otherwise stated.

2.5.1 Statistical analysis

The standard deviation s was calculated to highlight the variation in performance between replicate devices when measuring J-V curves:

$$s = \sqrt{\sum_i (x_i - \bar{x})^2 / (n - 1)} \quad (22)$$

Where:

x_i = Sum of the x-values

\bar{x} = Mean of the x-values

n = Sample size

The standard error of the mean (SEM) was calculated using:

$$\text{SEM} = \frac{s}{\sqrt{n}} \quad (23)$$

The coefficient of variation (CV) / relative standard deviation (RSD) was calculated using:

$$\text{CV} = 100 \frac{s}{\bar{x}} \quad (24)$$

2.6 References

1. Stolterfoht, M. *et al.* Voltage-Dependent Photoluminescence and How It Correlates with the Fill Factor and Open-Circuit Voltage in Perovskite Solar Cells. *ACS Energy Lett.* **4**, pp. 2887–2892 (2019).
2. Tvingstedt, K. *et al.* Radiative efficiency of lead iodide based perovskite solar cells. *Sci. Rep.* **4**, 6071 (2014).
3. Droseros, N., Tsokkou, D. & Banerji, N. Photophysics of Methylammonium Lead Tribromide Perovskite: Free Carriers, Excitons, and Sub-Bandgap States. *Adv. Energy Mater.* **10**, 1903258 (2020).
4. Lakowicz, J. R. (ed.) *Principles of Fluorescence Spectroscopy*. (2nd Ed.). Springer, Boston, MA. (2006). Available from: doi:10.1007/978-0-387-46312-4
5. O'Connor, D. V. & Phillips, D. 2 - Basic Principles of the Single Photon Counting Lifetime Measurement, in *Time-Correlated Single Photon Counting*. Academic Press, London, UK. (1984). Available from: doi:10.1016/b978-0-12-524140-3.50006-x
6. Becker, W. Building Blocks of Advanced TCSPC Devices, in *Advanced time-correlated single photon counting techniques*. Springer Series in Chemical Physics, Springer, Berlin, Heidelberg (2005). Available from doi: 10.1007/3-540-28882-1
7. Nayak, P. K., Garcia-Belmonte, G., Kahn, A., Bisquert, J. & Cahen, D. Photovoltaic efficiency limits and material disorder. *Energy Environ. Sci.* **5**, pp. 6022–6039 (2012).
8. Snaith, H. J. The perils of solar cell efficiency measurements. *Nat. Photonics* **6**, pp. 337–340 (2012).
9. Martín, C., Ziółek, M. & Douhal, A. Ultrafast and fast charge separation processes in real dye-sensitized solar cells. *Journal of Photochemistry and Photobiology C: Photochemistry Reviews* **26**, pp. 1–30 (2016).
10. Zhang, F. *et al.* Film-through large perovskite grains formation: Via a combination of sequential thermal and solvent treatment. *J. Mater. Chem. A* **4**, pp. 8554–8561 (2016).
11. Chen, Z. *et al.* Single-Crystal MAPbI₃ Perovskite Solar Cells Exceeding 21% Power Conversion Efficiency. *ACS Energy Lett.* **4**, pp. 1258–1259 (2019).
12. Stolterfoht, M. *et al.* Approaching the fill factor Shockley-Queisser limit in stable, dopant-free triple cation perovskite solar cells. *Energy Environ. Sci.* **10**, pp. 1530–1539 (2017).

13. Nelson, J. Properties of Semiconductor Materials, in *The Physics of Solar Cells*. Imperial College Press, London, UK (2003). Available from: doi:10.1142/9781848161269_0001
14. Singh, R., Sandhu, S. & Lee, J. J. Elucidating the effect of shunt losses on the performance of mesoporous perovskite solar cells. *Sol. Energy* **193**, pp. 956–961 (2019).
15. Baig, H., Kanda, H., Asiri, A. M., Nazeeruddin, M. K. & Mallick, T. Increasing efficiency of perovskite solar cells using low concentrating photovoltaic systems. *Sustain. Energy Fuels* **4**, pp. 528–537 (2020).
16. Christians, J. A., Manser, J. S. & Kamat, P. V. Best practices in perovskite solar cell efficiency measurements. Avoiding the error of Making Bad Cells Look Good. *J. Phys. Chem. Lett.* **6**, pp. 852–857 (2015).
17. Zimmermann, E. *et al.* Erroneous efficiency reports harm organic solar cell research. *Nat. Photonics* **8**, pp. 669–672 (2014).
18. Chung, F. H. & Smith, D. K. *Industrial Applications of X-Ray Diffraction*. CRC Press, Cleveland, Ohio (1999). Available from: doi:10.1201/b16940
19. Guinier, A., Lorrain, P., Lorrain, D. S. & Gillis, J. X-Ray Diffraction in Crystals, Imperfect Crystals, and Amorphous Bodies. *Phys. Today* **41**, pp. 292 (1964).
20. Zhang, M. *et al.* Composition-dependent photoluminescence intensity and prolonged recombination lifetime of perovskite CH₃NH₃PbBr_{3-x}Cl_xfilms. *Chem. Commun.* **50**, pp. 11727–11730 (2014).
21. Wang, K. H., Li, L. C., Shellaiah, M. & Sun, K. W. Structural and Photophysical Properties of Methylammonium Lead Tribromide (MAPbBr₃) Single Crystals. *Sci. Rep.* **7**, 13643 (2017).
22. Baikie, T. *et al.* A combined single crystal neutron/X-ray diffraction and solid-state nuclear magnetic resonance study of the hybrid perovskites CH₃NH₃PbX₃ (X = I, Br and Cl). *J. Mater. Chem. A* **3**, pp. 9298–9307 (2015).
23. Chang, B. Y. & Park, S. M. Electrochemical impedance spectroscopy. *Annu. Rev. Anal. Chem.* **3**, pp. 207–229 (2010).
24. Romero, B. *et al.* Characterization of organic and perovskite solar cells by impedance spectroscopy. in *Women in Renewable Energy (WiRE)* **7**, pp. 114–119 (2019).
25. Dualeh, A. *et al.* Impedance spectroscopic analysis of lead iodide perovskite-sensitized solid-state solar cells. *ACS Nano* **8**, pp. 362–373 (2014).
26. Pockett, A. *et al.* Characterization of planar lead halide perovskite solar cells by

- impedance spectroscopy, open-circuit photovoltage decay, and intensity-modulated photovoltage/photocurrent spectroscopy. *J. Phys. Chem. C* **119**, pp. 3456–3465 (2015).
27. Contreras-Bernal, L. *et al.* Impedance analysis of perovskite solar cells: A case study. *J. Mater. Chem. A* **7**, pp. 12191–12200 (2019).
 28. Aranda, C., Guerrero, A. & Bisquert, J. Ionic Effect Enhances Light Emission and the Photovoltage of Methylammonium Lead Bromide Perovskite Solar Cells by Reduced Surface Recombination. *ACS Energy Lett.* **4**, pp. 741–746 (2019).
 29. Bisquert, J. Chemical capacitance of nanostructured semiconductors: Its origin and significance for nanocomposite solar cells. *Phys. Chem. Chem. Phys.* **5**, pp. 5360–5364 (2003).
 30. Pockett, A. Characterization of Perovskite Solar Cells. *Univ. Bath* (2016).
 31. Van De Lagemaat, J., Park, N. G. & Frank, A. J. Influence of Electrical Potential Distribution, Charge Transport, and Recombination on the Photopotential and Photocurrent Conversion Efficiency of Dye-Sensitized Nanocrystalline TiO₂ Solar Cells: A Study by Electrical Impedance and Optical Modulation Tec. *J. Phys. Chem. B* **104**, pp. 2044–2052 (2000).

3 Optimisation and characterisation of methylammonium lead tri-bromide perovskite solar cells

3.1 Introduction

Following their introduction to photovoltaics over a decade ago, the vast amount of research concerning lead halide perovskites has mainly focussed on MAPbI₃ due to its broad absorption and high efficiencies. However, MAPbBr₃ offers alternative benefits such as: a larger band-gap, heightened stability and strong green emission (Figure 3.0 (d)) making it an attractive material for tandem/multi-junction solar cells¹ and light emitting diodes.^{2,3} In fact, some of the earliest developments in perovskite solar cells (PSC's) were completed using MAPbBr₃ including the first PV application published by Kojima *et al.* in 2009.⁴ Based on DSSC architecture, the cells incorporated a TiO₂ photo-electrode coated with MAPbBr₃ paired with a platinum coated counter electrode. The organic electrolyte consisted of a lithium halide/halogen redox couple in acetonitrile.⁴ Kojima also studied the use of MAPbI₃ using this cell format and reported efficiencies of 3.1% and 3.8% for MAPbBr₃ and MAPbI₃, respectively.⁴ Despite the bromide cells being outperformed by their iodide counterpart, other researchers discovered the introduction of bromide (Br) ions into the MAPbI₃ perovskite structure (MAPb-(I_{1-x}Br_x)₃) offered a myriad of benefits. These included: improved surface coverage,⁵ increased stability,⁶⁻⁸ band gap adjustment⁷ and perovskite colour tuning⁶ thereby highlighting the potential for compositional control *via* bromide addition. In a bid to achieve higher efficiencies, bromide addition is now often implemented in mixed ion perovskite blends (such as FA_{2/3}MA_{1/3}Pb(Br_{1/3}I_{2/3})₃) which have produced cell efficiencies exceeding 21%.⁹⁻¹³ For these derivatives, exchanging iodide for bromide echoes the same benefits as seen with MAPbI₃ however, this is only true for small quantity additions of bromide.¹¹ For mixed halide perovskites, greater quantities of bromide (≥50%)

were found to be detrimental to both cell performance and stability.^{12,13} Research by Hoke *et al.* suggested these issues result from photo-induced phase segregation where iodide-rich minority and bromide-rich majority domains form under photoexcitation due to halide migration.¹⁴ These domains consequently lower the band gap, decrease the open-circuit voltage and increase recombination due to defect trap states.^{1,14} The effects of photo-induced phase segregation are unique to mixed halide perovskites and are not observed for bromide only MAPbBr₃ cells however; the efficiencies of MAPbBr₃ PSC's are limited by other factors. The larger band gap of MAPbBr₃ (2.3 eV) blue-shifts the absorbance range to a higher energy region which limits the light harvesting efficiency and ultimately the photocurrent.⁶ Consequently, the leading efficiencies of MAPbBr₃ PSC's (Table 2) are significantly lower than those recorded for other lead halide perovskites. The current record of 10.4%, reported by Heo *et al.* was achieved by adding hydrogen bromide to the perovskite precursor solution.¹⁵ The next highest efficiency of 8.7% was reported by Sheng and co-workers when preparing MAPbBr₃ cells using vapour-assisted deposition.¹⁶

Table 2: Current highest reported photovoltaic performance parameters for MAPbBr₃ PSCs.

Publication year	Cell architecture	J_{sc} (mA/cm ²)	V_{oc} (V)	FF	η (%)
Heo ¹⁵ 2014	FTO/c-TiO ₂ /MAPbBr ₃ / PIF8-TAA ^(a)	8.4	1.51	82	10.4
Sheng ¹⁶ 2015	FTO/c-TiO ₂ /mp-TiO ₂ /MAPbBr ₃ / Spiro-OMeTAD	9.8	1.45	62	8.7
Ryu ¹⁷ 2014	FTO/c-TiO ₂ /mp-TiO ₂ /MAPbBr ₃ / PIF8-TAA ^(a)	6.1	1.4	79	6.7
Kulbak ¹⁸ 2016	FTO/c-TiO ₂ /mp-TiO ₂ /MAPbBr ₃ / PTAA ^(b)	5.9	1.37	71	5.8
Cai ¹⁹ 2013	FTO/c-TiO ₂ /MAPbBr ₃ / PCBDPP ^(c)	4.5	1.16	59	3.0
Edri ²⁰ 2013	FTO/c-TiO ₂ /mp-TiO ₂ /MAPbBr ₃ / PDI ^(d)	1.1	1.00	41	0.5

(a) Poly[[2,4-dimethylphenylimino]-1,4-phenylene(6,12-dihydro-6,6,12,12-tetraoctylindeno[1,2-b]fluorene-2,8-diyl)-1,4-phenylene], (b) Poly[bis(4-phenyl)(2,4,6-trimethylphenyl)amine], (c) Poly[N-9-hepta-decanyl-2,7-carbazole-alt-3,6-bis-(thiophen-5-yl)-2,5-dioctyl-2,5-di-hydropyrrolo[3,4-]pyrrole-1,4-dione], (d) N,N'-dialkyl perylenediimide.

In addition to perovskite processing, researchers have also attributed improved MAPbBr₃ efficiencies to the choice of HTL. Increases in V_{oc} are believed to result from shifting of the quasi Fermi levels (i.e. the electrochemical potentials) of the n-type TiO₂ and the p-type

HTL where the separation of these levels determines the V_{oc} .^{19,21} This is exemplified in Ryu and Kulbaks work where MAPbBr₃ cells manufactured using the poly triarylamine (PTAA) derivatives, PIF8-TAA and PTAA (as HTL's) produced photo-voltages of 1.4 V and 1.37 V and efficiencies of 6.7%¹⁷ and 5.8%¹⁸, respectively. The lower lying HOMO level of the PTAA derivatives increased separation between the quasi fermi levels which then increased the V_{oc} .²⁰ Heo *et al.* also attributed their record 10.4% efficiency in part, to the 1.51 V photo-voltage generated through the use of a PIF8-TAA HTL.¹⁵

The larger photo-voltages achievable with MAPbBr₃ PSC's highlight the potential for higher efficiencies if the light harvesting range could be extended. This could be achieved through co-sensitisation with organic dyes of complimentary absorbance. From a co-sensitisation perspective, the increased stability and wide band gap of MAPbBr₃ facilitates extended cell monitoring and separation of the sensitiser responses, which is ideal for studying the dye contribution in the cell.

This Chapter explores the characterisation and optimisation of MAPbBr₃ PSC's prior to co-sensitisation and demonstrates the development of a manufacturing method capable of producing MAPbBr₃ cells which consistently achieve >1%. An existing in-house method (previously optimised for MAPbI₃ cells) has been re-evaluated and tailored to MAPbBr₃ cell manufacture by investigating TiO₂ blocking layer deposition and the use of alternative HTL materials. Optimisation of the perovskite layer itself has been achieved by exploring: the annealing temperature, anti-solvent crystallisation, dimethyl sulfoxide solvent annealing and by implementing changes recommended within the literature.²² Optical microscopy and X-ray diffraction have been used to study the uniformity and crystallinity of the perovskite layer and improvements in cell performance have been documented by measuring and comparing cell efficiencies when manufactured using different variables.

3.2 Experimental methods

This section details the materials and methods used to fabricate MAPbBr₃ films and cells prior to method development. The composition and deposition of the compact/blocking TiO₂ layer, mesoporous layer and perovskite layer differ compared to the optimised process described in Sections 2.1.1 – 2.1.3:

A compact titanium dioxide layer was deposited on pre-cleaned FTO glass ($7 \Omega \text{ sq}^{-1}$, NSG Pilkington) by spin coating 100 μL of neat Ti nanoxide BL/SC (Solaronix) solution (3000 rpm/3000 rpm^{-1} for 30 seconds) followed by annealing on a pre-heated hotplate at 150 °C for 10 minutes. A mesoporous titanium dioxide (mp-TiO₂) solution was then deposited by spin coating 100 μL at 4500 rpm for 30 seconds. The substrates were dried on a hotplate at 150 °C for 10 minutes followed by sintering at 550 °C for 30 minutes.

A methyl-ammonium lead tri-bromide solution was prepared by dissolving a 60wt% 1:1 molar ratio of CH₃NH₃Br and PbBr₂ in 1 mL of DMF, 100 μL of this solution was then deposited onto the mp-TiO₂ layer by spin coating at 4000 rpm for 30 s. The films were then annealed at 100 °C for ten minutes on a pre-heated hotplate.

In June 2018, Saliba *et al.* released a comprehensive guide for the manufacture of >20% efficiency perovskite solar cells when using a n-i-p mesoporous architecture.²² The guidelines in this publication recommended alternative spin speed settings and sintering conditions for both the mp-TiO₂ and perovskite layer deposition. Subsequently for this research, the spin speed settings and sintering conditions for the mp-TiO₂ and perovskite layer were altered to mimic those as advised in the Saliba publication and are as described in Sections 2.1.1 – 2.1.3. In this Chapter, the cells built in Sections 3.3.2 and 3.3.2.1 were manufactured using the processes described above for the compact titanium dioxide layer, mesoporous layer and perovskite. Cells built in the Sections following Section 3.3.2.1 were then manufactured using Saliba's method as described in Sections 2.1.1 – 2.1.3.

3.2.1 Anti-solvent drip

The anti-solvent drip method investigated in Section 3.3.2.4 involved depositing 200 μL of the respective anti-solvent in the center of the film within the last 10 seconds of spin coating. The perovskite layer was then annealed on a pre-heated hot plate using the conditions described in Section 2.1.2.

3.2.2 PTAA hole transport layer

The PTAA HTL solution mentioned in Section 3.3.2.5 was prepared in a nitrogen-filled glovebox (<0.5 ppm H_2O , <0.5 ppm O_2 , MBraun). 15 mg of PTAA (Sigma-Aldrich) was dissolved in 1 mL of toluene and 7.5 μL of 4-tert-butylpyridine in acetonitrile (1:1) and 7.5 μL of lithium bis(trifluoromethanesulfonyl)- imide (LiTFSI) in acetonitrile (170 mg/mL) was subsequently added. This solution was then filtered (0.2 μm , Minisart, Sartorius) and deposited onto each thin-film via spin coating 70 μL of solution at 4000 rpm/2000 $\text{rpm}\cdot\text{s}^{-1}$ for 20 seconds. The films were stored overnight in a dark and dry atmosphere prior to gold contact deposition.

All cell efficiencies reported in the text have been measured under 1 sun conditions (AM 1.5 and 100 mW cm^{-2}) and are the results generated for the forward scan measurement unless otherwise stated.

3.3 Results and discussion

3.3.1 Characterisation of MAPbBr₃ perovskite

The colourless precursor solution of MAPbBr₃ perovskite (Figure 3.0 (a)) is formed through the dissolution of methylammonium bromide and lead bromide in dimethylformamide (DMF). Following deposition, thermal annealing encourages evaporation of the organic solvent causing a characteristic colour change (indicative of crystallisation) yielding a semi-transparent orange MAPbBr₃ thin-film. These were attractive features when considering co-sensitisation, as they allow visualisation of any dye uptake and colour tuning of the perovskite layer.

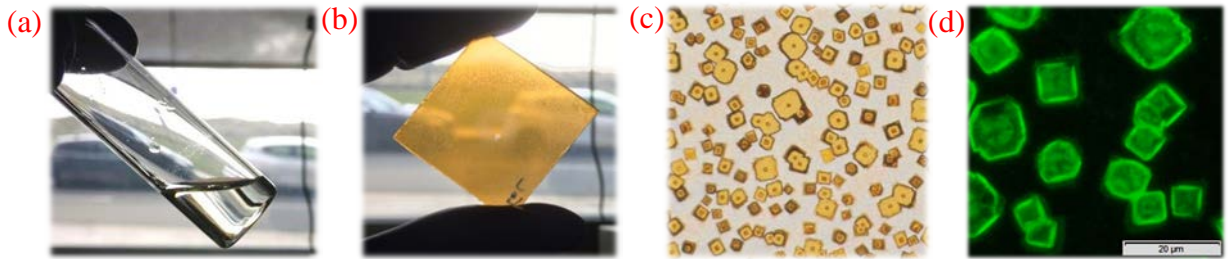


Figure 3.0: Photographs of (a) colourless MAPbBr₃ precursor solution, (b) semi-transparent orange annealed MAPbBr₃ film, (c) optical microscopy image of a MAPbBr₃ film taken using a $\times 20$ objective, (d) fluorescence microscopy image of a MAPbBr₃ film $\lambda_{\text{exc}} = \sim 390 \pm 9$ nm.

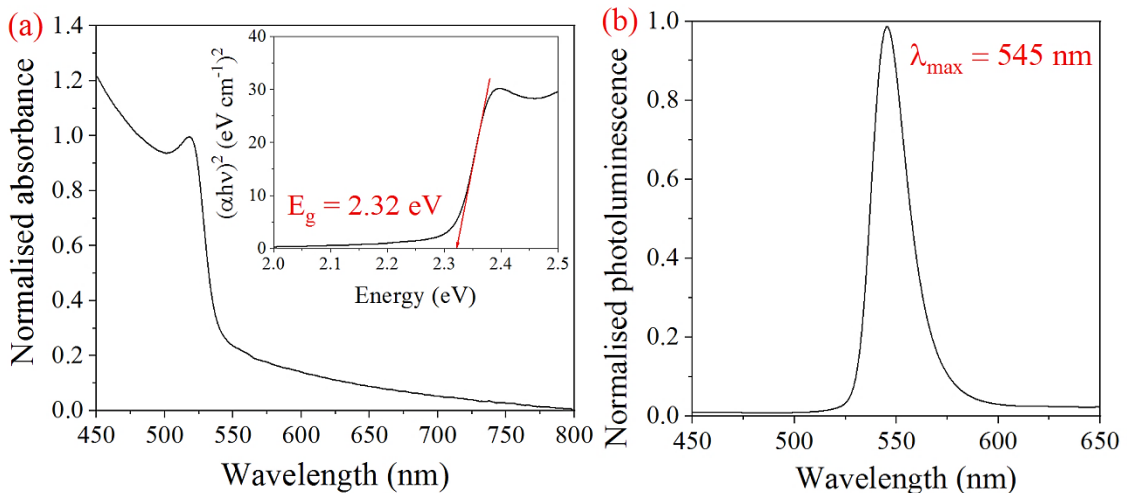


Figure 3.1: (a) Normalised absorbance of a MAPbBr₃ thin-film, inset gives the band gap derived from a Tauc plot. (b) Normalised photoluminescence emission of a MAPbBr₃ thin-film when excited at 405 nm.

Figure 3.1 (a) shows the normalised absorbance spectrum of a MAPbBr₃ perovskite thin-film, where a sharp band edge is observed at 540 nm. A Tauc plot, (Figure 3.1 (a), pictured inset) was used to determine a band gap (E_g) of 2.32 eV which is consistent with MAPbBr₃ band gap values given in the literature.^{11,23,24} Figure 3.1 (b) shows the measured photoluminescence (PL) emission of the same film which generates a narrow asymmetric emission peak centered at 545 nm when excited with 405 nm light. This peak represents the radiative band to band emission of the perovskite and is consistent with literature values reported for the cubic phase of MAPbBr₃.^{24–26} The asymmetry of the peak has previously been attributed to the presence of varying radiative recombination processes arising from disorder within the crystal lattice.^{27,28} For MAPbBr₃, intrinsic disorder can present as tail states in the sub bandgap region and as deep or shallow traps which lie deep within the bandgap or close to the conduction band edge, respectively. Broadening of the PL peak however, is generally indicative of radiative emission from shallow trap states.²⁶

When deposited as a thin layer on titania, MAPbBr₃ perovskite adopts a crystalline cubic structure which was characterised using X-ray diffraction (XRD).

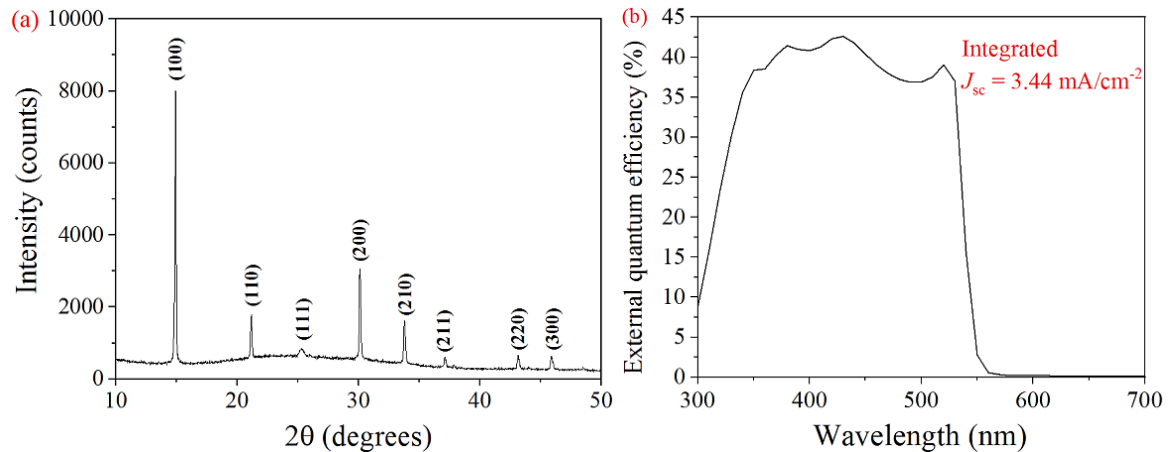


Figure 3.2: (a) X-ray diffraction pattern of a MAPbBr₃ perovskite thin-film deposited onto a mp-TiO₂ layer, (b) measured EQE spectral response for a MAPbBr₃ perovskite solar cell.

The diffraction pattern shown in Figure 3.3 (a) shows 8 distinguishable peaks at two-theta (2θ) values of: 14.92°, 21.24°, 25.33°, 30.23°, 33.95°, 37.22°, 43.12° and 45.96° corresponding to the (100), (110), (111), (200), (210), (211), (220) and (300) planes,

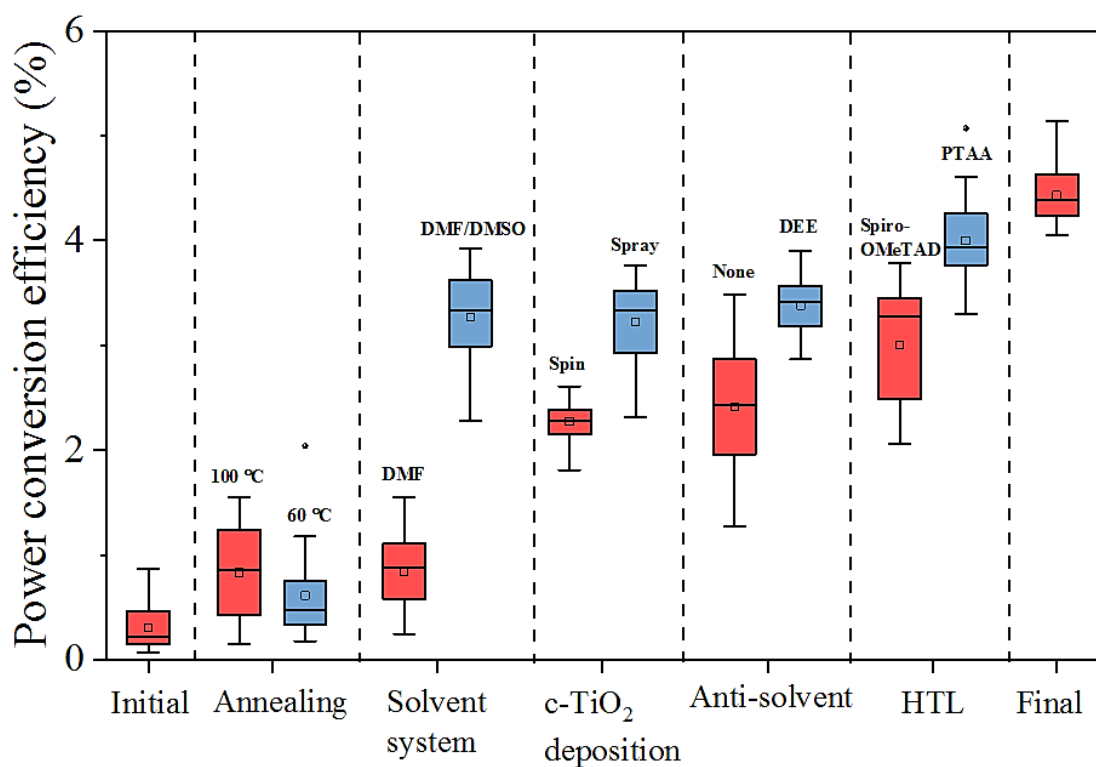
respectively of the cubic phase of MAPbBr₃ perovskite. These results are consistent with diffraction patterns previously reported for the cubic phase of MAPbBr₃ perovskite.²⁸⁻³⁰

The measured EQE of a MAPbBr₃ cell (Figure 3.2 (b)) shows that the maximum EQE response (42%) is reached at 430 nm. The EQE remains above 35% from 300 to 550 nm before the signal is then seen to drop sharply, indicating that the cell is successfully harvesting incident photons within the 300-550 nm wavelength range and converting them with a reasonable quantum yield into photocurrent. An integrated J_{sc} value of 3.44 mA/cm² was calculated from the graph which is lower than the majority of literature photocurrent values reported in Table 2. These results highlight the potential for increasing the photocurrent not only through method optimisation but also through the introduction of a complementary organic dye sensitiser which harvests incident photons >550 nm.

3.3.2 Method optimisation

MAPbBr₃ cells initially manufactured using an in-house method (previously optimised for MAPbI₃ PSC's) failed to achieve over 1% indicating the method was not directly transferrable when using MAPbBr₃ perovskite as the sensitiser. Method optimisation was required in order to achieve higher stabilised cell efficiencies prior to co-sensitisation.

As an overview of this Chapter, Figure 3.3 shows the power conversion efficiencies (PCE) generated for MAPbBr₃ PSC's at each stage of method optimisation. The red box plots represent the control results for each experiment where each cell has been prepared (at that stage) as described in the un-optimised in-house method. Each consecutive experiment then adopts the highest performing optimised condition realised from the previous experiment. The blue boxplots represent the highest performing variable for that experiment. Each stage of optimisation is discussed further in the text.



Optimisation method

Figure 3.3: Boxplots of PCE (%) generated for MAPbBr₃ PSC's at each stage of method optimisation. Red box plots represent the control condition and results for each experiment; blue boxplots represent the highest performing variable for that experiment.

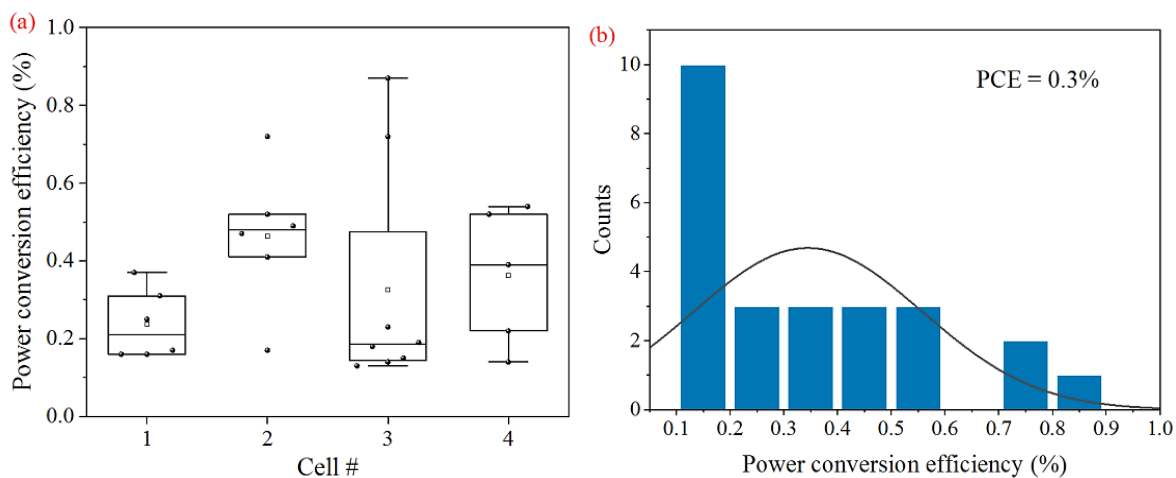


Figure 3.4: (a) Box plot showing the individual PCE's (%) for the four replicate MAPbBr₃ cells (b) histogram of PCE for the 32 pixels of the four MAPbBr₃ replicate cells.

The initial build results (Figure 3.4 (a-c)) are based on 4 replicate cells manufactured using the un-optimised in-house build method. The results show several non-working pixels and

large inconsistencies between replicate cells suggesting several defects within the perovskite layer. The average J_{sc} , V_{oc} , FF and PCE were 2.3 mA/cm², 0.44 V, 38, and 0.3%, respectively, which are considerably poorer than the literature performance values reported for MAPbBr₃ PSC's in Table 2. The efficiencies of each individual cell (Figure 3.4 (a)) show high variability between pixels and low efficiencies <0.5%. There is also considerable variability between the 32 pixels measured across the four cells (Figure 3.4 (b)) causing a high standard deviation (Table 3).

Table 3: standard deviation of the photovoltaic performance values for the four MAPbBr₃ cells built using the un-optimised in-house method.

Cell #	J_{sc} (mA cm ⁻²)	V_{oc} (V)	FF	PCE (%)
1	1.1	0.55	38	0.2
2	1.3	0.58	51	0.5
3	3.4	0.28	31	0.4
4	3.4	0.33	31	0.4
Standard deviation	1.27	0.15	9.43	0.13

Although the results of the initial build were poor, the hero pixel for this data set generated a J_{sc} , V_{oc} , FF and PCE of 3.5 mA/cm², 0.62 V, 39, and 0.9%, respectively with the PCE nearing 1%. Therefore, higher efficiencies could potentially be achieved through moderation of the build method and improvement of the perovskite layer morphology. It is well established that the photovoltaic performance of lead halide perovskites is largely dependent on the crystal morphology.^{31,32,41,33-40} Research in this area has shown how smaller crystals or 'grains' can increase trap-assisted non-radiative recombination due to more grain boundaries which harbour a higher density of trap states.³²⁻³⁵ Therefore, improved efficiencies are typically observed for larger crystals with less grain boundaries.^{32,37,38,41,42} Larger perovskite crystal growth has previously been achieved through optimising the perovskite annealing temperature.

3.3.2.1 Perovskite annealing temperature

One of the major advantages of lead halide perovskites is their solution processability whereby crystallised perovskite thin-films can be easily produced on annealing the deposited precursor solution. The perovskite annealing temperature is an important factor

which can strongly influence the crystal morphology as it defines the rate of solvent evaporation and dictates the amount of energy transferred to the crystallisation process.³⁹

For MAPbI₃ PSC's, an annealing temperature of 100-110 °C is typically used.^{22,32,38,39,41} A study by Dualeh *et al.* showed temperatures <80 °C lead to incomplete perovskite formation, whereas temperatures >140 °C caused decomposition of the organic methyl component leaving behind a lead iodide film.^{41,40}

The in-house method adopted in this research was developed for the manufacture of MAPbI₃ cells and, as above, recommends an annealing temperature of 100 °C. However, this was not necessarily optimal when using MAPbBr₃ perovskite. Little, if any, research into the annealing temperatures of MAPbBr₃ is currently published however, the leading MAPbBr₃ efficiencies show that MAPbBr₃ perovskite is typically annealed at lower temperatures between 60^{16,18,20} and 100 °C.^{15,17,19} Here, the nucleation and performance of MAPbBr₃ PSC's was studied when annealing the perovskite layer at temperatures between 50 and 100 °C. Optical microscopy was used to study the influence of the annealing temperature on the perovskite crystal morphology. Figure 3.6 shows the optical microscopy images of MAPbBr₃ thin films when annealing the perovskite layer at 60, 80 and 100 °C.

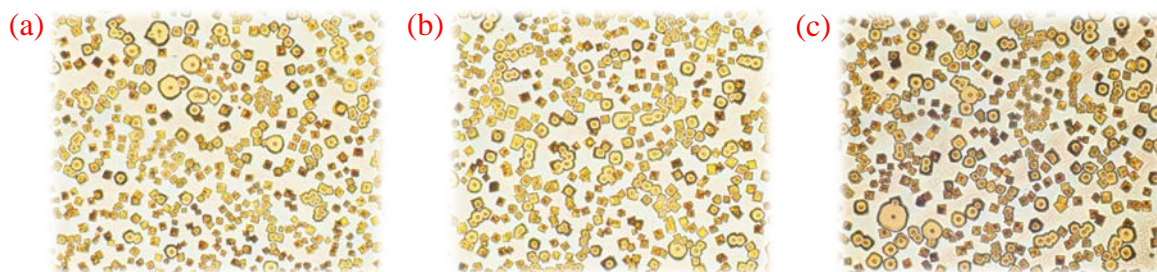


Figure 3.5: Optical microscopy images of MAPbBr₃ thin-films when annealing the perovskite layer at: (a) 60 °C (b) 80 °C and (c) 100 °C. Images captured using a x10 objective.

For each annealing temperature, the cubic crystal structure of MAPbBr₃ is clearly visible with good crystallite definition however; the crystals are small and separated by distinct gaps with no formation of a homogenous perovskite layer. There is no clear visible difference in the appearance of the films or the size of the crystallites despite the increase in annealing temperature.

Figure 3.6 (a) shows the average PCE's of MAPbBr₃ cells when annealing the perovskite layer between 50 and 100 °C.

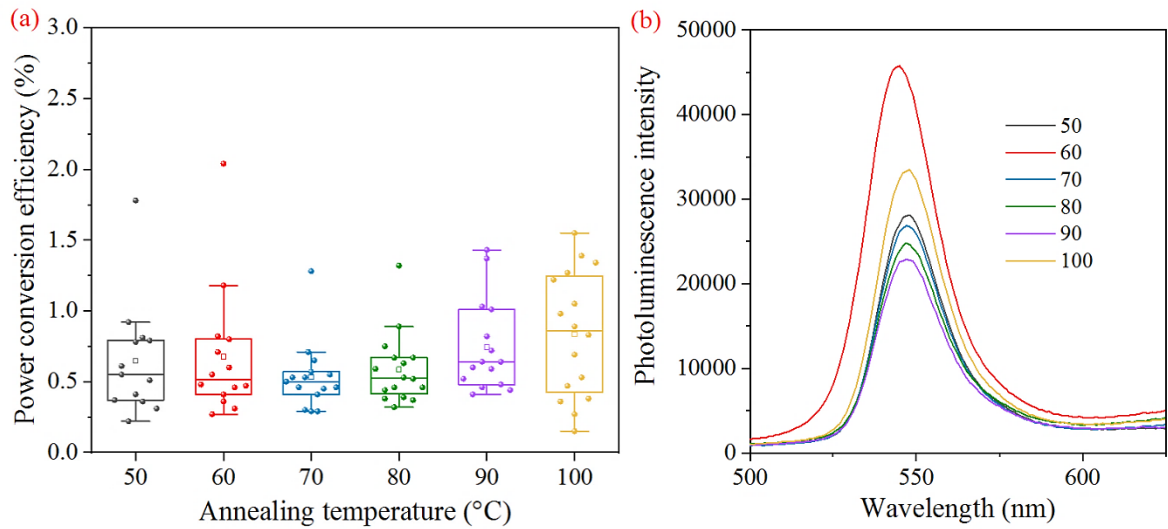


Figure 3.6: (a) Box plots of average PCE (%) for MAPbBr₃ PSC's and (b) Measured photoluminescence emission ($\lambda_{exc} = 405$ nm) of MAPbBr₃ perovskite spin-coated on glass, when annealing the perovskite layer at temperatures between 50 – 100 °C.

Despite the films appearing visually consistent, in Figure 3.6 we can see some variation in the average device efficiencies when altering the annealing temperature. Whilst there is no obvious trend, the variation in the efficiencies (between temperatures) suggests the annealing temperature does have some influence on the perovskite morphology. This, in turn, is affecting the device performance and causing some of the devices annealed at certain temperatures to perform better than others.

The lowest average efficiency (0.5%) was observed when annealing the perovskite layer at 70 °C but these devices also showed the lowest variability. Conversely, the highest average efficiency of 0.8% was observed with 100 °C however, this annealing temperature caused the highest variability between the device pixels. There was less variation between the average efficiencies of cells annealed at temperatures below 80 °C.

The devices annealed at 50 and 60 °C had average efficiencies of 0.6% and 0.7%, respectively and therefore did not largely differ in efficiency from those annealed at 100 °C. On studying the hero pixel data (Table 4), we see that each of the perovskite annealing temperatures produced hero pixel efficiencies above >1%. Interestingly, a lower annealing temperature of 60 °C produced the highest performing hero pixel (2.0%) of the entire data

set. This annealing temperature also produced higher J_{sc} and FF values compared to the cells annealed at 100 °C. This suggested that going forward; a lower annealing temperature may offer improved performance for MAPbBr₃ devices.

Table 4: Measured photovoltaic performance values for the hero pixels of MAPbBr₃ PSC's when annealing the perovskite layer at temperatures between 50 and 100 °C.

Annealing temperature (°C)	J_{sc} (mA cm ⁻²)	V_{oc} (V)	FF	PCE (%)
50	3.40	0.82	64	1.8
60	4.16	0.74	66	2.0
70	3.88	0.67	49	1.3
80	4.01	0.72	46	1.3
90	4.95	0.65	44	1.4
100	3.79	0.78	52	1.6

Figure 3.6 (b) shows the steady state PL emission measurements for MAPbBr₃ perovskite when annealed at the different temperatures on glass. For perovskite thin-films, enhanced PL emission can be indicative of a higher number of charge carriers generated as a result of lower defects and improved crystal morphology.⁴³ Here however, There was no discernible trend between PL intensity and annealing temperature as both the lowest and highest annealing temperatures, 50 and 100 °C, respectively produced similar PL emission intensities at 547 nm / λ_{max} . Despite this, the highest PL emission was observed when annealing the perovskite at 60 °C suggesting lower levels of non-radiative recombination possibly resulting from improved crystallinity when annealing at this temperature.

Overall, even though the films do not differ visually under the optical microscope, these results show that the annealing temperature of the perovskite does have some influence on the efficiency and PL of MAPbBr₃ devices and thin-films.

Despite observing the highest average efficiency when annealing the perovskite at 100 °C, devices annealed at this temperature showed high variability possibly due to elevated solvent evaporation rates or non-uniform evaporation which may have encouraged greater inconsistencies within the perovskite layer. In this Chapter, the aim is to develop a cell build method which reduces/limits variability within the perovskite as much as possible prior to

co-sensitisation. This is to ensure any effects any effects observed after adding a dye to the system have arisen due to the dye and not from variation within the perovskite layer.

Conversely, the devices annealed at 60 °C showed lower variability and only differed in average efficiency from those annealed at 100 °C by 0.1%. Devices annealed at this temperature also produced the highest hero pixel efficiency suggesting superior crystallisation in select areas of the perovskite layer which may in future yield higher performing devices with further optimisation. In addition to this, the highest PL intensity was seen for the thin-film annealed at 60 °C suggesting improved perovskite morphology and reduced non-radiative recombination pathways in comparison to the other annealing temperatures.

Therefore, the lower variability in average efficiency, higher PL intensity and greater hero pixel efficiency seen for the devices annealed at 60 °C would suggest that going forward, annealing the perovskite at this temperature may yield improved crystal formation and therefore device performance over MAPbBr₃ devices annealed at 100 °C.

3.3.2.2 Solvent system

Treatment of the perovskite layer with solvent vapour has been shown to improve the crystallinity and grain size of MAPbI₃ films yielding improved electronic properties.^{37,44–47}

The pre-formed perovskite film and solvent are gently heated in an enclosed environment, surrounding the perovskite in solvent vapour. Precursor solution diluents such as dimethyl sulfoxide (DMSO) and DMF are typically used for this technique, where it's believed that the solvent vapour slightly re-dissolves the film surface, eliminating grain boundaries and leading to improved crystallisation upon re-annealing.⁴⁴ On treating MAPbI₃ films with DMF and DMSO, Zuo *et al.* reported the development of a vapour induced intermediate phase (Figure 3.7) which yielded larger grains with less defects and generated cell efficiencies of 19.2%.⁴⁷

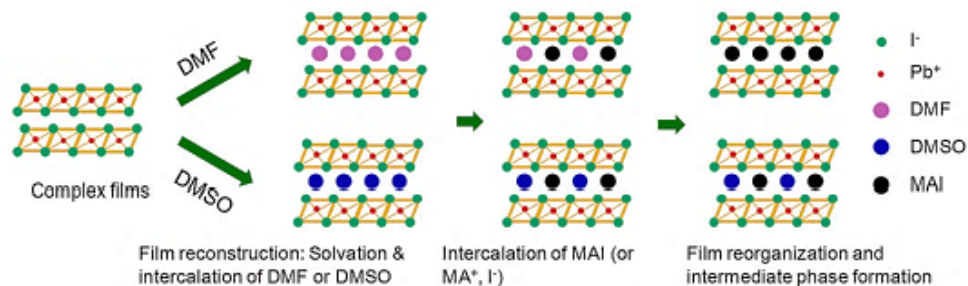


Figure 3.7: Schematic showing the formation of the solvent-vapour induced intermediate phase. The solvent expands the interlayer distance of the lead iodide (PbI_2) molecules leaving the methylammonium iodide (MAI) molecules to embed into the perovskite structure more easily. Image taken from ⁴⁷.

Larger grains and improved crystallinity were also reported by Xiao *et al.* through solvent annealing thicker MAPbI_3 films with DMF. Cell efficiencies of $>14.5\%$ were achieved when increasing the film thickness from 250-1015 nm. The average grain size was increased to 1 μm which exceeded the film thickness and allowed charges to be transported and collected through a single grain without encountering grain boundaries.³⁷ In addition to the benefits of introducing DMSO as a vapour, improvements in perovskite morphology were also seen when directly introducing DMSO into the precursor solution prior to sequential two-step deposition. It has been reported that mixing PbI_2 (dissolved in DMF) with varying volumes of DMSO prior to spin coating results in the formation of PbI_2 -DMSO complexes which improve the grain morphology and result in smoother mirror-like films when drop-casted with methylammonium iodide (MAI).⁴⁶

Here, the effect of solvent annealing (SA) using DMSO vapour was studied with MAPbBr_3 PSC's to determine if this process could improve the perovskite crystallinity and hence the cell performance. For MAPbBr_3 thin-films undergoing SA, the perovskite precursor solution was diluted in DMF only however, the introduction of DMSO solvent directly into the perovskite precursor solution was also investigated (solution preparation described in Section 2.1.2). A schematic describing the SA method used is shown in Figure 3.8.

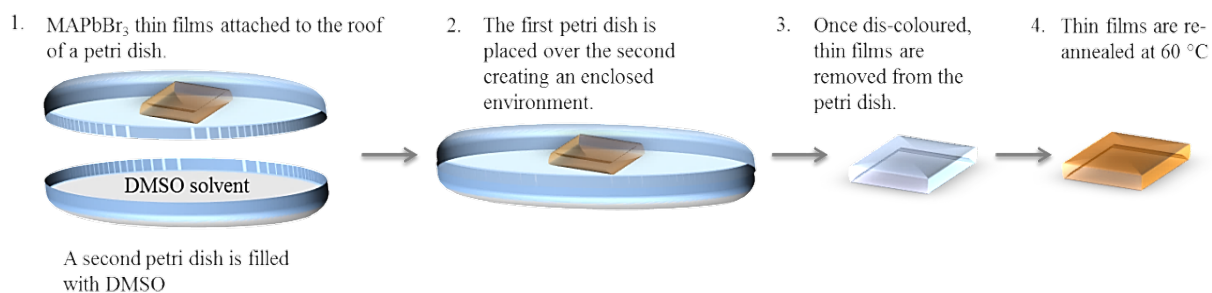


Figure 3.8: Schematic showing each stage of solvent annealing used for the MAPbBr₃ cells. For full devices, the hole transport layer and gold contacts were deposited following stage 4.

When encased in the solvent vapor, the MAPbBr₃ films transitioned from orange to colourless in a matter of minutes suggesting the vapour had re-dissolved the perovskite layer.

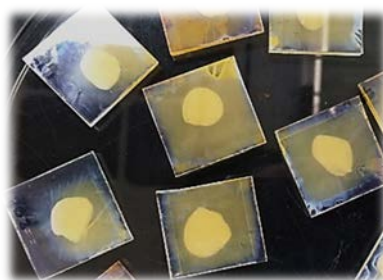


Figure 3.9: A photograph of MAPbBr₃ thin-films undergoing solvent annealing in DMSO vapour, during which the perovskite layer transitions from orange to colourless (stages 2 and 3, Figure 3.8).

Up on re-annealing, the films returned to an orange colour and appeared more ‘mirror-like’ in appearance when compared to untreated films. The optical microscopy images in Figure 3.10 show MAPbBr₃ thin-film’s prepared without (a) and with (b) DMSO SA. In Figure 3.10 (b) the previously cubic MAPbBr₃ crystals appear ‘fragmented’ and surrounded by a ‘halo’ of smaller interlinked crystals which may suggest improved homogeneity of the perovskite layer. The optical microscopy image in Figure 3.10 (c) shows the crystal morphology of a MAPbBr₃ thin-film prepared when adding DMSO to the perovskite precursor solution. Here, in comparison to the other images, the perovskite layer appears considerably more homogeneous and formed from larger crystals.

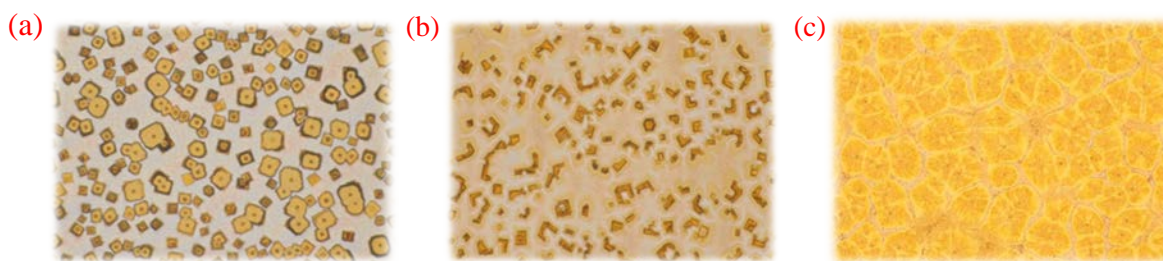


Figure 3.10: Optical microscopy images of MAPbBr₃ thin-films: (a) without DMSO SA, (b) with DMSO SA and (c) when DMSO solvent is directly added to the perovskite precursor solution. Images captured using a x20 objective.

Further insight into the effects of SA on the crystal morphology was provided by XRD analysis. The diffraction patterns for each variable are shown in Figure 3.11.

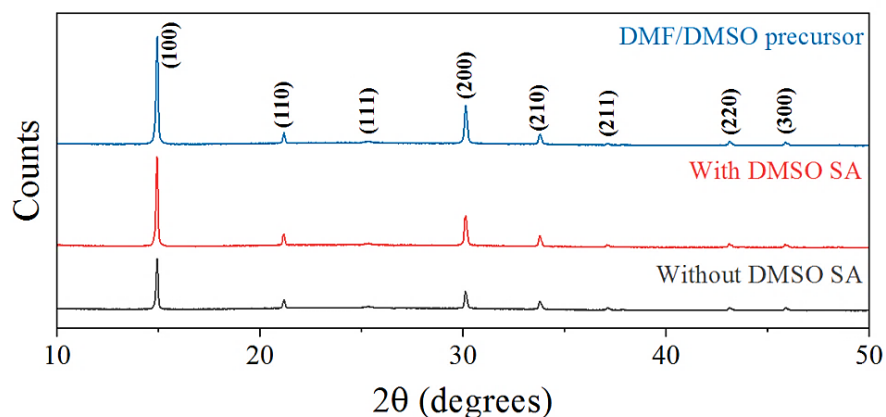


Figure 3.11: X-Ray diffraction patterns of MAPbBr₃ thin-films prepared without DMSO SA, with DMSO SA and when DMSO solvent is directly added to the perovskite precursor solution (DMF/DMSO precursor).

The XRD patterns are consistent and in agreement with the cubic structure of MAPbBr₃ and show no additional peaks between the perovskite solvent systems however, there is an overall increase in the intensity for MAPbBr₃ thin-films when introducing DMSO either through SA or by direct addition to the precursor solution. The increased count number observed for the DMSO systems suggests superior crystal formation and potentially improved growth which has reinforced the cubic formation. The effect of DMSO solvent annealing on the performance of MAPbBr₃ PSC's is given in Figure 3.12.

The performance of MAPbBr₃ cells which contain DMSO (with DMSO SA and DMF/DMSO precursor) are noticeably higher compared to those prepared using a DMF only system. Both DMSO systems demonstrated increased PCE, however the largest

increase was seen for cells prepared using a DMF/DMSO precursor solution. The observed increases in the J_{sc} and V_{oc} for the DMSO solvent systems suggest the addition of DMSO has improved crystal morphology resulting in higher charge generation, less grain boundaries and subsequently lower recombination.

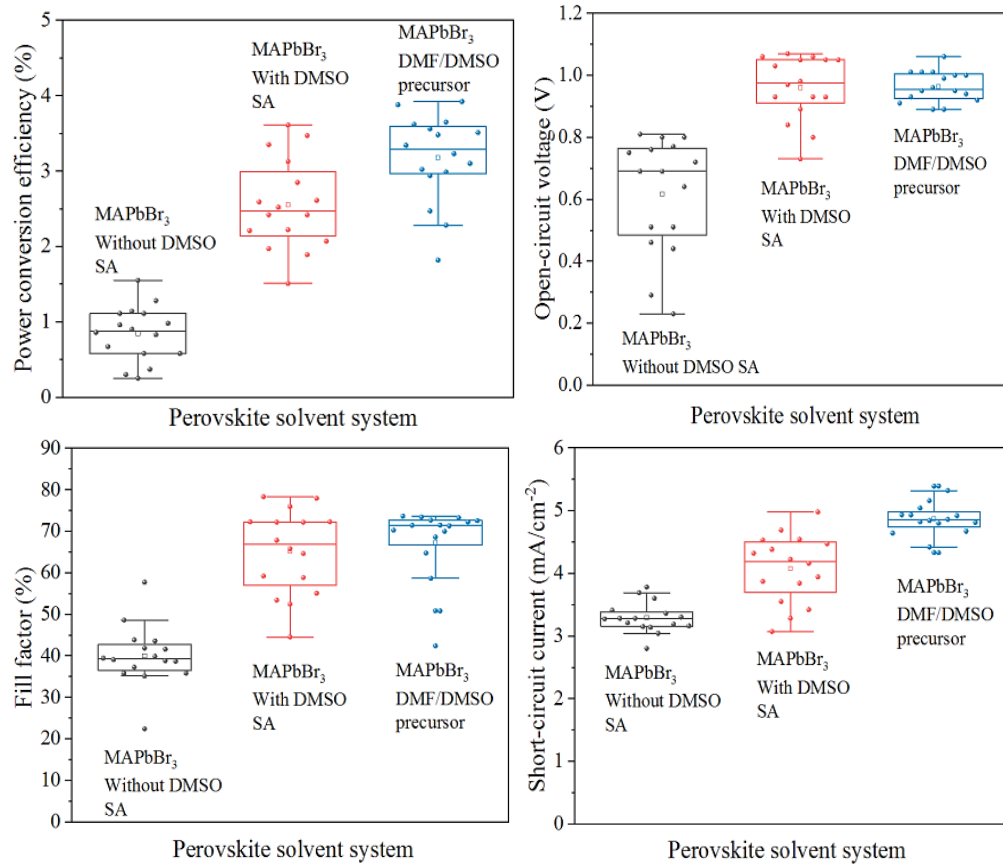


Figure 3.12: Box plots of performance parameters for MAPbBr₃ PSC's prepared without DMSO solvent annealing (SA), with DMSO SA and when DMSO solvent is directly added to the perovskite precursor solution (DMF/DMSO precursor).

This is also supported by the XRD data (Figure 3.11) which shows higher intensity for the diffraction patterns of DMSO solvent systems and the optical microscopy images which indicate improved homogeneity for DMSO systems (Figure 3.10). This theory is supported by literary sources which state, increases in performance when introducing DMSO result from longer charge recombination lifetimes due to a lower number of trap states and better homogeneity of the perovskite layer.⁴⁵ For MAPbI₃ cells, researchers have shown the absence of DMSO causes pinholes and increased surface roughness due to the rapid evaporation of DMF during annealing.⁴⁶ Whereas when including DMSO, crystal growth is

more regulated due to the formation of adducts (MAI·PbI₂·DMSO) which prevent premature crystallisation of PbI₂ prior to DMSO evaporation.⁴⁸

3.3.2.3 Blocking layer deposition

The compact titanium dioxide (c-TiO₂) layer is an inorganic n-type semiconducting layer which accepts photo-generated electrons from the perovskite and transfers them the FTO electrode. Also referred to as the hole blocking layer, this layer also prevents direct contact between the HTL and the FTO electrode which would otherwise cause recombination. The morphological properties of the c-TiO₂ layer can have a significant impact on the performance of PSC's. These properties are often governed by the deposition method where it's critical to achieve a dense and uniform layer free of pinholes. Reported deposition methods have included: screenprinting,⁴⁹ sol-gel,^{49,50} atomic layer deposition,⁵¹ DC magnetron sputtering,⁵² electrochemical deposition,⁵³ spray pyrolysis⁵⁴ and spin coating.⁵⁵ In this study, two commonly used deposition techniques were compared to determine their effect on the photovoltaic performance of MAPbBr₃ PSC's. A c-TiO₂ solution of titanium diisopropoxide bis(acetylacetonate) was prepared and deposited by spray pyrolysis as described in Section 2.1.1. A second c-TiO₂ solution of neat Ti nanoxide BL/SC was deposited by spin coating as described in the experimental section of this Chapter. Table 5 lists the average photovoltaic performance values for MAPbBr₃ PSC's prepared using each deposition method. Cells which contained a c-TiO₂ layer deposited using spray pyrolysis outperformed those prepared *via* spin coating by 1.1%. The higher J_{sc} , V_{oc} and FF of the sprayed cells suggests overall better perovskite crystallisation, reduced recombination losses and better charge collection efficiency in comparison to c-TiO₂ layers deposited by spin-coating.

Table 5: Average photovoltaic performance values for MAPbBr₃ PSC's prepared with a c-TiO₂ blocking layer deposited via spin coating and spray pyrolysis - also included is the standard deviation (σ) for each average value.

c-TiO ₂ deposition method	$\bar{x} J_{sc}$ (mA cm ⁻²)	$J_{sc} \sigma$	$\bar{x} V_{oc}$ (V)	$V_{oc} \sigma$	\bar{x} FF	FF σ	\bar{x} PCE (%)	PCE σ
Spin Coating	3.8	0.42	0.85	0.06	70	9.79	2.3	0.21
Spray Pyrolysis	4.3	0.59	1.00	0.02	72	4.76	3.2	0.39

3.3.2.4 Anti-solvent drip

The anti-solvent method was introduced in 2014 by Jeon *et al.* who reported an efficiency of 16.2% when drop casting toluene onto a $\text{MAPb}(\text{I}_{1-x}\text{Br}_x)_3$ precursor during spin coating.⁵⁶ Anti-solvents have proven beneficial when depositing perovskites using the one-step spin coating method as they promote better surface coverage, suppress charge recombination and yield denser, more uniform films.⁵⁷ Typically deposited during the final 10 seconds of spin coating, the anti-solvent acts to rapidly reduce the solubility of the perovskite in the mixed precursor solvent causing super saturation and driving rapid crystallisation.⁵⁸ The choice of solvent is an important factor, more non-polar solvents promote faster nucleation which subsequently encourages better homogenous nucleation.⁵⁷ This method of morphology engineering has been widely studied with various solvents such as: chlorobenzene (CB),⁵⁸ acetic acid,⁵⁹ dichloromethane,⁵⁷ and toluene,⁵⁶ whereas more recently greener solvents such as ethyl acetate (EA)⁶⁰ have been studied. Here, 5 anti-solvents of varying polarity were drop-casted onto MAPbBr_3 films during the last 10 seconds of spin-coating the perovskite. Optical microscopy images (Figure 3.13) were used to highlight the variability in nucleation of MAPbBr_3 perovskite thin-films when prepared using different anti-solvents.

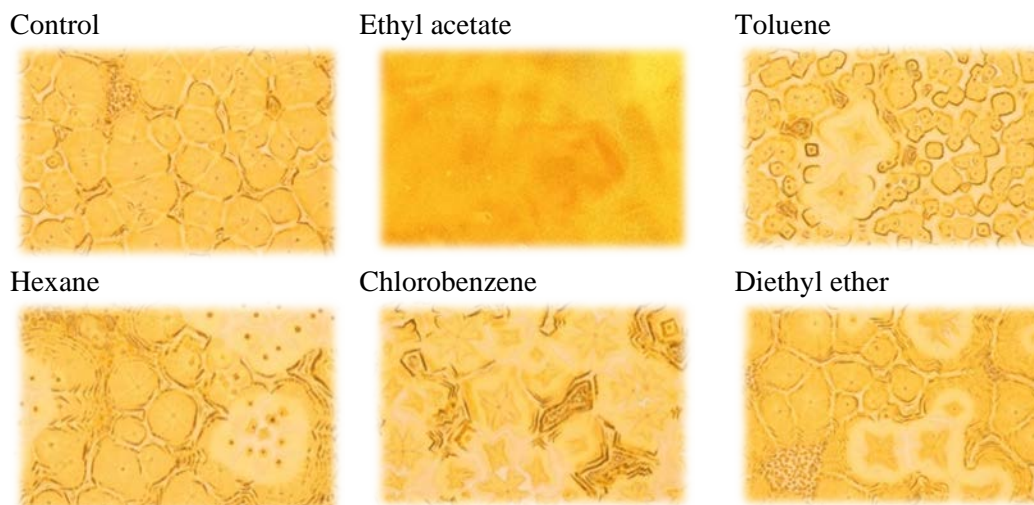


Figure 3.13: Optical microscopy images (captured using a $\times 10$ objective) of MAPbBr_3 thin-films when prepared using five different anti-solvents. The control film is MAPbBr_3 prepared without anti-solvent.

Toluene, hexane and diethyl ether (DEE) appear quite similar although slightly larger crystals are seen for hexane and DEE. Four of the solvents (hexane, toluene, CB and DEE)

have formed distinct star like crystals, with CB having the highest number. Films which have been prepared using an EA drip show the largest difference with no visible large crystals but a smooth layer of very small crystals.

XRD was used to determine if the visible differences in crystal shape observed in the optical microscopy images translated into differences in perovskite crystal structure. Figure 3.14 shows the diffraction patterns of MAPbBr₃ perovskite thin-films prepared using each anti-solvent.

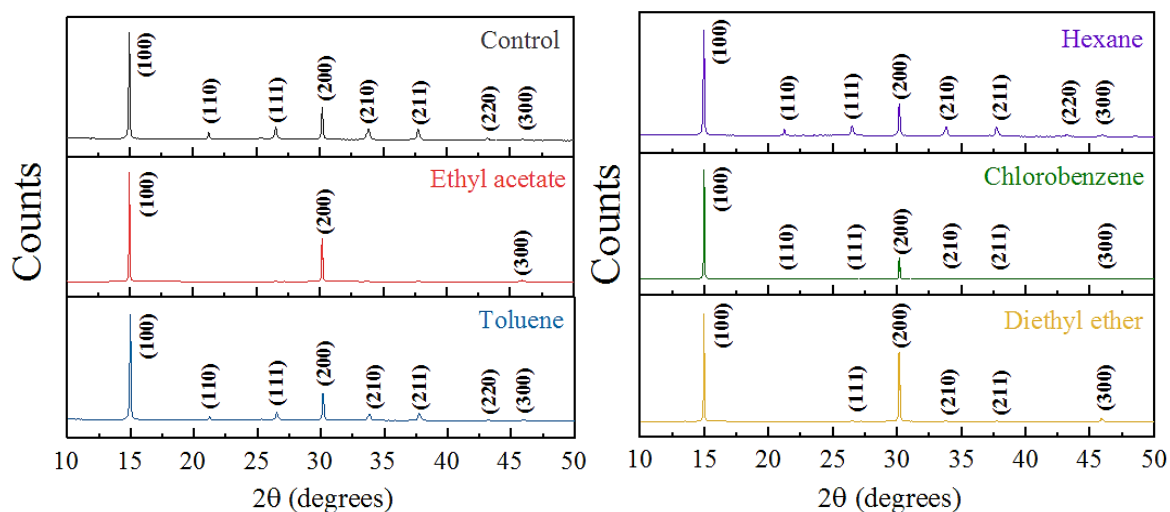


Figure 3.14: X-ray diffraction patterns of MAPbBr₃ perovskite thin-films prepared using various anti-solvents. The control film represents a MAPbBr₃ thin-film prepared without anti-solvent.

Each peak in the diffraction pattern represents a different lattice plane within the perovskite crystal. The hexane and toluene patterns closely resemble that of the control with 8 distinguishable peaks characteristic of the cubic MAPbBr₃ perovskite phase. The patterns of both CB and DEE show less peaks than the control, however the latter pattern shows the strongest intensity along the 200 plane. The EA pattern shows the least peaks of the anti-solvents tested which suggests less lattice planes within the crystal and potentially poorer crystal formation. The thin-films were then prepared as cells and subsequently tested under 1 sun irradiance to determine if the visual and crystalline differences observed between the anti-solvents improved the overall cell performance.

Figure 3.15 (a) and (b) show the PCE and FF, respectively of MAPbBr₃ perovskite solar cells prepared using each anti-solvent.

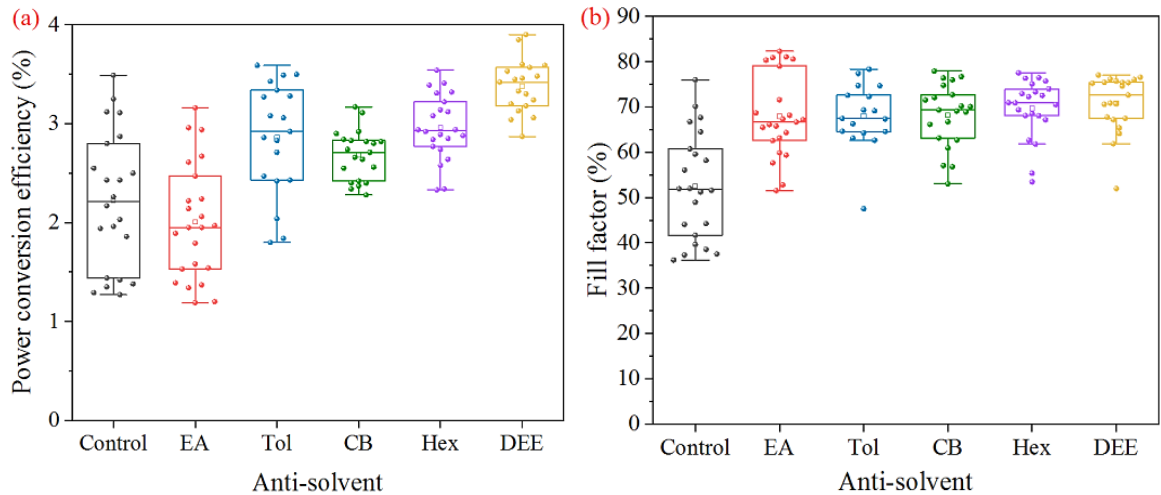


Figure 3.15: (a) Box plot of average PCE (%) and (b) box plot of average FF for MAPbBr₃ PSC's prepared using various anti-solvents.

Table 6: Average photovoltaic performance values for MAPbBr₃ PSC's prepared using various anti-solvents. The 'control' represents MAPbBr₃ PSC's prepared without anti-solvent - also included is the standard deviation, σ for each average value.

Anti-solvent	$\bar{x} J_{sc}$ (mA cm ⁻²)	J_{sc} σ	$\bar{x} V_{oc}$ (V)	V_{oc} σ	$\bar{x} FF$	FF σ	$\bar{x} PCE$ (%)	PCE σ
Control	4.6	0.37	0.90	0.12	52	11.87	2.2	0.69
Ethyl acetate (EA)	3.3	0.40	0.88	0.08	68	9.10	2.0	0.58
Toluene (Tol)	4.6	0.39	0.95	0.06	68	7.25	2.9	0.56
Chlorobenzene (CB)	4.2	0.25	0.95	0.03	68	7.05	2.7	0.25
Hexane (Hex)	4.4	0.23	0.97	0.03	70	6.44	3.0	0.33
Diethyl ether (DEE)	4.7	0.25	0.99	0.03	71	6.30	3.4	0.27

These results show an increase in average PCE for 4 out of 5 of the anti-solvents when compared to the untreated control cell. Ethyl acetate was the only solvent to show a decrease in PCE, which in agreement with the lack of diffraction peaks and visible crystals, suggests poorer perovskite crystallisation. The largest improvement in average PCE was seen for DEE where an increase of 1.2% was observed (Figure 3.15 (a)). The average values measured for J_{sc} and V_{oc} remain fairly consistent (Figure 3.15 (c)) whereas a noticeable difference in the average FF (Figure 3.15 (b)) seems to have mainly contributed to the observed increases in performance. Increases in FF can stem from fewer pinholes and

improved homogeneity in the perovskite layer which suggests the AS drip creates a smoother perovskite layer with less defects.⁶¹ In addition to improved performance when using anti-solvents, there is also noticeably less variation between cells, where CB and DEE appeared to show the least variation. Previously, Ahn *et al.* have shown the benefits of using a DEE anti-solvent with MAPbI₃ cells. They concluded that upon contact the DEE dissolves the DMF present in the precursor solution leaving the DMSO to form MAI·PbI₂·DMSO adducts which prevent the premature crystallisation of PbI₂. They also tested CB and toluene anti-solvents however, these solvents are miscible with DMSO and therefore removed the DMSO before adduct formation could occur.⁴⁸ In this study, as the best performing anti-solvent, it is possible that DEE formed beneficial adducts with the MABr and PbBr₂ which upon evaporation of the DMSO generated a homogenous perovskite layer with reduced defects. However, the presence of these adducts would need to be confirmed e.g. *via* infra-red spectroscopy.

3.3.2.5 Hole transport layer

In the introduction to this Chapter, the possibility of achieving a higher V_{oc} by selecting a hole transport layer with better energetic alignment with the perovskite was discussed. Better energy band alignment can reduce recombination and energy losses during hole transfer. Here, the performance of MAPbBr₃ PSC's prepared with a spiro-OMeTAD and PTAA HTL have been compared.

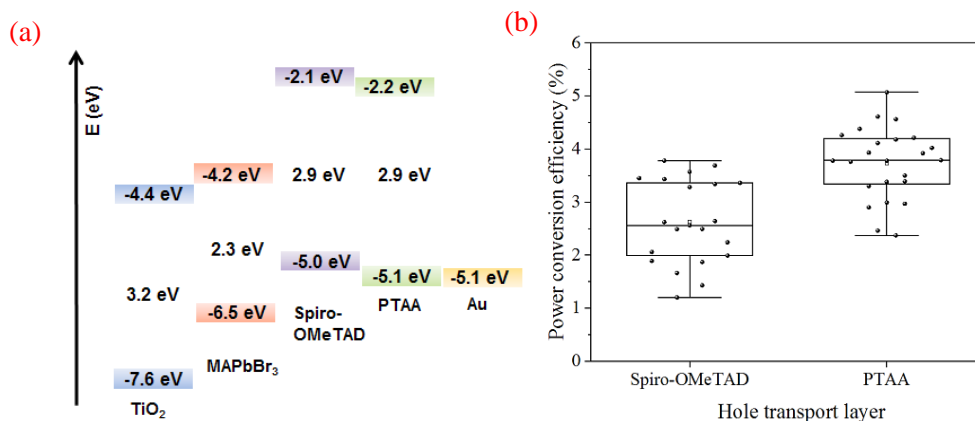


Figure 3.16: (a) Schematic of energy level positioning for the various components of a MAPbBr₃ PSC including literature values for the conduction and valence band edges of TiO₂ and MAPbBr₃,²⁰ the frontier orbital energy levels of PTAA and spiro-OMeTAD⁶² and the work function of the Au contact. (b) Box plot of average PCE (%) for MAPbBr₃ PSC's prepared using PTAA and spiro-OMeTAD HTLs.

Figure 3.16 (a) highlights how the HOMO level of PTAA sits slightly closer to the MAPbBr₃ valence band in comparison to spiro-OMeTAD. Therefore, PTAA is a slightly more energetically favourable HTL for MAPbBr₃ PSC's. The average PCE of both HTL's is shown in Figure 3.16 (b) where there is an increase of 1.1% for MAPbBr₃ PSC's prepared with PTAA.

The increases in the PCE observed for cells manufactured with PTAA stem from a higher average photocurrent and FF (Table 7). Generally, one might expect to see an increase in the V_{oc} when using a PTAA HTL with MAPbBr₃ due to the more favourable energy alignment. This has also been seen previously when using PTAA as a HTL with MAPbBr₃ PSC's in the literature.¹⁵ Here however, similar V_{oc} values were observed irrespective of the HTL.

Table 7: Average photovoltaic performance values for MAPbBr₃ PSC's prepared using PTAA and spiro-OMeTAD HTLs - also included is the standard deviation (σ) for each average value.

Hole transport layer	$\bar{x} J_{sc}$ (mA cm ⁻²)	J_{sc} σ	$\bar{x} V_{oc}$ (V)	V_{oc} σ	$\bar{x} FF$	FF σ	$\bar{x} PCE$ (%)	PCE σ
Spiro-OMeTAD	4.4	0.46	1.04	0.09	56	12.33	2.6	0.79
PTAA	5.5	0.35	1.03	0.07	65	8.51	3.7	0.67

The higher J_{sc} and FF observed for MAPbBr₃ PSC's prepared with PTAA suggests lower recombination and potentially better hole extraction as the PTAA HOMO level sits 0.1 eV closer the valence band of the perovskite. PTAA also has a higher hole mobility ($10^{-2} - 10^{-3} \text{ cm}^2 \text{ V}^{-1} \text{ s}^{-1}$) compared to spiro-OMeTAD ($1.67 \times 10^{-5} \text{ cm}^2 \text{ V}^{-1} \text{ s}^{-1}$) which would also promote better hole extraction efficiency.⁶³

3.3.2.6 Final build results

Here, the optimised build method developed through the experiments and findings discussed within this Chapter, has been used to build 5 replicate MAPbBr₃ PSC's. Each of the five films shows consistent absorbance spectra with a λ_{max} of 521 nm (Figure 3.17). The sharp absorbance edge visible for each measurement suggests good band-gap formation. There is some variation between the absorbance values obtained at λ_{max} however the standard deviation is low. The PL emission spectra for each film (Figure 3.17 (b)) show a consistent λ_{max} of 547 +/- 1 nm. There is slight variation in PL emission intensity with the greatest difference of 586 between cells 3 and 1. This is fairly consistent and positive for perovskite

thin-films which can often show high variability despite preparation in consistent conditions.

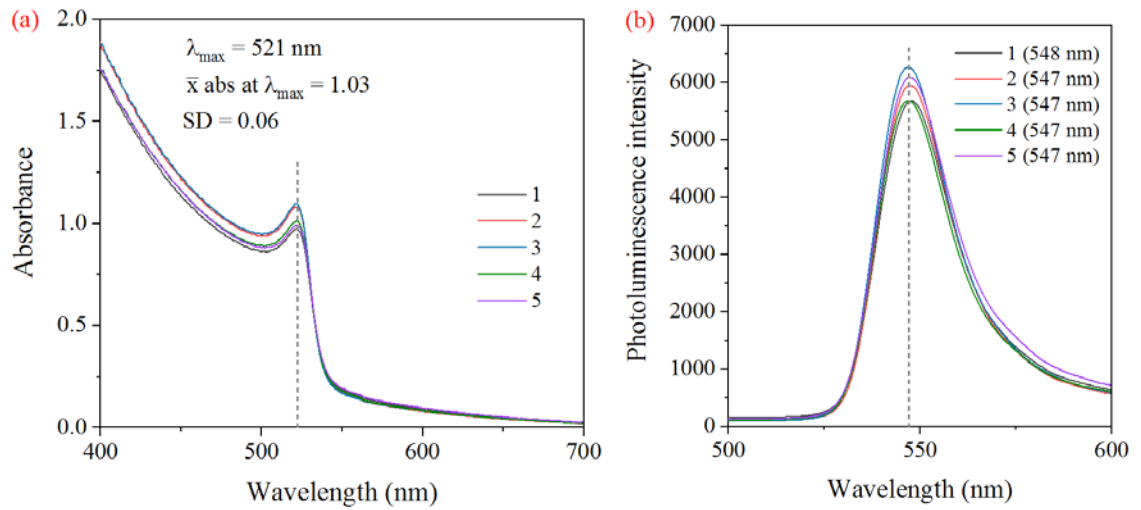


Figure 3.17: (a) Absorbance and (b) emission spectra ($\lambda_{\text{exc}} = 375 \text{ nm}$) of five replicate MAPbBr₃ perovskite thin-films prepared using the optimised build method. The dashed lines in each image represent the position of λ_{\max} , these values are also listed in brackets for each cell in image (b).

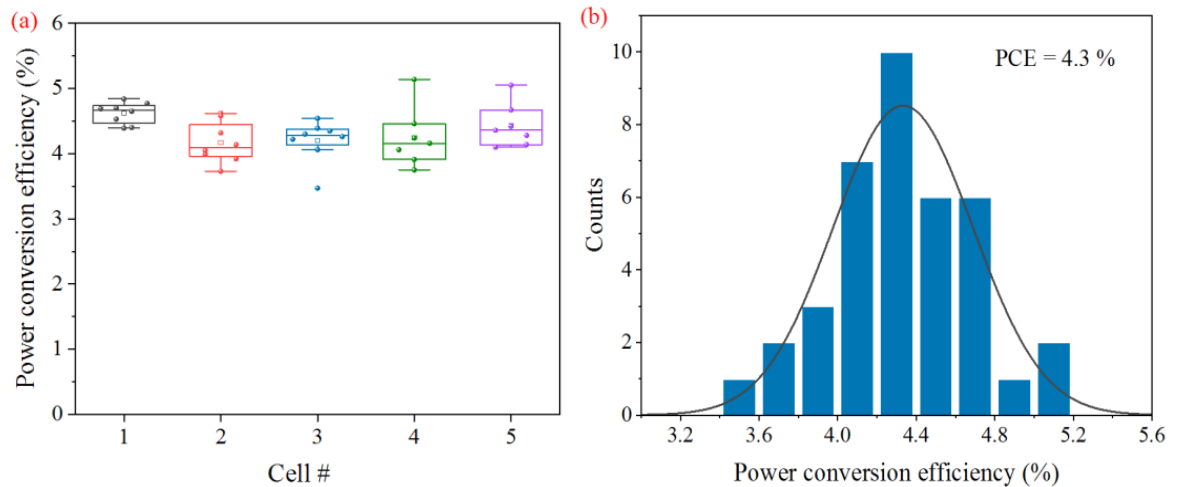


Figure 3.18: (a) Box plot showing the individual PCE's (%) for the five replicate MAPbBr₃ cells (b) histogram of PCE for the 40 pixels of the five MAPbBr₃ replicate cells.

The photovoltaic performance of the five replicate cells is shown in Figure 3.18. Each cell achieves an average efficiency $>4.0\%$ whilst hero pixels $>5\%$ were measured for cells 4 and 5. The standard deviation of the efficiencies of the five replicate cells is 0.36 with an 8% coefficient of variation showing low variation between the replicates. The photovoltaic parameters (Table 8) all typically remain very consistent between cells where the lowest

variation is seen for the average V_{oc} . In comparison to the results of the initial cell build, the average cell efficiency has increased from 0.2-0.5% to 4.2-4.6%. The histogram pictured in Figure 3.18 (b) shows the distribution of the efficiencies for the total 40 pixels measured from the 5 replicate cells (8 pixels per cell). When compared to the histogram of the 32 pixels measured in the initial cell build (Figure 3.4 (b)) the efficiency values here are significantly more uniform.

Table 8: standard deviation of the photovoltaic performance values for the five MAPbBr₃ cells built using the optimised manufacture method.

Cell #	J_{sc} (mA cm ⁻²)	V_{oc} (V)	FF	PCE (%)
1	5.5	1.09	77	4.6
2	5.3	1.02	77	4.2
3	5.2	1.09	75	4.2
4	5.2	1.06	76	4.2
5	5.3	1.07	77	4.4
Standard deviation	0.122	0.029	0.894	0.179

Overall when compared to the initial cell results, the performance of cells built using the optimised method is largely improved with little variability and consistent performance. Thus, through using the optimised method, it is possible to achieve a well formed, high performing MAPbBr₃ perovskite layer suited to a n-i-p device architecture.

3.4 Conclusions

In summary, the optical characterisation of MAPbBr₃ perovskite has shown a sharp band edge, located at 540 nm with a 2.3 eV bandgap. Co-sensitising dyes which absorb in the red to NIR region would therefore, potentially offer the best opportunity to extend the absorbance response of MAPbBr₃.

An existing in-house cell build method has been re-evaluated and tailored for the manufacture of MAPbBr₃ PSCs by optimising the materials and methods used during fabrication. Investigation of the layers adjacent to the perovskite revealed deposition of the compact titania layer by spray pyrolysis and the use of a PTAA HTL contributed to higher cell efficiencies. Morphology of the perovskite layer was optimised by introducing DMSO into the perovskite precursor solution, using a lower annealing temperature (60°C) and on introducing an anti-solvent drip. When collectively implemented in a final build method these findings produced average MAPbBr₃ PSC efficiencies >4% whilst hero pixels >5% have been measured. The efficiencies of five replicate cells prepared using the optimised method produced a standard deviation of 0.36 and an 8% coefficient of variation showing low variability between replicate cells despite preparation in an ambient environment. The consistent performance of the MAPbBr₃ cells achieved here will ensure any effects (detrimental or beneficial) observed following co-sensitisation have arisen due to the inclusion of the dye and not from variation in the perovskite layer.

3.5 References

1. Yang, T. C. J., Fiala, P., Jeangros, Q. & Ballif, C. High-Bandgap Perovskite Materials for Multijunction Solar Cells. *Joule* **2**, pp. 1421–1436 (2018).
2. Cho, H. *et al.* Overcoming the electroluminescence efficiency limitations of perovskite light-emitting diodes. *Science (80-.)*. **350**, pp. 1222–1225 (2015).
3. Kim, Y. H. *et al.* Multicolored organic/inorganic hybrid perovskite light-emitting diodes. *Adv. Mater.* **27**, pp. 1248–1254 (2015).
4. Kojima, A., Teshima, K., Shirai, Y. & Miyasaka, T. Organometal Halide Perovskites as Visible-Light Sensitizers for Photovoltaic Cells. *J. Am. Chem. Soc.* **131**, pp. 6050–6051 (2009).
5. Dong, G. *et al.* Regulated Film Quality with Methylammonium Bromide Addition in a Two-Step Sequential Deposition to Improve the Performance of Perovskite Solar Cells. *Energy Technol.* **5**, pp. 1873–1879 (2017).
6. Noh, J. H., Im, S. H., Heo, J. H., Mandal, T. N. & Seok, S. Il. Chemical management for colorful, efficient, and stable inorganic-organic hybrid nanostructured solar cells. *Nano Lett.* **13**, pp. 1764–1769 (2013).
7. Tanaka, K. *et al.* Comparative study on the excitons in lead-halide-based perovskite-type crystals $\text{CH}_3\text{NH}_3\text{PbBr}_3$ $\text{CH}_3\text{NH}_3\text{PbI}_3$. *Solid State Commun.* **127**, pp. 619–623 (2003).
8. Tanaka, K. & Kondo, T. Bandgap and exciton binding energies in lead-iodide-based natural quantum-well crystals. *Sci. Technol. Adv. Mater.* **4**, pp. 599–604 (2003).
9. Jiang, Q. *et al.* Planar-Structure Perovskite Solar Cells with Efficiency beyond 21%. *Adv. Mater.* **29**, 1703852 (2017).
10. Bi, D. *et al.* Efficient luminescent solar cells based on tailored mixed-cation perovskites. *Sci. Adv.* **2**, pp. 118–122 (2016).
11. Jeon, N. J. *et al.* Compositional engineering of perovskite materials for high-performance solar cells. *Nature* **517**, pp. 476–480 (2015).
12. Correa-Baena, J. P. *et al.* The rapid evolution of highly efficient perovskite solar cells. *Energy Environ. Sci.* **10**, pp. 710–727 (2017).
13. Jesper Jacobsson, T. *et al.* Exploration of the compositional space for mixed lead halogen perovskites for high efficiency solar cells. *Energy Environ. Sci.* **9**, pp. 1706–1724 (2016).
14. Hoke, E. T. *et al.* Reversible photo-induced trap formation in mixed-halide hybrid perovskites for photovoltaics. *Chem. Sci.* **6**, pp. 613–617 (2015).

15. Heo, J. H., Song, D. H. & Im, S. H. Planar CH₃NH₃PbBr₃ hybrid solar cells with 10.4% power conversion efficiency, fabricated by controlled crystallization in the spin-coating process. *Adv. Mater.* **26**, pp. 8179–8183 (2014).
16. Sheng, R. *et al.* Methylammonium lead bromide perovskite-based solar cells by vapor-assisted deposition. *J. Phys. Chem. C* **119**, pp. 3545–3549 (2015).
17. Ryu, S. *et al.* Voltage Output of Efficient Perovskite Solar Cells with high Open-Circuit Voltage and Fill Factor. *Energy Environ. Sci.* **7**, pp. 2614–2618 (2014).
18. Kulbak, M. *et al.* Cesium Enhances Long-Term Stability of Lead Bromide Perovskite-Based Solar Cells. *J. Phys. Chem. Lett.* **7**, pp. 167–172 (2016).
19. Cai, B., Xing, Y., Yang, Z., Zhang, W.-H. & Qiu, J. High performance hybrid solar cells sensitized by organolead halide perovskites. *Energy Environ. Sci.* **6**, 1480 (2013).
20. Edri, E., Kirmayer, S., Cahen, D. & Hodes, G. High open-circuit voltage solar cells based on organic-inorganic lead bromide perovskite. *J. Phys. Chem. Lett.* **4**, pp. 897–902 (2013).
21. Nayak, P. K., Garcia-Belmonte, G., Kahn, A., Bisquert, J. & Cahen, D. Photovoltaic efficiency limits and material disorder. *Energy Environ. Sci.* **5**, pp. 6022–6039 (2012).
22. Saliba, M. *et al.* How to Make over 20% Efficient Perovskite Solar Cells in Regular (n-i-p) and Inverted (p-i-n) Architectures. *Chem. Mater.* **30**, pp. 4193–4201 (2018).
23. Fru, J. N., Nombona, N. & Diale, M. Synthesis and characterisation of methylammonium lead tri-bromide perovskites thin-films by sequential physical vapor deposition. *Phys. B Condens. Matter* **578**, 411884 (2020).
24. Guo, D. *et al.* Photoluminescence from Radiative Surface States and Excitons in Methylammonium Lead Bromide Perovskites. *J. Phys. Chem. Lett.* **8**, pp. 4258–4263 (2017).
25. Richter, J. M. *et al.* Direct Bandgap Behavior in Rashba-Type Metal Halide Perovskites. *Adv. Mater.* **30**, 1803379 (2018).
26. Droseros, N., Tsokkou, D. & Banerji, N. Photophysics of Methylammonium Lead Tribromide Perovskite: Free Carriers, Excitons, and Sub-Bandgap States. *Adv. Energy Mater.* **10**, 1903258 (2020).
27. Priante, D. *et al.* The recombination mechanisms leading to amplified spontaneous emission at the true-green wavelength in CH₃NH₃PbBr₃ perovskites. *Appl. Phys. Lett.* **106**, 081902 (2015).

28. Wang, K. H., Li, L. C., Shellaiah, M. & Sun, K. W. Structural and Photophysical Properties of Methylammonium Lead Tribromide (MAPbBr₃) Single Crystals. *Sci. Rep.* **7**, 13643 (2017).
29. Zhang, M. *et al.* Composition-dependent photoluminescence intensity and prolonged recombination lifetime of perovskite CH₃NH₃PbBr_{3-x} Cl_xfilms. *Chem. Commun.* **50**, pp. 11727–11730 (2014).
30. Baikie, T. *et al.* A combined single crystal neutron/X-ray diffraction and solid-state nuclear magnetic resonance study of the hybrid perovskites CH₃NH₃PbX₃ (X = I, Br and Cl). *J. Mater. Chem. A* **3**, pp. 9298–9307 (2015).
31. Chen, Q. *et al.* Controllable self-induced passivation of hybrid lead iodide perovskites toward high performance solar cells. *Nano Lett.* **14**, pp. 4158–63 (2014).
32. Bi, C. *et al.* Non-wetting surface-driven high-aspect-ratio crystalline grain growth for efficient hybrid perovskite solar cells. *Nat. Commun.* **6**, 7747 (2015).
33. Shao, Y., Xiao, Z., Bi, C., Yuan, Y. & Huang, J. Origin and elimination of photocurrent hysteresis by fullerene passivation in CH₃NH₃PbI₃ planar heterojunction solar cells. *Nat. Commun.* **5**, 5784 (2014).
34. Noel, N. K. *et al.* Enhanced photoluminescence and solar cell performance via Lewis base passivation of organic-inorganic lead halide perovskites. *ACS Nano* **8**, pp. 9815–9821 (2014).
35. Shkrob, I. A. & Marin, T. W. Charge trapping in photovoltaically active perovskites and related halogenoplumbate compounds. *J. Phys. Chem. Lett.* **5**, pp. 1066–71 (2014).
36. Ren, X. *et al.* Reaction temperature modulating crystal grain size and optoelectronic properties of perovskite film for solar cell application. *Nanoscale* **8**, pp. 3816–3822 (2016).
37. Xiao, Z. *et al.* Solvent Annealing of Perovskite-Induced Crystal Growth for Photovoltaic-Device Efficiency Enhancement. *Adv. Mater.* **26**, pp. 6503–6509 (2014).
38. Im, J. H., Jang, I. H., Pellet, N., Grätzel, M. & Park, N. G. Growth of CH₃ NH₃ PbI₃ cuboids with controlled size for high-efficiency perovskite solar cells. *Nat. Nanotechnol.* **9**, pp. 927–932 (2014).
39. Jaysankar, M. *et al.* Crystallisation dynamics in wide-bandgap perovskite films. *J. Mater. Chem. A* **4**, pp. 10524–10531 (2016).
40. Dualeh, A. *et al.* Effect of annealing temperature on film morphology of organic-inorganic hybrid perovskite solid-state solar cells. *Adv. Funct. Mater.* **24**, pp. 3250–3258 (2014).

41. Supasai, T., Rujisamphan, N., Ullrich, K., Chemseddine, A. & Dittrich, T. Formation of a passivating CH₃NH₃PbI₃/PbI₂ interface during moderate heating of CH₃NH₃PbI₃ layers. *Appl. Phys. Lett.* **103**, 183906 (2013).
42. Chen, Q. *et al.* Planar heterojunction perovskite solar cells via vapor-assisted solution process. *J. Am. Chem. Soc.* **136**, pp. 622–625 (2014).
43. Zhou, Y., Hu, X., Xie, D. & Tian, Y. Mechanisms of Oxygen Passivation on Surface Defects in MAPbI₃ Revealed by First-Principles Study. *J. Phys. Chem. C* **124**, pp. 3731–3737 (2020).
44. Liu, J. *et al.* Improved Crystallization of Perovskite Films by Optimized Solvent Annealing for High Efficiency Solar Cell. *ACS Appl. Mater. Interfaces* **7**, pp. 24008–24015 (2015).
45. Lian, J., Wang, Q., Yuan, Y., Shao, Y. & Huang, J. Organic solvent vapor sensitive methylammonium lead trihalide film formation for efficient hybrid perovskite solar cells. *J. Mater. Chem. A* **3**, pp. 9146–9151 (2015).
46. Li, W., Fan, J., Li, J., Mai, Y. & Wang, L. Controllable grain morphology of perovskite absorber film by molecular self-assembly toward efficient solar cell exceeding 17%. *J. Am. Chem. Soc.* **137**, pp. 10399–10405 (2015).
47. Zuo, L. *et al.* Morphology Evolution of High Efficiency Perovskite Solar Cells via Vapor Induced Intermediate Phases. *J. Am. Chem. Soc.* **138**, pp. 15710–15716 (2016).
48. Ahn, N. *et al.* Highly Reproducible Perovskite Solar Cells with Average Efficiency of 18.3% and Best Efficiency of 19.7% Fabricated via Lewis Base Adduct of Lead(II) Iodide. *J. Am. Chem. Soc.* **137**, pp. 8696–8699 (2015).
49. Zhang, C. *et al.* Influence of different TiO₂ blocking films on the photovoltaic performance of perovskite solar cells. *Appl. Surf. Sci.* **388**, pp. 82–88 (2016).
50. Kavan, L., Zúkalová, M., Vik, O. & Havlicek, D. Sol-gel titanium dioxide blocking layers for dye-sensitized solar cells: Electrochemical characterization. *ChemPhysChem* **15**, pp. 1056–61 (2014).
51. Wu, Y. *et al.* Highly compact TiO₂ layer for efficient hole-blocking in perovskite solar cells. *Appl. Phys. Express* **7**, 5 (2014).
52. Waita, S. M. *et al.* Electrochemical characterization of TiO₂ blocking layers prepared by reactive DC magnetron sputtering. *J. Electroanal. Chem.* **637**, pp. 79–83 (2009).
53. Su, T. Sen, Hsieh, T. Y., Hong, C. Y. & Wei, T. C. Electrodeposited Ultrathin TiO₂ Blocking Layers for Efficient Perovskite Solar Cells. *Sci. Rep.* **5**, 16098 (2015).
54. Möllmann, A. *et al.* Highly Compact TiO₂ Films by Spray Pyrolysis and Application in Perovskite Solar Cells. *Adv. Eng. Mater.* **21**, 1801196 (2019).

55. Jeong, I. *et al.* Solution-Processed Ultrathin TiO₂ Compact Layer Hybridized with Mesoporous TiO₂ for High-Performance Perovskite Solar Cells. *ACS Appl. Mater. Interfaces* **9**, pp. 36865–36874 (2017).
56. Jeon, N. J. *et al.* Solvent engineering for high-performance inorganic–organic hybrid perovskite solar cells. *Nat. Mater.* 2014 139 **13**, pp. 897–903 (2014).
57. Zheng, X., Chen, B., Wu, C. & Priya, S. Room temperature fabrication of CH₃NH₃PbBr₃ by anti-solvent assisted crystallization approach for perovskite solar cells with fast response and small J-V hysteresis. *Nano Energy* **17**, pp. 269–278 (2015).
58. Xiao, M. *et al.* A fast deposition-crystallization procedure for highly efficient lead iodide perovskite thin-film solar cells. *Angew. Chemie - Int. Ed.* **126**, pp. 10056–10061 (2014).
59. Li, Y. *et al.* Acetic Acid Assisted Crystallization Strategy for High Efficiency and Long-Term Stable Perovskite Solar Cell. *Adv. Sci.* **7**, 1903368 (2020).
60. Xu, L. *et al.* Towards green antisolvent for efficient CH₃NH₃PbBr₃ perovskite light emitting diodes: A comparison of toluene, chlorobenzene, and ethyl acetate. *Appl. Phys. Lett.* **115**, 033101 (2019).
61. Shen, D. *et al.* Understanding the solvent-assisted crystallization mechanism inherent in efficient organic-inorganic halide perovskite solar cells. *J. Mater. Chem. A* **2**, pp. 20454–20461 (2014).
62. Stolterfoht, M. *et al.* The impact of energy alignment and interfacial recombination on the internal and external open-circuit voltage of perovskite solar cells. *Energy Environ. Sci.* **12**, pp. 2778–2788 (2019).
63. Vivo, P., Salunke, J. K. & Priimagi, A. Hole-transporting materials for printable perovskite solar cells. *Materials (Basel)*. **10**, 1087 (2017).

4 Photochemical characterisation of organic dyes for co-sensitisation

4.1 Introduction

Over the past thirty years, and through various advancements in material and architectural design, the efficiencies of DSSC's have almost doubled from 7.9% to over 14%.^{1,2} Many of the earliest DSSC's used ruthenium (II) polypyridyl complexes which were particularly popular as they provided the necessary redox, spectroscopic and excited-state properties required for a sensitising dye.³⁻⁶ Despite these qualities, the expensive manufacture, complicated synthesis and low extinction coefficients of ruthenium dyes has overtime rendered them less attractive to metal free sensitisers.⁷ Alternatives such as organic dyes, offer better design flexibility and higher extinction coefficients in the visible which facilitates the manufacture of thinner devices requiring less material. Most organic dyes are structurally comprised of donor- π -acceptor (D- π -A) molecules in which electron rich (donor) and electron deficient (acceptor) groups are covalently linked to a π -conjugated bridge or 'backbone' (Figure 4.0).

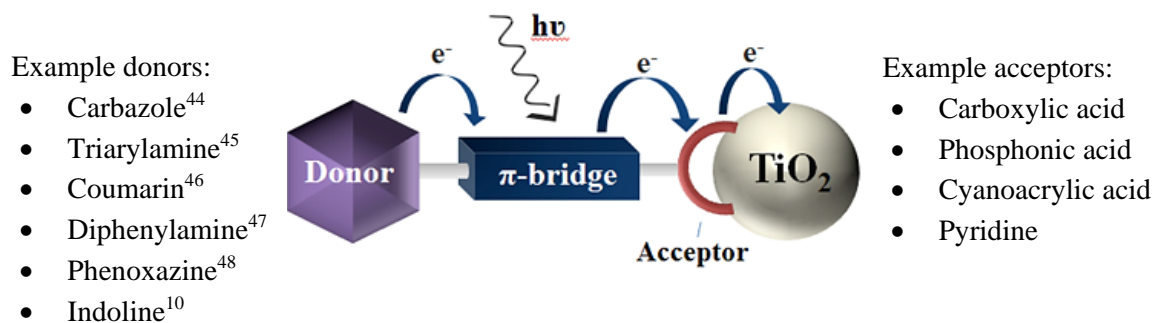


Figure 4.0: Structural schematic of a donor- π -acceptor organic dye showing electron transfer upon excitation. Also listed are examples of typical donor and acceptor groups.

Up on photoexcitation, D- π -A dyes undergo intramolecular charge transfer (ICT) transitions which involve electron transfer from the donor to the acceptor causing a shift in the electron distribution.⁸ The electron is then injected into the TiO₂ conduction band by the acceptor which is bound to the semiconductor surface. In order to create an efficient charge-separated

state, the HOMO must be localised across the donor and π -bridge whereas the LUMO should be localised across the π -bridge and acceptor.⁹ Both donor and acceptor groups can be altered which allows ‘tuning’ of the structural, electronic and spectroscopic properties of the dye. This in turn has led to the development of a wide variety of sensitisers capable of injecting electrons into titania with a high quantum yield.

Here, the photochemistry of six organic D- π -A dyes has been studied to determine their suitability for the co-sensitisation of MAPbBr₃ PSC’s. The dyes were selected on the basis of their commercial availability and their performance as DSSC’s in the literature. Table 9 lists the six dyes considered, their leading literature efficiencies and the preparation conditions used.

Table 9: Current highest reported efficiencies and preparation conditions for the six organic dyes studied in this chapter.

Publication year	Dye	Dye concentration	Dye solvent	Dye time	η (%)
Ito ¹⁰ 2008	D205	0.5 mM (1.0 mM CDCA ^(b))	ACN/TBA ^(c)	4 Hours	9.5
Ito ¹¹ 2006	D149	0.5 mM (1.0 mM CDCA)	ACN/TBA	4 Hours	9.0
Ozawa ¹² 2012	D131	0.14 mM (2.0 mM CDCA)	Isopropanol	20 Hours	4.8
Geiger ¹³ 2009	SQ2	0.1 mM (0.1 mM CDCA)	Ethanol	4 Hours	5.4
Hao ¹⁴ 2016	DB ^(a)	0.025 mM	ACN/TBA	18 Hours	7.3
Ellis ¹⁵ 2013	LEG4	0.2 mM	Ethanol	16 Hours	7.7

(a) Dyenamo blue, (b) chenodeoxycholic acid, (c) acetonitrile/tert-butanol (50:50), (d) room temperature.

For each dye listed, the molecular structure is compared and discussed, with the donor and acceptor units identified and the electron distribution of the HOMO and LUMO level highlighted. Dyes which offer complementary absorbance to MAPbBr₃ perovskite have been identified through measuring their respective absorbance and emission ranges. The molar extinction coefficient of each dye has also been determined as discussed below. The final section of this chapter assesses the performance of two dyes (D205 and SQ2) when prepared as solid state DSSC’s using a range of concentrations.

4.2 Experimental methods

4.2.1 Co-sensitising dyes

Table 10: Systematic name, formula and molecular weight for the six organic dyes studied in this chapter.

Dye name	Systematic name	Formula	Molecular weight (g/mol)
D149	5-[[4-[4-(2,2-Diphenylethenyl)phenyl]-1,2,3-3a,4,8b-hexahydrocyclopent[b]indol-7-yl]methylene]-2-(3-ethyl-4-oxo-2-thioxo-5-thiazolidinylidene)-4-oxo-3-thiazolidineacetic acid.	C ₄₂ H ₃₅ N ₃ O ₄ S ₃	741.94
D205	5-[[4-[4-(2,2-Diphenylethenyl)phenyl]-1,2,3,3a,4,8b-hexahydrocyclopent[b]indol-7-yl]methylene]-2-(3-octyl-4-oxo-2-thioxo-5-thiazolidinylidene)-4-oxo-3-thiazolidineacetic acid.	C ₄₈ H ₄₇ N ₃ O ₄ S ₃	826.10
D131	2-Cyano-3-[4-[4-(2,2-diphenylethenyl)phenyl]-1,2,3,3a,4,8b-hexahydrocyclopent[b]indol-7-yl]-2-propenoic acid.	C ₃₅ H ₂₈ N ₂ O ₂	508.61
SQ2	5-carboxy-2-[[3-[(2,3-dihydro-1,1-dimethyl-3-ethyl-1H-benzo[e]indol-2-ylidene)methyl]-2-hydroxy-4-oxo-2-cyclobuten-1-ylidene]methyl]-3,3-dimethyl-1-octyl-3H-indolium.	C ₄₁ H ₄₆ N ₂ O ₄	630.81
Dyename Blue	(E)-3-(5-(4-(4-(5-(4-(bis(2',4'-dibutoxy-[1,1'-biphenyl]-4-yl)amino)phenyl)thiophen-2-yl)-2,5-bis(2-ethylhexyl)-3,6-dioxo-2,3,5,6-tetrahydropyrrolo[3,4-c]pyrrol-1-yl)phenyl)furan-2-yl)-2-cyanoacrylic acid.	C ₈₆ H ₉₈ N ₄ O ₉ S	1363.81
LEG4	3-{6-[4-[bis(2',4'-dibutylloxybiphenyl-4-yl)amino-]phenyl]-4,4-dihexyl-cyclopenta-[2,1-b:3,4-b']dithiophene-2-yl]-2-cyanoacrylic acid.	C ₇₁ H ₈₄ N ₂ O ₆ S ₂	1125.58

4.2.2 UV-Visible-near Infrared (UV-Vis-NIR) spectroscopy of organic dyes

UV-Vis-NIR spectroscopy of solid state dyed thin-films and dye solutions was performed using a Perkin Elmer Lambda 9 UV–Visible-NIR spectrophotometer. The absorbance was measured over a wavelength range of 350-800 nm at a scan speed of 240 nm/s and a step rate of 1 nm. Any measurements involving thin-films were made prior to the deposition of the hole transport layer.

4.2.3 Steady-state fluorescence of organic dyes

Steady-state fluorescence emission spectra were recorded using a Horiba FluoroMax 4 spectrophotometer. The excitation wavelength and emission wavelength range used for the characterisation of each dye is included in Table 11. For each dye solution, slit widths of 1.5 mm and 0.5 mm were used for the excitation and emission monochromators, respectively.

Table 11: Excitation wavelength (λ_{exc}) and emission scan wavelength range (nm) used for each organic dye when measuring steady state photoluminescence.

Dye	λ_{exc} (nm)	Emission scan wavelength range (nm)
D149	400	520-750
D205	400	520-750
D131	425	450-750
SQ2	580	600-850
Dyename Blue	580	600-850
LEG4	500	550-800

4.2.4 Determination of dye molar extinction coefficients

The molar extinction coefficient (ϵ) of each organic dye was determined using a standard calibration method.¹⁶ For each dye, a dye stock solution with a theoretical concentration of 1 mM was used to prepare a minimum of five standards of increasing dye concentration. Each standard was prepared by diluting the dye stock solution in anhydrous toluene to a final volume of 7 mL. The actual concentration of each dye stock solution was calculated from the mass and molecular weight (M.Wt*) of the powdered dye and the volume of anhydrous toluene used to prepare the solution:

$$\text{Concentration (M)} = \frac{\text{Mass(g)}}{\text{Volume (L)} \times \text{M.Wt * (g/mol)}} \quad (25)$$

From this, the final concentrations (Table 12) of each calibration standard could then be calculated using:

$$C_2 = \frac{C_1 \times V_1}{V_2} \quad (26)$$

Where:

C_1 = actual concentration of stock dye solution

V_1 = volume of stock dye solution used to prepare the calibration standard

C_2 = final concentration of calibration standard

V_2 = final volume of calibration standard

Table 12: Final concentration (in μM) of each calibration standard prepared per dye.

	D149	D205	D131	SQ2	Dyename Blue	LEG4
Dye	2.9	3.0	6.2	0.5	6.0	3.0
concentration	5.9	6.0	12.4	1.0	12.1	6.0
per standard	7.4	7.5	15.6	2.0	15.2	7.6
(μM)	8.8	9.0	18.7	3.0	18.3	9.1
	11.8	12.1	25.1	4.0	24.5	12.2
	14.8	15.1	-	5.0	-	15.3

The absorbance spectrum of each calibration standard was measured using a quartz cuvette with a 1cm path length. A blank standard of toluene was also included and measured as a reference to ensure the background absorbance spectra remained consistent and did not contain any interfering chemistries. The standards for each dye were then measured in ascending concentration and the absorbance response plotted to determine the lambda max (λ_{max}).

Table 13: Determined lambda max λ_{\max} (nm) value for each dye when diluted in toluene.

Dye	λ_{\max} (nm)
D149	533
D205	533
D131	447
SQ2	663
Dyename Blue	582
LEG4	506

A calibration line was then plotted with the absorbance at λ_{\max} against the concentration of the standard (e.g. Figure 4.13). A linear trend line was then fitted and the regression statistics determined using the data analysis regression function in Excel.

The correlation coefficient, r can be used to determine the linearity of a calibration line:

$$r = \frac{\sum_i [(x_i - \bar{x})(y_i - \bar{y})]}{\{[\sum_i (x_i - \bar{x})^2][\sum_i (y_i - \bar{y})^2]\}^{1/2}} \quad (27)$$

Where:

x_i = sum of the x-values

\bar{x} = mean of the x-values

y_i = sum of the y-values

\bar{y} = mean of the y-values

The proximity of r to the value of 1 is indicative of both a positive and good correlation of the data points along the linear trend line. The coefficient of determination, R^2 which is calculated by squaring r describes the proximity of the data points to the linear regression line.¹⁶ The linear relationship between the dye concentration and absorbance response was then considered using the algebraic straight line equation:

$$y = mx + c \quad (28)$$

Where:

c = y-axis intercept

m = gradient of the line

The gradient of the line, m was determined using:

$$m = \frac{\sum_i [(x_i - \bar{x})(y_i - \bar{y})]}{\sum_i [(x_i - \bar{x})^2]} \quad (29)$$

The y-axis intercept, c was determined using:

$$c = \bar{y} - m\bar{x} \quad (30)$$

The absorbance of the dye is proportional to its concentration. Lamberts law states:

$$\ln(I_t/I_0) = bx \quad (31)$$

Where:

I_0 = initial irradiation intensity

I_t = transmitted intensity

b = a constant dependant on the sample

x = path length

Beer then showed that b is proportional to concentration, using \log_{10} this gives:

$$\log_{10}(I_t/I_0) = \log_{10}(I_t/(I_0 - I_{abs})) = \epsilon cx \quad (32)$$

Where:

I_{abs} = Absorbed intensity

ϵ = Molar extinction coefficient

c = concentration

x = path length

Therefore, the gradient of the line, m is equal to the molar extinction coefficient, ϵ of the dye.

4.2.5 Preparation of dye solutions and solid state thin-films

Dye solutions and solid state thin-films were prepared as described in Sections 2.2.1 and 2.2.1, respectively.

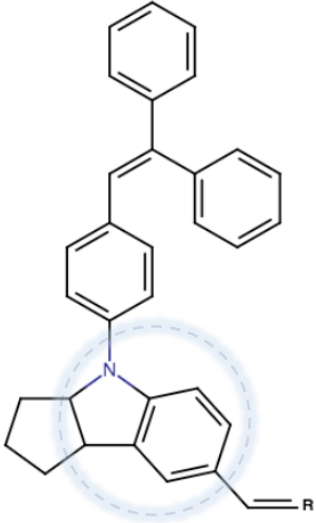
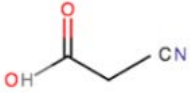
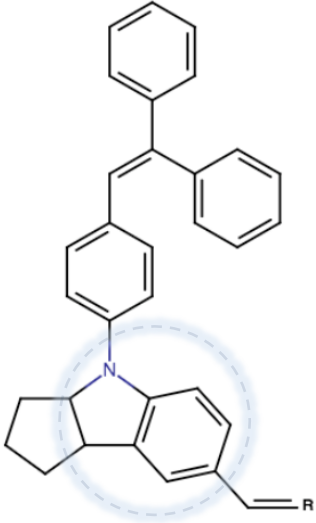
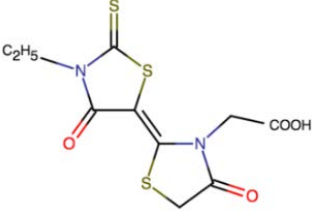
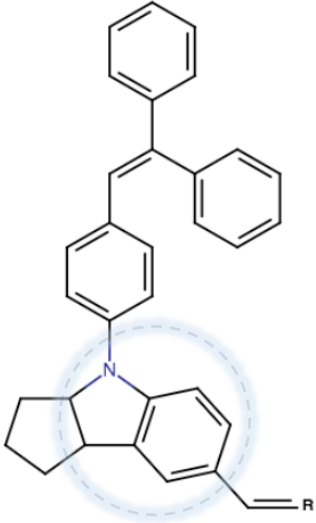
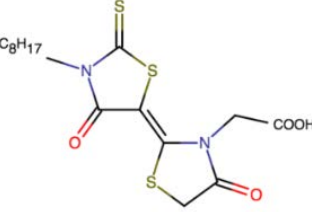
All cell efficiencies reported in the text have been measured under 1 sun conditions (AM 1.5 and 100 mW cm^{-2}) and are the results generated for the forward scan measurement unless otherwise stated.

4.3 Results and discussion

4.3.1 Indoline dyes – D149, D205 and D131

Indoline is a bicyclic compound comprised of a six-membered aromatic ring joined to a five-membered nitrogen containing ring (Table 14).¹⁷ Inherent within core structure of each dye, indoline acts as the electron rich donor due to the lone electron pair on the nitrogen. Indoline dyes were first introduced by Horiuchi, Miura and Uchida in 2003 who reported DSSC efficiencies of 6.1%.¹⁸ A follow-up paper later discussed the addition of rhodanine to the molecular structure which extended the absorbance range and ultimately pioneered the way for novel indoline dye synthesis.¹⁹ The molecular structures of three common indoline dyes, D131, D149 and D205 are shown in Table 14.

Table 14: Core molecular structure of three indoline dyes, D131, D149 and D205 and the R group that gives rise to each dye. The dashed circle highlights the indoline group present within the core structure.

Core structure	R group	Dye ID
		D131
		D149
		D205

Each dye contains a common core structure but differs due to the R-group present on the six-membered ring. At this position, D205 and D149 both contain a rhodanine dimer which acts as the acceptor due to the strong electron withdrawing nature of the amide groups.²⁰ The carboxylate group present in each dye also accepts electrons and anchors the dye to the titania surface. D205 is an amphiphilic derivative of D149 and differs only by the alkyl

group bound to the nitrogen on the terminal rhodanine ring. Replacing the ethyl (C_2H_5) of D149 for an octyl chain (C_8H_{17}) produces D205.^{21,22}

Due to the structural similarities of the dyes, they share very similar delocalisation of the HOMO and LUMO levels (Figure 4.1). The HOMO level is delocalised mainly over the indoline donor whereas the LUMO level is located on the rhodanine and carboxylate acceptor.²³ For both dyes, the delocalisation of the frontier molecular orbitals is of the π - π^* type and therefore the HOMO-LUMO transition to the first excited state is described as a π - π^* ICT.²⁴

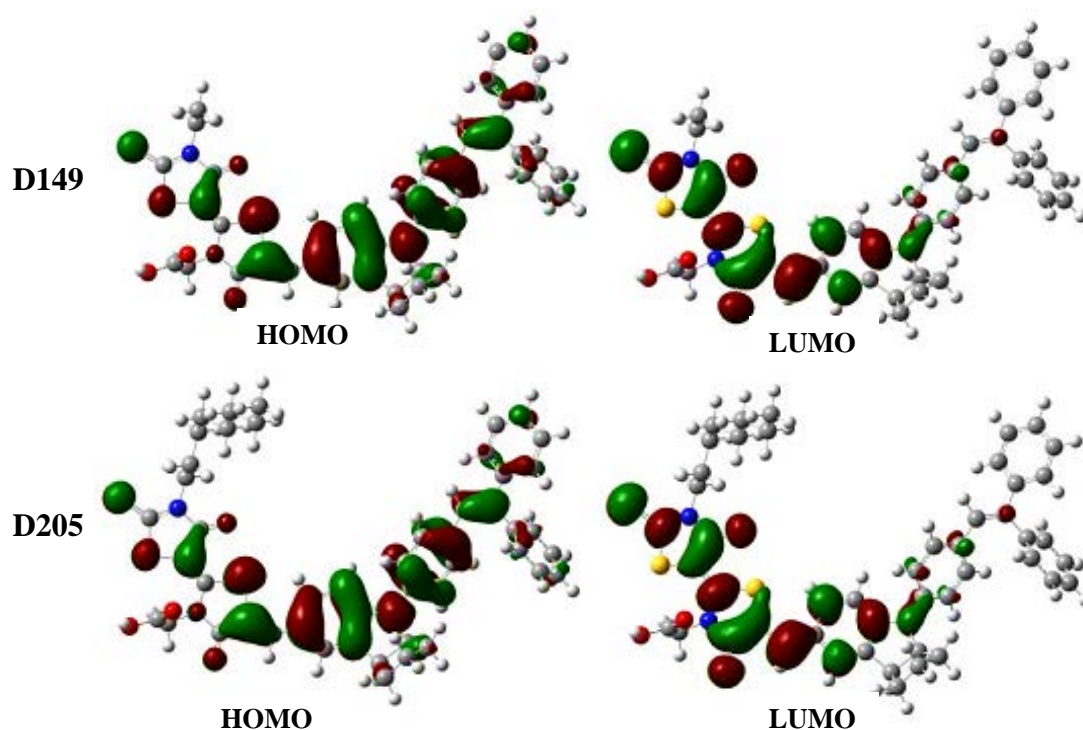


Figure 4.1: Frontier molecular orbitals of D149 (top) and D205 (bottom) dye calculated with Density Function Theory (DFT) at the B3LYP/6-311G(d,p) level in the gas phase.²³



Figure 4.2: Photographed cuvettes containing 1.0 mM concentrations of indoline dyes: D205, D149 and D131, respectively diluted in toluene (left) and photographed mesoporous thin-films sensitised with 1.0 mM of D205, D149 and D131, respectively (right).

When diluted in toluene, the absorbance spectra of D205 and D149 are almost identical and show two distinct bands (Figure 4.3). The higher energy peak at 391 nm results from a combination of ICT and $\pi-\pi^*$ excitation from the HOMO to the LUMO +1.²² The main absorbance peak at 533 nm results from a $\pi-\pi^*$ ICT transition from the HOMO to the LUMO.²⁰

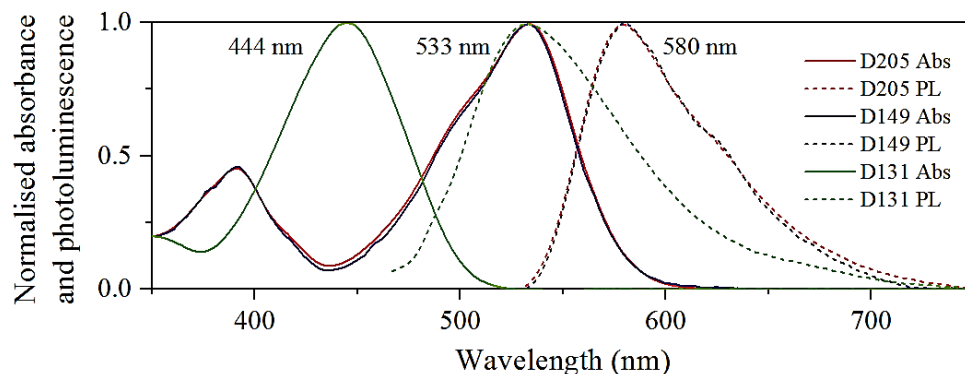


Figure 4.3: Normalised absorbance (Abs) and photoluminescence emission spectra of D205, D149 and D131 dyes diluted in toluene. Inset values represent the wavelength at the peak maximum. (D149 and D205 λ_{exc} = 400 nm, D131 λ_{exc} = 425 nm).

The PL emission spectra of both D149 and D205 (Figure 4.3) are also very similar. When using an excitation wavelength of 400 nm, we see a single broad peak at 580 nm which is attributed to radiative relaxation from the absorbance maximum.²²

The indoline dye D131, is smaller in size (compared to D149 and D205) due to the lack of the rhodanine dimer which is replaced by a cyanoacrylic acid acceptor (Table 14). In line with the other indoline dyes, the HOMO and LUMO of D131 are of $\pi-\pi^*$ type. The HOMO is delocalised on the indoline donor unit whereas the LUMO is situated on the cyanoacrylic acid acceptor.²⁴

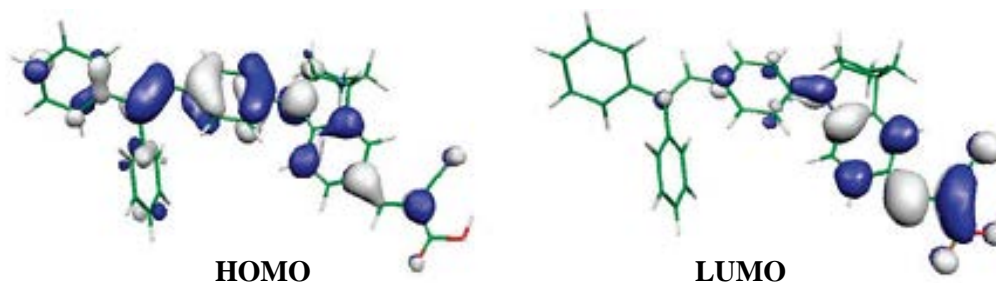


Figure 4.4: Frontier molecular orbitals of D131 dye calculated with DFT at the B3LYP/6-311G(d,p) level in the gas phase.²⁴

Due to its smaller size, the π -conjugation system of D131 has reduced spatial extent causing a narrower absorbance range in the visible. As a result, the absorbance spectra of D131 (Figure 4.3) is blue shifted and shows a distinct band at 444 nm arising from the HOMO to LUMO ICT π - π^* transition.^{20,25} The PL emission spectra of D131 shows a single broad peak at 533 nm when using an excitation wavelength of 425 nm (Figure 4.3).

4.3.2 Squaraine dye - SQ2

Squaraine dyes contain a characteristic four-membered squaraine ring (Figure 4.5) and are often referred to as symmetrical or unsymmetrical depending on the surrounding units. For symmetrical squaraine dyes, the squaric ring acts as the electron acceptor and is sandwiched between two identical electron donors giving rise to a donor-acceptor-donor (D-A-D) configuration.²⁶ Unsymmetrical squaraine dyes tend to have non-identical surrounding units and adopt a donor- π -spacer-acceptor configuration. SQ2 is an unsymmetrical blue/green squaraine dye comprised of a benzo[e]indolium electron donor connected to a squaraine ring attached to an indoline unit with a carboxylic acid anchor group.²⁷

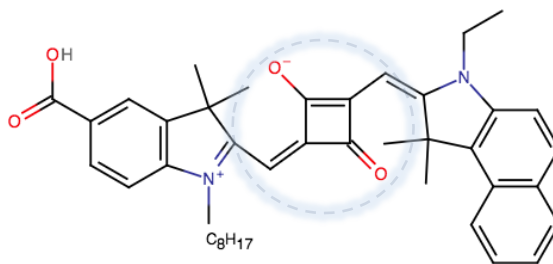


Figure 4.5: Chemical structure of the unsymmetrical SQ2 dye comprised of a benzo[e]indolium donor connected to a squaraine ring (circled) attached to an indoline unit with a carboxylic acid anchor group.

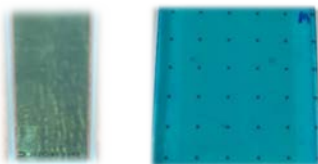


Figure 4.6: Photographed cuvette containing 1.0 mM of squaraine dye SQ2 diluted in toluene (left) and a photographed mesoporous thin-film sensitised with 1.0 mM of SQ2 (right).

SQ2 has a planar structure where the carboxylic acid, indoline and squaraine core are fully conjugated across the π orbitals of the C=C moieties creating an extended π -framework.^{26,28}

The HOMO and LUMO (Figure 4.7) are both delocalised throughout the dye structure and are of the π - π^* type, respectively giving rise to a high extinction coefficient.²⁹

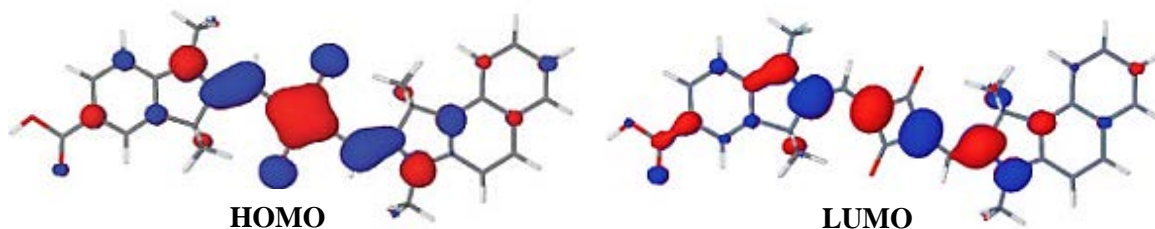


Figure 4.7: Frontier molecular orbitals of SQ2 dye calculated with DFT at the B3LYP/6-311G(d,p) level in the gas phase.¹³

Squaraine dyes notably demonstrate strong visible absorption in the deep red to NIR region which is an attractive property when compared to most dyes which typically absorb below 600 nm. Figure 4.8 shows the normalised absorbance and emission spectra measured for SQ2 dye diluted in toluene.

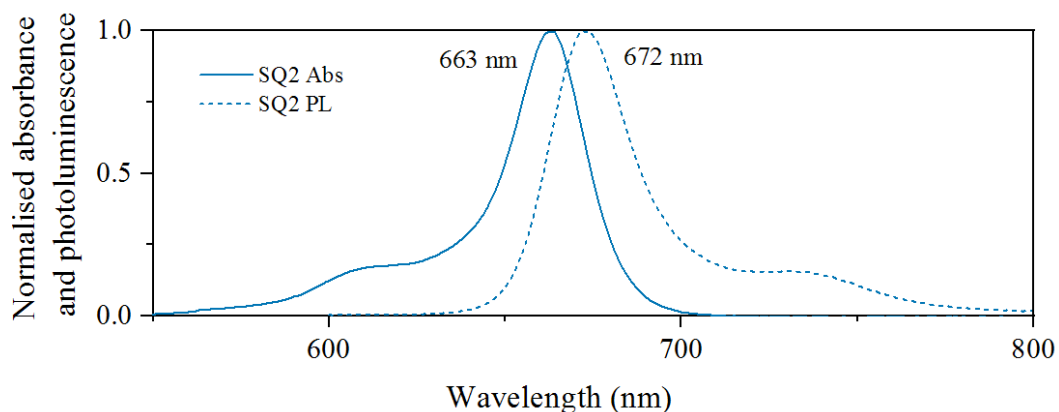


Figure 4.8: Normalised absorbance (Abs) and photoluminescence emission spectra of SQ2 dye diluted in toluene. Inset values represent the wavelength at the peak maximum ($\lambda_{exc}=580$ nm).

The absorbance spectra shows a single and strong band in the red region with an absorption maximum at 663 nm. This peak corresponds to a π - π^* ICT transition between the HOMO and LUMO level.³⁰ Although not seen here, other researchers have also reported HOMO-LUMO+1 transitions where the LUMO+1 is localised to the carboxylic acid acceptor.²⁹ The lower intensity peak at 608 nm suggests dye aggregation which can lead to self-quenching and reduced photoconductivity in DSSC's.³¹ The PL emission spectra of SQ2 shows an emission maxima at 672 nm when excited at 580 nm.

4.3.3 Diketopyrrolopyrrole dye - Dyenamo blue

Diketopyrrolopyrrole (DPP) dyes contain a 2,5-dihydropyrrolo[3,4-c]pyrrol-1,4-dione chromophoric core unit which is a planar bicyclic structure consisting of two condensed γ -lactam rings. The amide group of each γ -lactam provides the strong electron withdrawing properties required for a good electron acceptor.³² A linear alkyl chain is bound to each lactam nitrogen to increase the solubility of the DPP core in organic solvents.³³

The first DPP dye was discovered unintentionally in 1974 by Farnum *et al.* when attempting to synthesise 2-azetionones.³⁴ Since then, several derivatives have been developed and are widely used as efficient charge transporters with high extinction coefficients.^{33,35} Dyenamo blue is a novel blue DPP dye consisting of a triphenylamine donor and a furanylecyanoacrylic acid acceptor / anchor (Figure 4.9). The chromophoric DPP core acts as the π -bridge between the donor and acceptor units.³⁶

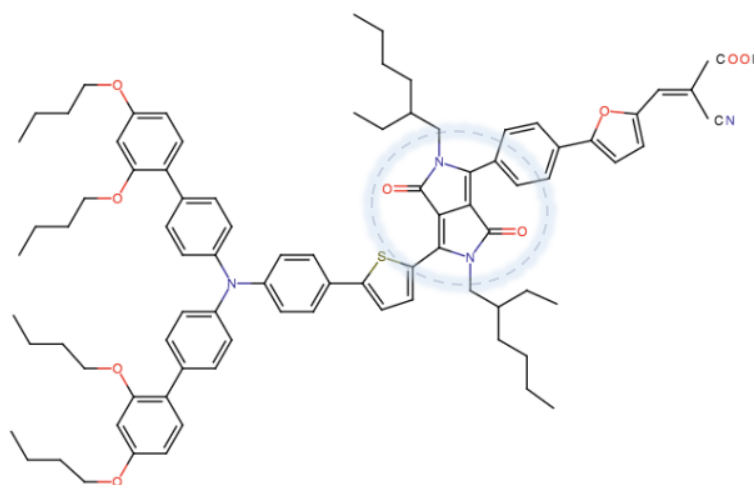


Figure 4.9: Chemical structure of dyenamo blue dye comprised of a triphenylamine donor bound *via* thiophene to the 2,5-dihydropyrrolo[3,4-c]pyrrol-1,4-dione unit (circled) connected to the furanylecyanoacrylic acid acceptor / anchor.

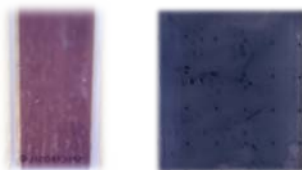


Figure 4.10: Photographed cuvette containing 1.0 mM of DPP dye Dyenamo blue diluted in toluene (left) and a photographed mesoporous thin-film sensitised with 1.0 mM of DPP (right).

When considering the frontier molecular orbitals of Dyenamo blue (Figure 4.11), the HOMO is mainly delocalised over the triphenylamine donor and DPP unit whilst the LUMO is delocalised over the phenyl ring, DPP core and the furanicyanoacrylic acceptor.^{14,37}

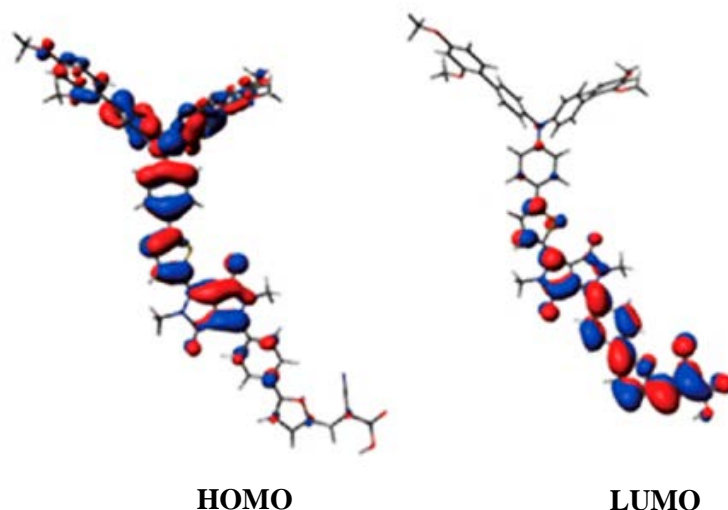


Figure 4.11: Frontier molecular orbitals of dyenamo blue dye (with shortened alkyl chains) calculated with DFT at the B3LYP/6-311G(d,p) level in the gas phase.¹⁴

The absorbance spectra of Dyenamo blue in toluene (Figure 4.12) shows two prominent bands of similar intensity but at different energies, a higher energy band at 339 nm and a lower energy band at 584 nm. The higher energy band in the UV region is attributed to transitions between the HOMO and higher energy states i.e. S_2 / LUMO+1.^{32,38} Whereas the lower energy band at 584 nm results from π - π^* / HOMO to LUMO ICT transitions.³²

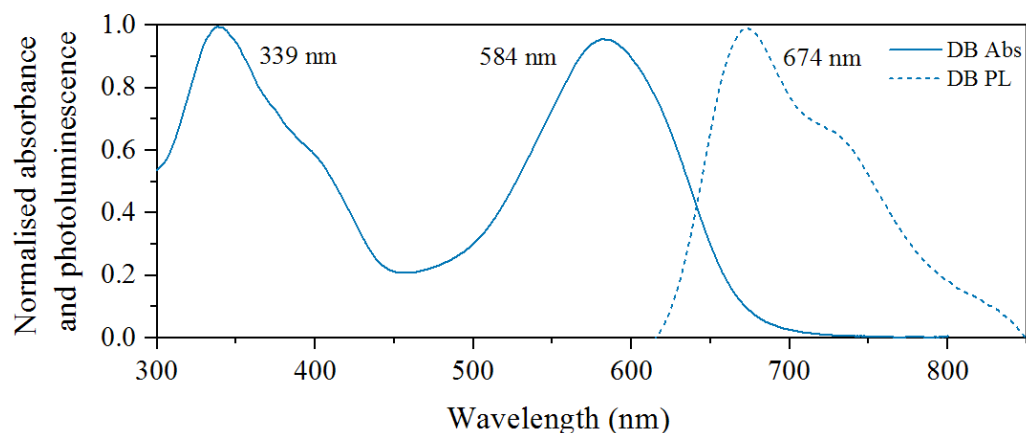


Figure 4.12: Normalised absorbance (Abs) and photoluminescence emission spectra of dyenamo blue (DB) dye diluted in toluene. Inset values represent the wavelength at the peak maximum (λ_{exc} = 580 nm).

The absorbance range of Dyenamo blue is also quite broad beginning in the UV region and tailing off at 700 nm which highlights the capabilities of this dye to absorb photons over a broad range and almost into the NIR region.

4.3.4 Triphenylamine dye - LEG4

LEG4 is a relatively new triphenylamine based dye first synthesised in 2013 by Gabrielsson *et al.* who modified the structure of the organic dye D35.³⁹ D35 consists of a triphenylamine donor attached to a thiophenyl π -linker and a cyanoacrylic acceptor/anchor. The triphenylamine group is an attractive electron donor due to its ability to slow electron recombination.⁴⁰ However, as an overall dye, D35 has a narrow absorption range limiting its light harvesting in the visible. To overcome this, Gabrielsson *et al.* modified the triphenylamine donor of D35 to include a 4,4-dialkyl-4H-cyclopenta[2,1-b:3,4-b']dithiophene (CPDT) linker which created LEG4, a new dye with extended absorption in the visible (Figure 4.13).³⁹

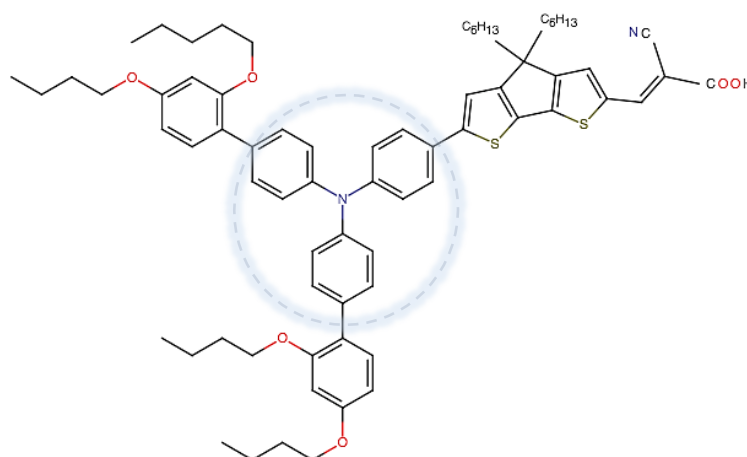


Figure 4.13: Chemical structure of LEG4 dye comprised of a triphenylamine donor (circled), a 4,4-dialkyl-4H-cyclopenta[2,1-b:3,4-b']dithiophene (CPDT) linker and a cyanoacrylic acid anchor/acceptor. The triphenylamine donor contains additional phenyl groups in the para-position functionalised with *p,o*-butoxy groups.

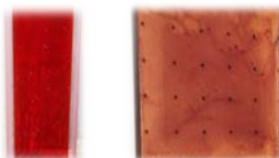


Figure 4.14: Photographed cuvette containing 1.0 mM of triphenylamine dye LEG4 diluted in toluene (left) and a photographed mesoporous thin-film sensitised with 1.0 mM of LEG4 (right).

Figure 4.15 shows the frontier molecular orbitals of LEG4, here we see the HOMO is located on the triphenylamine donor (namely the nitrogen) and partially delocalised over the CPDT linker. The LUMO is mainly located on the cyanoacrylic acceptor and CPDT linker.³⁹

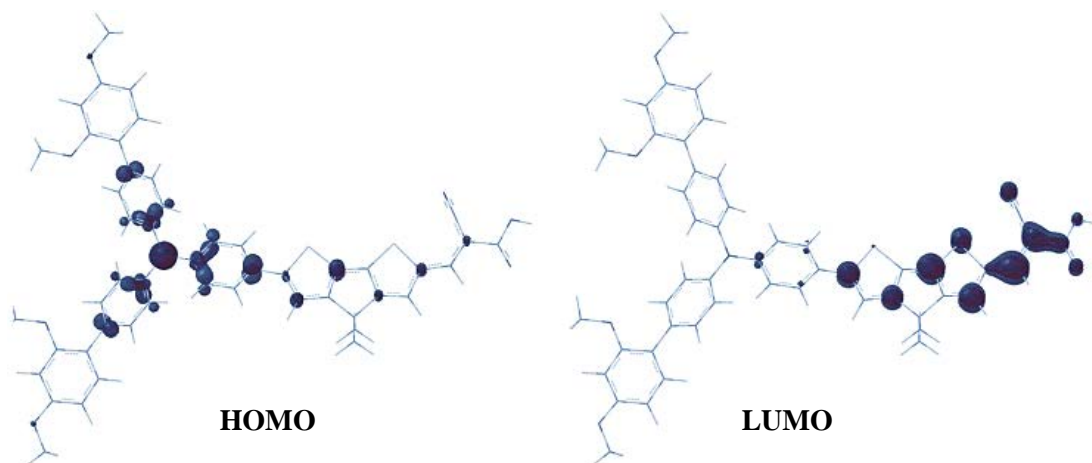


Figure 4.15: Frontier molecular orbitals of LEG4 dye calculated with DFT at the B3LYP/6-311G(d,p) level in the gas phase.³⁹

The absorbance spectra of LEG4 (Figure 4.16) shows dual band absorption in the blue-green-yellow region with the absorbance maximum at 507 nm corresponding to an ICT π - π^* transition between the HOMO and LUMO.³⁹

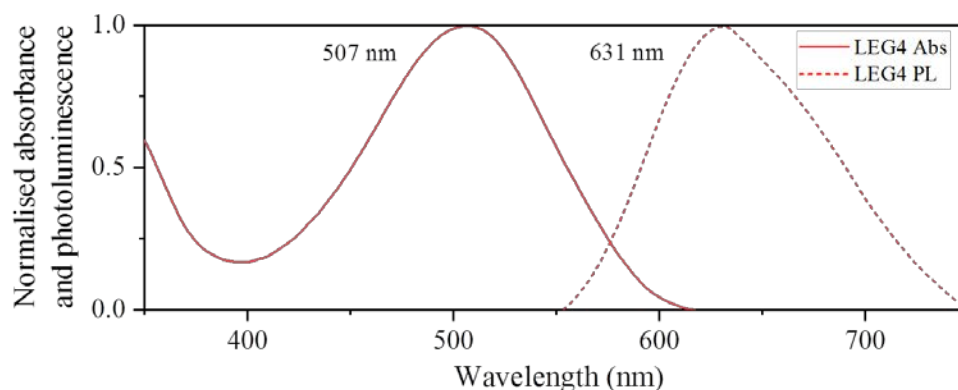


Figure 4.16: Normalised absorbance (Abs) and photoluminescence emission spectra of LEG4 dye diluted in toluene. Inset values represent the wavelength at the peak maximum (λ_{exc} = 500 nm).

A second higher energy peak in the UV region results from a second transition from HOMO-1 to LUMO.³⁹ When excited with 500 nm light, the PL emission spectra of LEG4 dye shows a peak maximum of 631 nm.

4.3.5 Comparison of dyes for co-sensitisation

An important objective of this chapter was to determine and compare the optical characteristics of each dye, in particular; the wavelength of maximum absorbance and the extinction coefficient. Dyes with a higher extinction coefficient could potentially show better performance when deposited as a thin layer in the thin-film format.

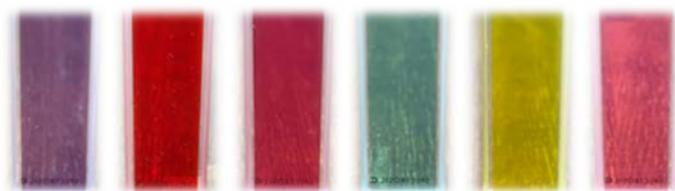


Figure 4.17: Photographed cuvettes showing a colour comparison of the six organic dyes (1.0 mM) diluted in toluene, from left to right: Dyenamo blue, LEG4, D205, SQ2, D131 and D149.

As discussed in the previous chapter, the absorbance range of MAPbBr₃ perovskite begins in the UV region and tails off in the blue region ending at approximately 520 nm. Due to the shorter absorbance range of MAPbBr₃, a dye which absorbs in the red to NIR region would potentially offer the best opportunity to extend the absorbance response and ultimately the light harvesting range when implemented in a co-sensitised system. Therefore, it was important to determine which dyes offer complementary absorption to MAPbBr₃ perovskite. Table 15 lists the optical characteristics of the six dyes when diluted in toluene.

Table 15: Optical characteristics of the six organic dyes diluted in toluene solution.

Dye	abs λ_{\max} (nm) ^(a)	ϵ_{\max} (M ⁻¹ cm ⁻¹) ^(b)	ems λ_{\max} (nm) ^(c)	λ_s (nm) ^(d)	abs λ_{onset} (nm) ^(e)	E_g (eV) ^(f)
D149	533	56782	580	47	575	2.15
D205	533	64701	580	47	575	2.15
D131	444	47326	533	89	499	2.48
SQ2	663	233290	672	9	683	1.81
DB	584	48192	674	90	672	1.84
LEG4	507	89333	631	124	591	2.09

(a) Absorbance maximum, (b) molar absorption coefficient determined from a calibration line, (c) emission maximum, (d) Stokes shift $\lambda_s = \text{abs } \lambda_{\max} - \text{ems } \lambda_{\max}$, (e) onset absorbance edge, (f) optical bandgap (eV) = $hc/\text{abs } \lambda_{\text{onset}} = 1239.83/\text{abs } \lambda_{\text{onset}}$.

When considering the indoline dyes, due to structural similarities, D149 and D205 have the same abs λ_{\max} (533 nm) which would offer slight extension of the MAPbBr₃ absorption

range. The abs λ_{\max} of D131 (444 nm) however, falls within the MAPbBr₃ absorption range and therefore would fail to extend the range in a co-sensitised system. This is also the case for LEG4 where the maximum absorbance of this dye also falls below the band edge of MAPbBr₃. Overall, the largest extension of the MAPbBr₃ absorbance range could potentially be achieved using DB and SQ2 which have an abs λ_{\max} of 584 nm and 663 nm, respectively. SQ2 has a fairly narrow absorption range in the visible but does absorb at longer wavelengths when compared to most dyes and would therefore; potentially offer the best complementary absorbance to MAPbBr₃. Dyenamo blue (DB) also absorbs in the orange to red region but has a significantly lower extinction coefficient compared to SQ2.



Figure 4.18: Photographed mesoporous thin-films sensitised with, from left to right: Dyenamo blue, LEG4, D205, SQ2, D131 and D149. Each thin-film is prepared using a 1.0 mM dye concentration.

The extinction coefficient of each dye was measured and calculated using the method discussed in Section 4.2.4. As an example, Figure 4.19 shows the calibration line used to calculate the extinction coefficient for SQ2 dye, where the extinction coefficient is equivalent to the gradient of the line, m multiplied by 1000.

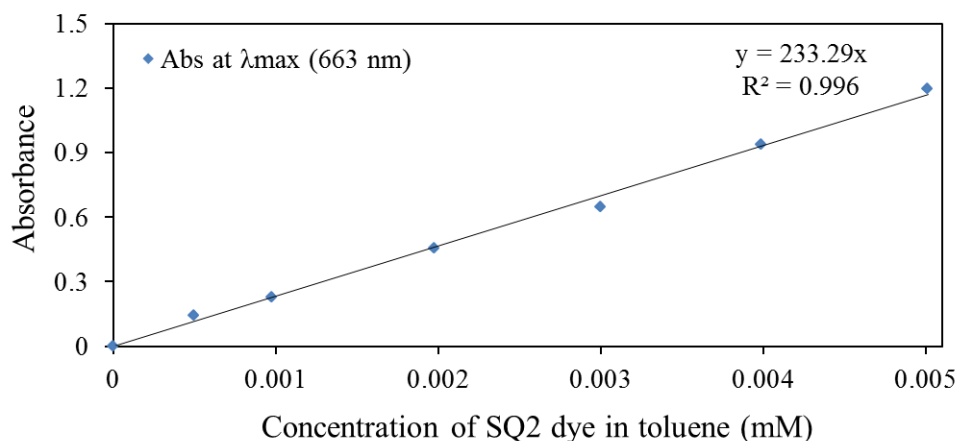


Figure 4.19: Calibration line of absorbance vs concentration for seven SQ2 calibration standards (in toluene). Also included is the straight line equation: $y = mx + c$ with the value of c (0), m (233.29) and the coefficient of determination value, R^2 (0.996).

The extinction coefficients of the six dyes, listed in Table 15 decrease in following order: SQ2>LEG4>D205>D149>DB>D131. When comparing the calculated values, the extinction coefficient of SQ2 ($2.3 \times 10^5 \text{ M}^{-1}\text{cm}^{-1}$) is considerably higher than the other dyes. LEG4 has the second highest extinction coefficient but, as mentioned above, does not offer complementary absorbance to MAPbBr₃ perovskite. The indoline dye, D205 has a fairly high extinction coefficient ($6.5 \times 10^4 \text{ M}^{-1}\text{cm}^{-1}$) and could also offer a slight extension of the MAPbBr₃ absorbance range.

4.3.6 Solid state DSSC performance

Solid state DSSC's were prepared using various concentrations of D205 and SQ2 to determine the performance and individual photocurrent contribution of each dye when implemented as standalone sensitisers prior to co-sensitisation. It was also important to assess if the dyes were capable of working in the thin-film format when using a ~200 nm mesoporous titania layer as opposed to the much thicker titania layer (~6 μm) typically used in DSSC's.

Figure 4.20 shows photographed solid state D205 and SQ2 thin-films prepared with increasing dye concentrations. For both dyes, there is an evident increase of colour intensity with concentration.



Figure 4.20: Photographed sections of thin-films of solid state D205 (pink films) and SQ2 (aqua films) when prepared with increasing concentration of dye. Each dye concentration (in mM) is listed above the image.

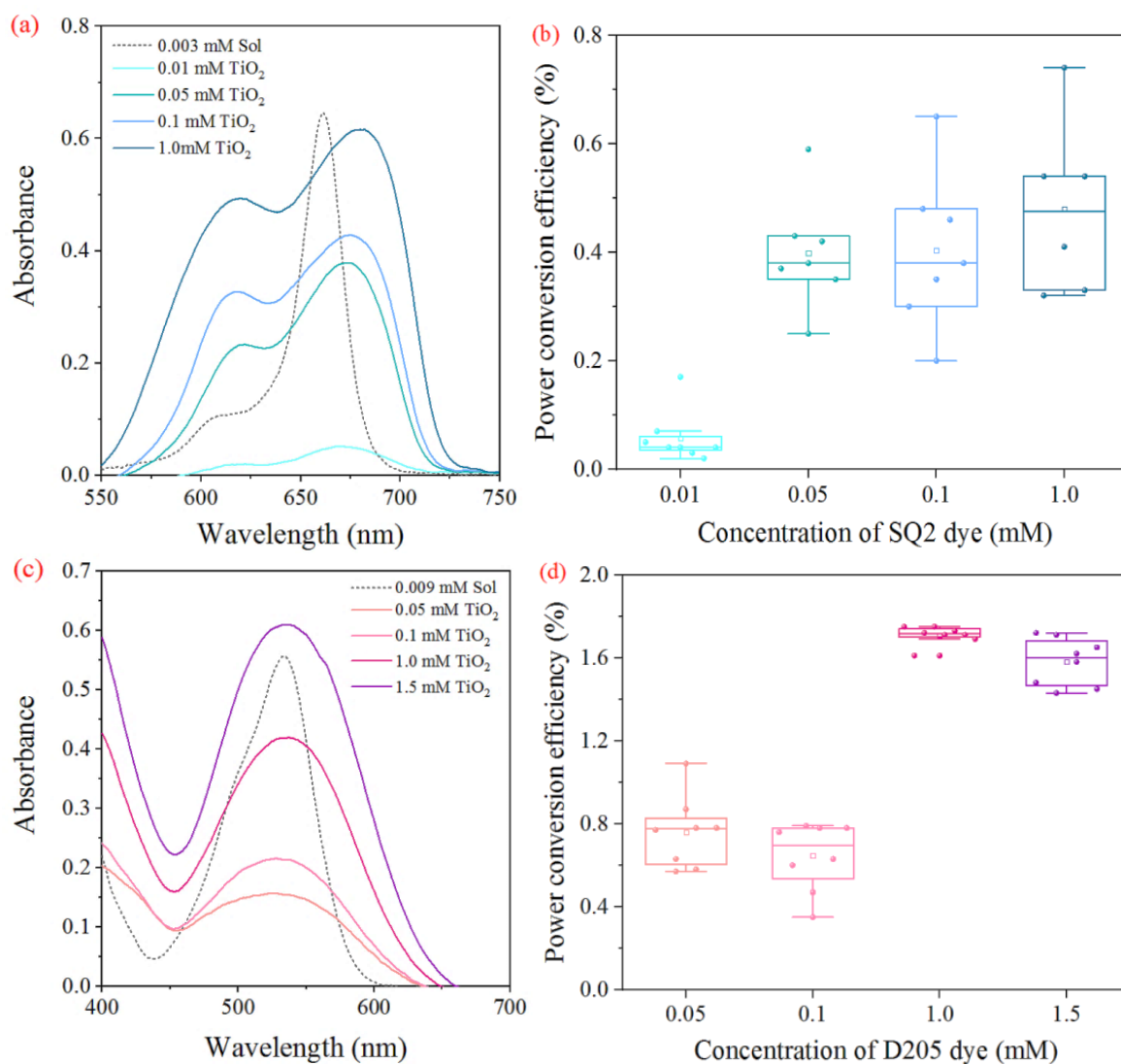


Figure 4.21: (a) Absorbance spectra and (b) box plots of PCE (%) for solid state SQ2 thin-films and devices, respectively manufactured with increasing concentration of dye. (c) Absorbance spectra and (d) box plots of PCE (%) for solid state D205 thin-films and devices, respectively manufactured with increasing concentration of dye. Each box plot is generated from a single device composed of 8 pixels.

Figure 4.21(a) and (c) show the measured absorbance of the D205 and SQ2 films, respectively. In line with the visual colour increase, the absorbance of each film also increases with dye concentration suggesting more dye is bound to the semiconductor. These results also suggest, at lower concentrations, the film is not fully saturated despite the use of a much thinner mesoporous layer.

Also included in Figure 4.21 (a) and (c) is the absorbance of each dye when measured in toluene solution (grey dashed line). When comparing this absorbance with the solid state

spectra we can observe the latter shows substantial band broadening and shifting to a lower energy. Red-shifting of the abs λ_{\max} (as seen here) can often result from aggregation of dye molecules which can lead to self-quenching and losses in photocurrent.⁴¹ Here, we also see more pronounced band broadening for the higher dye concentrations which suggests increased aggregation with concentration. Broadening and shifting to lower energies can also indicate strong interaction between the dye and titania where the polar semiconductor surface enhances delocalisation of the π -framework.²² Photoexcitation shifts the electron density toward the anchoring group which causes strong coupling between the excited state and the titania surface followed by directional electron injection into the semiconductor conduction band.^{13,42}

In order to confirm the successful injection and collection of electrons under photoexcitation, the solid state thin-films were prepared as full cells and the performance measured. For both dyes, Figures 4.21 (b) and (d) show an increase in average efficiency with dye concentration. Higher efficiencies and lower variation are observed for cells prepared using D205 where a hero pixel efficiency of 1.8% was recorded when using a 1.0 mM dye solution.

In contrast, cells prepared using SQ2 failed to achieve an efficiency $>1\%$. Despite having a higher extinction coefficient, SQ2 has narrower absorbance compared to D205 which limits its light harvesting range. Squaraine dyes are also widely known to suffer from aggregation, poor electron injection and low stability which ultimately affect the cell efficiency.¹⁴ Despite this, SQ2 has previously shown to be beneficial in a co-sensitised system where an efficiency of 7.8% was achieved using SQ2 alongside a ruthenium dye (Z907) whereas the individual sensitiser cells achieved 1.4% and 5.1% respectively.⁴³

Table 16 lists the performance values of the solid state cells. The V_{oc} and FF values for the SQ2 cells show no discernible trend with dye concentration whereas for D205 there are some increases in these values with concentration. For both dyes however, the main increase in efficiency can be attributed to increased J_{sc} , where the higher dye concentrations generate the largest photocurrents.

Table 16: Average photovoltaic performance values and standard deviation (σ) for solid state D205 and SQ2 cells manufactured with increasing concentration of dye. Also included are the EQE generated short-circuit current values (EQE J_{sc}) for the hero pixel of each system.

Dye	Dye conc (mM)	EQE J_{sc} (mA cm ⁻²)	$\bar{x} J_{sc}$ (mA cm ⁻²)	$J_{sc} \sigma$	$\bar{x} V_{oc}$ (V)	$V_{oc} \sigma$	$\bar{x} FF$	$FF \sigma$	$\bar{x} PCE$ (%)	$PCE \sigma$
D205	0.05	2.8	1.9	0.29	0.77	0.02	52	5.34	0.8	0.17
	0.1	2.3	1.7	0.19	0.77	0.09	49	10.13	0.6	0.65
	1.0	3.7	2.9	0.04	0.84	0.01	69	1.94	1.7	0.04
	1.5	3.6	2.8	0.28	0.83	0.01	69	4.13	1.6	0.11
SQ2	0.01	0.60	0.31	0.13	0.5	0.13	31	5.36	0.06	0.05
	0.05	1.76	1.19	0.47	0.7	0.03	52	7.98	0.4	0.10
	0.1	2.32	1.29	0.23	0.7	0.13	47	13.02	0.4	0.14
	1.0	2.98	1.38	0.16	0.7	0.05	49	10.75	0.5	0.16

In theory, when using a higher dye concentration there would be more dye bound to the titania surface and therefore increased levels of charge generation, injection and extraction. This is supported by the aforementioned increase in the absorbance response with dye concentration. However, the aim here is to simply find a balance between achieving a dye monolayer whilst avoiding dye aggregation on surface. The photocurrent contributions of the dyes were studied further using EQE measurements.

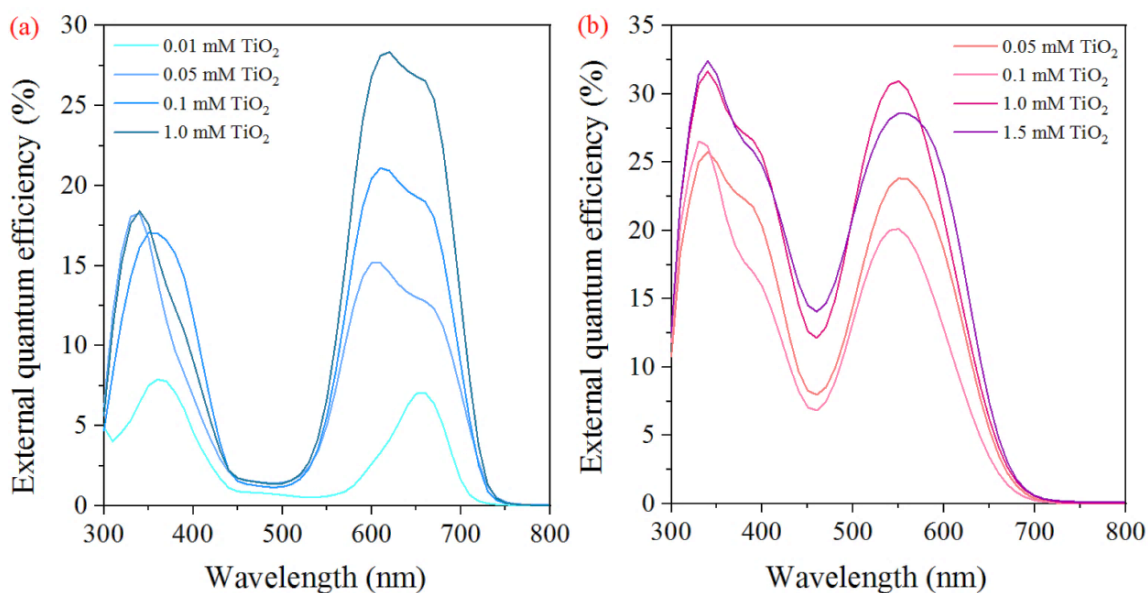


Figure 4.22: Measured EQE spectral response for the hero pixel of solid state SQ2 (a) and D205 (b) cells prepared with increasing concentration of dye.

Figure 4.22 (a) and (b) show the EQE response for the hero pixels of each concentration for SQ2 and D205, respectively. The EQE response of SQ2 shows two peaks, one of which

reaches maximum at 617 nm before sharply decreasing at 661 nm. Similarly for D205, there is a dual peak response however; each peak is of similar intensity reaching maximum at 340 and 549 nm before a sharp decline in signal at approximately 600 nm.

Also listed in Table 16 are the EQE generated short-circuit current values (EQE J_{sc} (mA cm⁻²)). When considering these values and Figure 4.22, there is a general increase in photocurrent with concentration for both SQ2 and D205 cells which confirms increased charge injection with concentration. The largest response for both dyes was achieved using a concentration of 1.0 Mm. At this concentration, both dyes demonstrate similar signal intensity and a photocurrent contribution of about 25-33%.

4.4 Conclusions

The optical properties of six organic D- π -A dyes were characterised and compared to determine their suitability as co-sensitisers to MAPbBr₃ perovskite. Evaluation of the absorbance ranges and molar extinction coefficients revealed the red indoline dye, D205 and the blue-green squaraine dye, SQ2 could potentially offer the highest complementary absorbance when used to co-sensitise MAPbBr₃ perovskite. Solid state DSSC's prepared with D205 and SQ2 proved the dyes capable of working in a thin-film format where the highest efficiencies (1.7% and 0.5%, respectively) were achieved using a 1.0 mM dye concentration. At this concentration, both dyes demonstrated similar individual photocurrent contributions of ~25-33%.

4.5 References

1. O'Regan, B. & Grätzel, M. A low-cost, high-efficiency solar cell based on dye-sensitized colloidal TiO₂ films. *Nature* **353**, pp. 737–740 (1991).
2. Kakiage, K. *et al.* An achievement of over 12 percent efficiency in an organic dye-sensitized solar cell. *Chem. Commun.* **50**, pp. 6379–6381 (2014).
3. Nazeeruddin, M. K. *et al.* Conversion of light to electricity by cis-X₂bis(2,2'-bipyridyl-4,4'-dicarboxylate)ruthenium(II) charge-transfer sensitizers (X = Cl-, Br-, I-, CN-, and SCN-) on nanocrystalline titanium dioxide electrodes. *J. Am. Chem. Soc.* **115**, pp. 6382–6390 (1993).
4. Zakeeruddin, S. M. *et al.* Molecular Engineering of Photosensitizers for Nanocrystalline Solar Cells: Synthesis and Characterization of Ru Dyes Based on Phosphonated Terpyridines. *Inorg. Chem.* **36**, pp. 5937–5946 (1997).
5. Nazeeruddin, M. K. *et al.* Acid–Base Equilibria of (2,2'-Bipyridyl-4,4'-dicarboxylic acid)ruthenium(II) Complexes and the Effect of Protonation on Charge-Transfer Sensitization of Nanocrystalline Titania. *Inorg. Chem.* **38**, pp. 6298–6305 (1999).
6. Polo, A. S., Itokazu, M. K. & Murakami Iha, N. Y. Metal complex sensitizers in dye-sensitized solar cells. *Coordination Chemistry Reviews* **248**, pp. 1343–1361 (2004).
7. Lee, C. P., Li, C. T. & Ho, K. C. Use of organic materials in dye-sensitized solar cells. *Mater. Today* **20**, pp. 267–283 (2017).
8. Gao, P., Gratzel, M. & Nazeeruddin, M. D. K. CHAPTER 6 Chemistry of Sensitizers for Dye-sensitized Solar Cells, in *Advanced Concepts in Photovoltaics*. Energy and Environment Series. Royal Society of Chemistry, London, UK (2014). Available from: doi:10.1039/9781849739955-00186
9. Bahng, H. W., Hagfeldt, A. & Moser, J. E. Lateral intermolecular electronic interactions of diketopyrrolopyrrole D- π -A solar dye sensitizers adsorbed on mesoporous alumina. *J. Phys. Chem. C* **122**, pp. 19348–19358 (2018).
10. Ito, S. *et al.* High-conversion-efficiency organic dye-sensitized solar cells with a novel indoline dye. *Chem. Commun.* **41**, pp. 5194–5196 (2008).
11. Ito, S. *et al.* High-efficiency organic-dye-sensitized solar cells controlled by nanocrystalline-TiO₂ electrode thickness. *Adv. Mater.* **18**, pp. 1202–1205 (2006).
12. Ozawa, H., Shimizu, R. & Arakawa, H. Significant improvement in the conversion efficiency of black-dye-based dye-sensitized solar cells by cosensitization with organic dye. *RSC Adv.* **2**, pp. 3198–3200 (2012).
13. Geiger, T. *et al.* Molecular design of unsymmetrical squaraine dyes for high efficiency conversion of low energy photons into electrons using TiO₂

- nanocrystalline films. *Adv. Funct. Mater.* **19**, pp. 2720–2727 (2009).
14. Hao, Y. *et al.* Novel Blue Organic Dye for Dye-Sensitized Solar Cells Achieving High Efficiency in Cobalt-Based Electrolytes and by Co-Sensitization. *ACS Appl. Mater. Interfaces* **8**, pp. 32797–32804 (2016).
 15. Ellis, H. *et al.* Linker unit modification of triphenylamine-based organic dyes for efficient cobalt mediated dye-sensitized solar cells. *J. Phys. Chem. C* **41**, pp. 21029–21036 (2013).
 16. Miller, J. & Miller, J. *Statistics and Chemometrics for Analytical Chemistry* (4th ed.). *Stat. Chemom. Anal. Chem.* Prentice Hall, Harlow, UK (2000).
 17. Schwarz, M. *et al.* Model Catalytic Studies of Novel Liquid Organic Hydrogen Carriers: Indole, Indoline and Octahydroindole on Pt(111). *Chem. - A Eur. J.* **23**, pp. 14806–14818 (2017).
 18. Horiuchi, T., Miura, H. & Uchida, S. Highly efficient metal-free organic dyes for dye-sensitized solar cells. *J. Photochem. Photobiol. A Chem.* **30**, pp. 3036–3037 (2004).
 19. Horiuchi, T., Miura, H., Sumioka, K. & Uchida, S. High efficiency of dye-sensitized solar cells based on metal-free indoline dyes. *J. Am. Chem. Soc.* **126**, pp. 12218–12219 (2004).
 20. Magne, C., Urien, M. & Pauporté, T. Enhancement of photovoltaic performances in dye-sensitized solar cells by co-sensitization with metal-free organic dyes. *RSC Adv.* **3**, pp. 6315–6318 (2013).
 21. Kuang, D., Uchida, S., Humphry-Baker, R., Zakeeruddin, S. M. & Grätzel, M. Organic dye-sensitized ionic liquid based solar cells: Remarkable enhancement in performance through molecular design of indoline sensitizers. *Angew. Chemie - Int. Ed.* **47**, pp. 1923–1927 (2008).
 22. Cheng, H.-M. & Hsieh, W.-F. Electron transfer properties of organic dye-sensitized solar cells based on indoline sensitizers with ZnO nanoparticles. *Nanotechnology* **21**, 485202 (2010).
 23. Lambert, C. *et al.* Characterization of high-performance organic dyes for dye-sensitized solar cell: A DFT/TDDFT study. *Can. J. Chem.* **94**, 12 (2016).
 24. Le Bahers, T., Pauporté, T., Scalmani, G., Adamo, C. & Ciofini, I. A TD-DFT investigation of ground and excited state properties in indoline dyes used for dye-sensitized solar cells. *Phys. Chem. Chem. Phys.* **11**, pp. 11276–11284 (2009).
 25. Madili, N., Pogrebnoi, A. & Pogrebnyaya, T. Theoretical Design of Complex Molecule via Combination of Natural Lawsone and Synthetic Indoline D131 Dyes for Dye Sensitized Solar Cells Application. *Comput. Chem.* **6**, 4 (2018).

26. Sreejith, S., Carol, P., Chithra, P. & Ajayaghosh, A. Squaraine dyes: A mine of molecular materials. *J. Mater. Chem.* **18**, pp. 264–274 (2008).
27. Tsai, H. H. G., Tan, C. J. & Tseng, W. H. Electron transfer of squaraine-derived dyes adsorbed on TiO₂ clusters in dye-sensitized solar cells: A density functional theory investigation. *J. Phys. Chem. C* **119**, pp. 4431–4443 (2015).
28. Paterson, M. J., Blancafort, L., Wilsey, S. & Robb, M. A. Photoinduced electron transfer in squaraine dyes: Sensitization of large band gap semiconductors. *J. Phys. Chem. A* **106**, pp. 11431–11439 (2002).
29. Yum, J. H. *et al.* Efficient far red sensitization of nanocrystalline TiO₂ films by an unsymmetrical squaraine dye. *J. Am. Chem. Soc.* **129**, pp. 10320–10321 (2007).
30. Patwari, J., Sardar, S., Liu, B., Lemmens, P. & Pal, S. K. Three-in-one approach towards efficient organic dye-sensitized solar cells: Aggregation suppression, panchromatic absorption and resonance energy transfer. *Beilstein J. Nanotechnol.* **8**, pp. 1705–1713 (2017).
31. Das, S. *et al.* Aggregation behavior of water soluble bis(benzothiazolylidene)squaraine derivatives in aqueous media. *J. Phys. Chem.* **100**, pp. 17310–17315 (1996).
32. Pop, F., Lewis, W. & Amabilino, D. B. Solid state supramolecular structure of diketopyrrolopyrrole chromophores: Correlating stacking geometry with visible light absorption. *CrystEngComm* **18**, pp. 8933–8943 (2016).
33. Naik, M. A. & Patil, S. Diketopyrrolopyrrole-based conjugated polymers and small molecules for organic ambipolar transistors and solar cells. *J. Polym. Sci. Part A Polym. Chem.* **51**, pp. 4241–4260 (2013).
34. Farnum, D. G., Mehta, G., Moore, G. G. I. & Siegal, F. P. Attempted reformatskii reaction of benzonitrile, 1,4-diketo-3,6-diphenylpyrrolo[3,4-C]pyrrole. A lactam analogue of pentalene. *Tetrahedron Lett.* **15**, pp. 2549–2552 (1974).
35. Chandran, D. & Lee, K. S. Diketopyrrolopyrrole: A versatile building block for organic photovoltaic materials. *Macromol. Res.* **21**, pp. 272–283 (2013).
36. Yum, J. H. *et al.* Blue-coloured highly efficient dye-sensitized solar cells by implementing the diketopyrrolopyrrole chromophore. *Sci. Rep.* **3**, 2446 (2013).
37. Fan, W., Tan, D., Zhang, Q. & Wang, H. Computational study of diketopyrrolopyrrole-based organic dyes for dye sensitized solar cell applications. *J. Mol. Graph. Model.* **57**, pp. 62–69 (2015).
38. Liu, P. *et al.* Molecular Engineering of D- π -A Type of Blue-Colored Dyes for Highly Efficient Solid-State Dye-Sensitized Solar Cells through Co-Sensitization. *ACS Appl. Mater. Interfaces* **10**, pp. 35946–35952 (2018).

39. Gabrielson, E. *et al.* Convergent/divergent synthesis of a linker-varied series of dyes for dye-sensitized solar cells based on the D35 donor. *Adv. Energy Mater.* **3**, pp. 1647–1656 (2013).
40. Hagberg, D. P. *et al.* Symmetric and unsymmetric donor functionalization. comparing structural and spectral benefits of chromophores for dye-sensitized solar cells. *J. Mater. Chem.* **19**, pp. 7232–7238 (2009).
41. Jose, R., Kumar, a, Thavasi, V. & Ramakrishna, S. Conversion efficiency versus sensitizer for electrospun TiO(2) nanorod electrodes in dye-sensitized solar cells. *Nanotechnology* **19**, 424004 (2008).
42. Wang, X. *et al.* Highly efficient unsymmetrical squaraines for panchromatic dye-sensitized solar cells: A computational study. *RSC Adv.* **3**, pp. 5227–5237 (2013).
43. Younas, M. *et al.* Performance enhancement of dye-sensitized solar cells via cosensitization of ruthenizer Z907 and organic sensitizer SQ2. *Int. J. Energy Res.* **42**, pp. 3957–3965 (2018).
44. Tan, L. L. *et al.* Novel organic dyes incorporating a carbazole or dendritic 3,6-diiodocarbazole unit for efficient dye-sensitized solar cells. *Dye. Pigment.* **100**, pp. 269–277 (2014).
45. Ning, Z. *et al.* Starburst triarylamine based dyes for efficient dye-sensitized solar cells. *J. Org. Chem.* **73**, pp. 3791–3797 (2008).
46. Hara, K. *et al.* Oligothiophene-containing coumarin dyes for efficient dye-sensitized solar cells. *J. Phys. Chem. B* **109**, pp. 15476–15482 (2005).
47. Kang, S. H. *et al.* Novel D- π -A structured porphyrin dyes with diphenylamine derived electron-donating substituents for highly efficient dye-sensitized solar cells. *J. Mater. Chem. A* **1**, pp. 3977–3982 (2013).
48. Karlsson, K. M. *et al.* Phenoxazine dyes for dye-sensitized solar cells: Relationship between molecular structure and electron lifetime. *Chem. - A Eur. J.* **17**, pp. 6415–6424 (2011).

5 Co-sensitisation of perovskite solar cells with organic dyes.

Work in this Chapter was published in Chemical Communications (T. D. McFarlane, C. S. De Castro, P. J. Holliman and M. L. Davies, *Chem. Commun.*, 2019, **55**, 35-38).

5.1 Introduction

Over 154 years ago, in 1856, William Henry Perkin serendipitously discovered the first synthetic organic dye, aniline purple, whilst attempting to synthesise quinine for the treatment of malaria.¹ This discovery, and Perkins subsequent research paved the way for organic dye development and a new era of molecular engineering was born. Organic dyes aimed at PV use were designed to achieve maximum absorbance in the visible, particularly within the region of highest solar spectral irradiance (450-600 nm, Figure 5.0). As a result, the majority of organic dyes for PV are tailored to absorb below 600 nm leaving a substantial section of the solar spectrum (up to 1200 nm) un-utilised.

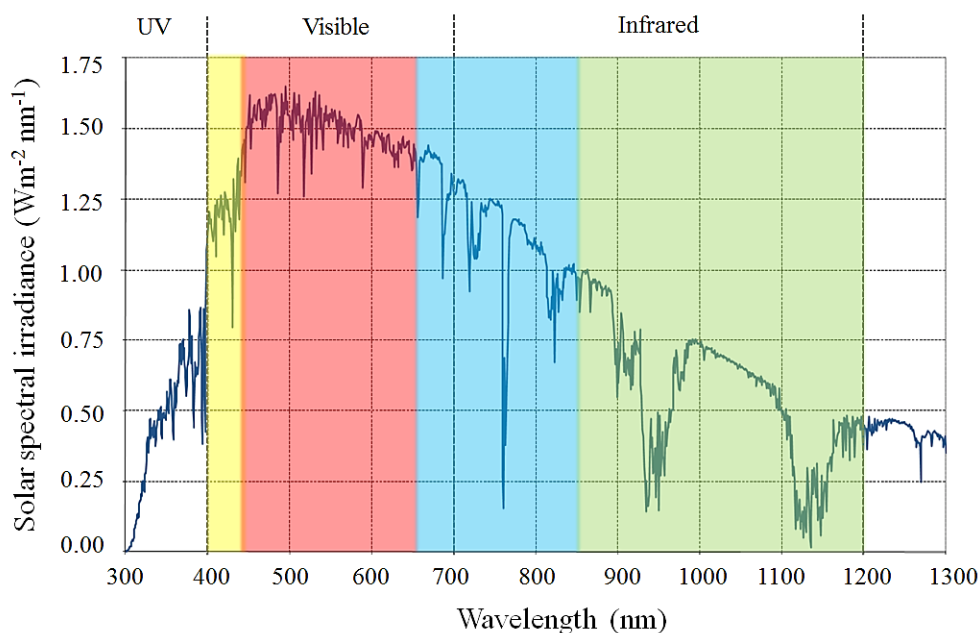


Figure 5.0: Spectrum of solar radiation at Air Mass 1.5, 12 noon. Each coloured section represents the visual colour of dyes which would absorb over that wavelength range.

The possibility of achieving higher efficiencies exists if the spectral response can be extended above 600 nm and into the NIR region. One method to achieve this is through co-sensitisation. Co-sensitisation involves sensitising the same titania film with multiple dyes (of complementary absorbance) in a bid to extend the absorption range and therefore, the light harvesting capabilities of the system.² This concept was first demonstrated in 2001 by Ehret *et al.* who reported increased photocurrent and sensitisation over the entire visible spectrum when combining three cyanine dyes in a single system.³ In 2013, Sharma *et al.* combined a triphenylamine dye (TA-St-CA) with a dithienylthienothiadiazole based dye (D) and achieved broad visible absorption from 350 to 780 nm. The PCE of the co-sensitised DSSC (6.3%) was improved in comparison to DSSC's prepared with the individual dyes TA-St-CA (5.0%) and D (4.2%).⁴ Ogura *et al.* reported an impressive efficiency of 11% when co-sensitising the ruthenium black dye 'N749' (a panchromatic absorber that absorbs into the NIR) with the organic yellow indoline dye, D131.⁵ In many cases, the use of co-sensitisation has proven beneficial, perhaps most notably is the current DSSC record efficiency held by Kakiage *et al.* who achieved >14% through co-sensitising an alkoxy-silyl-anchor dye (ADEKA-1) and a triphenylamine dye (LEG4).⁶

Here, in an attempt to replicate the benefits of co-sensitisation in PSC's, organic dyes are introduced into the cell architecture in a bid to extend the light harvesting range and ultimately improve cell performance. Sensitising dyes which absorb in the red and NIR region of the visible spectrum are typically blue or green in colour (Figure 5.0). If successfully co-sensitised with MAPbBr₃ perovskite, these dyes could increase the spectral response to also absorb light in the 600-700 nm wavelength range (Figure 5.1). As shown in Figure 5.0, wavelengths >600 nm offer lower spectral irradiance however, the aim here is to maximise light harvesting in the visible whilst using an IR absorber to supply a 'top-up' photocurrent contribution.

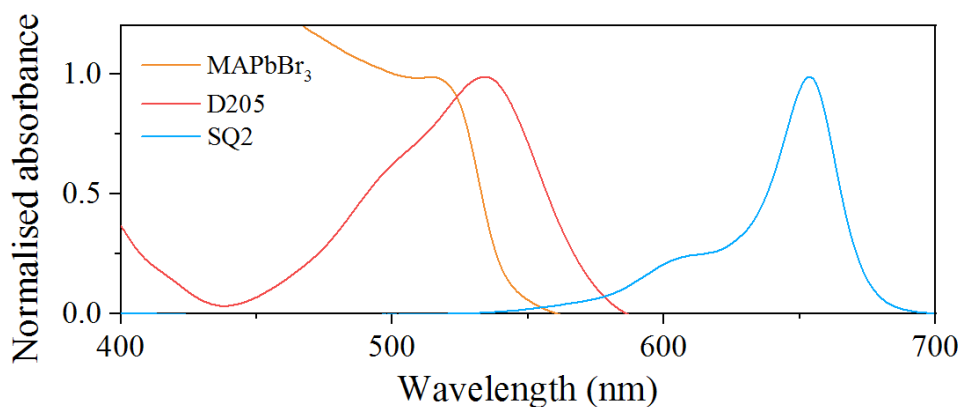


Figure 5.1: Normalised absorbance of a MAPbBr₃ thin-film, indoline dye, D205 dissolved in toluene solution and squaraine dye, SQ2 dissolved in toluene solution.

Due to the many attractive features of lead halide perovskites, unsurprisingly they have previously been investigated as co-sensitisers in DSSC systems. In 2013, Kakiage *et al.* studied the use of MAPbBr₃ perovskite as a co-sensitiser to the ruthenium dye, Z907. The dye was adsorbed to a 5.0 μm TiO₂ electrode and the perovskite subsequently spin coated on top. Introduction of the perovskite improved the photocurrent and co-sensitised cells (3.4% PCE) outperformed standalone dye cells (3.1% PCE) by 0.3%.⁷ Using the same deposition method, Miyasaka *et al.* later studied the effects of co-sensitising solid state D149 cells with MAPbBr₃. The perovskite reportedly reduced dye aggregation and improved light harvesting achieving an efficiency of 3.1% as opposed to 2.6% achieved for dye only cells.⁸

Researchers have also studied various ways of introducing organic dyes into the architecture of perovskite solar cells. In 2018, Balis *et al.* sensitised the compact titania layer of planar MAPbI₃ PSC's with triarylamine dye, D35. The observed improvements in performance were attributed to enhanced electron transfer and superior perovskite growth on the dye sensitised titania layer.⁹

More recently, Xiong *et al.* reported enhanced efficiencies (from 18.3 to 20.2%) for planar MAPbI₃ PSC's through the addition of 5-chloroisatin (a chlorinated indoline dye) to the perovskite precursor solution. Increases in performance were attributed to the carbonyl groups of the dye passivating grain boundaries and lowering recombination through hydrogen bonding with the perovskite.¹⁰ The co-sensitisation of PSC's has also been

investigated with alternative perovskite blends. Li *et al.* added AQ310, a triarylamine dye to the anti-solvent solution when preparing formamidinium lead iodide/MAPbBr₃ (FAPbI₃)_{0.85}(MAPbBr₃)_{0.15} PSC's. Following crystallisation, the dye was found in the grain boundaries at the perovskite surface where it was suspected to passivate Pb²⁺ trap states leading to efficiency increases from 18 to 19.4%.¹¹

This Chapter explores two different routes of dye introduction into the perovskite cell architecture using two organic dyes prepared in an optimised solvent system. As proof of concept, the co-sensitisation of MAPbBr₃ has been investigated using the indoline dye, D205 and the squaraine dye, SQ2. These dyes absorb light in the green and red region of the visible spectrum allowing optical characterisation of the dye uptake. After establishing a working format, experimentation has focussed on maximising dye loading within the cell through varying dye concentration and mesoporous titania (mp-TiO₂) layer thickness. Anticipated increases in performance are predicted to result from increased photocurrent due to the presence of two sensitisers which, when combined, offer extended absorption. The optimised method of co-sensitisation has then been tested with MAPbI₃ PSC's to ascertain its transferability and impact on higher performing perovskites.

5.2 Experimental methods

The MAPbBr₃ cells prepared in Section 5.3.2 were co-sensitised using either a 0.01 mM SQ2 dye solution or a 0.05 mM D205 dye solution. The solutions were prepared in toluene from a 1 mM stock dye solution.

5.2.1 Mesoporous titania preparation for varied thickness

Seven mesoporous titania solutions were prepared by adding: 0.5, 1.0, 1.5, 2.0, 2.5, 3.0 and 3.5 g of isopropanol to 1 g of titania paste (30-NRD, GreatCell Solar). The viscosity of each solution was increased by reducing the weight of added isopropanol. This, in theory, would then produce a thicker mesoporous layer when desposited *via* spin coating. The mesoporous titania layer was then deposited onto pre-prepared substrates *via* spin coating 100 μ L at 4500 rpm for 30 seconds. The substrates were annealed at 150 °C for 10 minutes followed by sintering at 550 °C for 30 minutes.

5.2.2 Determination of molar extinction coefficient of D205 in DMSO

The molar extinction coefficient (ϵ) of D205 dye was measured and calculated using the method described in Section 4.2.2. Here however, DMSO has been used as the dye diluent in place of toluene and seven calibration standards have been used in place of five. The final concentrations of the seven calibration standards are listed in below in Table 17.

Table 17: Final concentration of each calibration standard prepared to determine the molar extinction coefficient of D205 in DMSO.

Standard N ^o	D205 dye concentration (mM)
Blank	0.000
1	0.001
2	0.003
3	0.006
4	0.0075
5	0.009
6	0.012

Each calibration standard was found to have a lambda max λ_{max} (nm) of 543 nm.

5.2.3 Desorption of D205 from co-sensitised thin-films

The co-sensitised MAPbBr₃ thin-films were prepared as standard as described in Section 2.2. The perovskite layer was removed from each film by washing with water. The dye was then desorbed from the mesoporous titania layer by soaking each film in DMSO for 24 hours. The absorbance spectrum of each DMSO solution was measured and the absorbance value at λ_{max} (543 nm) recorded. The absorbance values were then used with the extinction coefficient to determine the concentration of D205 in each DMSO solution by rearranging the Beer Lambert law:

$$c = \frac{\log_{10} \left(\frac{I_t}{I_0} \right) = A}{\epsilon x} \quad (33)$$

Where:

I_0 = initial irradiation intensity

I_t = transmitted intensity

A = absorbance

ϵ = molar extinction coefficient

c = concentration

x = path length

5.3 Results and discussion

5.3.1 Proof of principle

Lead halide perovskites ($\text{CH}_3\text{NH}_3\text{PbX}_3$) are notoriously sensitive moieties due to the inorganic ammonium cation inherent within the crystal structure.¹² This makes them particularly susceptible to dissolution in polar solvents. For DSSC's, organic dyes are typically prepared in polar solvents such as ethanol (ETOH) or acetonitrile:tert-butanol (ACN:TBA (50:50)) however, for the aforementioned reason, these solvents would be unsuitable to co-sensitise the perovskite layer. Therefore, it was necessary to find a solvent capable of dissolving the dye whilst leaving the perovskite layer intact. As a non-polar chemistry, toluene has previously shown benefits when used as an anti-solvent during the crystallisation process of perovskite solar cells.¹³⁻¹⁵ With this in mind, a squaraine, SQ2 (0.05 mM) dye solution was prepared in toluene and used to soak MAPbBr_3 thin-films over an increasing period of minutes. On visual inspection, the perovskite layer of the dyed thin-films (Figure 5.2) appeared intact but also underwent an evident colour change from orange to green. This colour change provided instant visual confirmation of successful dye uptake into the active layer following co-sensitisation.

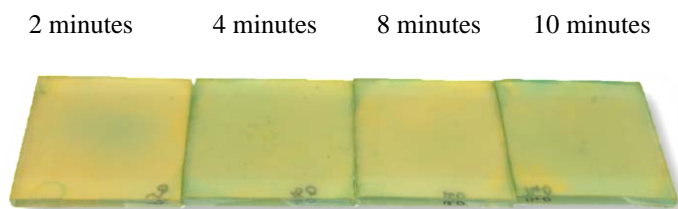


Figure 5.2: Photographed MAPbBr_3 films submerged in 0.05 mM SQ2 dye for increasing lengths of time.

Absorbance measurements of each thin-film showed that the dye uptake increased with dyeing time. The dyed films show clear absorbance from the squaraine dye between 550-725 nm with the longer dyeing times (8 to 10 minutes) showing slightly higher absorbance (Figure 5.3). The absorbance of the perovskite appeared consistent for both the control MAPbBr_3 thin-film (grey line) and the dyed films suggesting the perovskite was unaltered by the dyeing process.

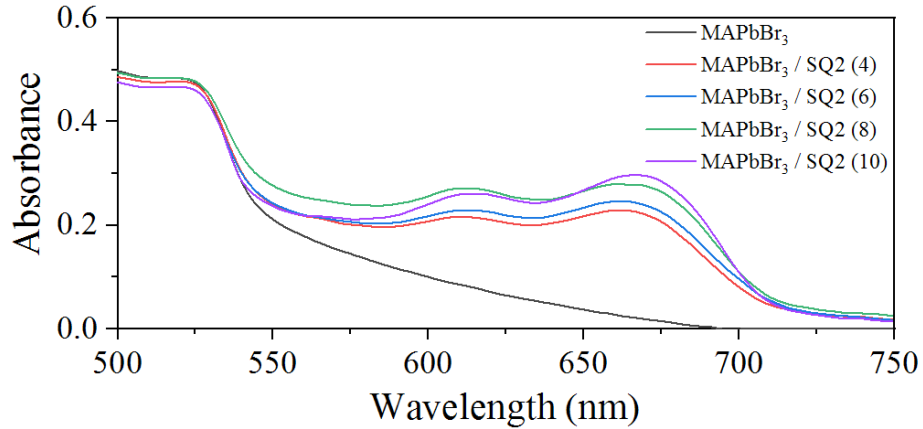


Figure 5.3: Absorbance spectra for MAPbBr₃ films submerged in 0.05 mM SQ2 dye prepared in toluene. The bracketed values represent the number of minutes each film was submerged in the dye solution.

As proof on concept and to correlate the measured photochemical properties with cell functionality, the 10 minute dyed thin-film was prepared as a full PSC and the performance measured and compared with that of a control MAPbBr₃ cell.

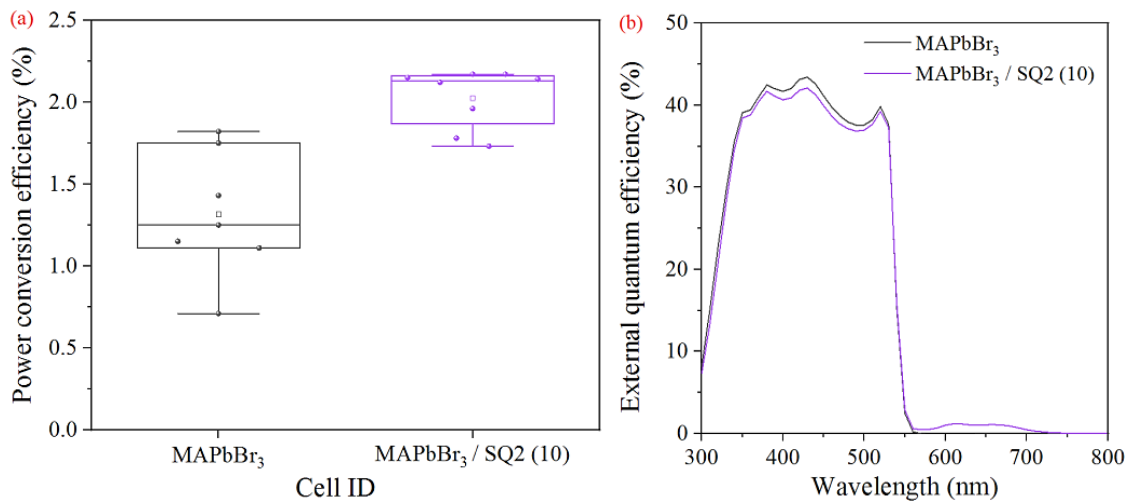


Figure 5.4: (a) Box plots of PCE (%) and (b) Measured external quantum efficiency (EQE) spectral response for a control MAPbBr₃ PSC and a MAPbBr₃ PSC dyed for 10 minutes with 0.05 mM SQ2 dye (MAPbBr₃/SQ2). EQE measurements were made for the hero pixel of each cell.

A higher average PCE is seen for the co-sensitised cell (MAPbBr₃/SQ2 (10)), with less variability between the measured pixels (Figure 5.4 (a)). These results suggest that not only is the perovskite performance enhanced by co-sensitisation, but the cell is also capable of working with the dye in place and without it negatively affecting the perovskite. The absorbance measurements in Figure 5.3 confirmed the presence of the dye in the co-

sensitised thin-film however, it was necessary to confirm if the dye was adsorbed to the titania layer and capable of contributing to the photocurrent or if the dye was simply sitting on the perovskite surface. External quantum efficiency (EQE) measurements performed for the control and co-sensitised cells are shown in Figure 5.4 (b). The EQE signal of the co-sensitised cell (MAPbBr₃/SQ2 (10)) shows a slight response from the dye between 550-720 nm. This shows that the overall absorbance range of the system has been extended above the 540 nm limit of the MAPbBr₃ only system. These results also reveal that the dye is adsorbed to and capable of injecting into the titania with subsequent electron extraction leading to an active contribution to the overall photocurrent.

5.3.2 Methods of co-sensitisation

After establishing a dye solvent which did not negatively impact the perovskite layer, the next challenge focussed on investigating the effects of introducing the dye at different stages of cell fabrication. As discussed in the introduction to this Chapter, various literary methods have studied introducing the dye *via* the perovskite precursor solution, in the perovskite anti-solvent or by dye sensitising the compact titania layer.^{10,11,16} Here, two methods of dye introduction were investigated to determine the effect of co-sensitising the cell at different stages of cell fabrication. The two methods were named based on the point of dye introduction with respect to the perovskite layer i.e. before or after perovskite deposition.

Figure 5.5 shows the ‘dye before’ (DB) method which involves dyeing the mp-TiO₂ layer prior to deposition of the perovskite. The mp-TiO₂ thin-film is submerged in a dye solution for 10 minutes. The dyed thin-film is then dried and the perovskite layer spin coated on top followed by annealing.

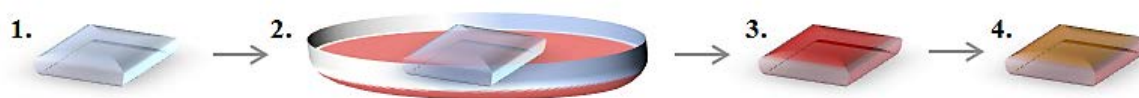


Figure 5.5: Schematic showing each stage of the ‘dye before’ (DB) method used for the co-sensitisation of MAPbBr₃ cells. (1) Pre-prepared mesoporous titania thin-film, (2) dyeing of mesoporous titania thin-film for 10 minutes, (3) removal from dye solution and drying, (4) perovskite layer is spin coated on top and annealed.

Figure 5.6 shows the ‘dye after’ (DA) method which involves dyeing the crystallised perovskite film. The perovskite layer is spin coated onto the mp-TiO₂ thin-film and annealed as standard. The perovskite thin-film is then submerged in a dye solution for 10 minutes followed by removal and drying.



Figure 5.6: Schematic showing each stage of the ‘dye after’ (DA) method used for the co-sensitisation of MAPbBr₃ cells. (1) Pre-prepared mesoporous titania thin-film, (2) perovskite layer is deposited by spin coating followed by annealing, (3) perovskite thin-film is dyed for 10 minutes by submerging in a dye solution, (4) dyed perovskite thin-film is removed from the dye solution and dried.

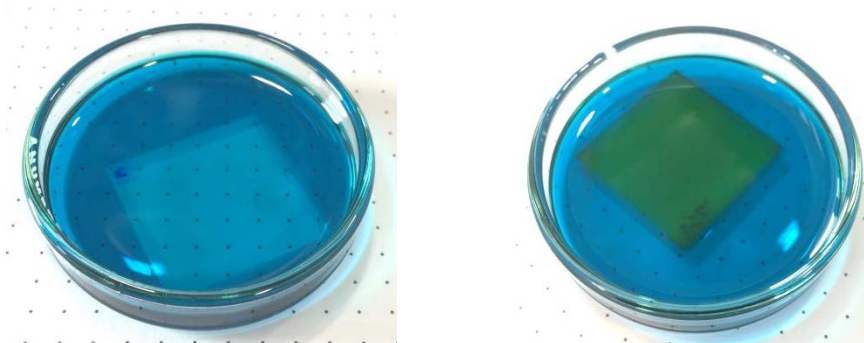


Figure 5.7: Photographs of: a mesoporous titania film submerged in SQ2 dye prior to perovskite deposition i.e. the dye before method (left) and a MAPbBr₃ film submerged in SQ2 dye prior to HTL deposition i.e. the dye after method (right).

Figure 5.8 shows a series of MAPbBr₃ thin-films following co-sensitisation with the squaraine dye SQ2, and the indoline dye D205. For both co-sensitisation methods, the thin-films underwent an evident colour change from orange to green and orange/red when sensitised with SQ2 and D205 respectively. Perhaps the most attractive feature of DSSC’s is their distinct and vibrant array of colours. Here, through co-sensitisation, the aforementioned attractive feature has been replicated in the perovskite active layer. This highlights the potential for coloured PSCs which could be advantageous for applications such as building integrated PV, product-integrated PV or in tandem systems.

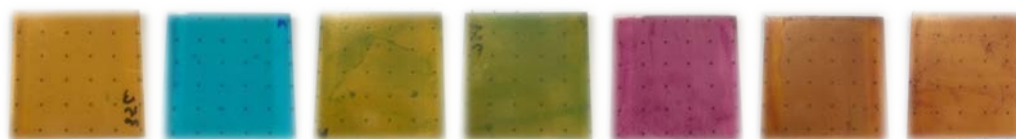


Figure 5.8: Photographed thin-films, left to right: control MAPbBr₃, solid state SQ2, MAPbBr₃ co-sensitised with SQ2 using the dye before method, MAPbBr₃ co-sensitised with SQ2 using the dye after method, solid state D205, MAPbBr₃ co-sensitised with D205 using the dye before method and MAPbBr₃ co-sensitised with D205 using the dye after method.

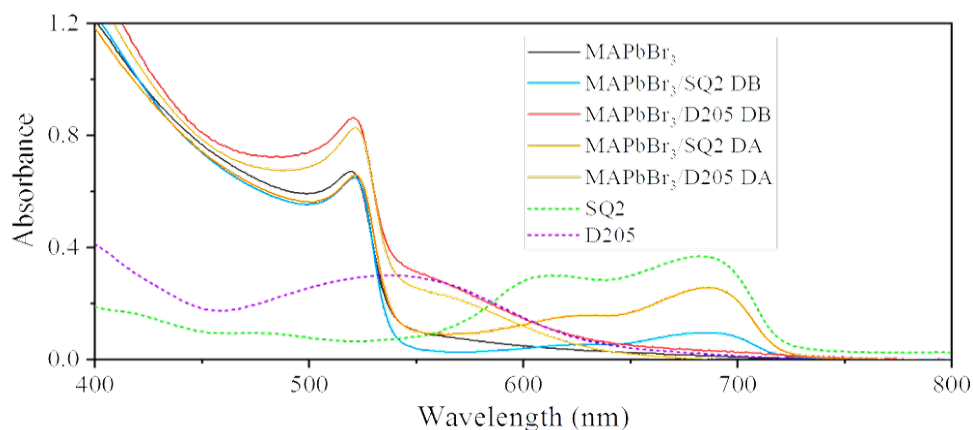


Figure 5.9: Absorbance spectra of control MAPbBr₃ films, MAPbBr₃ films co-sensitised with SQ2 and D205 using the dye before (DB) method (MAPbBr₃/SQ2 DB and MAPbBr₃/D205 DB, respectively) and MAPbBr₃ films co-sensitised with SQ2 and D205 using the dye after (DA) method (MAPbBr₃/SQ2 DA and MAPbBr₃/D205 DA, respectively). The dashed lines represent the absorbance spectra for solid state dyed films of D205 and SQ2.

Absorbance measurements were used to confirm the presence of each dye in the co-sensitised thin-films (Figure 5.9). As discussed previously, the absorbance response of MAPbBr₃ perovskite (grey line) displays a sharp band edge around 540 nm. For thin-films co-sensitised with SQ2 dye, there is increased absorbance between 550 and 725 nm which is consistent with the solid state spectra for SQ2 (green dashed line). Thin-films co-sensitised with D205, show an extension of the absorbance response beyond 550 nm also consistent with the solid state spectra for D205 (purple dashed line). When comparing the two co-sensitisation methods; the results appear to be dye dependent. The perovskite/SQ2 sensitised films have a higher absorbance from the dye for the DA method whereas for D205, a slightly higher absorbance from the dye is observed using the DB method. The efficiencies of MAPbBr₃ PSC's prepared using both the DA and DB method are compared in Figure 5.10.

Control MAPbBr₃ cells achieved an average PCE of 1.7% whereas MAPbBr₃ cells co-sensitised with SQ2 and D205 using the DB method showed a decrease in average PCE to 1.3% and 1.1%, respectively. Cells co-sensitised using the DA method showed increased average PCE values of 2.1% and 2.3% with SQ2 and D205 respectively.

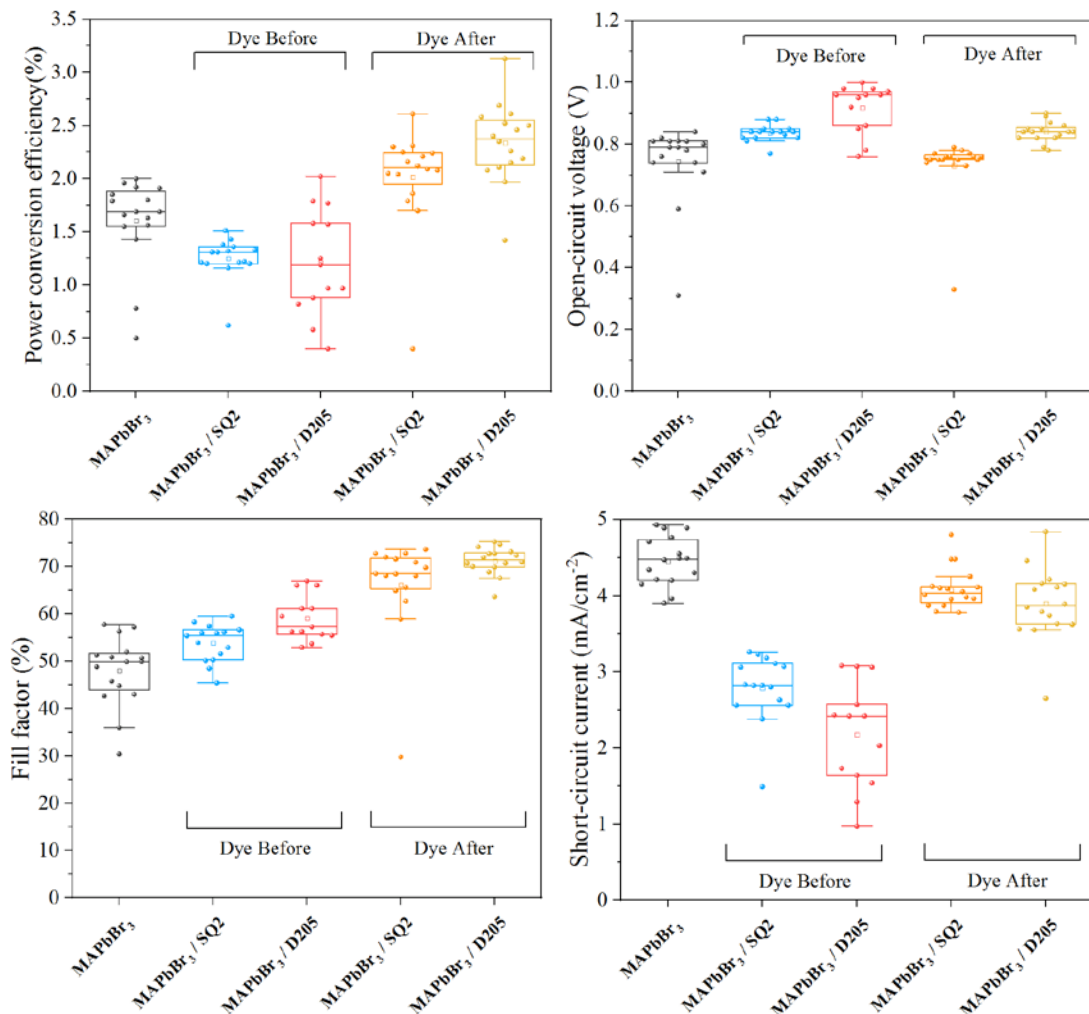


Figure 5.10: Box plots of performance parameters for for control MAPbBr₃ cells, MAPbBr₃ cells co-sensitised with SQ2 and D205 using the dye before method and MAPbBr₃ cells co-sensitised with SQ2 and D205 using the dye after method.

The losses in PCE observed for cells prepared using the DB method appear to stem from large losses in the J_{sc} (Figure 5.10). The decreases in J_{sc} possibly occurred due to the dye occupying space within the mesoporous layer and negatively affecting the perovskites ability to nucleate and form a dense uniform layer. The J_{sc} losses could also be attributed to increased recombination due to the dye having a detrimental effect on charge separation and

transfer. However, this is contradicted by a higher average V_{oc} for DB cells where the observed increase in V_{oc} may result from reduced recombination (Figure 5.10). Interestingly, for cells prepared with the DA method, the average J_{sc} also decreases. However, when comparing the performance parameters of the hero MAPbBr₃ cell and the hero cells co-sensitised using the DA method (Table 18), there is an increase in the J_{sc} for both SQ2 and D205 (MAPbBr₃/SQ2 DA and MAPbBr₃/D205 DA, respectively).

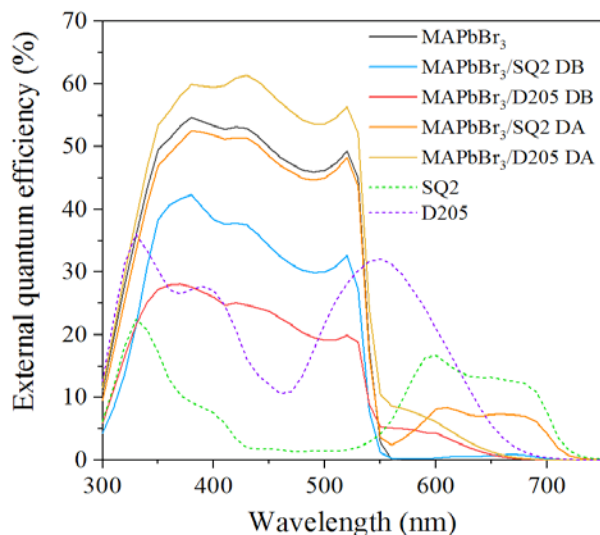
Table 18: Measured performance parameters for the highest performing ‘hero’ pixel of control MAPbBr₃ cells, MAPbBr₃ cells co-sensitised with SQ2 and D205 using the dye before method (MAPbBr₃/SQ2 DB and MAPbBr₃/D205 DB, respectively) and MAPbBr₃ cells co-sensitised with SQ2 and D205 using the dye after method (MAPbBr₃/SQ2 DA and MAPbBr₃/D205 DA, respectively).

Cell ID	J_{sc} (mA/cm ²)	V_{oc} (V)	FF	PCE (%)
MAPbBr ₃ (control)	4.49	0.79	56	2.0
MAPbBr ₃ /SQ2 DB	3.18	0.85	55	1.5
MAPbBr ₃ /D205 DB	3.08	0.98	67	2.0
MAPbBr ₃ /SQ2 DA	4.80	0.75	72	2.6
MAPbBr ₃ /D205 DA	4.84	0.89	72	3.1

With the addition of a dye into the active layer, one would typically expect an increase in J_{sc} however, as observed; this is not always the case. This suggests that there is a delicate balance between maximising the dye response whilst maintaining the photocurrent generated from the perovskite. Interestingly, whilst hero co-sensitised cells demonstrate improved J_{sc} and an overall improvement compared to non-sensitised cells, improvement in the FF appears to be the main contributor to increased cell efficiencies. The increases in FF may, in part, be attributed to the dye solvent, toluene. Toluene has previously been shown to increase overall performance when used as an anti-solvent for lead halide perovskites and in many cases has yielded denser films with improved uniformity.^{13–15} Here, the observed increases in FF are believed to result from both dye and solvent which are thought to improve the active layer homogeneity and increase the photocurrent, respectively. The impact of toluene on the active layer (in the absence of a dye) has been further studied and discussed in Section 6.3.1. Increased efficiencies (derived from improved FF and J_{sc}) were observed for toluene soaked MAPbBr₃ cells thereby confirming that toluene alone, can

enhance the perovskite layer. However; the data was less consistent and unable to replicate the efficiencies of the co-sensitised MAPbBr₃ devices.

EQE measurements were performed to determine the individual photocurrent contributions of the dye and perovskite. As shown in Figure 5.11, the EQE signal of the hero MAPbBr₃ cell reaches maximum at 380 nm and remains above 50% up to 520 nm. For hero cells co-sensitised using the DA method, the EQE results (Figure 5.11) follow the same trend but also show an additional contribution of photocurrent over the 550 – 750 nm range. The tabulated values included in Figure 5.11 show this contribution to be 14% and 7% when co-sensitising with SQ2 (MAPbBr₃/SQ2 DA) and D205 (MAPbBr₃/D205 DA), respectively. These results confirm that both dyes are harvesting incident photons within this wavelength range and contributing to the overall cell photocurrent.



Cell ID	EQE J_{sc}	Integrated J_{sc}
	(mA/cm ²) 300 – 750 nm	(mA/cm ²) 550 – 750 nm
MAPbBr ₃	4.24	0.00
MAPbBr ₃ /SQ2 DB	2.93	0.05
MAPbBr ₃ /D205 DB	2.23	0.26
MAPbBr ₃ /SQ2 DA	4.85	0.70
MAPbBr ₃ /D205 DA	5.36	0.35

Figure 5.11: Measured EQE spectral response and tabulated EQE generated short-circuit current values (EQE J_{sc}) for the hero pixel of control MAPbBr₃, MAPbBr₃ co-sensitised with SQ2 and D205 using the dye before method (MAPbBr₃/SQ2 DB and MAPbBr₃/D205 DB, respectively) and MAPbBr₃ co-sensitised with SQ2 and D205 using the dye after method (MAPbBr₃/SQ2 DA and MAPbBr₃/D205 DA, respectively). The dashed lines represent the absorbance spectra for solid state dyed films of D205 and SQ2.

Contrastingly, when studying the EQE spectra of the DB cells, we observe a lower EQE response from both the perovskite and dye. The decreased perovskite signal (300 - 550 nm) supports the theory that the DB method affects perovskite formation, potentially by reducing the space available within the mesoporous layer. For the SQ2 co-sensitised cell (MAPbBr₃/SQ2 DB) the lower EQE dye signal suggests that little to no dye remains in the system, possibly due to degradation of the dye during the annealing of the perovskite layer. In comparison, a higher EQE dye signal is seen for the D205 co-sensitised cell (MAPbBr₃/D205 DB) however, this failed to exceed the dye signal of the cells co-sensitised using the DA method. In addition to dye loss through annealing, it is also possible that some dye may have been partially dissolved by the DMF/DMSO perovskite solvent during spin coating of the perovskite layer.

When considering the performance and EQE results for both co-sensitisation methods, the DB method potentially limits and/or influences perovskite nucleation as the dye occupies space on the titania surface which would otherwise be available to the perovskite. This in turn limits the effectiveness of the DB method and ultimately reduces the PCE. Alternatively, it is thought that the DA method encourages the dye to fill any unoccupied space on the titania surface allowing colour tuning whilst increasing the overall photocurrent and improving the FF of the cell *via* solvent treatment.

5.3.3 Dye loading

In the previous section, the EQE results showed a small contribution of photocurrent from the dye when co-sensitising MAPbBr₃ PSC's. Although increased PCE was observed for cells co-sensitised using the DA method, the dye response was perhaps lower than anticipated. The next two sections focus on maximising the dye response through saturation of the active layer in an attempt to increase the amount of dye in the system and achieve higher efficiencies without compromising the performance of the perovskite.

5.3.3.1 Dye concentration

In the previous Chapter (Section 4.3.6), for solid state cells prepared using SQ2 and D205, it was found that higher dye concentrations generated the largest photocurrents. Here,

MAPbBr₃ PSC's have been co-sensitised (using the DA method) with increasing dye concentration in an attempt to saturate the active layer and limit the time the perovskite is exposed to the dye solvent. In Figure 5.12 we see the colour of the active layer intensifies (with dye concentration) when treating MAPbBr₃ thin-films with increasing concentrations of SQ2 (green films) and D205 (red/orange).

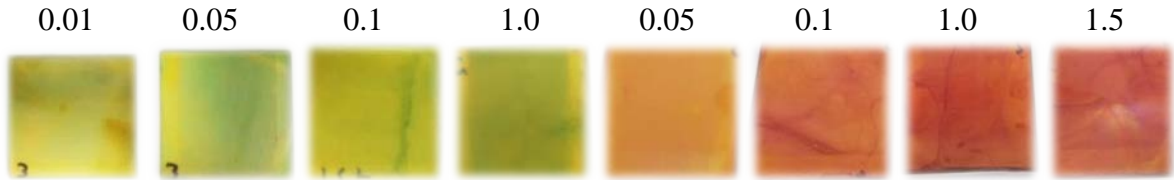


Figure 5.12: Photographed thin-films of MAPbBr₃ co-sensitised with increasing concentrations of SQ2 dye (green films) and D205 dye (red/orange films). Each dye concentration (in mM) used for co-sensitisation is listed above the image.

Figure 5.13 shows the absorbance spectra of MAPbBr₃ thin-films co-sensitised with varying concentrations of D205 and SQ2 dye.

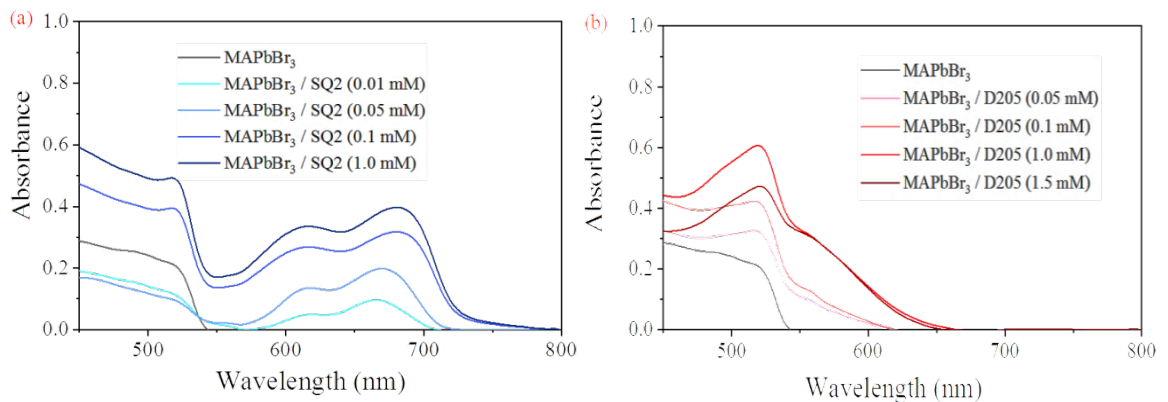


Figure 5.13: Absorbance spectra of control and co-sensitised MAPbBr₃ thin-films prepared with increasing concentrations of SQ2 dye (a) and D205 dye (b). The values in brackets represent the concentrations of dye used for co-sensitisation.

For both spectra, the control absorbance (grey line) decreases just before 550 nm whereas the co-sensitised films show an extended absorbance range attributed to the dye. These ranges are observed between 550-750 nm and 550-650 nm for SQ2 and D205, respectively. For both dyes, the dye absorbance increases with dye concentration which suggests a higher level of dye loading has been achieved. These results also suggest that the active layer is not

fully saturated when co-sensitising with a lower dye concentration. The thin-films were subsequently prepared as complete cells and their performance measured and compared.

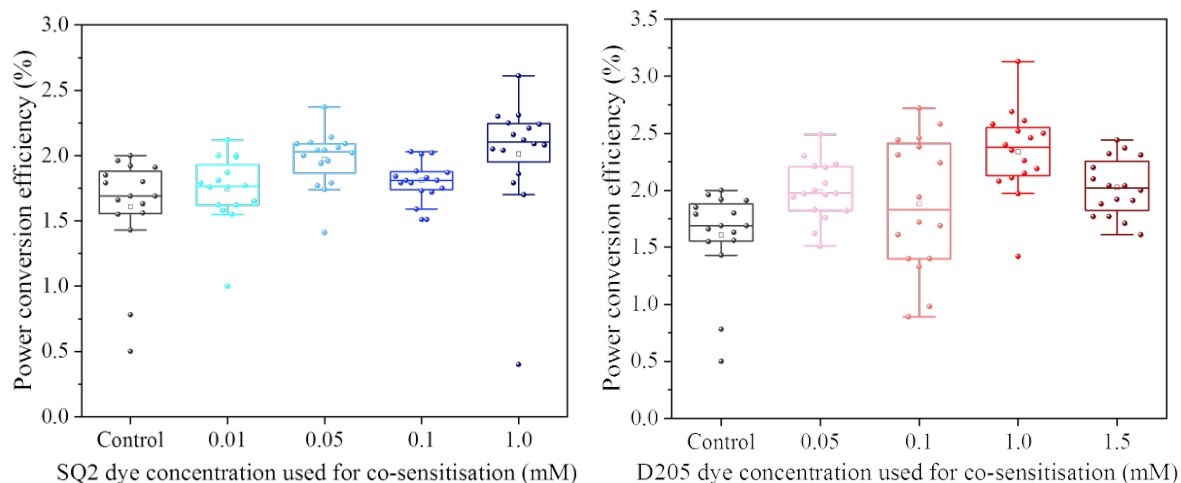


Figure 5.14: Box plots of PCE (%) for control and co-sensitised MAPbBr₃ cells manufactured with increasing concentrations of SQ2 dye (left) and D205 dye (right).

When studying the average performance parameters of the co-sensitised cells (Table 19), it was anticipated that the average J_{sc} would increase with dye concentration however, this was not the case. Compared to the control, the average J_{sc} decreased for all co-sensitised cells irrespective of dye or concentration. In spite of this, the co-sensitised cells outperformed the controls and demonstrated higher efficiencies as shown in Figure 5.14. For cells co-sensitised with SQ2, there is a steady increase in PCE with dye concentration and a hero pixel efficiency of 2.6% was achieved for the 1.0 mM dye solution. For cells co-sensitised with D205, the average efficiencies generally increase with dye concentration up to 1.0 mM, a hero pixel efficiency of 3.1% was also achieved using this concentration.

The observed increases in average PCE appear to stem from enhanced FF (Table 19). As seen in the previous section, there are large increases in the average FF of co-sensitised cells when compared to control devices, however, there does not appear to a discernible trend between FF and dye concentration. For cells co-sensitised with D205, there is also an increase in the average V_{oc} which contributes to the increased efficiency.

Table 19: Average photovoltaic performance values for control and co-sensitised MAPbBr₃ cells manufactured using increasing concentrations of SQ2 and D205 dye also included is the standard deviation, σ for each average value.

Cell ID	$\bar{x} J_{sc}$ (mA/cm ²)	$J_{sc} \sigma$	$\bar{x} V_{oc}$ (V)	$V_{oc} \sigma$	\bar{x} Fill Factor	FF σ	\bar{x} PCE (%)	PCE σ
MAPbBr ₃ / Control	4.45	0.32	0.71	0.13	48	7.4	1.6	0.41
MAPbBr ₃ /SQ2 0.01 mM	3.47	0.32	0.72	0.03	69	7.7	1.7	0.26
MAPbBr ₃ /SQ2 0.05 mM	4.06	0.47	0.74	0.02	67	6.5	1.8	0.22
MAPbBr ₃ /SQ2 0.1 mM	3.96	0.18	0.71	0.02	65	2.8	1.8	0.14
MAPbBr ₃ /SQ2 1 mM	4.07	0.26	0.73	0.11	66	10.5	2.0	0.48
MAPbBr ₃ /D205 0.05 mM	3.62	0.22	0.78	0.03	70	4.9	2.0	0.26
MAPbBr ₃ /D205 0.1 mM	3.67	0.70	0.85	0.02	59	9.2	1.9	0.58
MAPbBr ₃ /D205 1 mM	3.89	0.48	0.84	0.03	71	2.9	2.3	0.38
MAPbBr ₃ /D205 1.5 mM	3.33	0.28	0.84	0.02	72	4.1	2.0	0.25

Interestingly, a loss in average PCE was observed when co-sensitising with a D205 concentration of 1.5 mM. The FF and V_{oc} remain high however; there is a reduction in J_{sc} possibly arising from dye aggregation due to the high concentration.

Figure 5.15 (a) and (b) both show the EQE response of control and co-sensitised cells, the perovskite signal is between 300-550 nm.

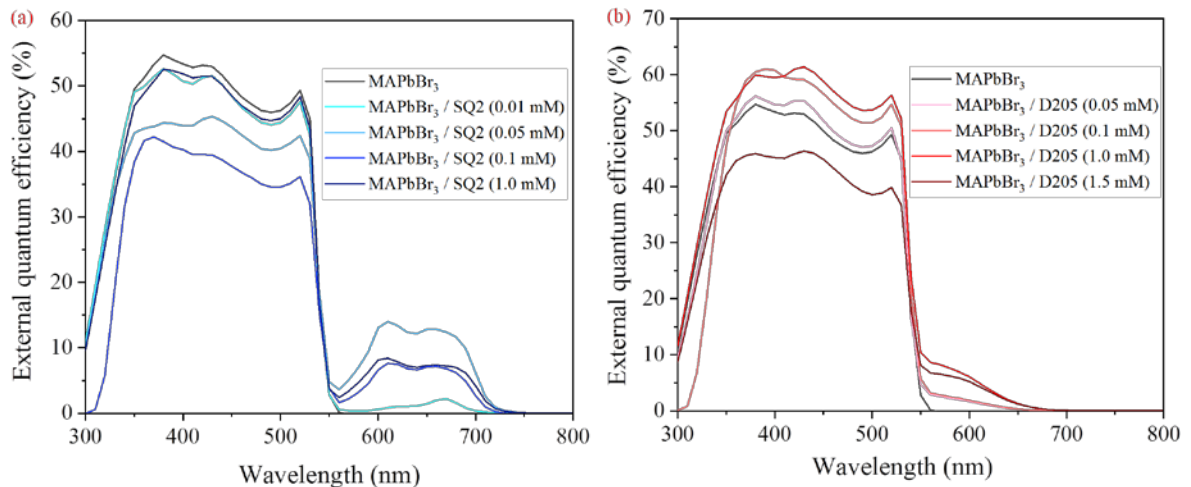


Figure 5.15: Measured EQE spectral response for the highest performing 'hero' pixel of control and co-sensitised MAPbBr₃ cells manufactured with increasing concentrations of SQ2 and D205 dye. The values in brackets represent the concentrations of dye used for co-sensitisation.

For the SQ2 co-sensitised cells in Figure 5.15 (a), the perovskite EQE signal does not increase with the dye. However, for D205 co-sensitised cells, the perovskite EQE signal is enhanced (between 2 – 15%) for three of the dye concentrations (0.05 – 1.0 mM) which suggests D205 may play some role in improving the perovskite layer. For cells co-sensitised

with the highest D205 concentration (1.5 mM) there is a reduction in the perovskite signal which may further support the theory that dye aggregation has occurred. This in turn has potentially affected charge extraction of the perovskite, caused increased recombination and a subsequent reduction in the EQE signal. When considering the dye EQE responses, for SQ2 and D205 the spectra have peaks between 550-730 nm and 550-670 nm, respectively. Interestingly, the largest dye signal was observed when co-sensitising MAPbBr₃ with a 0.05 mM SQ2 solution which contributed 1.16 mA to the overall photocurrent (Table 20). For D205, the largest dye signal is observed when co-sensitising with the 1.0 mM solution with a photocurrent contribution of 0.35 mA.

Table 20: EQE generated short-circuit current values (EQE J_{sc}) and the contribution to J_{sc} over the wavelength ranges of 300 – 550 and 550 – 700 nm for the highest performing ‘hero’ pixel of control and co-sensitised MAPbBr₃ cells manufactured using increasing concentrations of SQ2 and D205 dye.

Cell ID	EQE J_{sc} (mA/cm ²) 300 – 800 nm	EQE J_{sc} (mA/cm ²) 550 – 800 nm
MAPbBr ₃ / Control	4.44	0.00
MAPbBr ₃ /SQ2 0.01 mM	4.22	0.11
MAPbBr ₃ /SQ2 0.05 mM	4.87	1.16
MAPbBr ₃ /SQ2 0.1 mM	3.81	0.56
MAPbBr ₃ /SQ2 1 mM	4.85	0.70
MAPbBr ₃ /D205 0.05 mM	4.49	0.1
MAPbBr ₃ /D205 0.1 mM	4.87	0.11
MAPbBr ₃ /D205 1.0 mM	5.36	0.35
MAPbBr ₃ /D205 1.5 mM	4.03	0.30

Contrary to the average J_{sc} values included in Table 19, the tabulated data above shows that several of the co-sensitised hero J_{sc} values exceed that of the control. This suggests that it is possible to achieve increased photocurrent through co-sensitisation but further reinforces the idea of a fine balance in maximising the dye response whilst not reducing the photocurrent generated from the perovskite.

5.3.3.2 Mesoporous layer thickness

The mesoporous titania layer plays a key role in the performance of a perovskite solar cell as it not only provides a scaffold for perovskite crystallisation, but also increases contact between the perovskite and titania thereby encouraging efficient electron injection and

charge separation. It is well documented that the structure of this layer is an important factor in the overall device efficiency.¹⁷⁻²⁰

Highly porous mesoporous layers facilitate improved infiltration of the perovskite into the meso-pores. This in turn increases the perovskite surface coverage which is key to achieving a high photocurrent and efficiency.²¹ The layer porosity and pore-size is generally governed by the size of the TiO₂ nanoparticles used. Smaller nanoparticles (below 15 nm) create a dense layer with small pores which can impede perovskite infiltration and formation.²² On the other hand, larger nanoparticles (above 25 nm) can decrease the total pore volume. A study conducted by *Yang et al.* showed the surface area of 15 nm titania nanoparticles to be 139.8 m² g⁻¹ with a pore size, pore volume and porosity of 14.7 nm, 0.515 cm³g⁻¹ and 66.8%, respectively. On increasing the TiO₂ nanoparticle size to 30 nm, Yang found that the pore size increased (25.8 nm), but the specific surface area (59.6 m² g⁻¹), pore volume (0.385 cm³g⁻¹) and the porosity (60.1%) decreased.²³

Increased perovskite-pore filling however, has previously been achieved without altering the TiO₂ nanoparticle size. *Leitjens et al.* improved the pore filling of mesoporous CH₃NH₃PbI_{3-x}Cl_x devices (prepared with 18 nm titania nanoparticles) by reducing the titania thickness (from 750 to 260 nm) and increasing the concentration of the perovskite precursor solution (from 30 to 40 wt%). Thicker films of 750 nm showed only 70% pore filling as opposed to the 100% pore filling observed for 440 and 200 nm films. *Leitjens* showed that the degree of pore filling is largely dependent on the mesoporous layer thickness and increased pore filling is generally seen for thinner films with a perovskite 'capping layer'.²⁴ A capping layer is a thick perovskite layer which forms on top of the mesoporous layer. It is thought that this layer absorbs most of the photons, separates the charges, facilitates electron transfer and suppresses recombination thereby increasing the charge collection efficiency.^{25,26} Literary sources have shown perovskite capping layers typically form for mesoporous thicknesses below 400 nm and capping layer thickness decreases with increasing mesoporous layer thickness.^{17,24,27} Therefore, the perovskite capping layer is considered to be a key factor in the device performance and highlights the

importance of optimising the active layer thickness to establish a working balance which ensures maximum light absorption whilst minimising charge recombination.

Dye sensitised solar cells typically contain a characteristically thick mesoporous layer (4-6 μm) which ensures high dye loading but also requires a long dyeing time (ca. 12-16 h). This is in stark contrast to lead halide PSC's where active layer thicknesses of 200-300 nm are typically favoured.^{19,28-31} In spite of this, lead halide perovskites remain capable of successfully operating in a thicker cell format.³²⁻³⁵ This is primarily due to their long charge diffusion lengths, reported as 0.3-1 μm ³⁶⁻³⁸ and 0.1-1 μm ³⁹⁻⁴¹ for MAPbBr₃ and MAPbI₃, respectively.

The PSC's previously discussed in this thesis were prepared using an active layer thickness of ~200 nm. Although this thickness was optimised for the perovskite, it was not necessarily optimal for the co-sensitising dye. Here, the active layer thickness of co-sensitised PSC's was varied in a bid to increase dye loading and optimise the cell architecture. Seven different mesoporous layer thicknesses were prepared as described in the experimental methods (Section 5.2) of this Chapter. The titania paste (30-NRD, Dyesol) and size of nanoparticles (30 nm) used were kept constant when preparing each of the mesoporous layer thicknesses. Profilometry measurements were conducted to determine the thickness (referred to as 'height') of each layer. Measurements were made on three separate films per thickness and an average taken (Table 21, average height). The average height values calculated for the seven mp-TiO₂ layers confirm an increase in layer thickness when reducing the weight of added isopropanol. The most dilute titania solution (1:3.5 g, TiO₂: isopropanol) produced an average height of 247 nm whereas the most viscous solution (1:0.5 g, TiO₂: isopropanol) yielded an average height of 3941 nm.

Table 21: Profilometry measurements of the seven annealed mesoporous titania layers. Tabulated values represent the three thicknesses (height) measured per variable and the average value generated. Also included is the standard deviation, σ for the average measurements.

Weight of ethanol (g) added to 1 g of titania paste	Measured height (μm)	Measured height σ	Average height (μm)	Average height to the nearest 100 (μm)
3.5	0.236	0.00985	0.247	~0.2
	0.255			
	0.250			
3.0	0.424	0.03439	0.395	~0.4
	0.357			
	0.404			
2.5	0.667	0.02851	0.696	~0.7
	0.697			
	0.724			
2.0	1.033	0.03934	1.027	~1.0
	1.063			
	0.985			
1.5	1.596	0.14022	1.444	~1.4
	1.320			
	1.415			
1.0	1.873	0.11381	2.000	~2.0
	2.041			
	2.090			
0.5	3.882	0.05401	3.941	~3.9
	3.988			
	3.953			

For clarity, in the remainder of the text, the average height values for each mesoporous layer have been rounded to the nearest 100 and written as approximate values. After measuring the thickness of the mesoporous layers, control and co-sensitised MAPbBr₃ thin-films were then prepared per variable. As seen previously, when co-sensitised with D205, the MAPbBr₃ thin-films underwent an evident colour change from light orange to red (Figure 5.16).

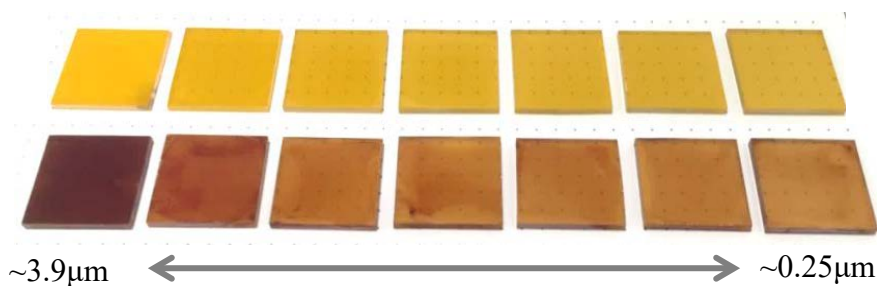


Figure 5.16: Photographed thin-films, top row, right to left: control MAPbBr₃ thin-films prepared on mesoporous titania layers of increasing thickness. Bottom row, right to left: MAPbBr₃ thin-films co-sensitised with D205 and prepared on mesoporous titania layers of increasing thickness.

The colour of both control and co-sensitised films intensified with increasing mp-TiO₂ layer thickness suggesting both increased perovskite formation and dye loading. When depositing the perovskite layer, the same volume of precursor solution (100 μ L) was used for each of the mesoporous layer thicknesses studied. However, during spin-coating, some of the precursor solution was expelled from the film surface and was visible on the inside of the spin coater. This was particularly evident for the thinner mesoporous films and suggested variability in the amount of perovskite retained within the mesoporous layers prior to annealing. It is possible that the thicker mesoporous layers retained more of the perovskite solution leading to increased perovskite formation. Absorbance measurements were conducted on the control and co-sensitised thin-films to qualitatively assess the levels of both perovskite and dye with increasing mesoporous thickness.

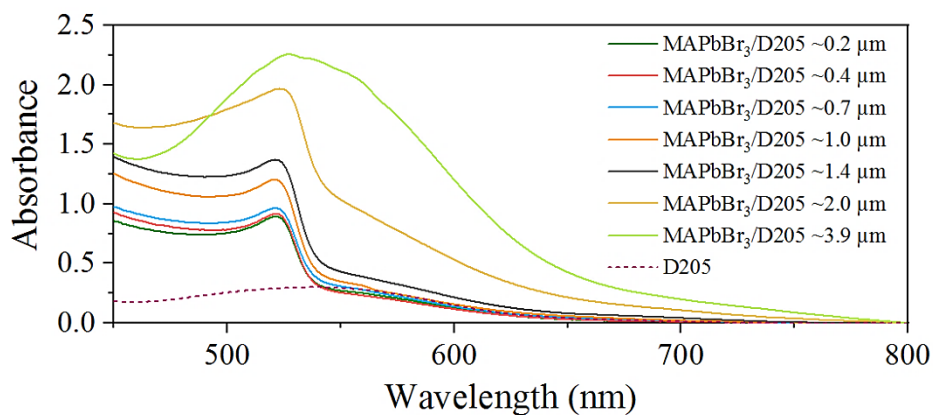


Figure 5.17: Absorbance spectra of MAPbBr₃ thin-films co-sensitised with D205 prepared on mesoporous titania layers of increasing thickness, also included is the absorption response of solid state D205.

In Figure 5.17 above, we see an evident increase in the dye response (between 540-650 nm) with increasing mesoporous layer thickness suggesting increased dye uptake into the active layer. In-line with the visual appearance, as expected, the thickest co-sensitised film (MAPbBr₃/D205 \sim 3.9 μ m) demonstrated the highest absorbance however; the perovskite band edge is no longer visible due to the large dye signal. For the thicker films (\sim 1.0, \sim 1.4, \sim 2.0 and \sim 3.9 μ m) there also appears to be an increase in the optical density of the perovskite.

Figure 5.18 shows a comparison between the control and co-sensitised absorbance responses of thin-films prepared on three mp-TiO₂ thicknesses: ~1.4, ~0.7 and ~0.2 μm.

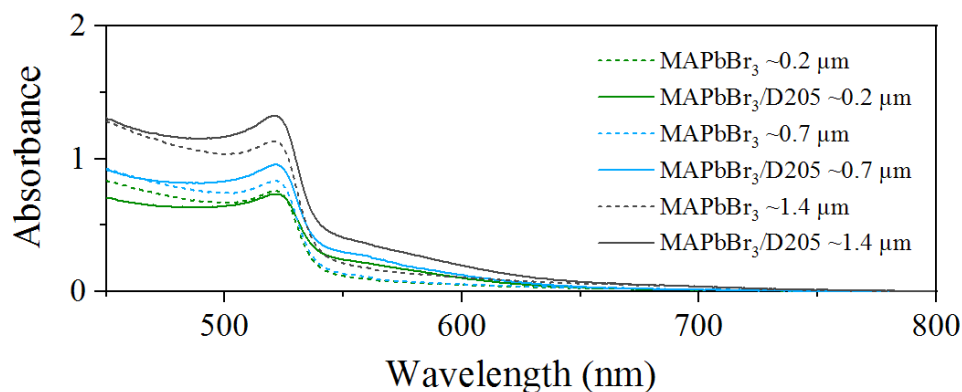


Figure 5.18: Absorbance spectra of control MAPbBr₃ and MAPbBr₃ thin-films co-sensitised with D205 on three thicknesses (~0.2, ~0.7 and ~1.4 μm) of mesoporous layer.

For the control films, the optical density of the perovskite appears to increase with mesoporous layer thickness suggesting the thicker layers do retain more of the perovskite precursor solution during spin-coating. These results also confirm an increase in the absorption of the perovskite with co-sensitisation which may further support the theory that the dye solution potentially enhances formation of the perovskite as is evidenced with increased dye loading.

The morphology of the co-sensitised thin-films was further studied using optical microscopy.

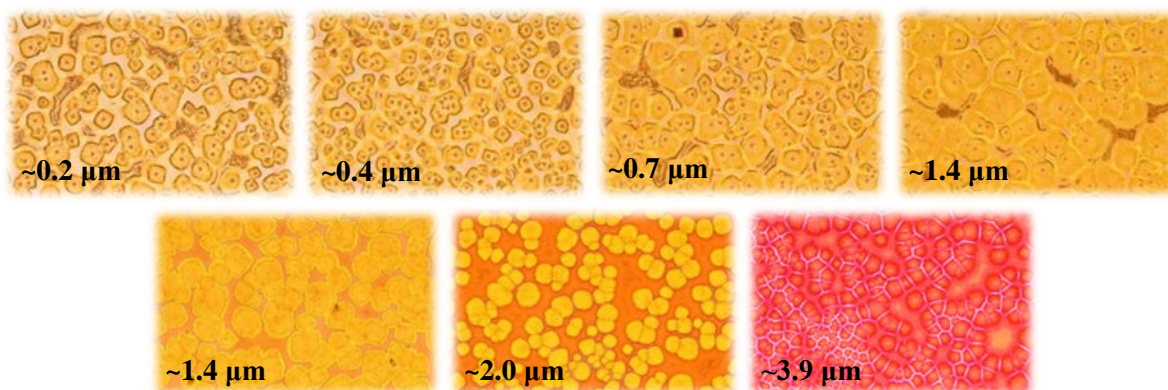


Figure 5.19: Optical microscopy images of MAPbBr₃ thin-films co-sensitised with D205 and prepared on mesoporous titania layers of increasing thickness. Images were captured using a x10 objective.

As with the photographed thin-films, we see an evident increase in the intensity of the coloured dye with increasing active layer thickness. Interestingly, for the thickest films (~ 2.0 and ~ 3.9 μm), there is a clear loss in the perovskite crystal definition, potentially due to increased dye levels or due to the increasing mesoporous layer thickness. For the thinnest films (~ 0.2 and ~ 0.4 μm), it's possible that a perovskite capping layer is present giving rise to the clear crystal definition. Capping layers are not expected to form above 400 nm and therefore, as we move to the thicker layers, we lose the capping layer and see a loss in the crystal definition. It's possible that as the thickness increases, the perovskite forms more deeply within the layer/meso-pores meaning the mesoporous layer dominates in the optical microscopy images and the perovskite crystals are not as clearly defined.

Based on the literature described at the start of this Section, the level of perovskite pore filling would also be expected to vary with increasing mesoporous layer thickness. Thicker films, with a larger titania interface, would be expected to have a lower degree of pore filling as the same volume of perovskite precursor (100 μL) was used across all thicknesses. However, the remaining space can be occupied by a dye as evidenced by the increased dye absorbance (Figure 5.17). It would be interesting to confirm the absence or presence of a capping layer, the pore volume and the location of the perovskite/dye within the layer/pores however, this would need to be studied further using scanning electron microscopy and Brunauer–Emmett–Teller (BET) surface area analysis.

Although increased dye levels were successfully achieved, the resultant photovoltaic effects were yet to be determined. The thin-films were further prepared as full cells and their performance subsequently tested in order to establish the effects of increased dye loading on the device efficiency.

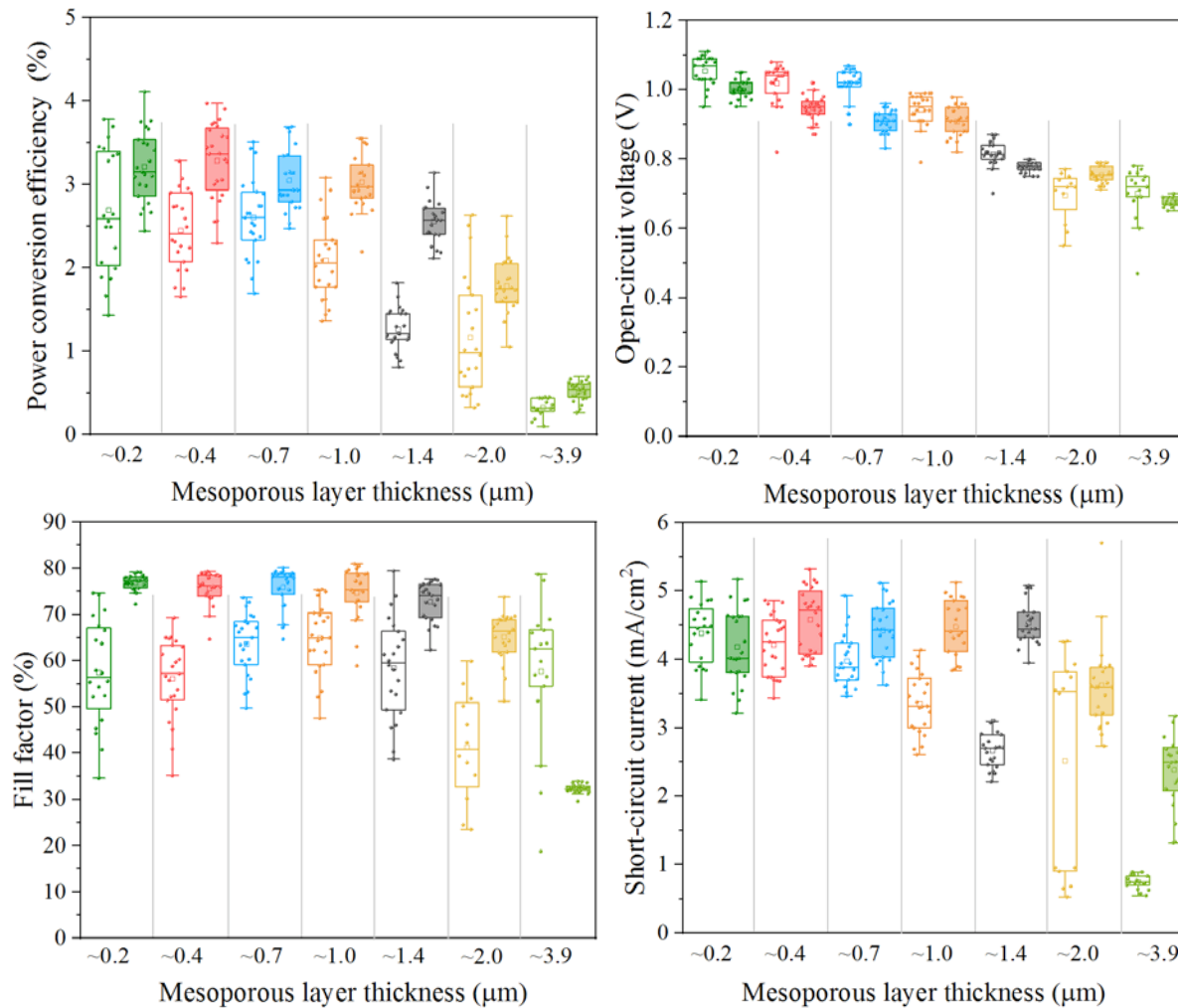


Figure 5.20: Box plots of performance parameters for control (non-filled plots) and co-sensitised (filled plots) MAPbBr₃ cells prepared on increasing thickness of mesoporous titania. Each box plot is generated from the measurement of 24 pixels (three cells) measured per variable.

The average PCE of both the control and co-sensitised cells decreases with increasing active layer thickness (Figure 5.20). Thicker films may lead to a higher concentration of defects as it becomes increasingly difficult to control the uniformity of the layer. Also, if the perovskite is not adequately in contact with the mesoporous layer, this would lead to higher levels of charge recombination as a result of reduced pore filling and poorer perovskite coverage. For thicker cells, it should also be considered that there may be poorer infiltration of the hole transport layer leading to reduced pore filling (within the active layer) and ultimately lower charge extraction.^{18,42} In addition to this, the charges have to navigate longer distances and due to the sheer number generated and there is an increased chance of charge accumulation at the interfaces. When combined, all of these processes are likely to cause increased recombination leading to a reduction in photovoltaic performance. This is supported by the gradual decrease of the J_{sc} and V_{oc} for control cells with increasing mp-TiO₂ thickness (Fig 5.20). When considering the co-sensitised cells, there is a slight decrease in the V_{oc} , however the J_{sc} values are less affected and only begin to decrease at thicknesses $> \sim 1.4 \mu\text{m}$.

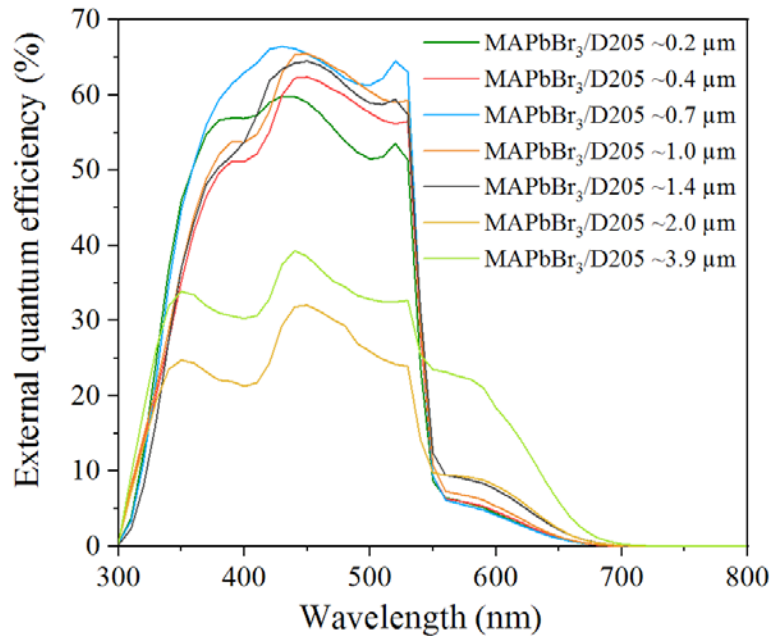
When comparing the photovoltaic performance of the control and co-sensitised cells, the latter out-perform the controls across all thicknesses. The largest increase in average PCE between the control and co-sensitised cells was observed for the $\sim 1.4 \mu\text{m}$ thick active layer. Here, an average control PCE of 1.3% was measured compared to the average co-sensitised PCE of 2.6%.

The increased performance of the co-sensitised cells is from improvements in both the FF and J_{sc} , in line with previous results. Here, increases in the average FF are once again evident for the co-sensitised cells with the largest increase of 20 % observed for the thinnest cells containing a $\sim 0.2 \mu\text{m}$ thick mp-TiO₂ layer (Fig. 5.20). Co-sensitised cells prepared on active layer thicknesses below $\sim 2.0 \mu\text{m}$ each have a large average FF of between 70-80%. Previous research conducted in 2014 by Xiao *et al.* saw similar large increases in FF when solvent annealing MAPbI₃ films with DMSO. Xiao claimed that the average grain size of the solvent annealed films exceeded the film thickness and therefore charges could pass through a single grain without encountering a grain boundary. This in turn was believed to

limited parasitic non-radiative recombination and boost performance.³⁵ Here, it is possible that we see a similar synergistic benefit when using both the dye and dye solvent, toluene in that the former, increases the photocurrent whereas the latter improves the homogeneity of the perovskite layer.

The average J_{sc} of both the control and co-sensitised cells decreases with increasing active layer thickness. However, the average J_{sc} values of the co-sensitised cells vary between 2.38 to 4.18 mA/cm² for the range of thicknesses i.e. ~ 3.9 μm to ~ 0.2 μm , whereas the control cells overall generated lower average J_{sc} values in comparison. Here, values range from 4.38 to 0.74 mA/cm² for the thinnest and thickest cells, respectively. Larger increases in average J_{sc} are evident for the thicker co-sensitised cells, with the largest increase of 1.85 mA/cm² observed for ~ 1.4 μm . These results suggest there is a higher level of dye loading and therefore contribution of photocurrent from the dye for the thicker co-sensitised cells. In addition to this, the observed increases in photocurrent could also be akin to the dye solvent or solution (as a whole) passivating defects within the perovskite layer resulting in reduced non-radiative recombination and enhanced performance. It's also possible in these devices, that the dye has occupied the remaining pore space and reduced recombination at the perovskite-titania interface thereby improving charge extraction and increasing performance. Further investigation into recombination losses (conducted in Section 6.3.2) have revealed that in comparison to control devices, co-sensitised MAPbBr₃ cells show: higher V_{oc} values, increased recombination resistance and increased capacitance at low light intensities. Co-sensitised cells also show DSSC-type behaviour indicative of charge accumulation in the mesoporous titania layer. However, due to the low levels of dye loading observed in Section 5.3.3.3, this accumulation is unlikely to result from direct charge injection from the dye. This suggests that the dye either improves charge injection from the perovskite into the titania or reduces recombination of the charge stored in the mesoporous layer by passivating trap states at the interface. These effects also appeared particularly more beneficial for thicker devices. Therefore, despite being detrimental for control devices, a thicker mesoporous layer and a higher level of dye loading appears to be particularly beneficial for the performance of co-sensitised cells.

Figure 5.21 below, compares the EQE response of the co-sensitised cells.



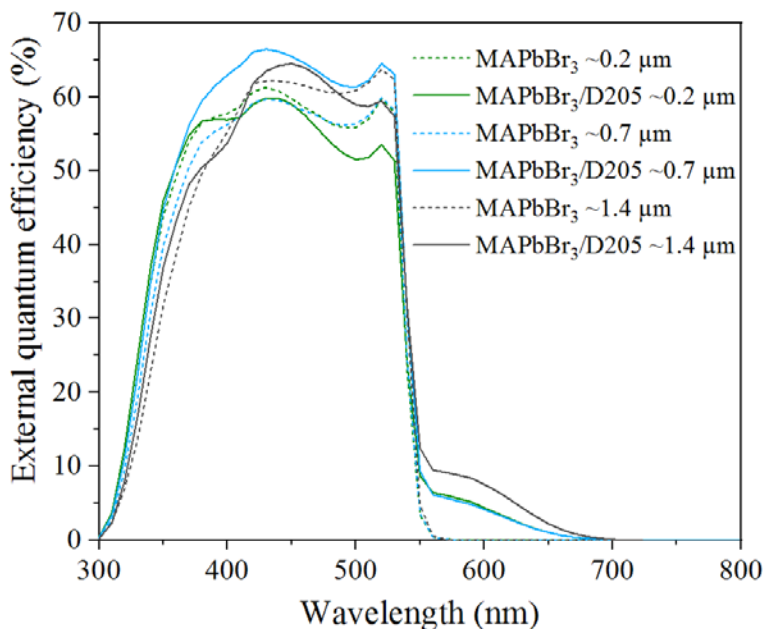
mp-TiO ₂ thickness (μm)	EQE J_{sc} 300-800 nm (mA/cm ²)	EQE J_{sc} 550-800 nm (mA/cm ²)
~0.2	5.08	0.31
~0.4	5.27	0.32
~0.7	5.76	0.30
~1.0	5.57	0.37
~1.4	5.67	0.52
~2.0	2.90	0.54
~3.9	4.40	1.29

Figure 5.21: Measured EQE spectral response and tabulated EQE generated short-circuit current values (EQE J_{sc}) for the hero pixel of MAPbBr₃ cells co-sensitized with D205 when prepared on mesoporous titania layers of increasing thickness.

The highest overall photocurrent of 5.76 mA/cm² is observed for a thickness of ~0.7 μm whereas the lowest (2.90 mA/cm²) is observed for ~2.0 μm. The perovskite EQE signal (300-550 nm) does not vary significantly for thicknesses below ~1.4 μm however, a large reduction in the perovskite EQE is observed for the thickest layers (~2.0 and ~3.9 μm). Here, it is possible that the device thickness has exceeded the diffusion length leading to poor charge collection, increased recombination and a drop in performance. It is also possible, due to the high dye content that the dye is negatively impacting the perovskite

possibly through aggregation. The dye contribution for each thickness is evident between 550-700 nm. The photocurrent contribution from the dye up to a thickness of $\sim 1.0 \mu\text{m}$ is fairly consistent. We then see a slight increase in the contributed photocurrent followed by a more substantial increase for the thicker films, with the thickest co-sensitised cell, $\sim 3.9 \mu\text{m}$ showing the largest dye contribution (approximately 30%). In agreement with the absorption spectra (Fig. 5.17), these results further confirm a thicker mesoporous layer has led to increased dye loading within the cell and ultimately increased photon harvesting within this wavelength range.

For the EQE response of the control cells, measurements were made using a smaller data set consisting of MAPbBr₃ PSC's prepared on three cell thicknesses: ~1.4, ~0.7 and ~0.2 μm. Figure 5.22 below compares the EQE of both control and co-sensitised MAPbBr₃ cells.



Cell ID	mp-TiO ₂ thickness (μm)	EQE J_{sc} 300-800 nm (mA/cm ²)	EQE J_{sc} 550-700 nm (mA/cm ²)
MAPbBr ₃	~0.2	4.98	-
MAPbBr ₃ /D205		5.08	0.31
MAPbBr ₃	~0.7	4.93	-
MAPbBr ₃ /D205		5.76	0.3
MAPbBr ₃	~1.4	5.15	-
MAPbBr ₃ /D205		5.67	0.52

Figure 5.22: Measured EQE spectral response and tabulated EQE generated short-circuit current values (EQE J_{sc}) for the hero pixel of control MAPbBr₃ and MAPbBr₃ cells co-sensitised with D205 when prepared on three thicknesses of mesoporous layer.

For all three thicknesses, the co-sensitised cells show a higher overall photocurrent in comparison to the controls. The perovskite response also appears higher for the thicker co-sensitised cells, with a 0.38 and 0.68 mA/cm² increase observed for ~1.4 μm (grey solid line) and ~0.7 μm (blue solid line), respectively. In agreement with the increased FF values, this further suggests improvement of the perovskite layer as a result of the dye or dye solvent, toluene.

In a separate study, the hysteresis of control and co-sensitised devices prepared on three mesoporous thicknesses (~ 0.2 , ~ 0.7 and ~ 1.4 μm) was evaluated. Hysteresis in PSC's represents the difference between the forward and reverse current-voltage (J-V) scans and has previously been shown to result from ion migration as a result of defects within the perovskite layer.⁴³⁻⁴⁵ Figure 5.23 shows the J-V curves measured for the hero pixel of each device where each device shows some degree of hysteresis. The J-V curves of the control cells (grey lines) show increased hysteresis with increasing mesoporous layer thickness. This is possibly due to a higher density of trap states and charge accumulation at the perovskite interface(s) in the thicker films. The co-sensitised devices (red lines) however, appear to have lower levels of hysteresis. This is particularly evident for the devices prepared using a ~ 0.7 μm thick mesoporous layer (MAPbBr₃/D205 ~ 0.7 μm).

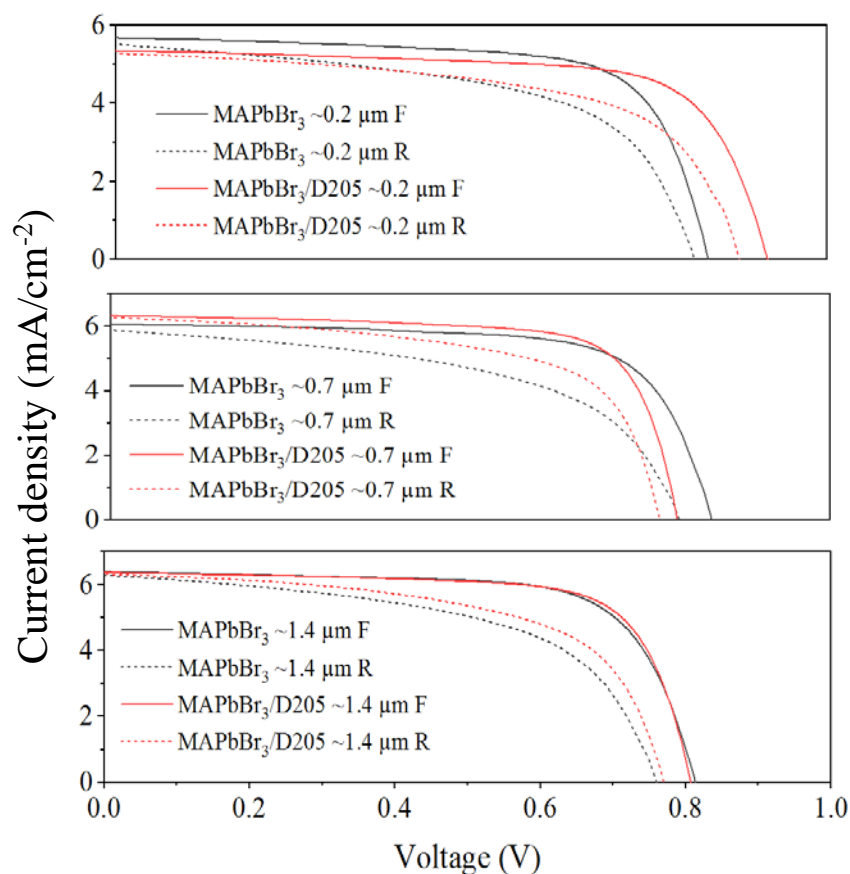


Figure 5.23: Hero J-V curves showing the reverse (R) scan (V_{oc} to J_{sc}) and the forward (F) scan (J_{sc} to V_{oc}) for control and co-sensitised MAPbBr₃ devices prepared on three thicknesses of mesoporous layer (~ 0.2 , ~ 0.7 and 1.4 μm , top, bottom and middle, respectively).

Therefore, the dye acts to reduce hysteresis in the MAPbBr₃ perovskite layer possibly through trap state passivation which subsequently reduces the levels of ion migration and charge trapping at the perovskite/titania interface which overall results in improved charge extraction, increased photocurrent and increased efficiencies as is seen for the thicker co-sensitised devices in Figure 5.20.

5.3.3.3 Quantitation of dye loading

Here, the amount of dye present within each mesoporous layer is quantified by desorbing the dye and calculating its concentration using a calibration line. First and foremost, it was essential to remove the perovskite in order to isolate the dye. This required a solvent capable of desorbing MAPbBr₃ whilst ensuring the dye remained unaffected on the mesoporous titania layer. As an arch-enemy of lead halide perovskites, water was found to be exceptionally suited to this purpose (Figure 5.24).

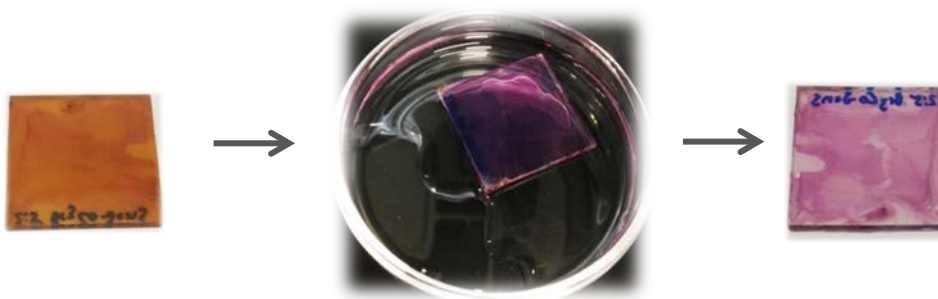


Figure 5.24: Photographs of a single co-sensitised MAPbBr₃ thin-film showing removal of the perovskite layer by washing with water. The photographed image to the left and right shows the co-sensitised perovskite thin-film before and after washing with water, respectively.

Figure 5.25 shows the absorbance response of a co-sensitised MAPbBr₃ film before (1) and after (2) washing with water.

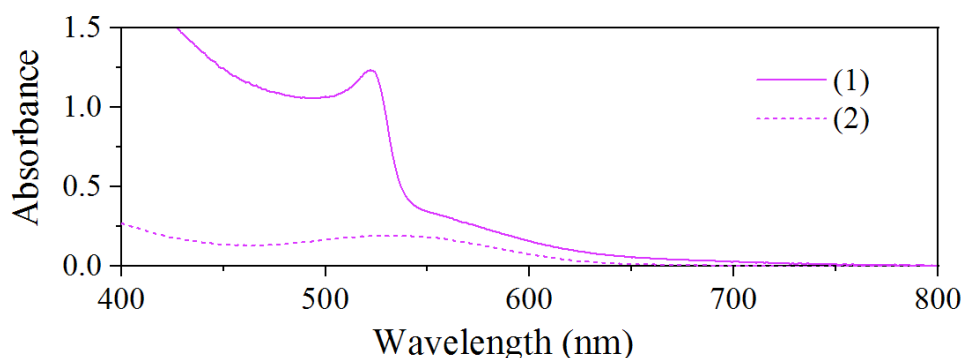


Figure 5.25: Absorbance spectra for a single thin-film of MAPbBr₃ co-sensitised with D205: (1) pristine thin-film (2) after washing with water.

Here, we see the dye absorbance (dashed purple line) is still present between stages (1) and (2) however, it appears the perovskite has been fully dissolved supported by the loss of

absorbance between 400 and 550 nm. There was no absorbance signal when measuring the water solution which confirmed the water did not affect or desorb the dye and was therefore, a suitable solvent for removing the perovskite layer. This is further supported by the photographed thin-film included in Figure 5.24. The dye is still visually evident but the orange MAPbBr₃ perovskite layer is no longer visible.

As discussed in Chapter 4, D205 dye molecules bind to titania *via* carboxylate anchor groups which form ester bonds with the hydroxyl groups located on the titania surface. Therefore, in order to successfully desorb the dye, it was important to find a strong basic solution which was capable of hydrolysing the dye-surface ester bonds without damaging or altering the dye molecules. Sodium hydroxide (NaOH) has previously been used for this purpose, particularly for the desorption of ruthenium dyes from the mesoporous titania electrode of DSSC's.⁴⁶⁻⁴⁸ Therefore, after removing the perovskite layer with water, the dyed thin-film was submerged and washed in a 40 mM NaOH solution for 10 minutes (Figure 5.26).

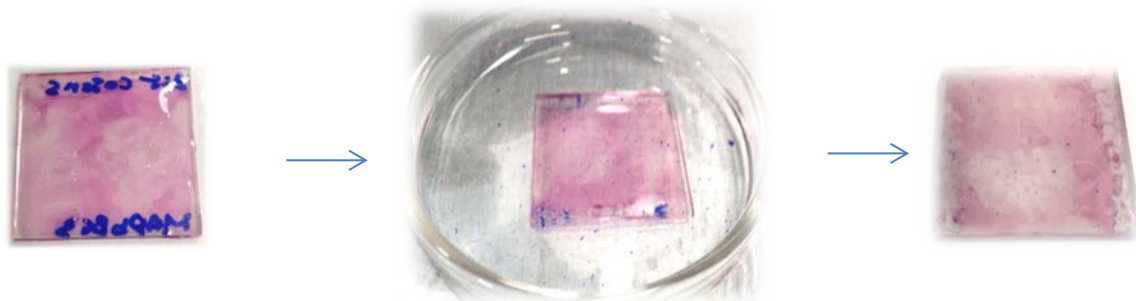


Figure 5.26: Photographs of a single co-sensitised MAPbBr₃ thin-film following removal of the perovskite layer by washing with water (left), during washing with 40 mM NaOH for 10 minutes (center) and following washing with 40 mM NaOH (right).

After ten minutes of washing the thin-film in the 40 mM NaOH solution, a large majority of the dye is still bound to the film and the NaOH solution remains clear as shown in Figure 5.26. Therefore, at this concentration, the NaOH solution was not capable of desorbing the dye from a thin-film prepared on ~0.2 μm mesoporous layer and therefore, would likely have little effect (if any) on thin-films prepared with thicker active layers. The same method was then carried out using DMSO as the desorbing solution. Figure 5.27 shows the dyed thin-film following washing and removal from a solution of DMSO.



Figure 5.27: Photographs of: the dyed thin-film following washing with DMSO (right). The DMSO solution used to wash the dyed thin-film (left).

After ten minutes of soaking some dye is still visible at the edges of the film however, the majority of the dye has been desorbed by the DMSO solution which has transitioned from colourless to pink. Absorbance measurements completed on the DMSO solution and the thin-film (following dye desorption) are shown in Figure 5.28.

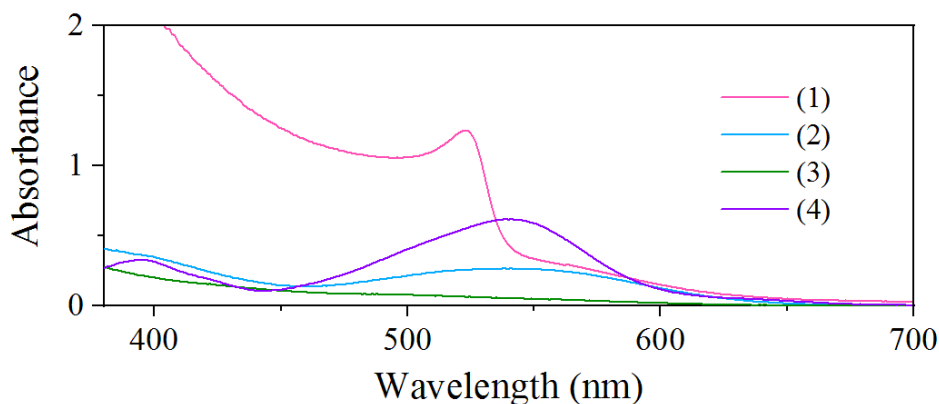


Figure 5.28: Absorbance spectra for a single thin-film of MAPbBr₃ co-sensitised with D205: (1) pristine thin-film, (2) after washing with water, (3) after washing with DMSO, (4) the DMSO solution used to desorb the dye.

We see an obvious difference when comparing the absorbance response of the thin-film before dye desorption ((2), blue line) and following dye desorption ((3), green line) which suggests a large portion of the dye has been extracted from the film. This is further confirmed by the absorbance response of the DMSO solution used for desorption of the dye ((4), purple line). Here, we observe two absorption peaks characteristic of D205 in solution which indicates a large concentration of the dye has been successfully desorbed. The studies here were completed on a 0.2 μm MAPbBr₃ thin-film co-sensitised with 1 mM of D205 dye therefore, thicker films with more dye may require a longer soaking time to ensure all of the dye is fully desorbed.

Figure 5.29 shows the calibration line used to calculate the extinction coefficient of the D205 dye in DMSO. The extinction coefficient of D205 in DMSO was calculated to be $68959 \text{ M}^{-1}\text{cm}^{-1}$ at 543 nm.

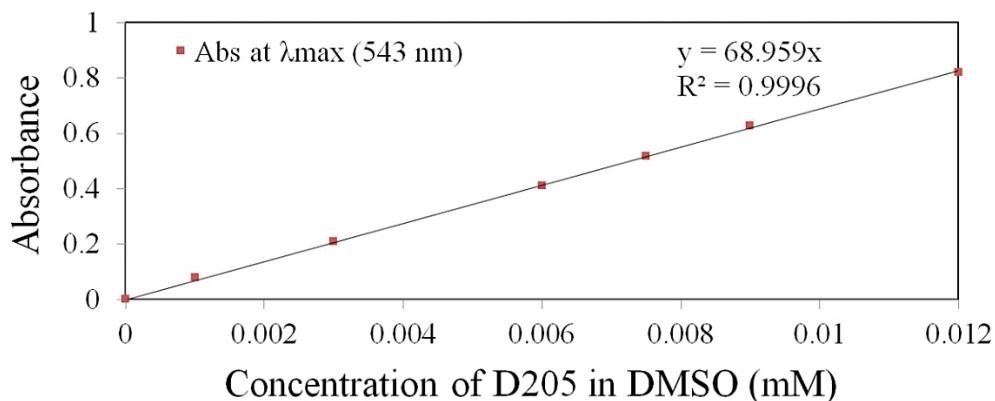


Figure 5.29: Calibration line of absorbance vs concentration for seven D205 calibration standards (in DMSO). Also included is the straight line equation: $y = mx + c$ with the value of c (0), m (68.959) and the coefficient of determination value, R^2 (0.9996).

MAPbBr₃ thin-films co-sensitised with 1 mM of D205 were prepared on the seven mesoporous layer thicknesses discussed in the previous section. For each film, the perovskite layer was removed with water followed by overnight soaking in DMSO for dye desorption.

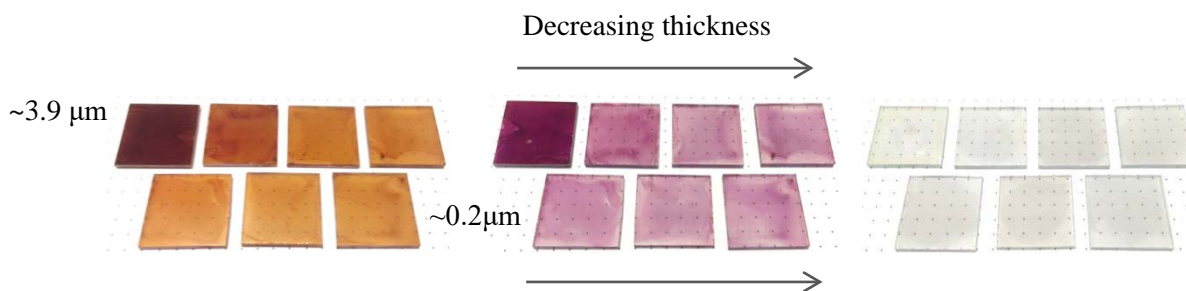


Figure 5.30: Photographs showing the seven co-sensitised MAPbBr₃ thin-films of varying active layer thickness during the two stages of sensitizer desorption. Left: pristine co-sensitised MAPbBr₃ thin-films, center: the dyed thin-films following removal of the perovskite layer through washing with water, right: the mesoporous layers following desorption of the dye through overnight soaking with DMSO. For each image, the films decrease in thickness from left to right where the top left film is the thickest and the bottom right is the thinnest.

Figure 5.30 shows the seven co-sensitised thin-films from initial pristine condition (left) through to complete dye desorption (right). When washed with water, the films lose their orange red colour consistent with removal of the perovskite layer.

When studying the dyed films following perovskite removal (center), as seen previously, the thickest mesoporous layers (top left) show a darker colour indicative of higher dye loading. Visually there is little variation in colour intensity between the thinner films (bottom row) which was further confirmed by absorbance measurements.

The absorbance response of the thinner layers here is very similar (Figure 5.31) however; we see a slight increase in absorbance for the $\sim 2.0 \mu\text{m}$ (gold line) film followed by a significant increase for thickest film ($\sim 3.9 \mu\text{m}$, light green line).

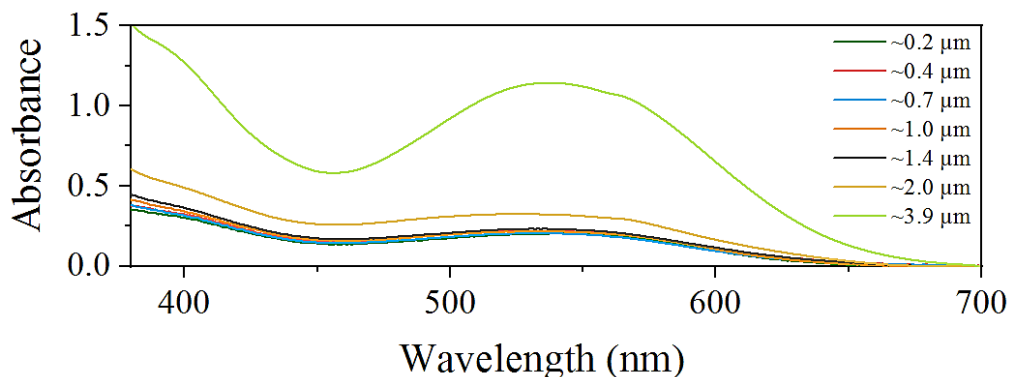


Figure 5.31: Absorbance spectra of the dyed thin-films following perovskite removal with water.

Following overnight soaking in DMSO, the dyed films appeared colourless as shown in Figure 5.30 (right) suggesting the dye had been fully desorbed into the DMSO solution. The absorbance of each DMSO solution was subsequently measured and the concentration of the D205 dye calculated. Table 22 includes the absorbance values at λ_{max} and the calculated dye concentration of each solution per mesoporous layer thickness.

Table 22: Absorbance values (A) generated at 543 nm (λ_{max}) and calculated D205 concentration (μM) for the DMSO solutions used to desorb the dye from co-sensitised MAPbBr_3 films prepared on increasing thickness of mesoporous titania (mp- TiO_2).

Mp- TiO_2 thickness (μm)	A at 543 nm (λ_{max}) of desorbed D205 solution	Calculated D205 concentration (μM)
~ 0.2	0.22	3
~ 0.4	0.24	3
~ 0.7	0.25	4
~ 1.0	0.26	4
~ 1.4	0.36	5
~ 2.0	0.39	6
~ 3.9	0.59	9

The calculated concentrations do show an increasing trend with mesoporous layer thickness however, there is perhaps less variation in concentration between the thicknesses than expected. The results here, in agreement with the absorbance and EQE of each film (Figure 5.18 and 5.22, respectively), show that for the thinnest mesoporous layers; there is little difference in the amount of dye present. It is thought that the dye fills any remaining space within mesoporous layer which has not been occupied by the perovskite. For the thinner layers especially, this suggests the perovskite occupies a lot of the space leaving little remaining for the dye. It is only when moving to considerably thicker layers that we see larger increases in dye loading, where the highest desorbed dye concentration is seen for the thickest layer. For thicker cells, in theory there is more space available within the mesoporous layer which, through co-sensitisation, can be occupied by the dye. However, when previously using a thicker mesoporous layer, we have seen large increases in the EQE dye response but also a loss in perovskite performance.

5.3.4 Co-sensitisation of MAPbI₃ perovskite

The experiments included in this Chapter have culminated in an optimised co-sensitisation method which has consistently shown benefits when used with MAPbBr₃ PSC's. This section explores the transferability of the method by applying it to MAPbI₃ PSC's in a bid to achieve higher efficiencies through co-sensitisation.

Here, both control and co-sensitised MAPbI₃ PSC's have been prepared on the seven mesoporous titania thicknesses previously discussed (Section 5.2.1). The mesoporous layer thickness has been varied to assess the effects of dye loading when co-sensitising MAPbI₃ with with 1 mM of D205. Unlike the semi-transparent orange colour of MAPbBr₃, MAPbI₃ films are opaque and dark brown to almost black in colour as shown below.



Figure 5.32: Photographs showing perovskite thin-films of: MAPbBr₃ (left) and MAPbI₃ (right) highlighting the dark brown / black colour of the latter perovskite.

Therefore, when co-sensitised with D205, there is no visible colour change of the MAPbI₃ perovskite layer. Figure 5.33 shows the absorbance spectra of control and co-sensitised MAPbI₃ thin-films prepared on three thicknesses of mesoporous layer. The ebony-esque appearance of MAPbI₃ perovskite arises from its broad absorbance response which extends well into the deep red region before decreasing at around 760 nm.

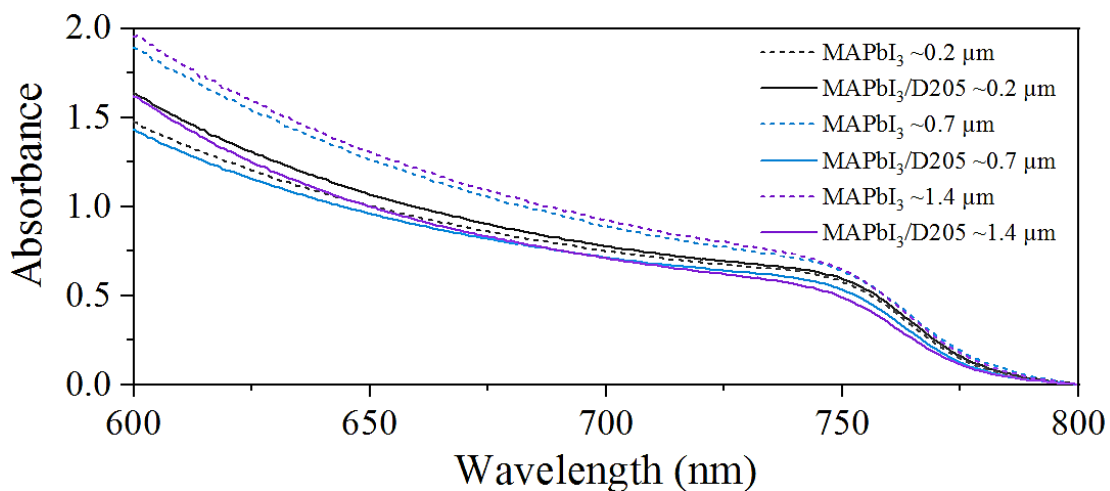


Figure 5.33: Absorbance spectra of control MAPbI₃ and MAPbI₃ films co-sensitised with D205 on three thicknesses of mesoporous layer.

In contrast to co-sensitised MAPbBr₃ thin-films, here we see little difference between the control and co-sensitised absorbance as the D205 signal is masked by the broad perovskite range. Due to this, it is not possible to separate the dye and perovskite response. The control and co-sensitised thin-films were prepared as full cells and their performance measured (Figure 5.34).

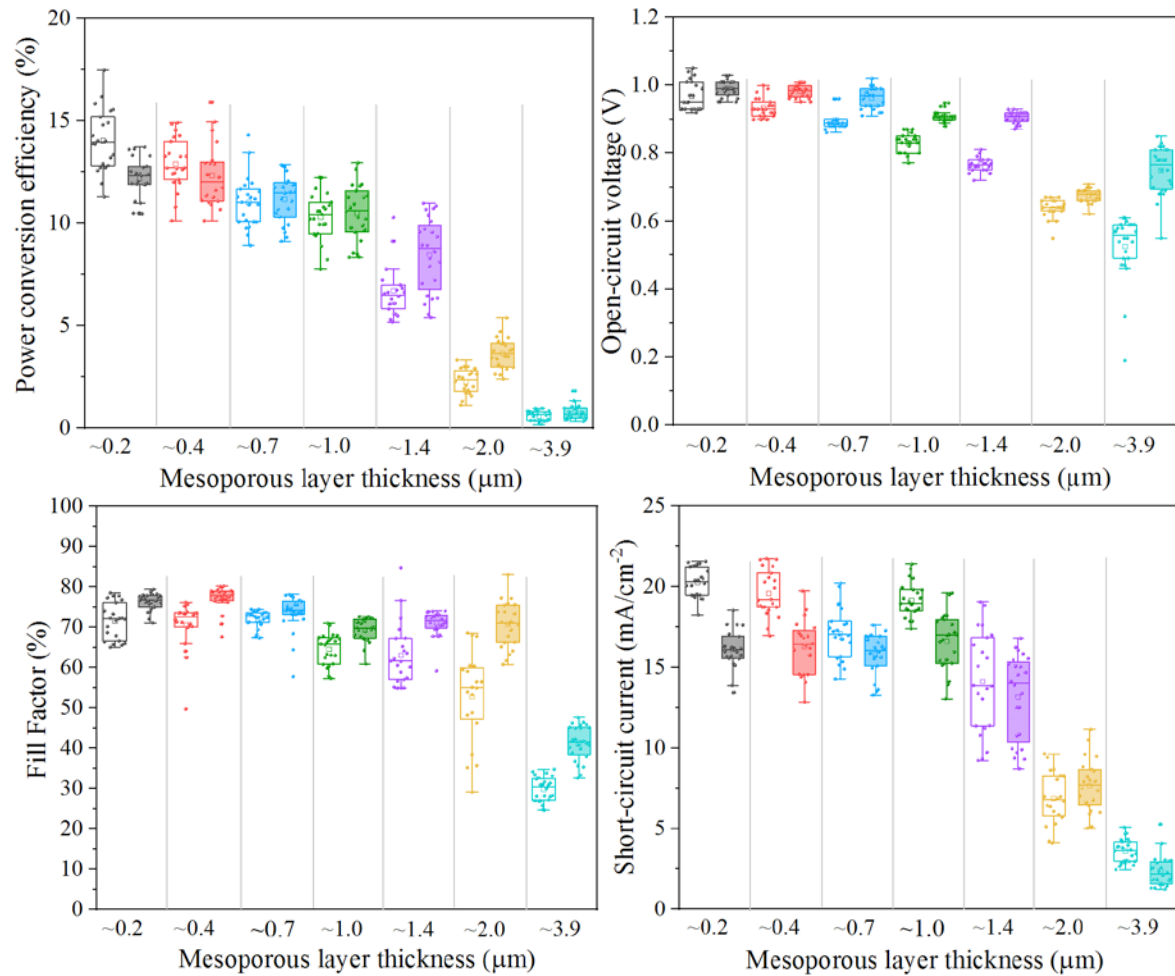


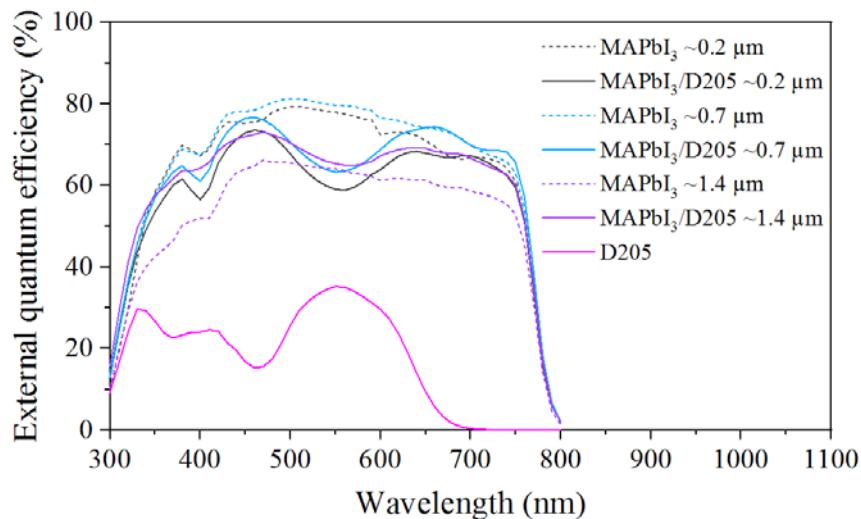
Figure 5.34: Box plots of photovoltaic parameters for control (non-filled plots) and co-sensitized (filled plots) MAPbI₃ cells prepared on increasing thickness of mesoporous titania. Each box plot is generated from the measurement of 24 pixels (three cells) measured per variable.

Generally, all four photovoltaic parameters decreased with increasing film thickness possibly due to increased levels of recombination. However, in the majority of cases, the performance of the controls decreased more sharply in comparison to the co-sensitised cells.

When comparing the average PCE of the control and co-sensitised cells (Figure 5.34), the latter showed an increase in efficiency for five out of seven of the mesoporous layer thicknesses (from $\sim 0.7 \mu\text{m}$ and $\sim 3.9 \mu\text{m}$). The largest average increase of 1.8% was observed for co-sensitised cells with a $\sim 1.4 \mu\text{m}$ active layer. The average V_{oc} values for control cells vary between 0.53 V for the thickest cells ($\sim 3.9 \mu\text{m}$) and 0.97 V for the thinnest cells ($\sim 0.2 \mu\text{m}$). Whereas, for co-sensitised cells, values vary between a narrower range of 0.75 V and 0.99 V for ~ 3.9 and $\sim 0.2 \mu\text{m}$, respectively. Overall, the average V_{oc} increased with co-sensitisation for all cell thicknesses studied, with the largest increases generally observed for the thicker cells. The average FF decreases with increasing mesoporous layer thickness for both control and co-sensitised cells as a result of the decreased photo-voltage and possibly due to increased charge transfer resistance. However as seen when co-sensitising MAPbBr_3 , the average FF values of the co-sensitised cells exceed those generated for the controls. The largest increase was observed for the $\sim 2.0 \mu\text{m}$ cells where average FF values of 53 and 71 were calculated for control and co-sensitised MAPbI_3 cells, respectively. As seen for the other parameters, the average J_{sc} is largely affected by the increasing cell thickness and declines more significantly for both control and co-sensitised cells at thicknesses above $\sim 1.0 \mu\text{m}$. Only one thickness ($\sim 2.0 \mu\text{m}$) showed increased average J_{sc} with co-sensitisation. These results are in contrast to the results generated for MAPbBr_3 , where the average J_{sc} increased with co-sensitisation.

Overall, the large majority of cell thicknesses show reduced photocurrent with co-sensitisation despite this however, both the FF and V_{oc} were enhanced which, for the thicker cells, saw an increase in the efficiency. For these cells, at this point, one must consider if it is simply the dye solvent, toluene improving the active layer homogeneity and ultimately charge transport within the thicker active layers. The observed improvements in FF would reinforce this theory however further investigation into the effects of toluene are required and have been addressed in the next Chapter.

EQE measurements were performed to further study the effects of the dye and dye loading on the photocurrent of MAPbI₃ PSC's. The measurements were made using a smaller data set consisting of control and co-sensitised devices prepared on three device thicknesses: ~1.4, ~0.7 and ~0.2 μm.



Cell ID	mp-TiO ₂ thickness (μm)	EQE J_{sc} 300-800 nm (mA/cm ²)
MAPbI ₃	~0.2	17.9
MAPbI ₃ /D205		16.2
MAPbI ₃	~0.7	18.5
MAPbI ₃ /D205		17.0
MAPbI ₃	~1.4	15.0
MAPbI ₃ /D205		16.7

Figure 5.35: Measured EQE spectral response and tabulated EQE generated short-circuit current values (EQE J_{sc}) for the hero pixel of control MAPbI₃ and MAPbI₃ films co-sensitised with D205 on three thicknesses of mesoporous layer. Also included is spectral response of a solid state D205 device.

In agreement with the absorbance spectrum, MAPbI₃ shows a broad EQE response which extends from 300 to 800 nm (Figure 5.35). The maximum EQE response of both control and co-sensitised MAPbI₃ cells occurs between 410 – 750 nm followed by a steep decline in signal at 760 nm. Within the maxima wavelength region, thinner control devices (~0.2 and ~0.7 μm, dashed grey and blue lines, respectively) generate ≥ 70% EQE whereas the thicker device (~1.4 μm, dashed purple line) generates a lower EQE (≥ 60%).

When considering the EQE response of the co-sensitised cells, the two thinner variables (~ 0.2 and ~ 0.7 μm) produced a lower J_{sc} compared to the controls (Fig 5.35). The thickest co-sensitised cell (~ 1.4 μm) however, demonstrated a higher photocurrent (compared to the control device) which could be attributed to the dye. However, due to the broad absorption range of MAPbI₃, the EQE response of D205 is masked and therefore the dye contribution here cannot be calculated. In contrast to the EQE's of the control devices, the co-sensitised cells each show a pronounced drop in EQE between 450 and 650 nm which interestingly, corresponds to the λ_{max} of the solid state D205 response. This drop in signal is potentially due to competitive light absorption between the two sensitiser. The solid state D205 cell has an EQE of ca. 40% in this region whilst the control MAPbI₃ EQE response is ca. 80%. Therefore, in a co-sensitised cell, the D205 dye may be absorbing light that doesn't reach the perovskite and thus lowers the perovskite EQE. This also implies that the dye is close to the electron transport layer interface.

When collectively considering the data in this section, we see some benefits when co-sensitising MAPbI₃ PSC's, especially for the thicker cells. However, when implemented in cells with a thinner active layer, co-sensitisation appears detrimental causing a large drop in photocurrent. Here, the dye acts to impede the performance of the perovskite rather than enhance it which is possibly due to competitive light absorption.

5.4 Conclusions

This initial series of investigations has shown that it is possible to co-sensitise perovskite solar cells with organic dyes which has not only allowed for colour alteration of the perovskite layer but also improved the overall device performance.

Cells co-sensitised using the ‘dye-after’ method (where the film is sensitised after perovskite deposition) demonstrated overall increased performance with efficiency increases of 0.4 and 0.6% observed for SQ2 and D205, respectively. Cells co-sensitised using the ‘dye-before’ method (where the film is sensitised before perovskite deposition) demonstrated reduced performance compared to controls where the dye is thought to negatively affect perovskite nucleation by reducing the space available within the mesoporous layer. Alternatively, the dye-after method is thought to encourage the dye to fill any unoccupied space on the titania surface, allowing colour tuning whilst increasing the overall photocurrent and improving the FF of the cell.

Increasing the dye loading with dye concentration showed a general trend of increased efficiency with concentration. The highest average PCE’s of 2.0 and 2.3% were observed for SQ2 and D205, respectively when using a 1 mM dye solution. However, as seen for D205, more concentrated dye solutions may prove detrimental to performance and therefore, there is a limit on the amount of dye that can beneficially added to a system before it begins to have a detrimental effect.

Higher dye loading was also achieved when co-sensitising MAPbBr₃ cells with a thicker active layer. When comparing the photovoltaic performance of the control and co-sensitised cells, the latter out-performed the controls across all thicknesses. The largest increase in average PCE (1.3 %) was observed for the ~1.4 μm thick active layer where increased efficiencies resulted from the fill factor and photocurrent. However, the thickest cells (~2.0 and ~3.9 μm) showed poorer performance and reduced perovskite EQE indicating a balance between maximising the response from the dye without hindering the performance of the perovskite.

Co-sensitisation of MAPbI₃ PSC’s showed increased efficiencies for thicker cells (>0.4 μm) with the largest increase of 1.8% observed for ~1.4 μm. Following co-sensitisation,

increases in both the FF and V_{oc} were observed for all active layer thicknesses however, the large majority of cell thicknesses showed reduced photocurrent.

Throughout this work, increased efficiencies were derived mainly from the FF which was consistently and often significantly enhanced following co-sensitisation. Co-sensitised here MAPbBr₃ cells also frequently demonstrated a higher short-circuit current in comparison to the controls. EQE measurements showed some additional photocurrent contribution from the dye however, this was not substantial enough to cause the observed increases. The main increase in the J_{sc} appeared to originate from the perovskite response which was often enhanced as a result of co-sensitisation. These findings, in part, suggest that the dye solution may improve the crystallinity of the perovskite layer thereby enhancing charge transfer and lowering recombination. By introducing the dye after perovskite deposition, it is possible that the dye solution effectively ‘heals’ defects within the perovskite layer and therefore, in a way, acts as an additive solvent treatment.

5.5 References

1. Perkin, W. H. *Producing a new coloring matter for dyeing with a lilac or purple color stuffs of silk, cotton, wool or other materials*. 1. GB1984/1856. Shelfmark IP Reserve South (1856).
2. Hardin, B. E. *et al.* Energy and hole transfer between dyes attached to titania in cosensitized dye-sensitized solar cells. *J. Am. Chem. Soc.* **133**, pp. 10662–10667 (2011).
3. Ehret, A., Stuhl, L. & Spitler, M. T. Spectral sensitization of TiO₂ nanocrystalline electrodes with aggregated cyanine dyes. *J. Phys. Chem. B* **105**, pp. 9960–9965 (2001).
4. Sharma, G. D. *et al.* Efficient dye-sensitized solar cells based on cosensitized metal free organic dyes with complementary absorption spectra. *J. Renew. Sustain. Energy* **5**, 043107 (2013).
5. Ogura, R. Y. *et al.* High-performance dye-sensitized solar cell with a multiple dye system. *Appl. Phys. Lett.* **94**, pp. 118–122 (2009).
6. Kakiage, K. *et al.* Highly-efficient dye-sensitized solar cells with collaborative sensitization by silyl-anchor and carboxy-anchor dyes. *Chem. Commun.* **51**, pp. 15894–15897 (2015).
7. Kakiage, K., Kyomen, T. & Hanaya, M. Improvement in photovoltaic performance of dye-sensitized solar cells by cosensitization with an organometal halide perovskite. *Chem. Lett.* **42**, pp. 1520–1521 (2013).
8. Pinpithak, P., Kulkarni, A., Chen, H. W., Ikegami, M. & Miyasaka, T. Solid-state thin-film dye-sensitized solar cell Co-sensitized with methylammonium lead bromide perovskite. *Bull. Chem. Soc. Jpn.* **91**, pp. 754–760 (2018).
9. Falaras, P. *et al.* Dye Sensitization of Titania Compact Layer for Efficient and Stable Perovskite Solar Cells. *ACS Appl. Energy Mater.* **1**, pp. 6161–6171 (2018).
10. Xiong, S. *et al.* Defect-Passivation Using Organic Dyes for Enhanced Efficiency and Stability of Perovskite Solar Cells. *Sol. RRL* **4**, 1900529 (2020).
11. Li, X. *et al.* Efficient Passivation of Hybrid Perovskite Solar Cells Using Organic Dyes with \square COOH Functional Group. *Adv. Energy Mater.* **8**, 1800715 (2018).
12. Ouedraogo, N. A. N. *et al.* Stability of all-inorganic perovskite solar cells. *Nano Energy* **67**, 104249 (2020).
13. Jeon, N. J. *et al.* Solvent engineering for high-performance inorganic–organic hybrid perovskite solar cells. *Nat. Mater.* **13**, pp. 897–903 (2014).

14. Sakai, N. *et al.* The mechanism of toluene-assisted crystallization of organic-inorganic perovskites for highly efficient solar cells. *J. Mater. Chem. A* **4**, pp. 4464–4471 (2016).
15. Kara, K. *et al.* Solvent washing with toluene enhances efficiency and increases reproducibility in perovskite solar cells. *RSC Adv.* **6**, pp. 26606–26611 (2016).
16. Falaras, P. *et al.* Dye Sensitization of Titania Compact Layer for Efficient and Stable Perovskite Solar Cells. *ACS Appl. Energy Mater.* **1**, pp. 6161–6171 (2018).
17. Yin, J. *et al.* Improved stability of perovskite solar cells in ambient air by controlling the mesoporous layer†. *J. Mater. Chem. A* **3**, pp. 16860–16866 (2015).
18. Kim, H.-S. *et al.* Lead Iodide Perovskite Sensitized All-Solid-State Submicron Thin Film Mesoscopic Solar Cell with Efficiency Exceeding 9%. *Sci. Rep.* **2**, 591 (2012).
19. Liu, M., Johnston, M. B. & Snaith, H. J. Efficient planar heterojunction perovskite solar cells by vapour deposition. *Nature* **501**, pp. 395–398 (2013).
20. Singh, R., Sandhu, S. & Lee, J. J. Elucidating the effect of shunt losses on the performance of mesoporous perovskite solar cells. *Sol. Energy* **193**, pp. 956–961 (2019).
21. Eperon, G. E., Burlakov, V. M., Docampo, P., Goriely, A. & Snaith, H. J. Morphological control for high performance, solution-processed planar heterojunction perovskite solar cells. *Adv. Funct. Mater.* **24**, pp. 151–157 (2014).
22. Liu, H. *et al.* Nano-structured electron transporting materials for perovskite solar cells. *Nanoscale* **8**, pp. 6209–6221 (2016).
23. Yang, Y. *et al.* The size effect of TiO₂ nanoparticles on a printable mesoscopic perovskite solar cell†. *J. Mater. Chem. A* **3**, pp. 9103–9107 (2015).
24. Leitjens, T., Lauber, B., Eperon, G. E., Stranks, S. D. & Snaith, H. J. The Importance of Perovskite Pore Filling in Organometal Mixed Halide Sensitized TiO₂-Based Solar Cells. *J. Phys. Chem. Lett.* **5**, pp. 1096–1102 (2014).
25. Correa-Baena, J.-P. *et al.* Unbroken Perovskite: Interplay of Morphology, Electro-optical Properties, and Ionic Movement. *Adv. Mater.* **28**, pp. 5031–5037 (2016).
26. Apostolopoulou, A., Sygkridou, D., Kalarakis, A. N. & Stathatos, E. High Efficiency Perovskite Solar Cells Fabricated under Ambient Conditions with Mesoporous TiO₂/In₂O₃ Scaffold. *Int. J. Electron. Commun. Eng.* **11**, pp. 113–116 (2017).
27. Ball, J. M. *et al.* Low-temperature processed meso-superstructured to thin-film perovskite solar cells. *Energy Environ. Sci.* **6**, 1739 (2013).
28. Chen, Q. *et al.* Planar heterojunction perovskite solar cells via vapor-assisted solution process. *J. Am. Chem. Soc.* **136**, pp. 622–625 (2014).

29. Lim, K. G. *et al.* Boosting the power conversion efficiency of perovskite solar cells using self-organized polymeric hole extraction layers with high work function. *Adv. Mater.* **26**, pp. 6461–6 (2014).
30. Momblona, C. *et al.* Efficient methylammonium lead iodide perovskite solar cells with active layers from 300 to 900 nm. *APL Mater.* **2**, 081504 (2014).
31. Zhang, B. *et al.* Carrier Transport in CH₃NH₃PbI₃ Films with Different Thickness for Perovskite Solar Cells. *Adv. Mater. Interfaces* **3**, 1600327 (2016).
32. Lee, D. G. *et al.* Effect of TiO₂ particle size and layer thickness on mesoscopic perovskite solar cells. *Appl. Surf. Sci.* **31**, pp. 131–136 (2019).
33. Dong, Q. *et al.* Electron-hole diffusion lengths > 175 μm in solution-grown CH₃NH₃PbI₃ single crystals. *Science (80-.)*. **347**, pp. 967–970 (2015).
34. Burschka, J. *et al.* Sequential deposition as a route to high-performance perovskite-sensitized solar cells. *Nature* **499**, pp. 316–319 (2013).
35. Xiao, Z. *et al.* Solvent Annealing of Perovskite-Induced Crystal Growth for Photovoltaic-Device Efficiency Enhancement. *Adv. Mater.* **26**, pp. 6503–6509 (2014).
36. Kedem, N. *et al.* Light-Induced Increase of Electron Diffusion Length in a p-n Junction Type CH₃NH₃PbBr₃ Perovskite Solar Cell. *J. Phys. Chem. Lett.* **6**, pp. 2469–2476 (2015).
37. Sheng, R. *et al.* Methylammonium lead bromide perovskite-based solar cells by vapor-assisted deposition. *J. Phys. Chem. C* **119**, pp. 3545–3549 (2015).
38. Brenner, T. M., Egger, D. A., Kronik, L., Hodes, G. & Cahen, D. Hybrid organic - Inorganic perovskites: Low-cost semiconductors with intriguing charge-transport properties. *Nat. Rev. Mater.* **1**, 15007 (2016).
39. Xing, G. *et al.* Long-range balanced electron-and hole-transport lengths in organic-inorganic CH₃NH₃PbI₃. *Science (80-.)*. **342**, pp. 344–347 (2013).
40. Wehrenfennig, C., Eperon, G. E., Johnston, M. B., Snaith, H. J. & Herz, L. M. High charge carrier mobilities and lifetimes in organolead trihalide perovskites. *Adv. Mater.* **26**, pp. 1584–1589 (2014).
41. Stranks, S. D. *et al.* Electron-hole diffusion lengths exceeding 1 micrometer in an organometal trihalide perovskite absorber. *Science (80-.)*. **342**, pp. 341–344 (2013).
42. Snaith, H. J. *et al.* Charge collection and pore filling in solid-state dye-sensitized solar cells. *Nanotechnology* **9**, pp. 42875–42882 (2008).
43. Eames, C. *et al.* Ionic transport in hybrid lead iodide perovskite solar cells. *Nat. Commun.* **6**, pp. 1–8 (2015).

44. Azpiroz, J. M., Mosconi, E., Bisquert, J. & De Angelis, F. Defect migration in methylammonium lead iodide and its role in perovskite solar cell operation. *Energy Environ. Sci.* **8**, pp. 2118–2127 (2015).
45. Van Reenen, S., Kemerink, M. & Snaith, H. J. Modeling Anomalous Hysteresis in Perovskite Solar Cells. *J. Phys. Chem. Lett.* **6**, pp. 3808–3814 (2015).
46. Holliman, P. J. *et al.* Development of selective, ultra-fast multiple co-sensitization to control dye loading in dye-sensitized solar cells. *RSC Adv.* **4**, pp. 2515–2522 (2014).
47. Heo, N., Jun, Y. & Park, J. H. Dye molecules in electrolytes: New approach for suppression of dye-desorption in dye-sensitized solar cells. *Sci. Rep.* **3**, pp. 284–289 (2013).
48. Chen, R. T. & Liao, C. F. Evaluation and optimization to recycle used TiO₂ photoelectrode for dye-sensitized solar cells. *Int. J. Photoenergy* **2014**, pp. 118–124 (2014).

6 The interaction between perovskite and dye

6.1 Introduction

It is widely known that solution based polycrystalline films are more susceptible to defects due to the rapid annealing and fast crystallisation of the perovskite during processing.^{1,2} Defects, which contribute to non-radiative recombination losses, generally arise due to un-coordinated ions at the crystal surface and also at the grain boundaries between neighbouring crystals.³ This in turn, is highly detrimental to the cell performance, limiting both the V_{oc} and FF. In an attempt to reduce defects, researchers have previously added modifying chemistries to the perovskite precursor solution to improve the perovskite morphology on annealing. Jin *et al.* reported an improvement in the performance of MAPbI₃ PSC's (from 16.4 to 18.2%) on adding zinc chloride (ZnCl₂) to the precursor solution which enhanced the grain size and crystal morphology.⁴ Improved performance was also observed by Mabrouk *et al.* on doping the MAPbI₃ perovskite precursor with lithium salts. Increases from 11.3% to 18%, 17% and 15.6% were achieved when including 1-butyl-3-methylimidazolium iodide, lithium iodide and bis(trifluoromethane)sulfonimide lithium salt to the perovskite precursor solutions, respectively.⁵ Similar benefits have also been seen when adding: ammonium chloride⁶, 1-5-aminovaleric acid⁷ and γ -butyrolactone⁸ to the MAPbI₃ perovskite precursor.

Post-annealing treatment, which involves treating the perovskite layer after deposition and annealing, is another morphology engineering method implemented by researchers to target and passivate surface defects. Various chemistries (typically deposited *via* spin coating) have been investigated and proven successful for such a purpose. In 2014, Noel *et al.* reported reduced non-radiative recombination by using organic Lewis bases, thiophene and pyridine to surface treat cells prepared using an iodide-chloride perovskite blend (CH₃NH₃PbI_{3-x}Cl_x). Cell efficiencies were enhanced from 13% to 15.3 and 16.5% for thiophene and pyridine treated cells, respectively where increases were attributed to the passivation of un-coordinated lead ions in the perovskite crystal.³ A similar effect was also

observed when treating the same hybrid halide blend with iodopenta-fluorobenzene (IPFB) which was reported to passivate excess iodine ions on the perovskite surface.⁹

More recently, the use of organic halide salts as a surface treatment has also proven beneficial. In 2019, Jiang *et al.* treated mixed perovskite films ($\text{FA}_{1-x}\text{MA}_x\text{PbI}_3$) with phenethylammonium iodide (PEAI) which reduced surface defects and suppressed non-radiative recombination resulting in higher-efficiency cells (23.3%).¹⁰ Similarly, Li *et al.* used phenethylammonium chloride (PEACl) to passivate the surface of a wide bandgap (1.75 eV) perovskite blend ($\text{FA}_{0.6}\text{MA}_{0.4}$)_{0.9} $\text{Cs}_{0.1}\text{Pb}(\text{I}_{0.6}\text{Br}_{0.4})_3$. Defect passivation here, lead to a high PCE of 18.3%, which is one of the highest reported efficiencies for an inverted wide-bandgap PSC.¹¹

Aside of spin coating additives onto the perovskite layer, an alternative introduction method termed ‘post-device ligand’ treatment was developed by Zhang *et al.* This method involves encapsulating the perovskite thin-film in a diethylenetriamine (DETA) ligand vapour environment. The ligand vapours formed a stable low-dimensional perovskite complex which passivated surface defects and protected the perovskite layer from moisture. This ultimately increased both the cell performance (from 18.7% to 20.13% efficiency) and stability.¹²

Thus, in some cases, additives have not only enhanced the performance of perovskite solar cells but also concurrently extended their stability. A recent publication by Guo *et al.* highlighted this by adding carbon quantum dots (CQDs) to the MAPbI_3 precursor solution. The CQD hydroxyl and amino groups were shown to bind with un-coordinated lead ions leading to grain boundary passivation. This not only increased the efficiency from 17.6 to 18.8% but the hydrophobicity of the CQDs increased the stability of the cells when stored under ambient conditions for 4 months.¹³ Thambidurai *et al.* found anilinium thiobenzoate (ATB) acted as a stabilising agent when spin-coated onto the surface of a mixed halide perovskite blend. The sulfur (–S) and ammonium (–NH₃) functional groups present within ATB were believed to passivate un-coordinated ions present on the perovskite surface. High efficiencies of 19.3% were achieved in combination with cells which retained ~92% of the initial efficiency even after 150 days of ambient storage.¹⁴

This Chapter further explores the effects observed when co-sensitising PSC's with a dye. The research included, aims to confirm if the dye is responsible for the improved performance of the co-sensitised cells or whether it is simply the dye solvent, toluene acting as a surface treatment. Co-sensitised MAPbBr₃ PSC's have previously shown increases in both J_{sc} and FF however, improvement in the latter appears to be an important parameter for the enhanced cell efficiencies. The observed increases in FF suggest that toluene may passivate trap states within the perovskite layer thereby suppressing non-radiative recombination. This has been further investigated using impedance spectroscopy and photoluminescence lifetime measurements. Finally, the effect of the dye solution on the stability of perovskite solar cells when stored under constant illumination has been also been investigated.

6.2 Experimental methods

6.2.1 Planar cells

Planar perovskite solar cells were prepared as standard using the cell build method described in Section 2.1 however, the mesoporous layer was omitted. The perovskite layer was prepared and deposited directly on to the compact titania layer (as described in Section 2.1.2) followed by co-sensitisation (where necessary) using the dye-after method as described in Section 2.2.3.2. The hole transport layer was subsequently deposited as described in Section 2.1.3.

6.2.2 Mesoporous titania preparation for varied thickness

Cells of varying mesoporous thickness were prepared as described in Section 5.2.1. Several of the studies conducted in this Chapter have been completed using a smaller set of mesoporous layer thicknesses (~0.2, ~0.7 and ~1.4 μm) in order to maintain clarity within the text.

6.2.3 Toluene soak

As a control measure and to assess the effect of the dye solvent, MAPbI_3 and MAPbBr_3 thin-films were submerged in anhydrous toluene for 10 minutes. The thin-films were then removed from the solution and subsequently dried with an air gun. The hole transport layer was subsequently deposited as described in Section 2.1.3.

6.2.4 Approximate series resistance

Approximate series resistance (R_s) values were obtained from J-V curves generated under 1 sun irradiation, where the values represent a forward sweep at a single speed. The series resistance values were calculated by finding the slope of the J-V curve at the open-circuit voltage point.

$$R_s = \frac{\Delta V_{oc}}{\Delta I_{oc}} \quad (34)$$

Where I_{oc} is the open-circuit current. The slope was then multiplied by the area of incidence (0.09 cm^2) to provide an estimate of R_s . The average values described in Section 6.3.3 were calculated from the R_s values of 24 pixels (i.e. 3 perovskite solar cells).

The instrumental details and settings for steady state PL emission, time correlated single photon counting (TCSPC), impedance spectroscopy (IS) and lightbox stability measurements are all listed in Sections 2.3.2.1, 2.3.2.2, 2.4.4 and 2.4.3, respectively.

6.3 Results and discussion

Optical microscopy and XRD measurements were used to study and compare the perovskite layer of control and co-sensitised MAPbBr₃ thin-films. Figure 6.0 (a) and (b) show that visually, the two films appeared very similar with no obvious variation between the size, shape and quantity of the cubic MAPbBr₃ crystals before and after co-sensitisation. The XRD patterns of control, co-sensitised and toluene soaked MAPbBr₃ thin-films are shown in Figure 6.0 (c).

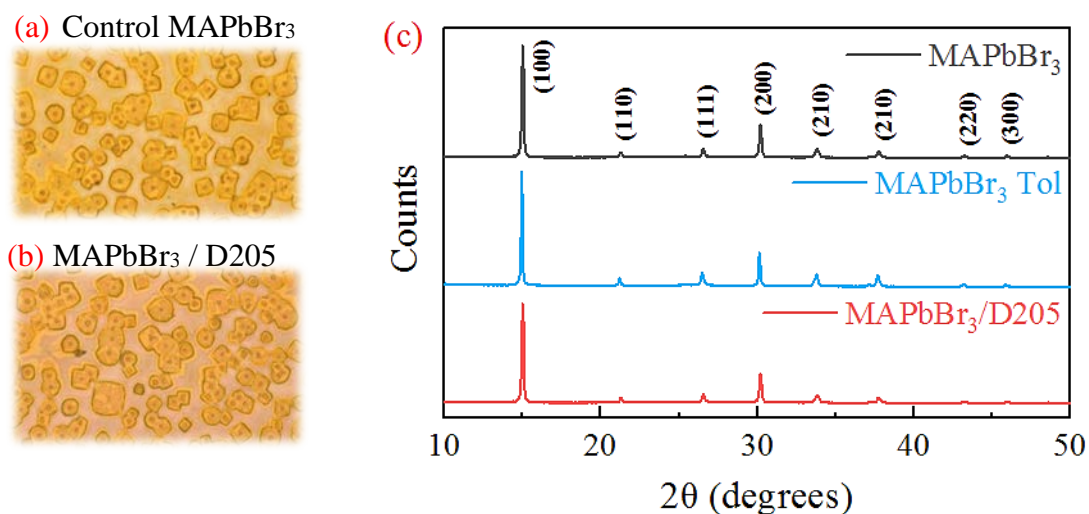


Figure 6.0: (a) and (b) Show optical microscopy images (captured using a x20 objective) of a control MAPbBr₃ thin-film and a MAPbBr₃ thin-film co-sensitized with 1.0 mM D205 dye using the ‘dye after’ method, respectively. (c) X-Ray diffraction patterns of control MAPbBr₃ and MAPbBr₃ co-sensitized with D205 dye (MAPbBr₃/D205). Also included is the X-ray diffraction pattern of a MAPbBr₃ thin-film soaked in toluene (MAPbBr₃ Tol).

The diffraction patterns of both the co-sensitized and toluene soaked films (Figure 6.0 (c) red and blue, respectively) are consistent with the cubic phase of the control MAPbBr₃ perovskite (grey pattern). Each diffraction pattern shows 8 distinguishable peaks located at consistent two-theta (2θ) values. These values and the corresponding planes have previously been identified and discussed in Section 3.3.1.

The similarity observed between the diffraction patterns confirms that the dye solution does not alter the orientation of the crystallographic perovskite structure. Interestingly, there was also little variation between the intensity of the control and co-sensitized films which

suggests there is no improvement in the crystal orientation following treatment with a dye solution. Due to the unaltered crystallography, these results suggest that the dye is not strongly bonding with the perovskite in a way which would otherwise alter the perovskite structure. Furthermore, this also suggests that the dye is binding to the mesoporous layer and/or potentially interacting with the perovskite *via* intermolecular bonding i.e. through dipole-dipole interactions.

Control and co-sensitised MAPbBr₃ PSC's were then manufactured using a planar architecture to establish if the dye remained visible or present in the absence of the mesoporous layer. Figure 6.1 (a) shows the measured absorbance response of both control and co-sensitised MAPbBr₃ thin-films prepared using planar and mesoporous cell architectures.

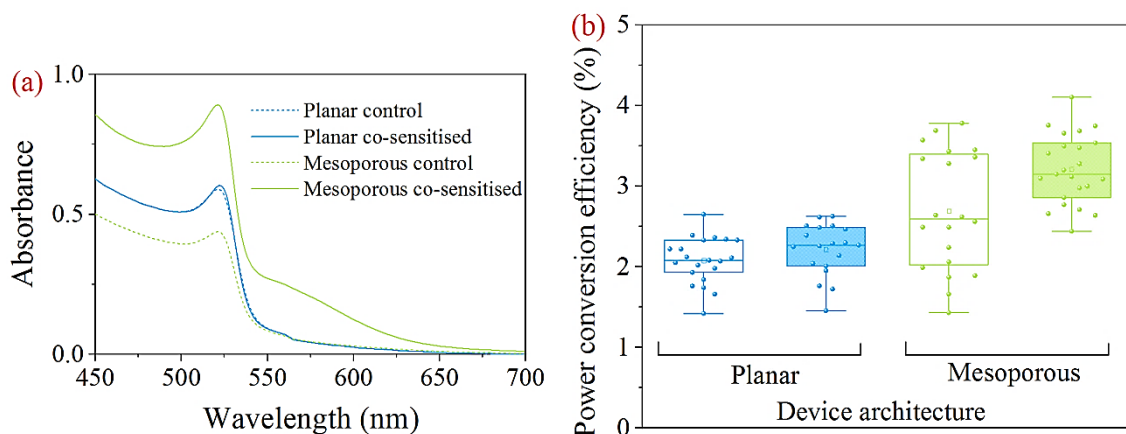


Figure 6.1: (a) Absorbance spectra of control and co-sensitised MAPbBr₃ (co-sensitised using a 1.0 mM D205 dye solution) thin-films prepared on both planar and mesoporous titania layers. (b) Box plots of PCE (%) generated for control and co-sensitised MAPbBr₃ PSC's prepared on both planar and mesoporous titania layers.

Table 22: Tabulated data lists the average photovoltaic performance data for control and co-sensitised MAPbBr₃ PSC's prepared on both planar and mesoporous titania layers - also included is the standard deviation, σ for each average value.

Cell ID	$\bar{x} J_{sc}$ (mA/cm ²)	$J_{sc} \sigma$	$\bar{x} V_{oc}$ (V)	$V_{oc} \sigma$	\bar{x} Fill factor	FF σ	\bar{x} PCE (%)	PCE σ
Planar control	3.40	0.51	1.02	0.07	61	4.81	2.1	0.29
Planar co-sensitised	3.74	0.32	0.98	0.03	60	6.95	2.2	0.32
Mesoporous control	4.38	0.45	1.04	0.04	57	11.4	2.7	0.74
Mesoporous co-sensitised	4.18	0.55	1.00	0.03	77	1.66	3.2	0.43

When comparing the control cells of both architectures, one might expect the mesoporous thin-film (Figure 6.1 (a) dashed green line) to have a higher absorbance due to a larger surface area for perovskite crystallisation. Here however, that is not the case and higher perovskite absorbance is observed for the planar thin-film (Figure 6.1 (a) dashed blue line). In contrast, when considering the co-sensitised thin-films, we see a notable difference between the perovskite and dye absorbance of the mesoporous and planar architectures. For the co-sensitised mesoporous film (Figure 6.1 (a) solid green line), there is an increase in the perovskite absorbance (450 – 540 nm) with additional absorbance from the dye between 540 and 650 nm. The response of the planar co-sensitised film (Figure 6.1 (a) solid blue line) however, shows almost identical absorbance to its control counter-part (dashed blue line) indicating that there has been little to no dye uptake in the co-sensitised film. This suggests that when co-sensitising MAPbBr₃ thin-films, successful dye uptake is strongly dependent on presence of a mesoporous layer.

The same thin-films were then prepared as full cells and their performance measured. Figure 6.1 (b) shows the average PCE increases not only when including a mesoporous layer but also when including a dye. For the planar architecture, the co-sensitised cells outperform the controls where the increase in average PCE appears to stem from the enhanced average J_{sc} (Figure 6.1, Table 22). This is also observed for the mesoporous cells, which overall show higher average J_{sc} values in comparison to their planar counterparts. Differences in J_{sc} are expected between the two cell designs due to the area available for both perovskite formation and dye loading. The mesoporous layer, in effect, provides a ~200 nm, high surface area scaffold for sensitisation whereas the planar architecture only includes a ~50 nm compact titania layer. Therefore, the mesoporous cells would experience increased sensitizer loading and ultimately increased current density. In addition to this, mesoporous architectures have also previously been shown to exhibit superior charge extraction efficiency (compared to the planar design) which would also contribute to the overall photocurrent.¹⁵ Interestingly, a lower average J_{sc} is observed for the mesoporous co-sensitised cells in comparison to the mesoporous controls. This effect has been observed previously (Section 5.3.3.1) and reinforces the theory that there is a delicate balance between maximising the dye response whilst maintaining the photocurrent generated from

the perovskite. Despite this, in comparison to both the planar cells and mesoporous controls, the co-sensitised mesoporous cells show a large increase in average FF (Figure 6.1, Table 22) which could suggest a reduction in the series resistance. Mesoporous architectures typically have a lower series resistance in comparison to planar designs due to better charge extraction.¹⁵ Here however, we only see a large increase in the average FF for the co-sensitised mesoporous cell. This would suggest the dye solution is acting to lower the series resistance through trap state passivation which subsequently improves charge transport/extraction within the cell. These results are in agreement with those seen previously (when co-sensitising MAPbBr₃ PSC's) and further show the inclusion of a mesoporous layer is essential in order to retain the dye within the active layer and achieve higher performance.

The EQE measurements depicted below (Figure 6.2) show that in line with the performance data, the mesoporous cells show a higher EQE and J_{sc} in comparison to the planar architecture. When further studying the mesoporous co-sensitised EQE response, the dye contribution is very low however, some dye signal is visible (550-650 nm).

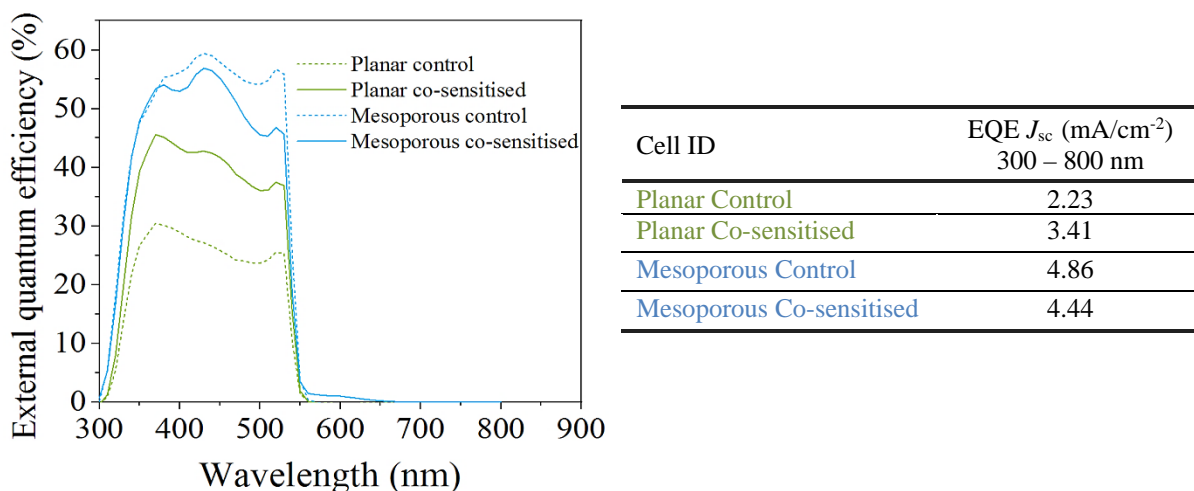


Figure 6.2: Measured EQE spectral response and tabulated EQE generated short-circuit current values (EQE J_{sc}) for the hero pixel of control MAPbBr₃ and MAPbBr₃ cells co-sensitised with D205 when prepared on both planar and mesoporous titania layers.

This is in contrast to the planar co-sensitised cell where there is no dye response (solid green line), which (in agreement with the absorbance data above, Figure 6.1) further confirms there is no dye present within the active layer. Despite this, the planar perovskite EQE (300-

550 nm, solid green line) is still enhanced as a result of co-sensitisation suggesting that the solvent, toluene is improving/healing defects in the perovskite layer in the absence of the dye.

6.3.1 Effect of toluene on active layer

The effect of toluene on the active layer was further investigated by submerging PSC's in toluene for 10 minutes. Here, the aim was to gain further understanding as to how the dye solvent affects the active layer in the absence of the dye. In the previous Chapter, co-sensitisation appeared to have a greater effect on cells prepared with a thicker mesoporous layer. Therefore, the effect of toluene was tested with three different cell thicknesses to determine if toluene has a more pronounced effect on a denser active layer. Figure 6.3 (a) and (b) below show the average PCE and average FF values, respectively generated when measuring control, toluene soaked and co-sensitised MAPbBr₃ PSC's.

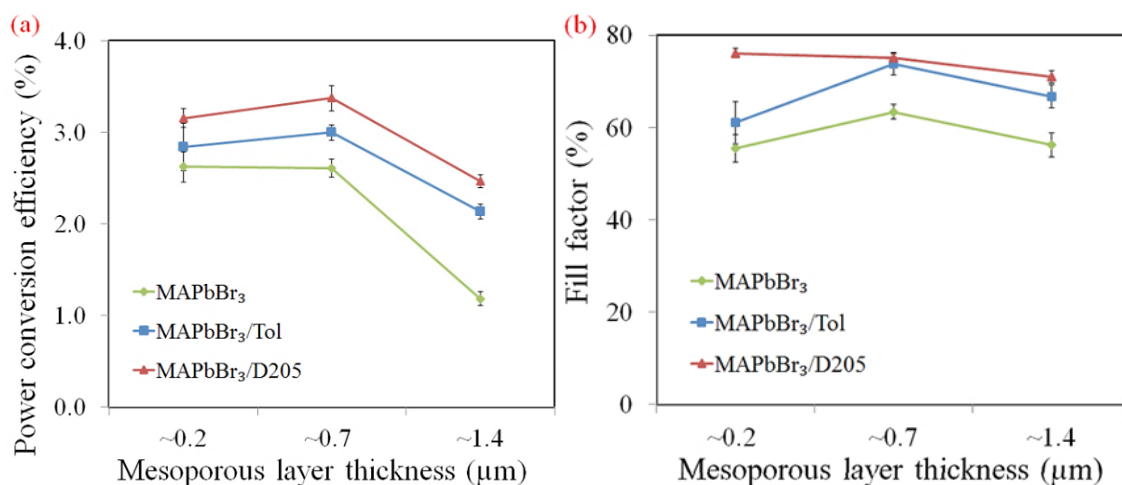


Figure 6.3: (a) Average PCE (%) and (b) Average FF (%) generated for control MAPbBr₃, MAPbBr₃ soaked in toluene (MAPbBr₃/Tol) and MAPbBr₃ co-sensitised with 1.0 mM of D205 dye (MAPbBr₃/D205) when prepared on three thicknesses of mesoporous titania layer. Each plot is generated from the measurement of 24 pixels (three cells) measured per variable.

When studying the average PCE values, the toluene soaked cells (Figure 6.3 (a), MAPbBr₃/Tol blue line) show an increased PCE compared to the control cells (green line) with the largest increase of +1.3% observed for the thickest cells (~1.4 μm). A similar trend is also seen for the average FF (Figure 6.3 (b)) and average J_{sc} values (Table 23). This suggests, in the absence of the dye, that toluene does enhance the perovskite layer and

possibly passifies defects, again having a more pronounced effect on cells with a thicker active layer. However, when considering the standard deviation values for the average J_{sc} and FF (Table 23), the toluene soaked cells generally show a higher degree of variability. Also, in spite of the increased average FF and J_{sc} values, the toluene soaked cells failed to outperform the results gained when co-sensitising the perovskite layer with a dye solution. This showed that collectively, both the dye and toluene, overall contribute to a higher FF, J_{sc} and therefore PCE when co-sensitising MAPbBr₃ PSC's using the dye after method.

Table 23: Average photovoltaic performance data for control MAPbBr₃, MAPbBr₃ soaked in toluene (MAPbBr₃/Tol) and MAPbBr₃ co-sensitised with 1.0 mM of D205 dye (MAPbBr₃/D205) when prepared on three thicknesses of mesoporous titania layer - also included is the standard deviation, σ for each average value.

Cell ID	$\bar{x} J_{sc}$ (mA/cm ⁻²)	$J_{sc} \sigma$	$\bar{x} V_{oc}$ (V)	$V_{oc} \sigma$	\bar{x} Fill Factor (%)	FF σ	\bar{x} PCE (%)	PCE σ
~0.2 μ m MAPbBr ₃	4.42	0.46	1.04	0.08	55	2.92	2.6	0.17
~0.2 μ m MAPbBr ₃ Tol	5.00	0.40	0.91	0.10	61	18.13	2.8	1.02
~0.2 μ m MAPbBr ₃ D205	4.66	0.55	1.00	0.03	76	0.97	3.2	0.10
~0.7 μ m MAPbBr ₃	3.98	0.38	1.02	0.04	63	1.53	2.6	0.10
~0.7 μ m MAPbBr ₃ Tol	4.40	0.43	0.94	0.07	74	2.33	3.0	0.08
~0.7 μ m MAPbBr ₃ D205	4.78	0.73	0.91	0.03	75	1.13	3.4	0.14
~1.4 μ m MAPbBr ₃	2.63	0.29	0.78	0.11	56	2.59	1.2	0.07
~1.4 μ m MAPbBr ₃ Tol	4.00	0.40	0.81	0.09	67	10.23	2.1	0.32
~1.4 μ m MAPbBr ₃ D205	4.47	0.33	0.77	0.02	71	1.31	2.5	0.07

The same experiment was repeated using MAPbI₃ perovskite. Surprisingly, following soaking in toluene, the thinnest MAPbI₃ thin-films (~0.2 and ~0.4 μ m) appeared partially degraded and heavily populated with newly formed 'pin-holes' (Figure 6.4). When co-sensitising with a dye solution, the pin-holes were not visually obvious although it's possible they were still present but not distinguishable due to the dyed/coloured active layer.

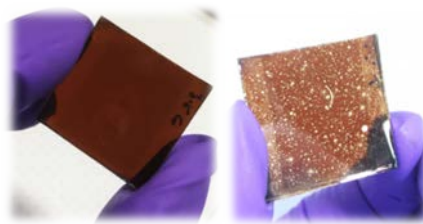


Figure 6.4: Photographed MAPbI₃ thin-film (~0.2 μm) before (left) and after (right) soaking in toluene for ten minutes.

On studying the performance of the cells (Figure 6.5 (a)), in contrast to the MAPbBr₃ results, here, the toluene soaked cells (MAPbI₃/Tol, blue line) generated the lowest average efficiencies. However, despite the lower efficiencies, the average FF (Figure 6.5 (b)) of the toluene soaked cells (MAPbI₃/Tol, blue line) closely matched the average FF values of the thinnest and thickest control (MAPbI₃, green line) cells (~0.2 and ~1.4 μm, respectively).

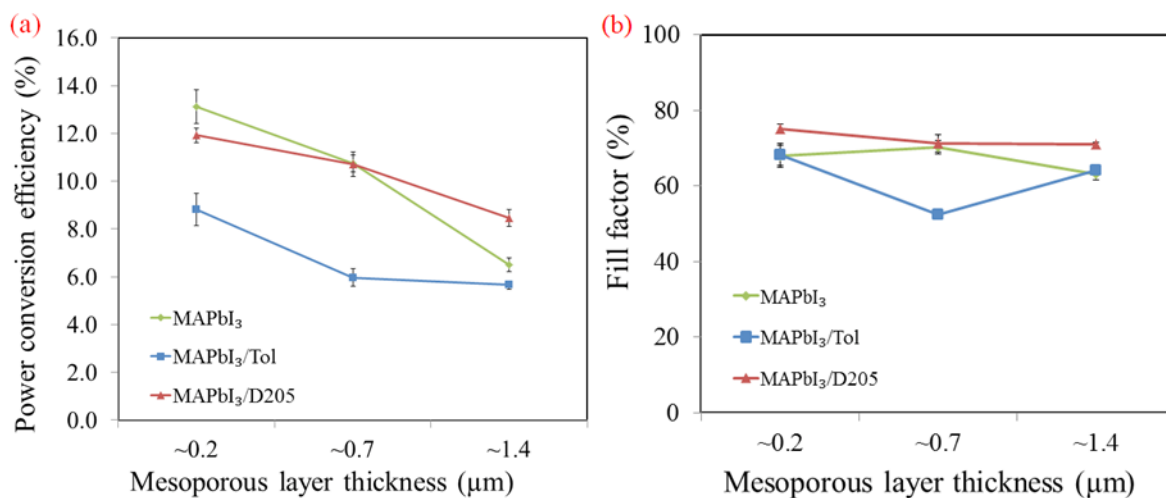


Figure 6.5: (a) Average PCE (%) and (b) average FF (%) generated for control MAPbI₃, MAPbI₃ soaked in toluene (MAPbI₃/Tol) and MAPbI₃ co-sensitised with 1.0 mM of D205 dye (MAPbI₃/D205) when prepared on three thicknesses of mesoporous titania layer. Each plot is generated from the measurement of 24 pixels (three cells) measured per variable.

As expected due to the compromised active layer, for all thicknesses, the toluene soaked cells show the lowest average J_{sc} and V_{oc} values (Table 24). There appears to be no obvious trend in the variability (Table 24, standard deviation values) of the toluene soaked cells (in comparison to the control and co-sensitised), however due to the large number of pin holes the variability could prove difficult to reduce.

Table 24: Average photovoltaic performance data for control MAPbI₃, MAPbI₃ soaked in toluene (MAPbI₃/Tol) and MAPbI₃ co-sensitised with 1.0 mM of D205 dye (MAPbI₃/D205) when prepared on three thicknesses of mesoporous titania layer - also included is the standard deviation, σ for each average value.

Cell ID	$\bar{x} J_{sc}$ (mA/cm ²)	$J_{sc} \sigma$	$\bar{x} V_{oc}$ (V)	$V_{oc} \sigma$	\bar{x} Fill Factor (%)	FF σ	\bar{x} PCE (%)	PCE σ
~0.2 μ m MAPbI ₃	20.17	0.93	0.94	0.11	68	14.65	13.8	3.45
~0.2 μ m MAPbI ₃ Tol	13.56	2.19	0.91	0.10	68	11.70	8.8	2.69
~0.2 μ m MAPbI ₃ D205	16.02	1.22	0.99	0.03	75	5.92	11.9	1.56
~0.7 μ m MAPbI ₃	17.21	1.60	0.89	0.02	70	8.92	10.8	1.73
~0.7 μ m MAPbI ₃ Tol	13.77	2.59	0.82	0.07	52	2.89	6.0	1.48
~0.7 μ m MAPbI ₃ D205	15.54	1.72	0.92	0.19	71	11.42	10.7	2.47
~1.4 μ m MAPbI ₃	13.66	3.34	0.76	0.02	63	7.16	6.5	1.43
~1.4 μ m MAPbI ₃ Tol	12.00	1.03	0.73	0.01	64	3.59	5.7	0.69
~1.4 μ m MAPbI ₃ D205	13.15	2.65	0.91	0.02	71	3.15	8.5	1.77

On consideration of this data set, for the thinnest MAPbI₃ cell architectures, co-sensitisation appears more detrimental than beneficial due to toluene degrading the perovskite layer. The effects seen here would also explain the results observed in the previous Chapter (Section 5.3.4) where the thinnest cells (~0.2 μ m and ~0.4 μ m) showed reduced efficiencies following co-sensitisation. Toluene has previously been shown to act as a solvent for I₂ and therefore here, it has contributed to the degradation of the MAPbI₃ layer.¹⁶ However, in both studies, the thicker cells, which have a denser active layer appear to be less affected by toluene and when including a dye we see an increase in the efficiency (Figure 6.5 (a) red line).

6.3.2 Photoluminescence

MAPbBr₃ thin-films prepared using the conditions described in the previous section were analysed using steady-state fluorescence spectroscopy. Figure 6.6 (a) shows the steady-state PL emission spectra of control, toluene soaked and co-sensitised MAPbBr₃ thin-films prepared on three thicknesses of mesoporous titania layer. For both the toluene soaked and control MAPbBr₃ thin-films (dotted and dashed lines, respectively) the lambda max (λ_{max}) falls between 546 and 547 nm which is consistent with literature values reported for the cubic phase of MAPbBr₃.¹⁷⁻¹⁹

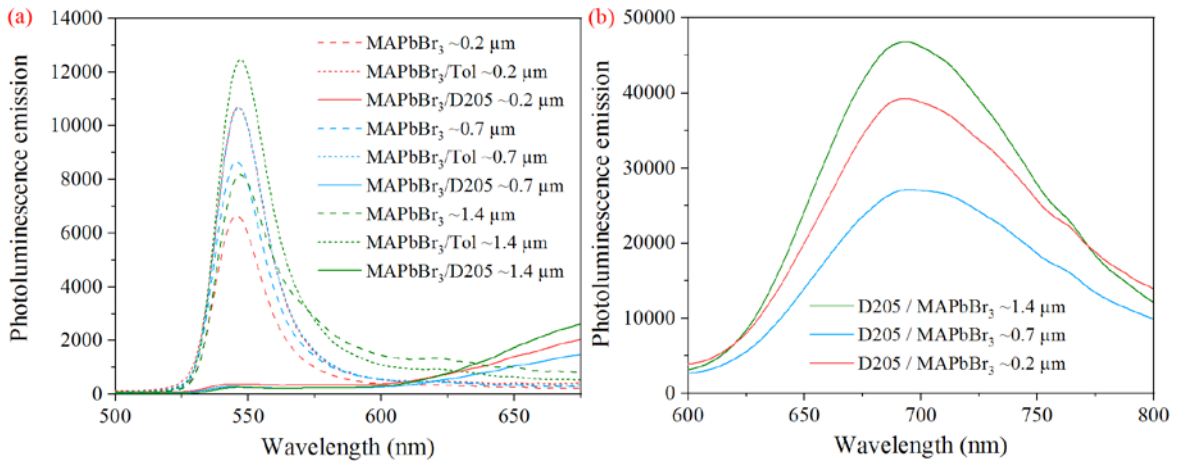


Figure 6.6: (a) Photoluminescence emission spectra ($\lambda_{\text{exc}} = 405 \text{ nm}$) of control MAPbBr₃ thin-films, MAPbBr₃ thin-films co-sensitised with 1.0 mM of D205 and MAPbBr₃ thin-films soaked in toluene when prepared on three thicknesses of mesoporous layer. (b) Photoluminescence emission spectra ($\lambda_{\text{exc}} = 531 \text{ nm}$) of the MAPbBr₃ thin-films co-sensitised with 1.0 mM of D205 when prepared on three thicknesses of mesoporous layer.

When comparing the control signals (dashed lines), broadening of the perovskite peak becomes more pronounced with increasing active layer thickness. For perovskites, peak or band broadening has previously been attributed to defects within the crystal lattice and is often indicative of trap state filling.¹⁹ For the thickest control film (MAPbBr₃ ~1.4 μm , green dashed line) there is a slight shoulder visible at 575 nm which is a characteristic of the MAPbBr₃ cubic phase and originates from the radiative decay of trapped charges.¹⁷ This response also shows a lower energy peak at 625 nm which has previously been attributed to surface and bulk defects in MAPbBr₃ thin-films.^{17,20} This peak is not as evident or pronounced in the thinner control films which, in addition to the peak broadening, suggests that the number of defects in the film increases with film thickness.

The toluene soaked films (dotted lines) all show a higher PL intensity (Table 25) compared to the controls with the largest increase of 61% observed for the thinnest film (MAPbBr₃ ~0.2 μm). Therefore, the toluene soaked films show a higher level of radiative recombination which suggests these films are of better quality, have lower a trap density and experience less non-radiative recombination in comparison to the controls. This theory would also be supported by the results in the previous section where toluene soaked MAPbBr₃ cells demonstrated improved performance over control MAPbBr₃ cells.

Table 25: Lambda max (λ_{\max}), PL intensity at lambda max and percentage difference of the PL intensity to the control PL intensity for: control MAPbBr₃ thin-films, MAPbBr₃ thin-films co-sensitised with 1.0 mM of D205 and MAPbBr₃ thin-films soaked in toluene when prepared on three thicknesses of mesoporous layer. The percentage difference values represent a qualitative estimate of the % change.

Cell ID	λ_{\max} (nm)	PL Intensity at λ_{\max}	% difference to control PL intensity at λ_{\max}
~0.2 μm MAPbBr ₃	546	6636	-
~0.2 μm MAPbBr ₃ /Tol	546	10699	61% \uparrow
~0.2 μm MAPbBr ₃ /D205	545	387	94% \downarrow
~0.7 μm MAPbBr ₃	546	8670	-
~0.7 μm MAPbBr ₃ /Tol	547	10650	23% \uparrow
~0.7 μm MAPbBr ₃ /D205	544	285	97% \downarrow
~1.4 μm MAPbBr ₃	547	8135	-
~1.4 μm MAPbBr ₃ /Tol	547	12461	53% \uparrow
~1.4 μm MAPbBr ₃ /D205	547	259	97% \downarrow

In complete contrast to the other variables, the perovskite signal of the co-sensitised thin-films is significantly quenched in the presence of the dye (Figure 6.6 (a) solid lines). In addition to this, each of the co-sensitised signals shows a broad lower energy peak which begins just after 600 nm. Figure 6.6 (b) shows the PL emission spectra of the same co-sensitised films when using an excitation wave length of 531 nm i.e. when exciting the D205 dye as opposed to the perovskite. Here, for each co-sensitised film, we see a broad peak beginning just after 600 nm resulting from fluorescence from the dye. Therefore, the emission from the perovskite is markedly quenched, whereas the emission from the dye increases with dye loading. As the thin-films are measured at open-circuit voltage i.e. with no load connected, the PL emission is maximised and any quenching is generally attributed to increased levels of non-radiative recombination.^{21,22} However, with the improvement in the performance of co-sensitised cells over the controls, it is unlikely that the observed quenching of the perovskite signal is due to increased non-radiative recombination. These results could be indicative of energy transfer processes such as Förster or fluorescence resonance energy transfer (FRET). FRET is a non-radiative process that transfers excitation energy between donor and acceptor chromophores coupled *via* dipole-dipole interaction and has previously been reported when combining fluorescent rhodamine dyes with lead halide perovskite nanocrystals.^{23,24} Both publications described significant quenching of the perovskite PL emission with increasing dye concentration and a subsequent rise in the dye

emission. Although the results seen above share similarities with those described in the publications mentioned, it is also possible there are alternate methods of energy transfer happening. However, the theory of energy transfer between the perovskite and the dye, and the methods by which it proceeds, would need to be confirmed by further analysis.

Time correlated single photon counting (TCSPC) was then used to study the time-resolved PL (TRPL) of control, co-sensitised and toluene soaked MAPbBr₃ films prepared on a single thickness of ~0.7 μm. Defects present within the perovskite layer can shorten the lifetime of charge carriers therefore, when studying TRPL, a longer lifetime is indicative of reduced trap density or trap-state passivation.¹⁹ Typically, the PL decay of perovskites is bi-exponential with a faster and slower component.¹⁹ The slower component (τ_1), is thought to correspond to the intrinsic radiative decay of excitons and is influenced by trap recombination within the bulk of the perovskite.²⁵ The faster decay component (τ_2), is believed to result from bound electron-hole pairs in the conduction and valence bands and is influenced by interfacial non-radiative recombination.²⁵⁻²⁷ The measured TRPL parameters were fitted using a bi-exponential decay function and the calculated lifetimes are shown in Table 26.

Table 26: the tabulated values include the fitting data from the TRPL spectra of each measured thin-film. The A values represent the corresponding decay amplitude.²⁷

Cell ID	τ_1 (ns)	τ_2 (ns)	A ₁	A ₂
~0.7 μm MAPbBr ₃	0.41	0.72	0.91	0.09
~0.7 μm MAPbBr ₃ /Tol	0.50	1.06	0.97	0.03
~0.7 μm MAPbBr ₃ /D205	0.76	1.84	0.96	0.04

For the co-sensitised films, the τ_1 and τ_2 lifetimes are 0.76 ns and 1.85 ns, respectively which is longer than the corresponding lifetimes of the control MAPbBr₃ film: 0.41 and 0.72 ns. This is also the case for the toluene soaked films, where τ_1 and τ_2 were calculated as 0.50 and 1.06 ns, respectively. These results show that the excited state lifetime of the perovskite is increased as a result of both toluene soaking and co-sensitisation. Therefore, soaking in toluene alone appears to improve the perovskite layer and reduce the level of trap-assisted emission. However, on adding the dye, we see a larger increase in the PL lifetime (Figure 6.7).

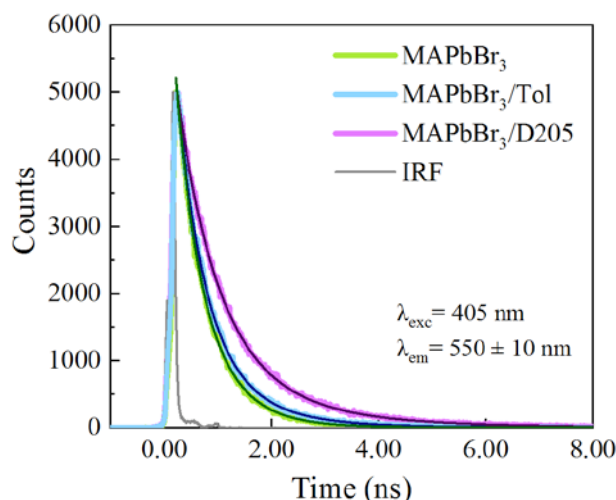


Figure 6.7: Photoluminescence emission decays for thin-films of: control MAPbBr₃ (green), MAPbBr₃ co-sensitised with D205 (purple) and MAPbBr₃ soaked in toluene (blue) and their respective bi-exponential decay functions. Each decay function had an r2 value of 1.00.

These results strongly suggest that the dye solution, as a whole, is passivating trap states in the bulk of the perovskite which in turn enhances charge transfer and lowers recombination. This then ultimately improves the overall cell performance giving rise to the results observed in Section 6.3.1 where we see enhanced efficiency on toluene soaking but a larger efficiency increase with co-sensitisation.

The steady-state and TRPL of MAPbI₃ thin-films prepared on a thickness of $\sim 1.4 \mu\text{m}$ were also measured.

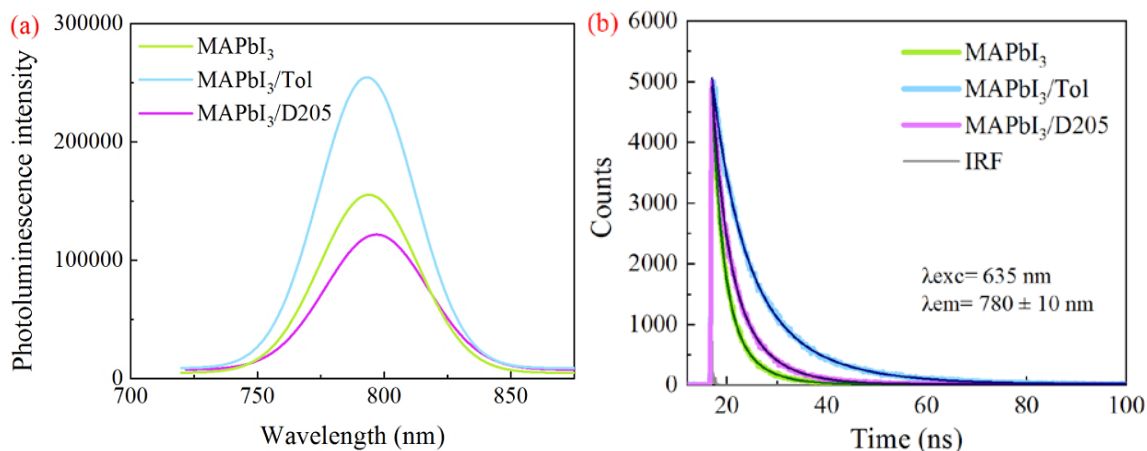


Figure 6.8: (a) Photoluminescence emission spectra ($\lambda_{exc} = 635 \text{ nm}$) of control, co-sensitised (using 1.0 mM D205) and toluene soaked MAPbI₃ thin-films. (b) Photoluminescence emission decays for thin-films of: control MAPbI₃ (green), MAPbI₃ co-sensitised with D205 (purple) and MAPbI₃ soaked in toluene (blue) and their respective bi-exponential decay functions. Each decay function had an r2 value of 1.00.

Table 27: Tabulated values include the fitting data from the TRPL spectra of each measured thin-film. The A values represent the corresponding decay amplitude.²⁷

Cell ID	τ_1 (ns)	τ_2 (ns)	A ₁	A ₂
~1.4 μm MAPbI ₃	1.94	5.26	0.998	0.002
~1.4 μm MAPbI ₃ /Tol	5.49	12.87	0.874	0.126
~1.4 μm MAPbI ₃ /D205	2.73	6.96	0.978	0.022

In Figure 6.8 (a) we see steady-state emission from MAPbI₃ thin-films with a single PL peak at 790 nm which corresponds to band-to-band radiative recombination of the perovskite. The highest steady-state PL emission was measured for the toluene soaked film (MAPbI₃/Tol) indicating increased radiative recombination potentially due to enhanced crystallisation. This was further confirmed by the TRPL analysis where the MAPbI₃/Tol film (Figure 6.8 (b)) shows the longest decay indicating reduced non-radiative recombination pathways. The co-sensitised thin-film (Figure 6.8 (a) MAPbI₃/D205) shows the lowest steady-state PL intensity which could be due to increased non-radiative recombination however, a longer decay lifetime (compared to the control film, MAPbI₃) is observed (Figure 6.8 (b)) which suggests lower non-radiative recombination. Interestingly, the co-sensitised steady-state PL response is not substantially quenched unlike the co-sensitised MAPbBr₃ thin-films (Figure 6.8 (a)). Overall both co-sensitised and toluene soaked MAPbI₃ thin-films show an increased PL lifetime over the control however, in contrast to the MAPbBr₃ thin-films, the largest lifetime increase is observed with toluene treatment. This is possibly due to the toluene selectively dissolving areas which have some form of defect or those which are not fully coordinated. Thus leaving less but better quality material however, this would need to be confirmed through further analysis.

6.3.3 Series resistance

Throughout this body of research there has been a consistent trend of increased FF following co-sensitisation. In polycrystalline PSC's, the FF is often considered the most challenging parameter to improve due to inevitable charge losses through non-radiative bulk and interface carrier recombination as a result of grain size and surface defects.^{28,29} Therefore, PSCs typically have a lower FF than they are capable of obtaining due to charge transport losses arising from poor charge extraction and photocurrent leakage.³⁰ In addition

to recombination losses, the FF of a PSC is also governed by the series resistance where losses in FF are generally attributed to increased series resistance.^{31,32}

Lower series resistance and therefore, increased FF, has previously been achieved through implementing highly conductive HTL materials and by reducing the contact resistance at the cell interfaces.³² Kim *et al.* increased the FF of MAPbI₃ PSC's from 72 to 77% by reducing the thickness of the spiro-OMeTAD HTL from 310 nm to 130 nm.³³ Stolterfoht *et al.* found that reducing the transit time through a PTAA HTL reduces charge transport losses and increases FF (>84%) when used with triple cation perovskite CsPbI_{0.05}[(FAPbI₃)_{0.83}(MAPbBr₃)_{0.17}]_{0.95}.³⁴ In both cases, the observed increases in FF were attributed to a reduction in series resistance and optimised / efficient charge collection leading to lower recombination.

An estimation of the series resistance of a cell can be obtained from the J-V curve. The curve is largely affected by the series resistance near the open-circuit voltage therefore; the series resistance can be estimated by calculating the slope of the J-V curve at open-circuit voltage. Here, the series resistance values of control, co-sensitised and toluene soaked PSC's of increasing mesoporous layer thickness have been compared using the J-V curve data. Figure 6.9 shows the average FF of the MAPbBr₃ cells prepared as in Section 5.3.3.2.

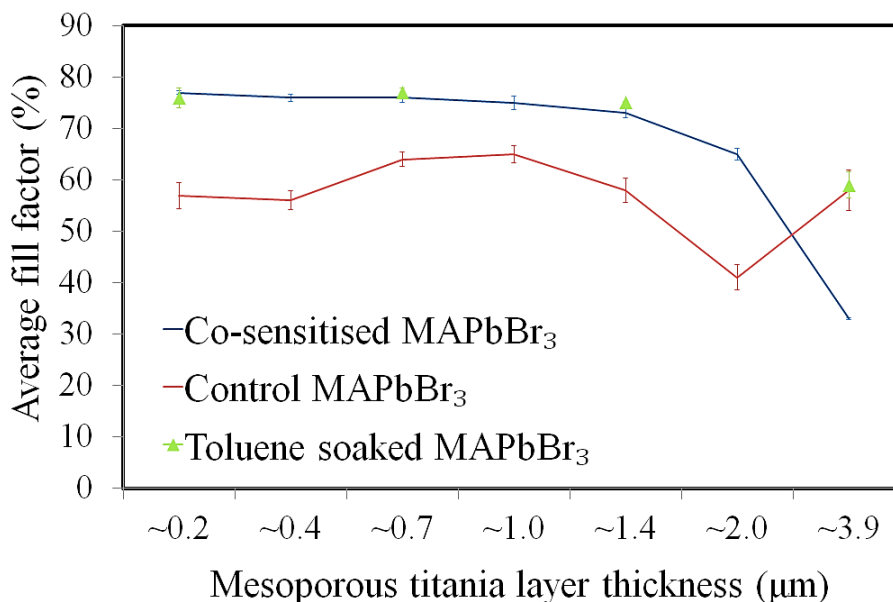


Figure 6.9: Average fill factor (%) of control, co-sensitised (using 1.0 mM D205) and toluene soaked MAPbBr₃ perovskite solar cells when prepared on increasing thickness of mesoporous layer - calculated from 24 pixels (i.e. 3 cells).

As seen previously, the co-sensitised cells (blue line) mainly demonstrate a higher average FF when compared to the controls (red line). The toluene soaked cells (green triangles) show a very similar average FF to the co-sensitised cells which again further highlights the enhancement of the perovskite layer following treatment with toluene. Figure 6.10 shows the average resistance at open-circuit voltage (i.e. the series resistance).

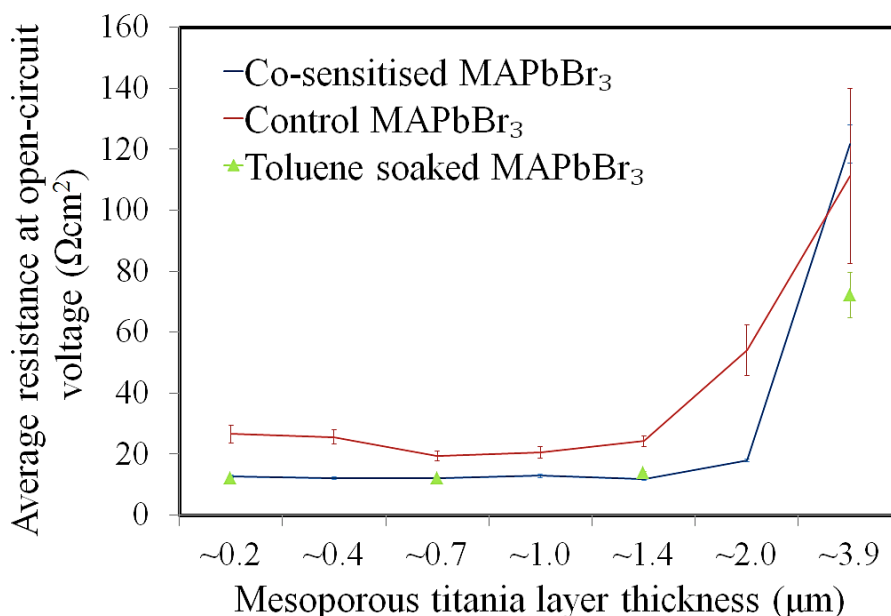


Figure 6.10: Average resistance at open-circuit voltage of control, co-sensitised (using 1.0 mM D205) and toluene soaked MAPbBr₃ perovskite solar cells when prepared on increasing thickness of mesoporous layer - calculated from 24 pixels (i.e. 3 cells).

On studying the average resistance at open-circuit (Figure 6.10), the co-sensitised cells (blue line) show lower average series resistance values in comparison to the control values (red line). In line with the FF values, the resistance values of the co-sensitised and toluene soaked cells are very similar which suggests toluene treatment alone acts to lower series resistance and increase the FF. On comparing the average FF and series resistance across the thicknesses, for the thickest cells ($\sim 1.4 \mu\text{m}$ upwards) there is a correlation between decreasing FF and increasing series resistance. Thicker devices can experience increased series resistance due to longer diffusion path lengths and insufficient pore filling by the HTL, both of which increase recombination and lower performance as fewer charges reach the electrodes.^{35,36} Here, on adding a dye and on treating with toluene, the thickest co-sensitised cells (~ 1.4 and 2.0) have a lower series resistance. This further suggests that co-sensitisation and toluene treatment is beneficial for thicker PSC's by possibly improving the

charge transport and carrier extraction process. However, as mentioned previously, the series resistance values extracted from the J-V curves only represent an estimate value. Therefore, to gain a more accurate representation of the series resistance, control and co-sensitised MAPbBr₃ devices prepared on three mesoporous layer thicknesses (~0.2, ~0.7 and ~1.4 μm) were studied using impedance spectroscopy. The performance of each cell was initially measured on the solar simulator using the standard 1 sun illumination intensity. This identified the highest performing ‘hero’ pixel of each cell which was then used for the impedance measurements. The hero pixel of each device was then scanned using a frequency range of 10 MHz to 1 Hz and an equivalent illumination intensity (the full experimental settings are listed in Section 2.4.4.) When plotting the data as a Nyquist plot, the high-frequency x-axis intercept is equivalent to the series resistance. Table 28 lists and compares the series resistance values extracted from the J-V curves and the high-frequency x-axis intercept of the Nyquist plot for the hero pixel of each device.

Table 28: Hero series resistance values for control and co-sensitised MAPbBr₃ cells prepared on three thicknesses of mesoporous layer (~0.2, ~0.7 and ~1.4 μm). The resistance at V_{oc} values are extracted from the J-V curves when measuring the hero pixel at 1 sun illumination intensity.

Mp-TiO ₂ thickness	Cell ID	Resistance at V_{oc} (Ωcm^2)	x-axis intercept of Nyquist plot (Ωcm^2)
~0.2 μm	Control	13.8	9.8
	Co-sensitised	12.5	9.5
~0.7 μm	Control	12.6	9.3
	Co-sensitised	9.4	8
~1.4 μm	Control	12.1	10.5
	Co-sensitised	8.5	8.6

Here, we can see there is difference between the J-V extracted values and the Nyquist plot values. However, the differences are not exceptionally large meaning that despite being an estimate, the resistance at V_{oc} values do provide some level of accuracy. In line with Figure 6.10, the co-sensitised devices show lower series resistance for both sets of values which is possibly contributing to the FF increases regularly observed when adding a dye to the device architecture.

The average FF and series resistance values were also extracted and calculated for MAPbI₃ PSC's. As seen in Section 6.3.1, treatment of thinner MAPbI₃ cells with toluene has previously proven detrimental due to the toluene degrading the perovskite layer.

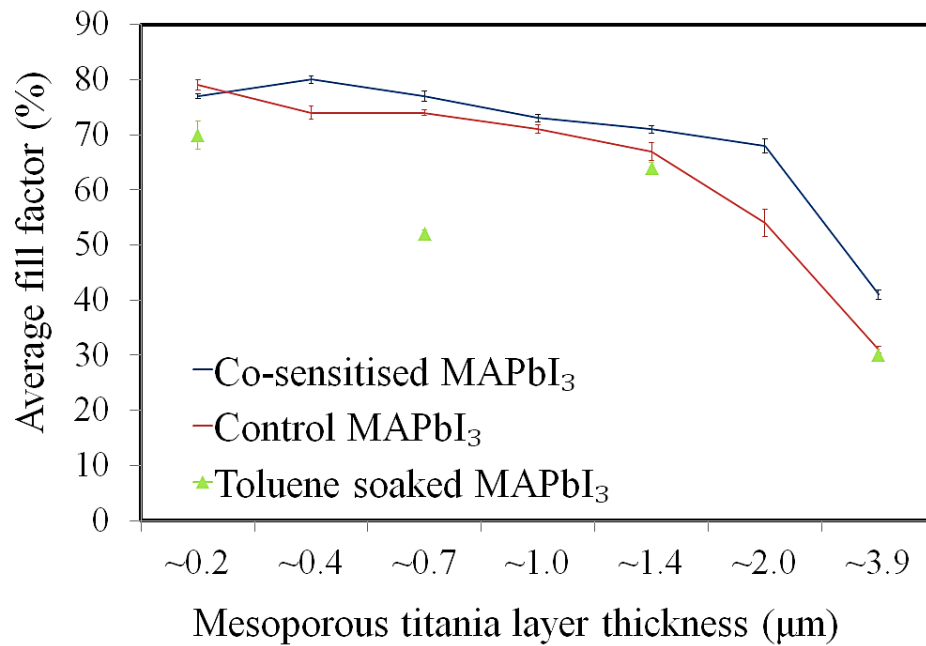


Figure 6.11: Average fill factor (%) of control, co-sensitised (using 1.0 mM D205) and toluene soaked MAPbI₃ perovskite solar cells when prepared on increasing thicknesses of mesoporous layer - calculated from 24 pixels (i.e. 3 cells).

Here, there is a slight improvement in the average FF with co-sensitisation (Figure 6.11) but not as pronounced as is seen for the MAPbBr₃ cells. The toluene soaked films also show a lower average FF in comparison to the controls particularly for the thinner cells.

As with MAPbBr₃, the average series resistance values (Figure 6.12) increase with thickness in line with the decreasing average FF however; there is little variation with treatment and the average resistance values here are very similar despite co-sensitisation or toluene soaking.

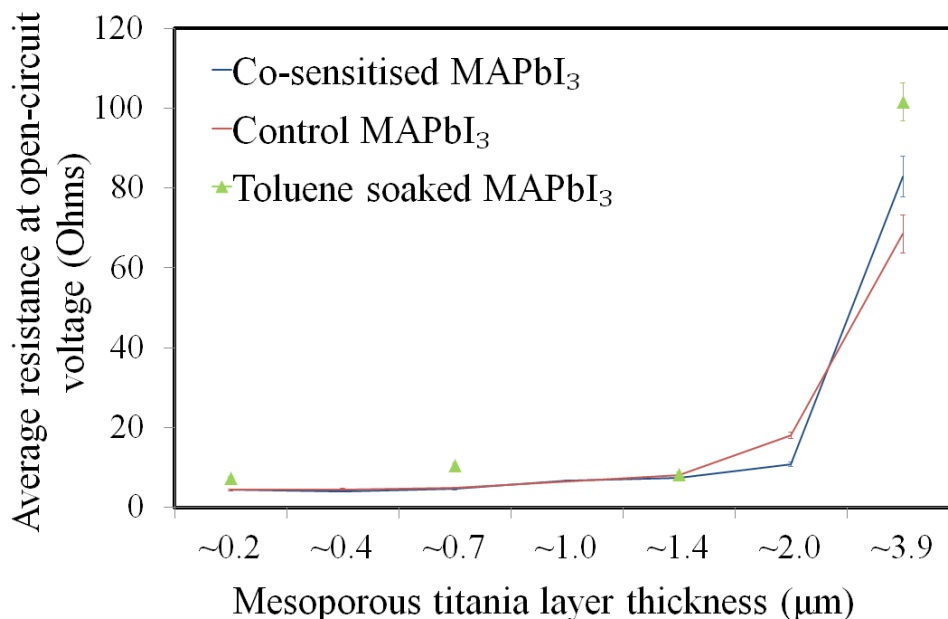


Figure 6.12: Average resistance at open-circuit voltage (right) of control, co-sensitised (using 1.0 mM D205) and toluene soaked MAPbI₃ perovskite solar cells when prepared on increasing thicknesses of mesoporous layer - calculated from 24 pixels (i.e. 3 cells).

Overall, for MAPbBr₃, the dye solution appears to reduce the device series resistance which is possibly improving charge extraction and lowering non-radiative recombination losses within the perovskite layer. We also observe the same benefits with toluene; however, previously this has not translated into superior performance (Section 6.3.1). Therefore, although toluene soaking alone has benefits, it is the dye and solvent together that generate a higher device efficiency. Overall, although analysis of the series resistance values has provided some insight, further investigation is required to fully confirm if the observed FF increases do result from reduced series resistance with co-sensitisation.

6.3.4 Impedance spectroscopy

Impedance spectroscopy (IS) can be further used to provide information about the charge transport and recombination properties of perovskite solar cells.³⁷ Here, control and co-sensitised PSC's prepared on three thicknesses of mesoporous titania layer have been studied using IS to further assess the effects of adding a dye to the active layer. The devices were measured on the solar simulator to identify the hero pixel. Table 29 lists the photovoltaic performance of the hero pixels when measured at 1 sun intensity.

Table 29: Measured photovoltaic performance values for the hero pixels of control and co-sensitised (using 1 mM D205) MAPbBr₃ PSC's prepared on three thicknesses of mesoporous titania layer. The values included are those generated when measuring the pixels on the solar simulator using a 1 sun illumination intensity.

Cell ID	J_{sc} (mA/cm ²)	V_{oc} (V)	Fill Factor (%)	PCE (%)
~0.2 μ m MAPbBr ₃	5.68	0.83	71	3.3
~0.2 μ m MAPbBr ₃ D205	5.23	0.85	74	2.3
~0.7 μ m MAPbBr ₃	6.01	0.81	71	3.4
~0.7 μ m MAPbBr ₃ D205	6.34	0.78	74	3.7
~1.4 μ m MAPbBr ₃	6.40	0.81	71	3.7
~1.4 μ m MAPbBr ₃ D205	6.26	0.76	74	3.6

The photo-voltage of PSC's is largely affected by the level of recombination therefore, measuring the V_{oc} under different illumination intensities can provide information about the recombination processes.³⁸ This can provide useful information into whether different recombination mechanisms are occurring despite comparable performance under 1 sun.³⁹ Each hero pixel was measured at open-circuit conditions and illuminated using intensities which ranged from 0.01 to 1 sun (AM1.5 illumination). The V_{oc} values generated were then plotted as a function of the light intensity using a semi-logarithmic plot (Figure 6.13).

The cells all generated a similar V_{oc} at an illumination intensity of 1 sun and show a reduction in V_{oc} with light intensity however, at lower light levels, co-sensitised devices have higher V_{oc} .

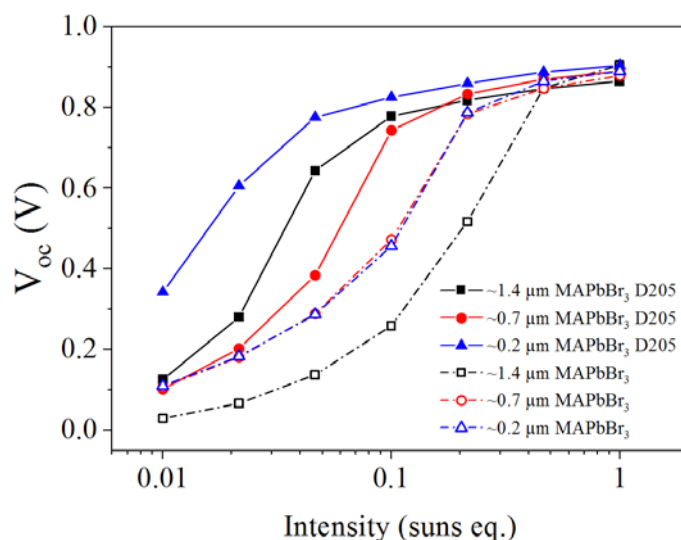


Figure 6.13: Semi logarithmic plot of open-circuit voltage vs illumination light intensity for control and co-sensitised MAPbBr₃ perovskite solar cells prepared on increasing thicknesses of mesoporous layer.

As the light intensity is reduced, the control cells (dashed lines) all show a sharper decrease in V_{oc} compared to the co-sensitised cells. The thinnest controls (~ 0.2 and ~ 0.7 μm MAPbBr₃) show a very similar trend in V_{oc} whereas the thickest control cell (~ 1.4 μm MAPbBr₃) shows the lowest V_{oc} values across the range of light intensities. This is most likely due to high trap state density and therefore high levels of non-radiative recombination. The co-sensitised cells also decrease with light intensity but to a lesser degree and generally show higher V_{oc} values at lower light intensities. There is considerable improvement in the V_{oc} values of the thickest cell with co-sensitisation (~ 1.4 μm MAPbBr₃ D205) suggesting suppression of non-radiative recombination. The thinnest co-sensitised cell (~ 0.2 μm MAPbBr₃ D205) generated the largest V_{oc} values over the range of intensities, including a V_{oc} of 0.34 V at the lowest intensity (0.01 suns). Overall, the larger V_{oc} values of the co-sensitised cells further suggests the dye lowers recombination pathways by passivating traps within the perovskite layer.

The radiative and non-radiative processes present within a cell are collectively represented by the voltage dependent recombination resistance, R_{rec} . A high R_{rec} is linked to slow recombination kinetics which is a desirable trait to maximise charge extraction. Therefore, a larger R_{rec} often translates to a larger V_{oc} due to decreased non-radiative recombination

processes.⁴⁰ IS analysis was carried using the same range of light intensities as above to determine the recombination resistance of the control and co-sensitised cells.

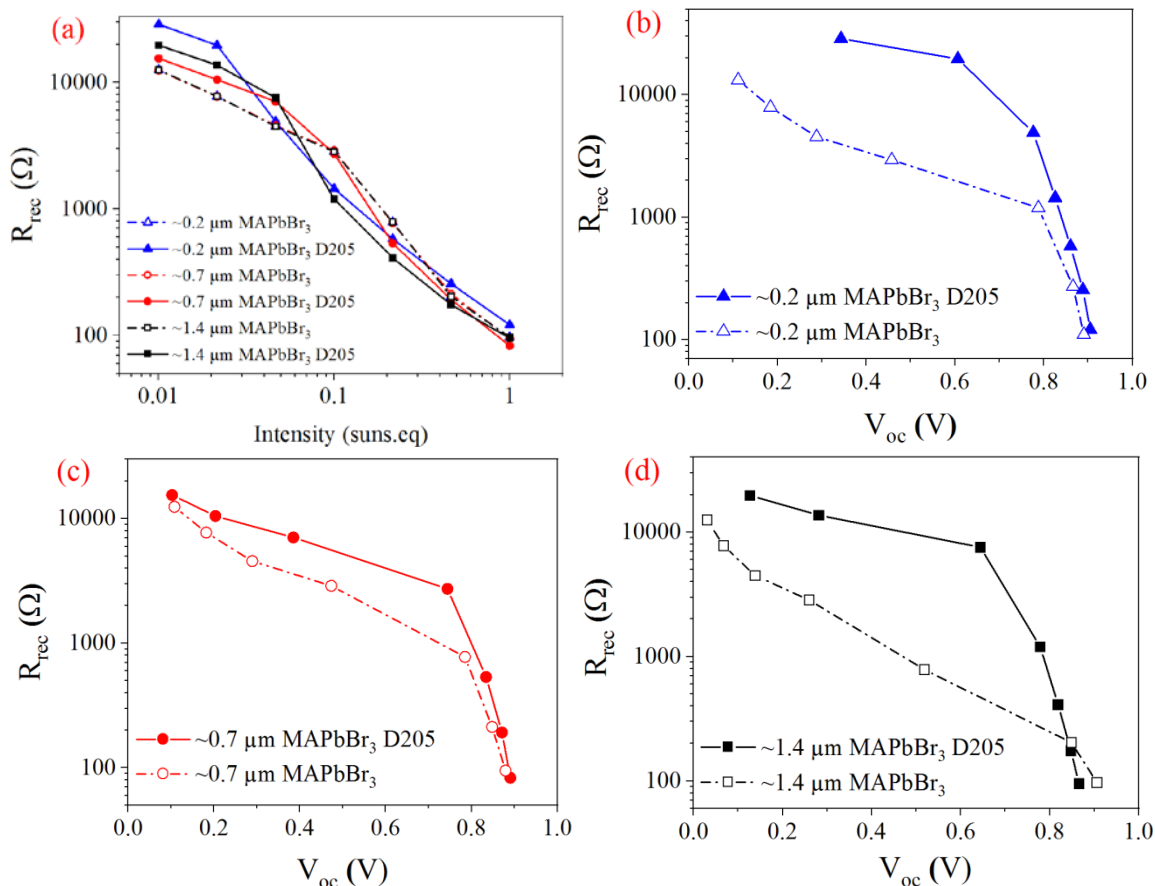


Figure 6.14: (a) Logarithmic plot of the recombination resistance (R_{rec}) vs illumination light intensity for the three thicknesses of control and co-sensitised MAPbBr₃ perovskite solar cells. Semi logarithmic plot of the recombination resistance (R_{rec}) vs the open-circuit voltage measured under varied illumination intensities for control and co-sensitised MAPbBr₃ PSC's prepared on mesoporous layer thicknesses of (b) $\sim 0.2 \mu\text{m}$ (c) $\sim 0.7 \mu\text{m}$ and (d) $\sim 1.4 \mu\text{m}$.

In Figure 6.14 (a) we see the R_{rec} values of each cell are strongly dependent on the light intensity where the recombination resistance decreases with light intensity. The co-sensitised cells show larger R_{rec} values at the lowest light intensity (0.01 suns.cq). The recombination resistance values were then plotted as a function of the measured V_{oc} values (Figure 6.14 (b, c and d)). As expected from the results above, for all thicknesses, the co-sensitised cells generally show larger recombination resistance values due to the dye effectively reducing recombination pathways which in turn increases the V_{oc} .

A similar effect has previously been observed by Balis *et al.* on sensitising the compact titania layer of MAPbI₃ PSC's with triarylamine dye, D35.⁴¹ The recombination resistance was increased in the presence of the dye which was believed to inhibit recombination through steric hindrance. The dye contains four butoxyl chains which were thought to provide surface blocking by increasing the distance between the electrons and holes which suppressed recombination and increased the V_{oc} . Balis and co-workers also suspected that the dye strengthened the electronic coupling at the perovskite titania interface and therefore, enhanced electron injection leading to higher photocurrent and increased efficiency.⁴¹

Some insight into the efficacy of charge injection can be afforded through measuring the capacitance of a cell. The chemical capacitance represents the photo generated charge of a cell and relates to the accumulation of charge due to the excitation of electrons into the conduction band.⁴² For DSSC's this corresponds to charge accumulation in the mesoporous titania layer, where an exponential dependence of capacitance on voltage is seen.⁴³

In contrast, the capacitance of PSC's relates to the dielectric properties of the perovskite and therefore, is geometric in nature, not bias dependent and varies with active layer area and thickness.³⁹ As a result, the exponential increase in capacitance (as is seen for DSSC's) is generally not observed in PSC's suggesting that charge is not accumulated in the mesoporous titania.⁴⁴⁻⁴⁷ Here, IS measurements were performed (using the range of light intensities described above) to determine whether the capacitance of MAPbBr₃ PSC's is altered on adding a dye.

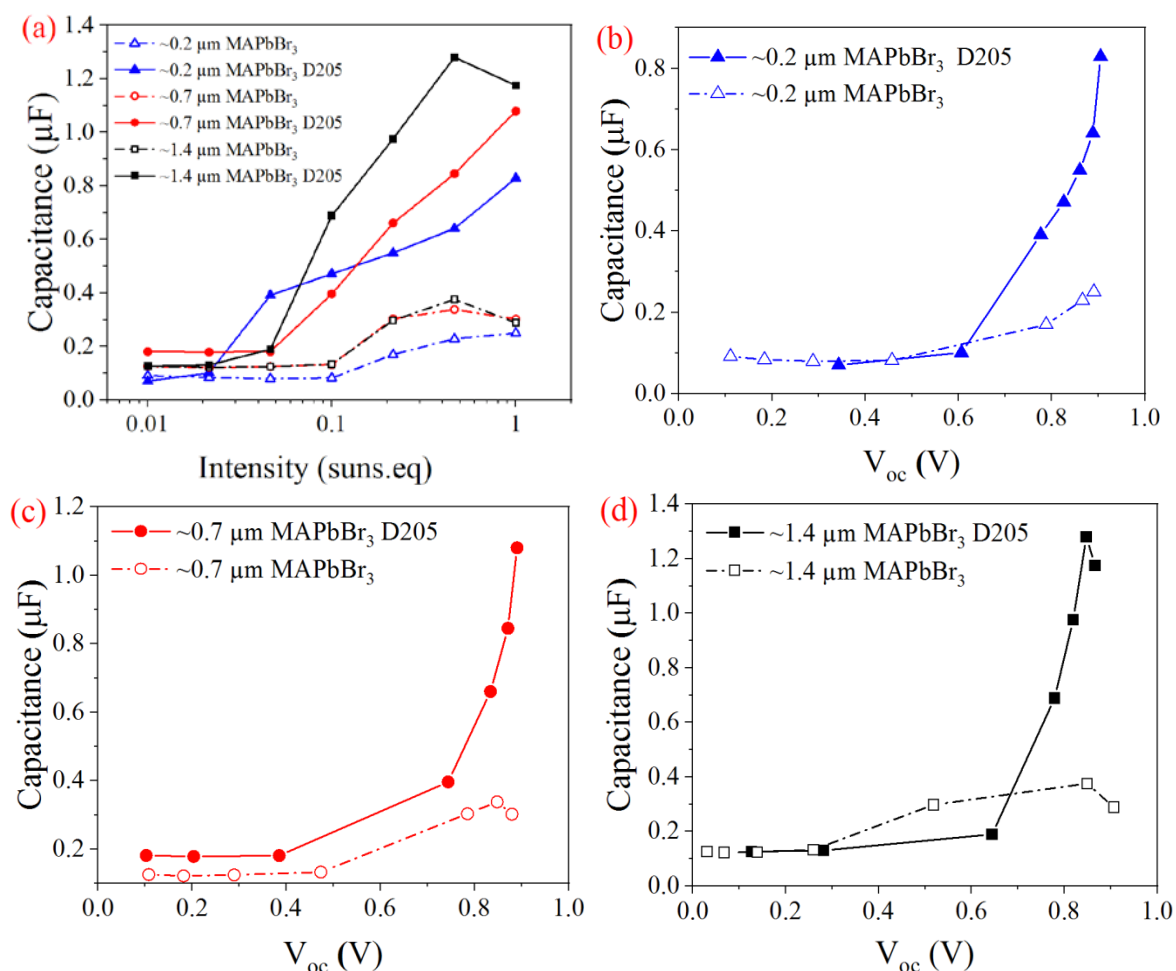


Figure 6.15: (a) Semi-logarithmic plot of the capacitance (μF) vs illumination light intensity for the three thicknesses of control and co-sensitised MAPbBr₃ perovskite solar cells. Capacitance (μF) vs the open-circuit voltage measured under varied illumination intensities for control and co-sensitised MAPbBr₃ PSC's prepared on mesoporous layer thicknesses of (b) $\sim 0.2 \mu\text{m}$ (c) $\sim 0.7 \mu\text{m}$ and (d) $\sim 1.4 \mu\text{m}$.

In Figure 6.15 (a) we see a higher capacitance for all co-sensitised cells over the range of light intensities studied. On studying Figure 6.15 (b, c and d) the control cells show a constant capacitance with increasing device V_{oc} , which highlights the geometric capacitance of the perovskite. In contrast, the co-sensitised cells show DSSC-type behaviour i.e. an increase in capacitance with voltage which is indicative of charge accumulation in the mesoporous TiO₂ layer. These results suggest that the dye either improves charge injection from the perovskite into the titania or reduces recombination of the charge stored in the mesoporous layer by passivating trap states at that interface. Injection of charge directly from the dye will also lead to charge accumulation in the TiO₂, but due to the low dye loading in these devices this effect is not likely to be significant.

As a final study of this section, the V_{oc} values of control and co-sensitised MAPbI₃ PSC's under different illumination intensities were also measured. Table 30 lists the photovoltaic performance of the hero pixels when measured at 1 sun intensity using the solar simulator. Initially, we observe similar V_{oc} values between the cells excluding the thickest control film.

Table 30: Measured photovoltaic performance values for the hero pixels of control and co-sensitised (using 1 mM D205) MAPbI₃ PSC's prepared on three thicknesses of mesoporous titania layer. The values included are those generated when measuring the pixels on the solar simulator using a 1 sun illumination intensity.

Cell ID	J_{sc} (mA/cm ²)	V_{oc} (V)	Fill Factor (%)	PCE (%)
~0.2 μ m MAPbI ₃	23.83	0.89	67	14.2
~0.2 μ m MAPbI ₃ D205	18.09	0.89	69	11.2
~0.7 μ m MAPbI ₃	20.39	0.82	73	12.2
~0.7 μ m MAPbI ₃ D205	18.35	0.91	69	11.5
~1.4 μ m MAPbI ₃	15.94	0.72	59	6.8
~1.4 μ m MAPbI ₃ D205	19.11	0.87	65	10.8

Similar V_{oc} values are observed for the impedance measured V_{oc} values at 1 sun (Figure 6.16), however as we move to lower light intensities (<0.1 suns.eq) we see a drop off in the V_{oc} of the control cells (dashed lines) whereas the co-sensitised cells (solid lines) maintain V_{oc} across the range of light intensities.

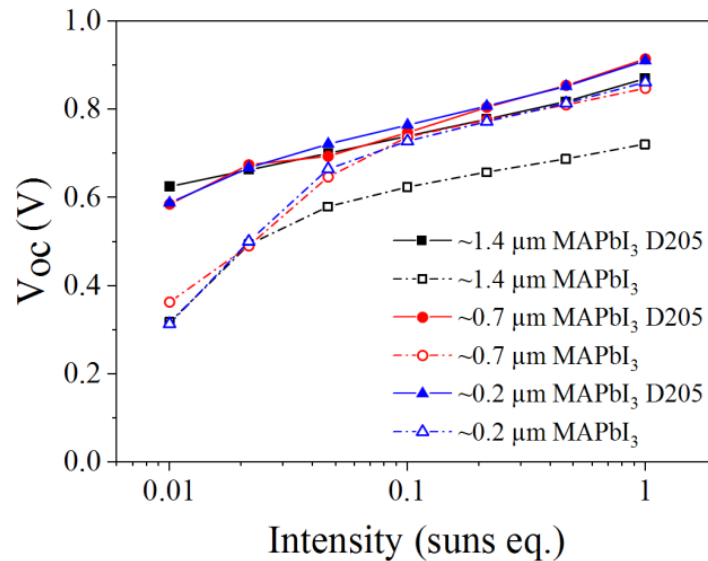


Figure 6.16: Semi logarithmic plot of open-circuit voltage vs illumination light intensity for control and co-sensitised MAPbI₃ perovskite solar cells prepared on increasing thicknesses of mesoporous layer.

The V_{oc} values of co-sensitised MAPbI₃ cells (solid lines) show a linear relationship with light intensity where the dye appears to inhibit additional V_{oc} losses, particularly for the thickest cell (~1.4 μm MAPbI₃ D205).

Overall, the results of this section indicate improved charge injection and/or reduced interfacial recombination as a result of co-sensitisation. These qualities appear to be more beneficial for thicker perovskite cells in which the carrier diffusion length becomes more comparable to the cell thickness. This has previously benefitted the cell performance where the largest improvements in efficiency (compared to control devices) have often been observed when co-sensitising cells with a thicker active layer (Section 5.3.3.2).

6.3.5 Stability

A final investigation of this work has studied the effect of co-sensitisation on the photo-stability of perovskite solar cells. Lead halide perovskites are notoriously sensitive to the ambient environment and susceptible to degradation on exposure to oxygen⁴⁸, moisture^{49,50} and UV light.⁵¹ In addition, instability can also arise due to defects which ultimately cause ion migration and molecular dissociation.⁵² Degradation has previously been found to begin at the perovskite surface due to high defect densities.⁵³⁻⁵⁶ Therefore, the use of treatments or additives capable of passivating surface defects is critical to the future development of PSC's. Here, the impact of co-sensitisation on the photo-stability of MAPbBr₃ and MAPbI₃ PSC's is assessed. Un-encapsulated control and co-sensitised (using 1.0 mM D205) PSC's prepared on three thicknesses of mesoporous layer were stored in ambient conditions (relative humidity ~50%) under constant illumination for 56 days / 8 weeks. The average cell performance and EQE response (of the hero pixels) was measured intermittently over the 8 weeks to monitor and compare any reductions in cell performance.

Figure 6.17 (a-d) show the average performance parameters for the MAPbBr₃ cells measured over the 56-day period.

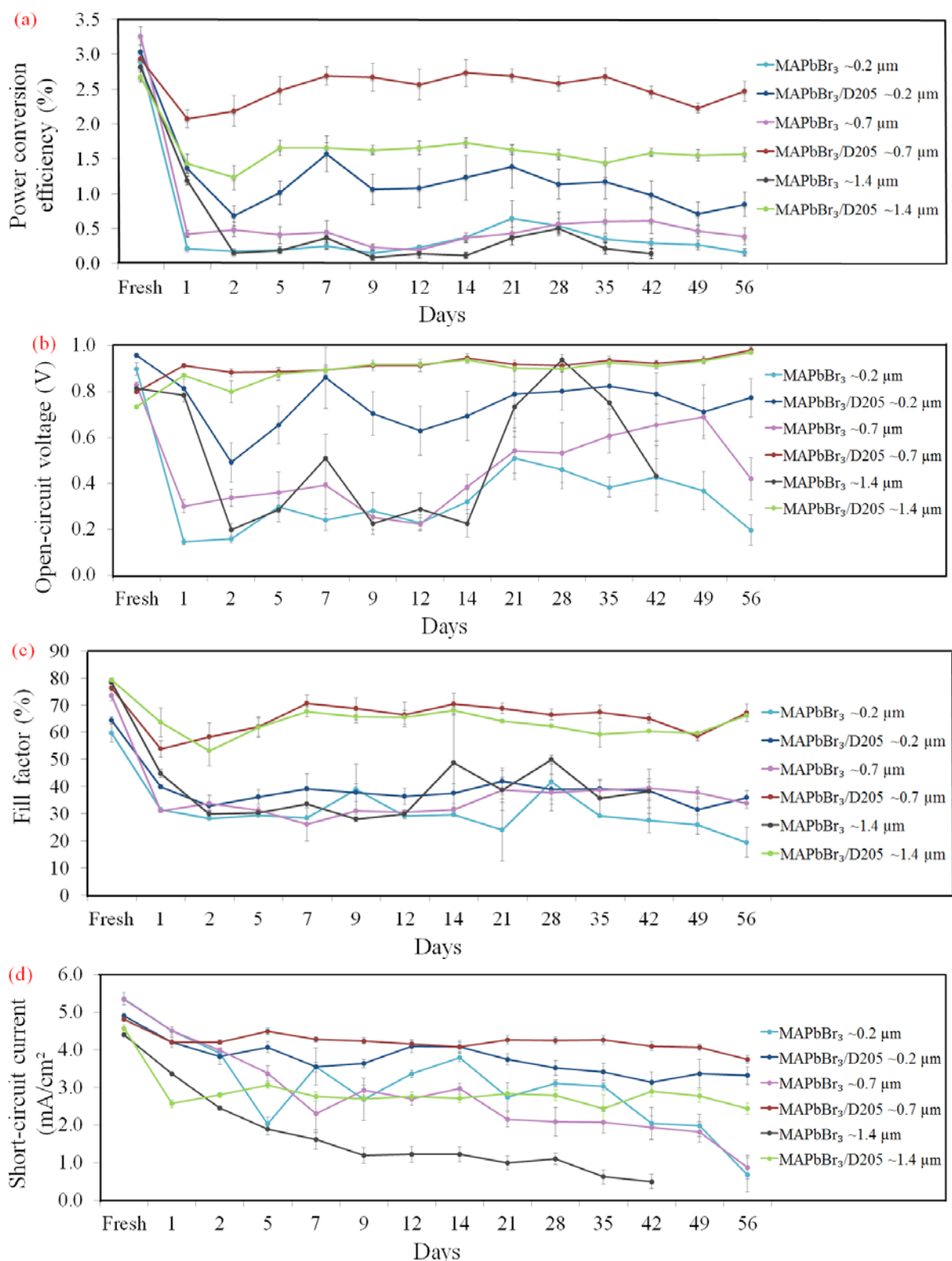


Figure 6.17: Average performance parameters (a) PCE, (b) V_{oc} , (c) FF and (d) J_{sc} for un-encapsulated control and co-sensitised MAPbBr₃ PSC's when stored ambiently under constant illumination for 56 days.

There is a decrease in PCE for all cells after 24 hours constant illumination however, the controls (Figure 6.17 (a) light blue, lilac and grey), all show a larger drop in efficiency compared to the co-sensitised cells (Figure 6.17 (a) dark blue, red and green). This is particularly noticeable for the thinnest control cells (MAPbBr₃ ~0.2 and ~0.7 μm). On studying the values in Table 31, we see the control cells all show an above 85% loss in PCE after 56 days storage. The co-sensitised cells however, show lower losses in efficiency with the lowest loss of only 14% observed for MAPbBr₃ /D205 ~0.7 μm after 8 weeks storage in a lightbox.

Table 31: Average power conversion efficiency (PCE) values and percentage loss in average PCE for the control and co-sensitised MAPbBr₃ PSC's when stored ambiently under constant illumination for 56 days.

Cell ID	Fresh PCE (%)	>56 days PCE (%)	% PCE loss
MAPbBr ₃ ~0.2 μm	2.9	0.2	93%
MAPbBr ₃ /D205 ~0.2 μm	3.0	0.8	73%
MAPbBr ₃ ~0.7 μm	3.3	0.4	88%
MAPbBr ₃ /D205 ~0.7 μm	2.9	2.5	14%
MAPbBr ₃ ~1.4 μm	2.8	0.1	96%
MAPbBr ₃ /D205 ~1.4 μm	2.7	1.6	41%

The drop in efficiency (of the control devices) appears to stem mainly from losses in V_{oc} (Figure 6.17 (b)) possibly due to increased non-radiative recombination from photo-degradation. There is also a higher degree of variability in the V_{oc} of the controls between measurements whereas the co-sensitised cells V_{oc} outputs appear more stable. Interestingly, the V_{oc} of the thickest co-sensitised cells (MAPbBr₃/D205 ~0.7 and ~1.4 μm) has increased by the end of the storage period. The co-sensitised cells also maintain higher FF values (Figure 6.17 (c)) which is particularly evident for the thickest cells (MAPbBr₃/D205 ~0.7 and ~1.4 μm). On studying the photo-current (Figure 6.17 (d)), the J_{sc} of the controls decreases with storage time indicative of material degradation. Higher J_{sc} values are observed for the co-sensitised cells due to reduced photo-degradation which possibly stems from passivated or reduced defects in the presence of the dye. Overall, the co-sensitised cells (dark blue, red, green) show better stability during the 8 week period retaining their performance and demonstrating better efficiencies in comparison to control cells. This is particularly evident for the thicker co-sensitised cells (MAPbBr₃ ~0.7 and ~1.4 μm) which

show a considerably lower degradation rate and further highlights the benefits of co-sensitisation for thicker architectures.

Figure 6.18 shows the EQE response for the hero pixel of the control and co-sensitised MAPbBr₃ cells measured ‘fresh’ after manufacture (solid lines) and following ambient storage under illumination for 56 days (dashed lines).

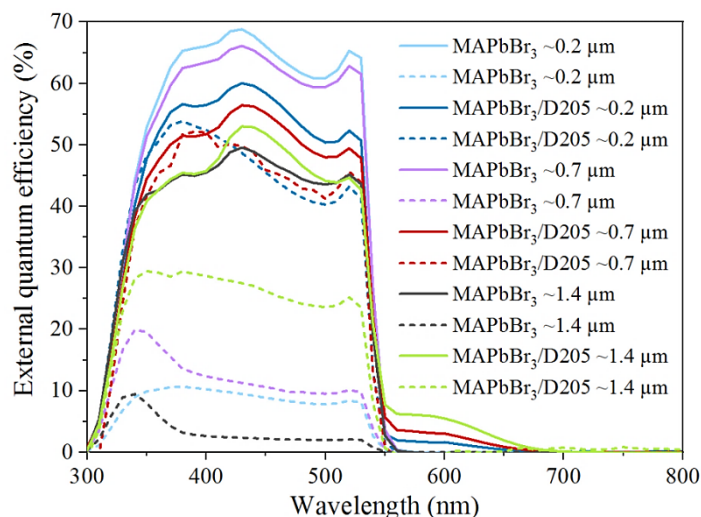


Figure 6.18: Measured EQE spectral response for the hero pixel of un-encapsulated control MAPbBr₃ and MAPbBr₃ PSC's co-sensitised with 1.0 mM D205 when prepared on three thicknesses of mesoporous titania layer. The solid and dashed lines represent measurements made when the cells were fresh and after 56 days storage in a light box, respectively.

Table 32: Tabulated values include the integrated J_{sc} values for each spectral response and the percentage loss in J_{sc} calculated from the fresh and >56 day J_{sc} values.

Cell ID	Fresh EQE J_{sc} (mA/cm ²)	>56 Days EQE J_{sc} (mA/cm ²)	% J_{sc} loss
MAPbBr ₃ ~0.2 μm	5.5	0.76	86%
MAPbBr ₃ /D205 ~0.2 μm	4.8	3.87	19%
MAPbBr ₃ ~0.7 μm	5.3	0.95	82%
MAPbBr ₃ /D205 ~0.7 μm	4.7	3.54	25%
MAPbBr ₃ ~1.4 μm	4.0	0.53	87%
MAPbBr ₃ /D205 ~1.4 μm	4.5	2.28	49%

When measured following manufacture, the co-sensitised cells (green, dark blue, red solid lines) show a clear response from the dye between 550 and 700 nm. However, after 8 weeks of continuous light soaking, this response is no longer visible showing the dye has degraded (green, dark blue, red dashed lines). Figure 6.19 includes the EQE spectral response of the

co-sensitised cells after 24 hours illumination where we see the dye signal is no longer present. Organic dyes can experience stability issues due to photo-oxidation when anchored to titania.⁵⁷ The degradation of indoline dyes in particular, has previously been reported to occur through the decarboxylation of the anchoring group which mediates desorption from the titania surface.⁵⁸ The absence of the dye response here shows the dye has degraded within the first 24 hours of lightbox storage possibly due to desorption.

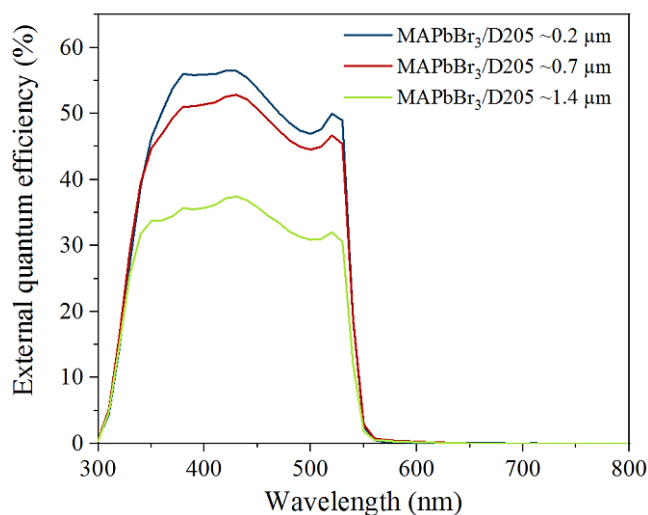


Figure 6.19: Measured EQE spectral response for the hero pixel of the un-encapsulated co-sensitised MAPbBr₃ PSC's after 24 hours illumination in a lightbox.

Despite degradation of the dye and in agreement with the performance J_{sc} data in Figure 6.17 (d), the tabulated values (Table 31) show the co-sensitised cells retain better stability in comparison to the controls, showing higher photocurrent values at the end of the 8 week stability period. The control cells show significant and similar percentage losses (Table 32) in photocurrent whereas the co-sensitised cells show lower losses with the highest loss of 49% seen for the thickest co-sensitised cell (MAPbBr₃/D205 ~1.4 μm). Despite degradation of the dye within the first 24 hours of illumination, it seems to provide some additional stability to the perovskite possibly through trap state passivation which reduces non-radiative recombination and increases the photo-stability of the material.

Figure 6.20 (a-d) shows the average performance parameters for the MAPbI₃ PSC's measured over the 56-day period.

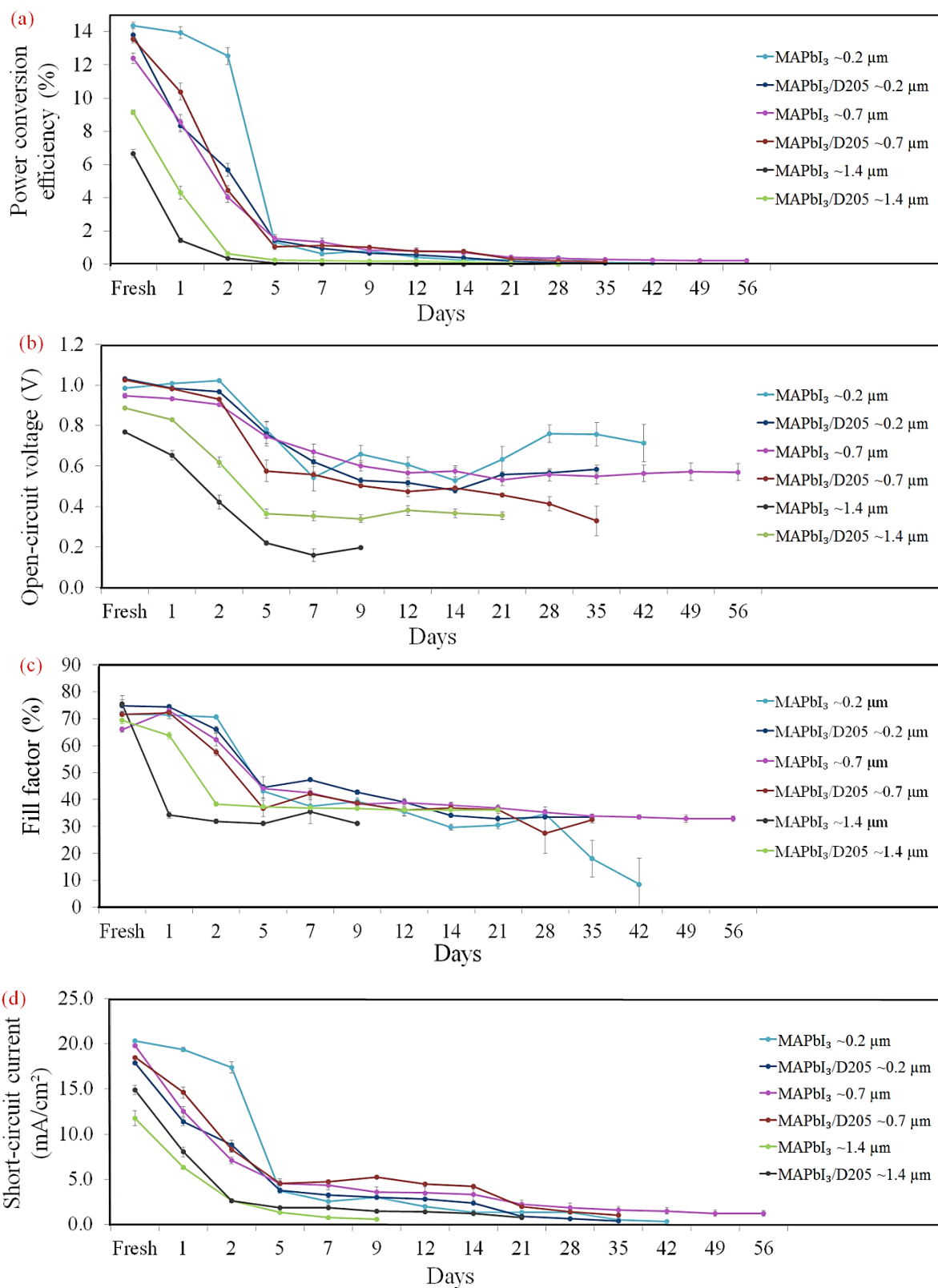


Figure 6.20: Performance parameters (a) PCE, (b) V_{oc} , (c) FF and (d) J_{sc} of un-encapsulated control and co-sensitized MAPbI₃ PSC's when stored ambiently under constant illumination for 56 days.

Initially, we see a large decrease in the PCE (Figure 6.20 (a)), where all MAPbI₃ cells have dropped below 2% efficiency by Day 5 of continuous illumination. The thinnest control cell (MAPbI₃ ~0.2 μm) initially shows slightly better stability (in terms of efficiency), but also drops significantly in PCE from Day 2. In comparison to the bromide cells, the iodide cells show very little difference in PCE following Day 5. On studying the percentage loss values in Table 33, we see all of the cells show a near 100% loss in PCE after 56 Days lightbox exposure and are therefore completely degraded.

Table 33: Average power conversion efficiency (PCE) values and percentage loss in average PCE for the control and co-sensitised MAPbI₃ PSC's when stored ambiently under constant illumination for 56 days.

Cell ID	PCE Fresh	PCE after 56 days	% PCE loss
MAPbI ₃ ~0.2 μm	14.4	0.1	99%
MAPbI ₃ /D205 ~0.2 μm	13.8	0.1	99%
MAPbI ₃ ~0.7 μm	12.4	0.2	98%
MAPbI ₃ /D205 ~0.7 μm	13.6	0.2	99%
MAPbI ₃ ~1.4 μm	6.7	0.0	100%
MAPbI ₃ /D205 ~1.4 μm	9.1	0.0	100%

The losses in PCE can be attributed to a general reduction in all parameters with lightbox storage however; the main contributor appears to be the J_{sc} (Figure 6.20 (d)) indicating a high degree of material degradation despite co-sensitisation. As mentioned previously, MAPbI₃ is less stable and more susceptible to ambient decomposition compared to MAPbBr₃ due to various compositional factors.⁵⁹ Increases in the stability of MAPbI₃ cells has previously been achieved through the use of post-annealing surface treatments^{60–62} however here, it is evident that the dye fails to increase the long term photo-stability of the MAPbI₃ cells.

6.4 Conclusions

The work completed in this Chapter has further studied the effect of co-sensitisation on the performance of lead halide perovskite solar cells. No dye-uptake was observed when co-sensitising planar MAPbBr₃ PSC's showing a mesoporous layer is essential in order to retain the dye within the active layer.

Investigations into the dye solvent revealed increased efficiencies (derived from improved FF and J_{sc}) for toluene soaked MAPbBr₃ cells thereby confirming that toluene alone, can enhance the perovskite layer and is particularly beneficial for thicker cells. In comparison to control films, toluene soaked films also showed a higher PL intensity and a longer decay lifetime, indicating better quality thin-films with a lower trap density but still failed to exceed the lifetime of the co-sensitised thin-film.

Both co-sensitised and toluene soaked MAPbBr₃ cells showed very similar series resistance values which were lower in comparison to control devices. Toluene, therefore, seems to play a key role in lowering recombination losses and improving charge transport within the active layer thereby enhancing the overall FF.

Overall, the toluene soaked data did show improved performance compared to control MAPbBr₃ cells however, the data was less consistent and unable to replicate the efficiencies of the co-sensitised MAPbBr₃ devices. These results indicate that it is the dye solution, as a whole, that further lowers recombination and enhances charge transfer in the device and therefore, there is a synergistic benefit when including both the dye and the solvent.

Further investigation into recombination losses revealed that in comparison to control devices, co-sensitised MAPbBr₃ cells showed: higher V_{oc} values, increased recombination resistance and increased capacitance at low light intensities. Co-sensitised cells also showed DSSC-type behaviour indicative of charge accumulation in the mesoporous titania layer. Due to the low levels of dye loading, this accumulation was unlikely to result from direct charge injection from the dye. This suggests that the dye either improves charge injection from the perovskite into the titania or reduces recombination of the charge stored in the mesoporous layer by passivating trap states at that interface.

Stability studies revealed co-sensitised MAPbBr₃ cells to have superior photo-stability in comparison to control devices following 56 days of storage under illumination. At the end of the 8 week period, control cells showed an >85% loss in PCE whereas the largest loss for a co-sensitised cell was 49%. Despite degradation of the dye within the first 24 hours of illumination, co-sensitised cells retained better stability, experienced reduced photo-degradation and demonstrated better efficiencies in comparison to control cells.

For MAPbI₃ PSC's, soaking in toluene was detrimental for the thinnest (~0.2 and ~0.7 μm) cells leading to perovskite degradation and compromised cell performance. Thicker MAPbI₃ cells appeared less affected by toluene soaking however, these cells still failed to outperform control devices. Steady state PL measurements of a thicker MAPbI₃ thin-film (~1.4 μm) revealed increased emission with toluene soaking, indicative of enhanced crystallisation. This was further confirmed by TRPL analysis where the toluene soaked thin-film showed the longest decay lifetime indicating reduced non-radiative recombination pathways.

Overall, treatment with toluene did show some additional benefits for thicker MAPbI₃ devices but degraded the perovskite layer of thinner cells. The thickest co-sensitised MAPbI₃ device overall showed superior performance and higher V_{oc} values (at low light intensity) indicating reduced levels of non-radiative recombination when adding a dye.

In contrast to MAPbBr₃, the stability of control and co-sensitised MAPbI₃ cells was poor. All of the cells had dropped below 2% efficiency by day 5 of continuous illumination and showed a near 100% loss in PCE after 56 days lightbox exposure indicating a high degree of material degradation despite co-sensitisation. For MAPbI₃, the dye failed to increase the long term photo-stability.

6.5 References

1. Wetzelaer, G. J. A. H. *et al.* Trap-Assisted Non-Radiative Recombination in Organic-Inorganic Perovskite Solar Cells. *Adv. Mater.* **27**, pp. 1837–1841 (2015).
2. Buin, A. *et al.* Materials processing routes to trap-free halide perovskites. *Nano Lett.* **14**, pp. 6281–6286 (2014).
3. Noel, N. K. *et al.* Enhanced photoluminescence and solar cell performance via Lewis base passivation of organic-inorganic lead halide perovskites. *ACS Nano* **8**, pp. 9815–9821 (2014).
4. Jin, J. *et al.* Enhanced Performance of Perovskite Solar Cells with Zinc Chloride Additives. *ACS Appl. Mater. Interfaces* **9**, pp. 42875–42882 (2017).
5. Mabrouk, S. *et al.* Higher efficiency perovskite solar cells using additives of LiI, LiTFSI and BMImI in the PbI₂ precursor. *Sustain. Energy Fuels* **1**, pp. 2162–2171 (2017).
6. Ding, L. & Zuo, C. An 80.11% FF record achieved for perovskite solar cells by using NH₄Cl additive. *Nanoscale* **6**, pp. 9935–9938 (2014).
7. Mei, A. *et al.* A hole-conductor-free, fully printable mesoscopic perovskite solar cell with high stability. *Science (80-.)*. **345**, pp. 295–298 (2014).
8. Kim, H.-B. *et al.* Mixed solvents for the optimization of morphology in solution-processed, inverted-type perovskite/fullerene hybrid solar cells. *Nanoscale* **6**, pp. 6679–6683 (2014).
9. Abate, A. *et al.* Supramolecular halogen bond passivation of organic-inorganic halide perovskite solar cells. *Nano Lett.* **14**, pp. 3247–3254 (2014).
10. Jiang, Q. *et al.* Surface passivation of perovskite film for efficient solar cells. *Nat. Photonics* **13**, pp. 460–466 (2019).
11. Li, Z. *et al.* Minimized surface deficiency on wide-bandgap perovskite for efficient indoor photovoltaics. *Nano Energy* **78**, 105377 (2020).
12. Zhang, H. *et al.* Improving the stability and performance of perovskite solar cells: Via off-the-shelf post-device ligand treatment. *Energy Environ. Sci.* **11**, pp. 2253–2262 (2018).
13. Guo, Q. *et al.* Passivation of the grain boundaries of CH₃NH₃PbI₃ using carbon quantum dots for highly efficient perovskite solar cells with excellent environmental stability. *Nanoscale* **11**, pp. 115–124 (2019).

14. Thambidurai, M. *et al.* Enhanced stability and photovoltaic performance of planar perovskite solar cells through anilinium thiobenzoate interfacial engineering. *J. Power Sources* **479**, 228811 (2020).
15. Xing, G. *et al.* Interfacial Electron Transfer Barrier at Compact TiO₂/CH₃NH₃PbI₃ Heterojunction. *Small* **11**, pp. 3606–3613 (2015).
16. Kim, G. Y. *et al.* Large tunable photoeffect on ion conduction in halide perovskites and implications for photodecomposition. *Nat. Mater.* **17**, pp. 445–449 (2018).
17. Guo, D. *et al.* Photoluminescence from Radiative Surface States and Excitons in Methylammonium Lead Bromide Perovskites. *J. Phys. Chem. Lett.* **8**, pp. 4258–4263 (2017).
18. Richter, J. M. *et al.* Direct Bandgap Behavior in Rashba-Type Metal Halide Perovskites. *Adv. Mater.* **30**, 1803379 (2018).
19. Droseros, N., Tsokkou, D. & Banerji, N. Photophysics of Methylammonium Lead Tribromide Perovskite: Free Carriers, Excitons, and Sub-Bandgap States. *Adv. Energy Mater.* **10**, 1903258 (2020).
20. Priante, D. *et al.* The recombination mechanisms leading to amplified spontaneous emission at the true-green wavelength in CH₃NH₃PbBr₃ perovskites. *Appl. Phys. Lett.* **106**, 081902 (2015).
21. Stolterfoht, M. *et al.* Voltage-Dependent Photoluminescence and How It Correlates with the Fill Factor and Open-Circuit Voltage in Perovskite Solar Cells. *ACS Energy Lett.* **4**, pp. 2887–2892 (2019).
22. Tvingstedt, K. *et al.* Radiative efficiency of lead iodide based perovskite solar cells. *Sci. Rep.* **4**, 6071 (2014).
23. Muthu, C., Vijayan, A. & Nair, V. C. CH₃NH₃PbBr₃ Perovskite Nanocrystals as Efficient Light-Harvesting Antenna for Fluorescence Resonance Energy Transfer. *Chem. - An Asian J.* **12**, pp. 988–995 (2017).
24. Bansal, P. & Kar, P. Probing the energy transfer process by controlling the morphology of CH₃NH₃PbBr₃ nanocrystals with rhodamine B dye. *J. Lumin.* **215**, 116609 (2019).
25. Liu, Y. *et al.* Temperature-dependent photoluminescence spectra and decay dynamics of MAPbBr₃ and MAPbI₃ thin films. *AIP Adv.* **8**, 095108 (2018).
26. Yang, Y. *et al.* Low surface recombination velocity in solution-grown CH₃NH₃PbBr₃ perovskite single crystal. *Nat. Commun.* **6**, 7961 (2015).
27. Feng, J. *et al.* Record Efficiency Stable Flexible Perovskite Solar Cell Using Effective Additive Assistant Strategy. *Adv. Mater.* **30**, 1801418 (2018).

28. Chen, Z. *et al.* Single-Crystal MAPbI₃ Perovskite Solar Cells Exceeding 21% Power Conversion Efficiency. *ACS Energy Lett.* **4**, pp. 1258–1259 (2019).
29. Stolterfoht, M. *et al.* Approaching the fill factor Shockley-Queisser limit in stable, dopant-free triple cation perovskite solar cells. *Energy Environ. Sci.* **10**, pp. 1530–1539 (2017).
30. Baig, H., Kanda, H., Asiri, A. M., Nazeeruddin, M. K. & Mallick, T. Increasing efficiency of perovskite solar cells using low concentrating photovoltaic systems. *Sustain. Energy Fuels* **4**, pp. 528–537 (2020).
31. Fong, K. C., McIntosh, K. R. & Blakers, A. W. Accurate series resistance measurement of solar cells. *Prog. Photovoltaics Res. Appl.* **21**, pp. 490–499 (2013).
32. Mundhaas, N. *et al.* Series Resistance Measurements of Perovskite Solar Cells Using Jsc–Voc Measurements. *Sol. RRL* **3**, 1800378 (2019).
33. Kim, H. Do & Ohkita, H. Potential Improvement in Fill Factor of Lead-Halide Perovskite Solar Cells. *Sol. RRL* **1**, 1700027 (2017).
34. Stolterfoht, M. *et al.* Approaching the fill factor Shockley-Queisser limit in stable, dopant-free triple cation perovskite solar cells. *Energy Environ. Sci.* **10**, pp. 1530–1539 (2017).
35. Schmidt-Mende, L., Zakeeruddin, S. M. & Grätzel, M. Efficiency improvement in solid-state-dye-sensitized photovoltaics with an amphiphilic Ruthenium-dye. *Appl. Phys. Lett.* **86**, 013504 (2005).
36. Schmidt-Mende, L. & Grätzel, M. TiO₂ pore-filling and its effect on the efficiency of solid-state dye-sensitized solar cells. *Thin Solid Films* **500**, pp. 296–301 (2006).
37. Contreras-Bernal, L. *et al.* Impedance analysis of perovskite solar cells: A case study. *J. Mater. Chem. A* **7**, pp. 12191–12200 (2019).
38. Correa-Baena, J. P. *et al.* Changes from Bulk to Surface Recombination Mechanisms between Pristine and Cycled Perovskite Solar Cells. *ACS Energy Lett.* **2**, pp. 681–688 (2017).
39. Pockett, A. Characterization of Perovskite Solar Cells. *Univ. Bath* (2016).
40. Aranda, C., Guerrero, A. & Bisquert, J. Ionic Effect Enhances Light Emission and the Photovoltage of Methylammonium Lead Bromide Perovskite Solar Cells by Reduced Surface Recombination. *ACS Energy Lett.* **4**, pp. 741–746 (2019).
41. Falaras, P. *et al.* Dye Sensitization of Titania Compact Layer for Efficient and Stable Perovskite Solar Cells. *ACS Appl. Energy Mater.* **1**, pp. 6161–6171 (2018).

42. Bisquert, J. Chemical capacitance of nanostructured semiconductors: Its origin and significance for nanocomposite solar cells. *Phys. Chem. Chem. Phys.* **5**, pp. 5360–5364 (2003).
43. Van De Lagemaat, J., Park, N. G. & Frank, A. J. Influence of Electrical Potential Distribution, Charge Transport, and Recombination on the Photopotential and Photocurrent Conversion Efficiency of Dye-Sensitized Nanocrystalline TiO₂ Solar Cells: A Study by Electrical Impedance and Optical Modulation Tec. *J. Phys. Chem. B* **104**, pp. 2044–2052 (2000).
44. Pockett, A. *et al.* Characterization of planar lead halide perovskite solar cells by impedance spectroscopy, open-circuit photovoltage decay, and intensity-modulated photovoltage/photocurrent spectroscopy. *J. Phys. Chem. C* **119**, pp. 3456–3465 (2015).
45. Pockett, A. *et al.* Microseconds, milliseconds and seconds: Deconvoluting the dynamic behaviour of planar perovskite solar cells. *Phys. Chem. Chem. Phys.* **19**, pp. 5959–5970 (2017).
46. Ebadi, F., Taghavinia, N., Mohammadpour, R., Hagfeldt, A. & Tress, W. Origin of apparent light-enhanced and negative capacitance in perovskite solar cells. *Nat. Commun.* **10**, 1574 (2019).
47. Moia, D. *et al.* Ionic-to-electronic current amplification in hybrid perovskite solar cells: Ionically gated transistor-interface circuit model explains hysteresis and impedance of mixed conducting devices. *Energy Environ. Sci.* **12**, pp. 1296–1308 (2019).
48. Bryant, D. *et al.* Light and oxygen induced degradation limits the operational stability of methylammonium lead triiodide perovskite solar cells. *Energy Environ. Sci.* **9**, pp. 1655–1660 (2016).
49. Frost, J. M. *et al.* Atomistic origins of high-performance in hybrid halide perovskite solar cells. *Nano Lett.* **14**, pp. 2584–2590 (2014).
50. Yang, J., Siempelkamp, B. D., Liu, D. & Kelly, T. L. An Investigation of CH₃NH₃PbI₃ Degradation Rates and Mechanisms in Controlled Humidity Environments Using in situ Techniques. *ACS Nano* **9**, pp. 1955–1963 (2015).
51. Leijtens, T. *et al.* Overcoming ultraviolet light instability of sensitized TiO₂ with meso-superstructured organometal tri-halide perovskite solar cells. *Nat. Commun.* **4**, 2885 (2013).
52. Zhang, S. & Han, G. Intrinsic and environmental stability issues of perovskite photovoltaics. *Prog. Energy* **2**, 2 (2020).

53. Azpiroz, J. M., Mosconi, E., Bisquert, J. & De Angelis, F. Defect migration in methylammonium lead iodide and its role in perovskite solar cell operation. *Energy Environ. Sci.* **8**, pp. 2118–2127 (2015).
54. Yang, B. *et al.* Perovskite Solar Cells with Near 100% Internal Quantum Efficiency Based on Large Single Crystalline Grains and Vertical Bulk Heterojunctions. *J. Am. Chem. Soc.* **137**, pp. 9210–9213 (2015).
55. Ball, J. M. & Petrozza, A. Defects in perovskite-halides and their effects in solar cells. *Nat. Energy* **1**, 16149 (2016).
56. Hou, M. *et al.* Aryl Diammonium Iodide Passivation for Efficient and Stable Hybrid Organ-Inorganic Perovskite Solar Cells. *Adv. Funct. Mater.* **30**, 2002366 (2020).
57. Sauvage, F. A Review on Current Status of Stability and Knowledge on Liquid Electrolyte-Based Dye-Sensitized Solar Cells. *Adv. Chem.* **16**, pp. 1–23 (2014).
58. Tanaka, H. *et al.* Long-term durability and degradation mechanism of dye-sensitized solar cells sensitized with indoline dyes. *Sol. Energy Mater. Sol. Cells* **93**, pp. 1143–1148 (2009).
59. Zheng, X. *et al.* The Controlling Mechanism for Potential Loss in CH₃NH₃PbBr₃ Hybrid Solar Cells. *ACS Energy Lett.* **1**, pp. 424–430 (2016).
60. Zheng, X. *et al.* Defect passivation in hybrid perovskite solar cells using quaternary ammonium halide anions and cations. *Nat. Energy* **2**, 17102 (2017).
61. Jiang, Y. *et al.* Post-annealing of MAPbI₃ perovskite films with methylamine for efficient perovskite solar cells†. *Mater. Horizons* **3**, pp. 548–555 (2016).
62. He, Q. *et al.* Surface passivation of perovskite thin films by phosphonium halides for efficient and stable solar cells. *J. Mater. Chem. A* **8**, pp. 2039–2046 (2020).

7 Conclusions and further work

An initial series of investigations sought to characterise MAPbBr₃ perovskite to define the wavelength range over which organic dyes could be implemented as complementary absorbers. From a co-sensitisation perspective, the band gap position of MAPbBr₃ (2.3 eV) is ideal as one can use a dye with absorbance >540 nm which allows the dye and perovskite response to be studied without signal overlap. The wide bandgap produces large photovoltages and therefore higher efficiencies are potentially achievable through co-sensitisation which may, in future, prove beneficial for tandem PV systems.

Through optimisation, higher MAPbBr₃ cell efficiencies were achieved by depositing the compact titania layer using spray pyrolysis as opposed to spin-coating and through the use of a PTAA hole transport as opposed to spiro-OMeTAD. The morphology of the perovskite layer was enhanced through introducing DMSO into the perovskite precursor solution, using a lower annealing temperature (60°C) and on introducing a diethyl ether anti-solvent drip, all of which increased the device efficiency. The initial aims of this Chapter were to characterise MAPbBr₃ perovskite and develop a reproducible cell build method capable of manufacturing MAPbBr₃ cells which consistently achieved >1% efficiency. The final optimised build method significantly exceeded this target and produced MAPbBr₃ cells >5% efficiency with low variability despite preparation in an ambient environment. Therefore, using the new optimised method, MAPbBr₃ PSC's could be reproducibly manufactured with limited variation in the perovskite layer allowing any effects produced through co-sensitisation to be quantified.

In Chapter 4, the photochemistry of six organic dyes was characterised to identify which could offer the best complementary absorbance to MAPbBr₃ perovskite. Two organic blue dyes which were characterised, included a squaraine dye (SQ2) and a diketopyrrolopyrrole dye (Dyename blue). Both dyes absorb in the 300 - 700 nm range however, whereas SQ2 has the largest extinction coefficient ($2.3 \times 10^5 \text{ M}^{-1}\text{cm}^{-1}$), Dyename blue was found to have one of the lowest molar extinction coefficients ($4.8 \times 10^4 \text{ M}^{-1}\text{cm}^{-1}$) of the dyes studied. In terms of red dyes, it was found that D205 could offer a slight extension of the MAPbBr₃

absorbance range in addition to a high molar extinction coefficient ($6.5 \times 10^4 \text{ M}^{-1} \text{ cm}^{-1}$). Therefore, D205 and SQ2 were selected as the organic dyes which would offer the strongest complementary absorbance to MAPbBr₃ perovskite.

Initial proof of principle investigations into the co-sensitisation of MAPbBr₃ perovskite thin films revealed successful dye uptake into the active layer, indicated by a colour change of the film, with no perovskite degradation when using toluene as the dye solvent.

This confirmed the possibility of colour tuning the perovskite layer (through co-sensitisation) to manufacture cells with greater colour control and an improved aesthetic appeal. In addition, the absorbance range of devices co-sensitised with SQ2 was extended from 540 nm to 720 nm and produced higher PCE values (+1%) with a 2% contribution of photocurrent from the dye.

Investigating two different routes of dye introduction into the perovskite cell architecture revealed that devices co-sensitised using the ‘dye-after’ method (where the thin-film was sensitised after annealing the perovskite) demonstrated overall increased performance where average efficiencies increases of 0.4 and 0.6% were observed for SQ2 and D205, respectively. Interestingly, while ‘hero’ co-sensitised devices showed improved J_{sc} and a general improvement in performance over non-sensitised devices, improvement in the fill FF appeared an important parameter for improved device efficiencies. Cells co-sensitised using the dye before method (where the thin-film was sensitised before perovskite deposition) showed losses in PCE possibly due to the dye occupying space within the mesoporous layer which negatively affected the crystallisation of the perovskite. Alternatively, it is thought that the dye-after method encouraged the dye to fill any remaining space on the titania surface allowing colour tuning whilst increasing the device efficiency.

In order to maximise dye loading, experimentation focussed on varying the dye concentration and mesoporous titania layer thickness.

The highest average PCE’s of 2.0 and 2.3% were observed for SQ2 and D205, respectively when using a 1.0 mM dye concentration. Despite increasing dye concentration, co-sensitised cells showed decreased average J_{sc} with efficiency increases resulting from enhanced FF. For D205 however, EQE measurements of hero pixels showed an increase in the perovskite

signal of between 2 and 15% for three of the four dye concentrations tested (0.05-1.0 mM) indicating that the dye solution played a role in improving the perovskite layer. Highly concentrated dye solutions (1.5 mM, D205) however, appeared detrimental to cell performance possibly due to dye aggregation indicating that there is a limit on the amount of dye that can beneficially added to a system.

On increasing the mesoporous layer thickness, the co-sensitised cells showed superior performance across the seven thicknesses tested. The largest benefits on adding a dye were seen for the thicker cells ($> 1 \mu\text{m}$) where increased efficiencies resulted from enhanced FF and J_{sc} . The largest contributions of photocurrent from the dye were also seen for the thickest cells confirming increased dye loading had been achieved by increasing the active layer thickness. However, a large reduction in the perovskite EQE signal was also observed for the thickest devices (~ 2.0 and $\sim 3.9 \mu\text{m}$) indicating a fine balance been maximising the dye response whilst maintaining the photocurrent generated from the perovskite.

Desorbing and quantitating the dye from co-sensitised cells further confirmed that dye loading had increased with active layer thickness where the desorbed dye concentration ranged from 3-9 μM for the thinnest and thickest cells, respectively.

The transferability of the dye after method was tested by co-sensitising MAPbI_3 perovskite solar cells. The opaque dark brown colour of MAPbI_3 perovskite prevented visual colour tuning of the active layer however, co-sensitised devices showed increased efficiencies for five out of seven of the mesoporous layer thicknesses ($> 0.4 \mu\text{m}$) tested with efficiency increases resulting from enhanced FF and V_{oc} . Co-sensitisation was detrimental for MAPbI_3 cells with a thinner active layer (~ 0.2 and $\sim 0.4 \mu\text{m}$) causing a large drop in the photocurrent. In Chapter 6, this was shown to result from the dye solvent, toluene degrading the perovskite layer therefore, re-evaluation of the dye solvent is needed for future studies when co-sensitising MAPbI_3 perovskite.

Prior to commencing this work, it was anticipated for MAPbBr_3 cells that increases in efficiency would generally result from the additional photocurrent contributed by the dye due to increased absorption in the visible. However, the efficiency increases were mainly derived from the fill factor which was consistently and often significantly enhanced with co-sensitisation. Increases in short-circuit current were occasionally seen when adding a dye

and EQE measurements showed some additional photocurrent contribution from the dye itself however, this was not substantial enough to cause the observed increases. The main increase in J_{sc} appeared to result from improved response from the perovskite EQE (300 nm – 550 nm) as a result of co-sensitisation. Co-sensitisation was also found to be more beneficial for thicker perovskite cells, which inherently have a higher defect density and where the carrier diffusion length became more comparable to the device thickness. These findings, suggest that the dye solvent or solution (as a whole) is passivating defects within the perovskite layer resulting in reduced non-radiative recombination and enhanced charge transfer. By introducing the dye after perovskite deposition, it was possible that the dye solution effectively ‘healed’ defects within the perovskite layer and therefore, in a way, acted as an additive treatment.

The effects of co-sensitisation and the relationship between the dye and perovskite were further investigated in Chapter 6. Planar MAPbBr₃ PSC’s showed no dye-uptake following co-sensitisation which showed the inclusion of a mesoporous layer was essential to retain the dye within the active layer. Despite failing to outperform the mesoporous architectures, the perovskite EQE in the planar co-sensitised cell was enhanced as a result of co-sensitisation suggesting that the dye solvent was improving the perovskite in the absence of the dye.

Further investigations into the effect of toluene revealed increased efficiencies for MAPbBr₃ cells after soaking in toluene. Increases were derived from improved FF and J_{sc} confirming that, toluene alone enhanced the perovskite layer, having a greater effect on thicker cells. In addition, toluene soaked thin-films generated a higher steady-state PL intensity and a longer PL decay over control thin-films showing the perovskite to be of better quality with less defects following toluene treatment.

When comparing the estimated series resistance, both co-sensitised and toluene soaked MAPbBr₃ cells showed very similar values which were lower in comparison to control devices. The dye solvent, therefore, potentially played a key role in reducing the series resistance which lowered recombination losses and improved charge extraction thereby enhancing the FF of the co-sensitised devices. The series resistance values in this study, however, were only approximate due to being calculated from the J-V curve. Therefore, in

future, impedance spectroscopy could be used to provide more accurate series resistance values which may provide further insight here.

Overall, despite an improvement in performance (compared to control devices), the toluene soaked data was less consistent and unable to replicate the efficiencies of the co-sensitised devices which showed higher FF and J_{sc} values. In addition to increased efficiencies, co-sensitised thin-films also showed a longer decay lifetime compared to control and toluene soaked thin-films indicative of a lower trap state density.

Therefore, as a collective solution, it's possible that during co-sensitisation, toluene acted as a passivating treatment to enhance the perovskite layer whilst the sensitising dye further acted to lower recombination losses *via* passivation but also provided an additional photocurrent contribution by extending the absorbance range. This then improved the overall cell performance and showed there was a synergistic benefit when including both the dye and the solvent.

Impedance studies performed on control and co-sensitised MAPbBr₃ devices, revealed co-sensitised devices to have higher recombination resistance and V_{oc} under lower light intensities. Co-sensitised cells also showed higher capacitance and DSSC-type behaviour indicative of charge accumulation in the mesoporous titania layer whereas control cells showed constant capacitance with increasing V_{oc} in line with the geometric nature of the perovskite. For the co-sensitised cells, injection directly from the dye would cause charge accumulation in the TiO₂ however; due to the low dye loading this affect was unlikely. Therefore, the dye either improved charge injection from the perovskite into the TiO₂ or was reducing recombination of the charge stored in the TiO₂ by trap state passivation. These effects were more evident for thicker co-sensitised devices where, in performance studies, they have proven highly beneficial and often translated into significant increases in device efficiency. In future, this may be beneficial for indoor or lower light level PV systems including within the rapidly expanding internet of things market.

Following 56 days of storage under illumination, co-sensitised MAPbBr₃ cells showed superior efficiency and photo-stability in comparison to control devices. Efficiency losses for the control devices were mainly derived from decreased V_{oc} and J_{sc} as a result of un-passivated defects which ultimately accelerated material degradation. Despite degradation

of the dye within the first 24 hours of storage, the co-sensitised cells still demonstrated better photo-stability, reduced photo-degradation and higher efficiencies. This was particularly evident for thicker co-sensitised devices (~ 0.7 and ~ 1.4 μm) which showed a considerably lower degradation rate due to greater defect passivation as a result of increased dye loading in the active layer.

In contrast to MAPbBr_3 devices, soaking in toluene appeared detrimental for MAPbI_3 PSC's leading to perovskite degradation and decreased cell performance. Thicker MAPbI_3 cells appeared less affected by toluene soaking but still failed to outperform control devices.

Despite this finding, a thicker MAPbI_3 film soaked in toluene showed increased PL emission and a longer decay lifetime compared to control and co-sensitised MAPbI_3 thin films indicating enhanced perovskite crystallisation and reduced defects. This is possibly due to toluene selectively dissolving defects in the perovskite layer thereby leaving less material which is of better quality however; this would need to be confirmed through further analysis. Overall, treatment with toluene did show some additional benefits for thicker MAPbI_3 devices but failed to exceed the efficiencies of both control and co-sensitised cells and degraded the perovskite layer of thinner cells. On including a dye, the thickest co-sensitised MAPbI_3 cell showed superior performance in comparison to the control devices with increased efficiencies having derived from V_{oc} and FF. Co-sensitised MAPbI_3 cells also showed higher V_{oc} values under reduced illumination showing the dye was inhibiting additional V_{oc} losses through trap state passivation.

On studying the stability of control and co-sensitised MAPbI_3 cells, all device efficiencies had dropped below 2% by day 5 of continuous illumination and showed a near 100% loss in PCE after 56 days lightbox exposure. Therefore, despite co-sensitisation, MAPbI_3 cells showed a high degree of material degradation and the dye failed to increase the long term photo-stability.

Overall the work presented in this thesis has shown the ability to tune the colour of perovskite solar cells and increase device efficiencies through co-sensitisation with organic dyes. Further investigation into the effects of co-sensitisation have shown that the dye solution can act as both a treatment and a second sensitizer in the device by passivating

defects and lowering recombination losses whilst increasing the light harvesting range and overall performance. For thicker PSC's which have a higher defect density, the added benefits of co-sensitisation have proven more beneficial and often generated significant increases in device efficiency. These findings could be beneficial for the scalability of PSC's where thicker active layers are more desirable for large scale manufacture and high throughput processing such as roll to roll printing. The successful co-sensitisation of MAPbI₃ PSC's has also confirmed the transferability of the method where benefits were seen for thicker cells however, toluene acts as a solvent for I₂ and therefore, an alternative dye solvent would be needed in future to avoid the degradation of thinner MAPbI₃ devices. In addition, when co-sensitising MAPbI₃ devices during this research, it was not possible to quantify the photocurrent contribution from the dye as its EQE signal was completely masked by the perovskite. With this in mind, investigation into the co-sensitisation of MAPbI₃ with near infrared dyes could provide insight here and may prove beneficial if of a complementary absorbance range to MAPbI₃.

The 'dye-after' co-sensitisation method used in this work could be considered analogous to the use of additive treatments or SAM's. However, co-sensitising lead halide PSC's with organic dyes has increased functionality as it can not only colour the perovskite layer but also offer additional photocurrent by extending the absorption range. Akin to SAMS, it would be interesting in future to investigate the effects of sensitising the compact titania layer/blocking layer prior to deposition of the perovskite to determine if adding a dye here could reduce interfacial recombination.